Sediment-Hosted Pb-Zn-Ba Mineralisation at Macmillan Pass, Yukon (Canada) –
Hydrothermal Fluid Chemistry and Mineralising Processes

By

Joseph Michael Magnall

A thesis submitted in partial fulfillment of the requirements for the degree of

Doctor of Philosophy

Department of Earth and Atmospheric Sciences

University of Alberta

Abstract

Sediment-hosted massive sulphide (SHMS) deposits form huge enrichments of reduced sulphur in sedimentary basins, typically in the form of pyrite, galena and sphalerite. In the Selwyn Basin (Canada), this type of metallogenesis occurs as stratiform and stratabound (bedded) sulphides within carbonaceous mudstones (clastic-dominated; CD-type). Previous models have interpreted this relationship to be the direct result of a stagnant water column, enriched in reduced sulphur (euxinic), trapping metal rich hydrothermal fluids and forming sedimentary exhalative (SEDEX) style mineralisation. However, there are limited constraints on vent fluid geochemistry in CD-type systems and there are periodic debates concerning the environment of mineralisation (i.e. whether the ore forms in the water column vs. sub seafloor).

In this thesis, work has focused on two Late Devonian SEDEX-style deposits at Macmillan Pass. The complete deposit architecture is preserved at these localities – samples of the vent complex, which represents the primary conduit of fluid up-flow, overlying bedded sulphides, and surrounding host rock provide the opportunity to evaluate how hydrothermal fluids evolved geochemically in these settings. Particular focus has been directed towards evaluating the extent to which carbonaceous mudstones impact metal solubility, and determining the relative importance of euxinic conditions, and diagenetic processes operating beneath the seafloor. This has been attempted using a variety of techniques, including: petrography and thermodynamic modeling; bulk rock geochemistry; isotopic microanalysis (δ^{34}S values in pyrite and barite); analysis of sulphide mineral separates for δ^{34}S values; in situ (LA-ICP-MS) rare earth element analysis in carbonates; strontium isotope analysis of carbonates;

fluid inclusion microthermometry and gas analysis.

Combined, the results presented in this thesis provide evidence of steep thermal and chemical gradients that developed spatially and temporally during the evolution of hydrothermal activity at Macmillan Pass. Importantly, this has led to the development of a new model to explain mineralisation at this locality, which has implications for the interpretation of similar systems in the Selwyn Basin as well as in other sedimentary basins from the geologic record. The radiogenic composition of strontium isotopes in carbonate from the vent complex is evidence that metals were sourced from deep within the basin – likely from clastics derived from the underlying crystalline basement. Importantly, the tectonic activity that promoted fluid up-flow from deep within the basin also led to enhanced circulation of fluids at shallower levels of the basin. Specifically, reducing, methane-bearing diagenetic fluids – highly effective at mobilising barium from organic rich lithologies – precipitated barite upon interaction with sulphate in a shallow diagenetic setting. In this diagenetic environment, both barite precipitation and sulphate reduction associated with methane oxidation served to enrich partially lithified sediments in sulphur. The metal rich hydrothermal fluid, which was hot (>275°C), entered this environment and precipitated sulphides in a sub-seafloor setting, with barite dissolution providing an important source of sulphur for metal deposition. High biological productivity, host rock organic matter content, fluid mobility in partially lithified sediments, deep basin penetrating faults, hot fluids (metal transport) and concentration of sulphur in the host rock were the most important factors for the development of CD-type systems at Macmillan Pass.

In a broader context, the lower concentrations of seawater sulphate, relative to modern day oceans, is an important factor to consider in terms of the mass balance of SHMS

systems in the geologic record. This specifically relates to sulphate availability, pathways of sulphate reduction and the formation of an effective metal trap. The work in this thesis provides evidence that a combination of pathways were more effective than single step processes operating in a euxinic water column.

Preface

This thesis presents research conducted under the supervision of Dr. Sarah Gleeson at the University of Alberta.

Chapter 2 of the thesis is accepted and in press as: Magnall, J.M., Gleeson, S.A., Paradis, S., 2015. The importance of siliceous, radiolarian bearing mudstones in the sediment-hosted Zn-Pb ± Ba mineralisation in the Selwyn Basin, Yukon, Canada. *Scientific Communications, Economic Geology*.

J. Magnall and Drs. S. Gleeson and S. Paradis collected the samples. J. Magnall was responsible for conceptualisation of the paper. ACME laboratories produced lithogeochemical analyses of major elements. Drs. Gleeson and Paradis contributed to discussions in the field and manuscript edits.

Chapter 3 has been submitted and is in review with *Geochimica et Cosmochimica Acta* as: Magnall, J.M., Gleeson, S.A., Stern, R.A., Newton, R.J., Poulton, S. and Paradis, S., 2015. The role of diagenetic processes in the formation of shale hosted massive sulphide deposits - a sulphur and oxygen isotopic study of barite and pyrite from the Late Devonian Tom and Jason deposits, Selwyn Basin, Canada.

J. Magnall and Dr Gleeson collected the samples. Petrographic analysis was conducted by J. Magnall, and sample preparation for SIMS analysis by J. Magnall with assistance from Dr. Stern. Dr. Poulton trained J. Magnall in the Fe-extraction technique for bulk-rock pyrite sulphur isotope analysis. Drs. R. Newton and R. Stern performed analysis of sulphur isotopes via respective gas source mass spectrometry and secondary ion mass spectrometry. J. Magnall was responsible for manuscript composition, and all

authors contributed to manuscript edits.

Chapter 4 has been prepared for submission to *Geochimica et Cosmochimica Acta* as: Magnall, J.M., Gleeson, S.A., Blamey, N.F., Paradis, S., Luo, Y., 2015. Vent complex geochemistry in sediment-hosted massive sulphide systems at Macmillan Pass, Yukon.

J. Magnall and Dr. Gleeson collected the samples. J. Magnall conducted the petrography, thermodynamic modeling and fluid inclusion microthermometry. Dr. Blamey acquired the fluid inclusion gas data. Dr. Steve Taylor (University of Calgary Isotope Laboratory) was responsible for sulphur isotope analysis via gas source mass spectrometry. Dr. Luo tuned and operated the LA-ICP-MS system and J. Magnall reduced the data with assistance from Dr. Luo. J. Magnall was responsible for manuscript composition, and all authors contributed to manuscript edits.

Chapter 5 has been prepared for submission to *Economic Geology* as: Magnall, J.M., Gleeson, S.A., Creaser, R.A. and Paradis, S. Mineralising processes in sediment-hosted Zn-Pb-Ba systems – deposit genesis at Macmillan Pass, Yukon.

J. Magnall conducted all petrography. Dr. Creaser was responsible for the strontium isotope analysis of carbonates. Dr. Steve Taylor (University of Calgary Isotope Laboratory) was responsible for carbon and oxygen isotope analysis via gas source mass spectrometry. J. Magnall was responsible for manuscript composition.

Acknowledgements

First and foremost, I would like to warmly thank and acknowledge my PhD supervisor, Dr Sarah Gleeson for her continued enthusiasm, patience and also friendship, which has contributed enormously to all aspects of this project. In particular, I have valued immensely the working environment you have fostered, one in which there has been the opportunity and resources to work without restriction as the project has evolved and interests have peaked in certain areas. The freedom to pursue ideas, combined with your judgment, interest and availability in discussion, has been integral for producing this thesis. I know I have been very lucky in this regard, and it is remarkable that you continued to tolerate such an accident-prone Englishman during not one, but two field seasons up north! For all the financial and logistical support, and the discussions that occurred up at Macmillan Pass, acknowledgement is given to the GSC (TGI-4 initiative), and specifically Suzanne Paradis, along with Dan Lleyton-Matthews, Jan Mike Gadd and Jan Peter.

The work presented in this thesis has also benefited from ideas developed through discussions with a number of other people, including those on my committee, Nicholas Harris and Rob Creaser; Robert Newton and Simon Poulton during time spent in the department at Leeds; and Duane Petts, Tom Chacko and Jeremy Richards. I would also like to acknowledge Richard Stern and Andrew Locock for their commitment and expertise in producing high quality data, and the interested questions asked along the way. Jesse, Josh, and Duane – you have all been both great colleagues and friends, and conversations with you regarding many different aspects of geology have frequently left me feeling inspired and with enthusiasm renewed. The number of friends I have been fortunate to meet in Edmonton, who have made my experience here immeasurably better, are too numerous to mention; I thank those of you who welcomed me at the beginning, and those who put up with my less fun, more stressed appearance towards the end. I look forward to having a network of such great people – living in exciting places and doing interesting things – to visit in the future! Finally, special acknowledgement goes to Janina, for her kindness, love and friendship, and to Mum, Dad and the rest of the family – thank-you for your support and encouragement throughout my academic journey, it would not have been possible without you.

Table of Contents

LIST OF TABLES

LIST OF FIGURES

Chapter 1. Introduction

1.1. Sediment-hosted Pb-Zn deposits

Ore deposits are economic enrichments of minerals or mineral aggregates formed via geological processes, and may occur in a range of different lithologies and tectonic settings. For global resources of Pb and Zn, deposits in sedimentary basins are most important (Singer, 1995; Leach et al., 2005). In recent history, Pb and Zn have been mined for their respective uses in the production of lead-acid batteries and galvanised steel. Between 2009 and 2013, global production of Pb increased by 52% and Zn by 16% (Brown et al., 2015), and looking forward, continued industrialisation and economic growth in countries such as China and India mean consumption of these resources is set to continue. Therefore new discoveries will be essential for sustaining this growth, and understanding why certain sedimentary basins are host to anomalous enrichments of Pb and Zn is a fundamental question of both economic and geological value.

A variety of mineralisation styles (epigenetic, stratabound, stratiform, replacement) and host-lithologies (carbonate, mudstone, siltstone, sandstone) occur in sediment-hosted Pb-Zn deposits, and these parameters are used as a basis for sub-classification (e.g. Leach et al. 2005; Wilkinson, 2014): (1) Mississippi Valley-type (MVT) deposits are hosted in carbonate platform sequences, form epigenetic and replacement-style mineralisation, and are thought to form tens to hundreds of million years after deposition of the host rock (Leach and Sangster, 1993; Leach et al., 2005), (2) Irish-type deposits are hosted in mixed carbonate-siliciclastic sequences, with

replacement-style mineralisation occurring pre-lithification during diagenesis (Wilkinson, 2003), (3) Clastic-Dominated (CD-type) deposits are hosted by siliciclastic lithologies (mudstones, siltstones, sandstones), and have complex mineralisation styles (stratabound and stratiform) that are laterally extensive and can appear bedding parallel (Leach et al. 2005) – this has led to the suggestion that CD-type mineralisation occurs during sedimentation of the host rock (i.e. syn-sedimentary). The three sediment-hosted Pb-Zn deposit types (MVT, Irish-type, CD-type) described above, although different in many ways, have unifying features that include an absence of direct magmatic input, and a source of sulphur that is ultimately derived from seawater sulphate. In general the sub-classification of sediment-hosted deposits is based upon host lithology and ore morphology, not by mineralisation processes.

Clastic Dominated-type deposits host more than 50% of known global Pb and Zn reserves, often in high tonnage systems (>50 Mt Pb+Zn; Goodfellow and Lydon, 2007). Indeed, 9 of the 10 largest sediment-hosted Pb-Zn systems have been classified as CD-type deposits (Leach et al., 2010). Some sedimentary basins are particularly fertile in CD-type deposits; these include the Paleoproterozoic Mt. Isa-McArthur Basin (Australia; Large et al., 2005), and the Paleozoic Kuna Basin (Alaska; Kelley and Jennings, 2004) and Selwyn Basin (Canada; Goodfellow, 2007). For the Paleozoic basins (Kuna and Selwyn), stratiform barite can be an important component of CD-type mineralisation (Gardner and Hutcheon, 1985; Ansdell et al., 1989; Kelley et al., 2004). However, the model of barite formation, via hydrothermal (e.g. Goodfellow and Lydon, 2007) or diagenetic processes (e.g. Torres et al., 2003), has important implications for the geochemistry of the metal transporting fluid (Cooke et al., 2000). The stratiform appearance of sulphides in Selwyn Basin CD-type deposits means they are commonly referred to as sedimentary-exhalative (SEDEX; Carne and Cathro,

1982). A defining feature of the SEDEX model involves the exhalation of metal-bearing hydrothermal fluids above the sediment-water interface (SWI), and precipitation of sulphides (PbS, ZnS, FeS_2) from a H_2S-rich (euxinic) water column (Goodfellow and Lydon, 2007). Together, these periods of base metal sulphide and barite enrichment represent major perturbations of the sulphur cycle in these basins. It is also possible that the irregular distribution of CD-type deposits in the geologic record may in some way be linked to secular changes in the redox state of seawater (Goodfellow, 1987; Turner, 1992; Lyons et al., 2006; Farquhar et al., 2010; Leach et al., 2010), and in the Selwyn Basin, a strong argument has been made linking CD-type mineralisation to periods of water column anoxia and euxinia (Goodfellow and Jonasson, 1984; Goodfellow and Jonasson, 1986; Goodfellow, 1987; Turner, 1992).

Regardless of the model of sulphide precipitation (i.e., occurring above or below the SWI), an important component of a CD-type deposit is the vent complex, where the up-flow of the hydrothermal fluids is focused. In all sediment-hosted Pb-Zn deposits (MVT, Irish-type, CD-type), faults are assumed to be the primary fluid flow conduit. In MVT systems, fracture breccias and epigenetic vein mineralisation are evidence of focused fluid flow, and commonly provide appropriate samples for fluid inclusion analyses and reconstruction of fluid chemistry (e.g. Stoffell et al. 2008; Appold and Wenz, 2011; Conliffe et al., 2013). However in Irish- and CD-type deposits this style of mineralisation is rarely preserved. There are only very limited examples of CD-type deposits where vent complexes have been identified, and for which a clear relationship between vent and overlying mineralisation is well preserved (e.g. Gardner and Hutcheon, 1985; Ansdell et al., 1989; Rajabi et al., 2014). Therefore, the nature of the hydrothermal fluid input into these systems is poorly understood.

The focus of this thesis will be the Tom and Jason CD-type deposits, which are hosted by Late Devonian mudstones at Macmillan Pass, Selwyn Basin (Yukon Territory, Canada). The mineralisation at Macmillan Pass is commonly described as SEDEX (Goodfellow and Lydon, 2007), and it is one of the few locations where vent complexes are well preserved beneath the overlying stratabound and stratiform mineralisation. In the following sections of this introduction, further background information on the Macmillan Pass deposits will be presented, and some of the relevant research questions concerning CD-type deposits will be outlined to provide a framework for the objectives of this thesis.

1.2. Geological Background – Selwyn Basin

The Selwyn Basin (see Figure 1.1) was originally defined by Gabrielse (1967) as a thick, westward thickening sequence of clastic sedimentary rocks of Precambrian to Middle Devonian age, deposited along the western margin of Laurentia (ancestral North America). The oldest exposed rocks in the Selwyn Basin are the Windermere Supergroup, a 4-6km thick sequence of Hadrynian-Cambrian clastic sedimentary rocks deposited following erosion of the crystalline basement during the continental breakup of Rodinia (~760 Ma; Eisbacher, 1985). The sedimentary rocks overlying the Windermere Supergroup are dominated by fine-grained mud- and siltstones, interpreted as deep-water facies that were deposited in the off-shelf environment of a passive margin setting (Gordey and Anderson, 1993).

Three periods of extrusive and intrusive igneous activity have been identified during this period of passive margin sedimentation, including mafic volcanic flows,

dykes and tuffs observed in Early Cambrian, Middle Ordovician, and Middle to Late Devonian strata (Goodfellow, 2007). The volcanic rocks are alkalic and ultrapotassic, and incompatible element chemistry is similar to alkaline basalts formed in continental rifts, and provides evidence for episodic extension and subsidence along the passive margin (Goodfellow et al., 1995).

The tectonic environment changed during the late Devonian-Mississippian, as slab rollback in a distal back-arc setting produced regional extension, and resulted in the deposition of coarse clastic sedimentary rocks over the deeper-water facies (Nelson et al., 2002; Nelson et al., 2006). Subsequent Jurassic-Cretaceous accretionary deformation led to the incorporation of strata into the northern Cordilleran fold and thrust belt (Nelson and Colpron, 2007). Selwyn Basin strata form part of the inner belt (basinal facies of Ancestral North America), characterised by regional-scale folds and thrusts, slaty cleavage and tight isoclinal folding; platformal carbonates form the outer belt (platform facies of ancestral North America) and represent the eastern most extent of deformation (Gordey et al. 2010).

Three main periods of CD-type metallogenesis occurred in the Selwyn Basin, with mineralisation hosted in Cambrian (Anvil District), Ordovician (Howard's Pass District) and Late Devonian (Macmillan Pass and Gataga District) strata; over 55 Mt of Zn and Pb are hosted within 17 separate deposits (Goodfellow and Lydon, 2007). These deposits coincide temporally (but not spatially) with igneous activity and are hosted within carbonaceous mudstone and shale lithologies (Goodfellow, 1987; Goodfellow, 2007). At Macmillan Pass, Late Devonian strata have only undergone sub-greenschist facies metamorphism, and many primary sedimentary and hydrothermal features are well preserved. Therefore the genetic model for Selwyn Basin mineralisation

(Goodfellow and Lydon, 2007) has been developed largely from work conducted at the Tom and Jason deposits (Carne, 1976; Large, 1980; Carne and Cathro, 1982; Gardner and Hutcheon, 1985; Ansdell et al. 1989; Turner, 1990).

1.2.1. The Selwyn Basin SEDEX model

A critical component of any sediment-hosted Pb-Zn system is the source of reduced sulphur (metal trap). In all sediment-hosted systems this is ultimately derived from seawater sulphate, but the geochemical pathway by which it is reduced can vary. In normal, low temperature marine environments, biological reduction of sulphate is an important source of reduced sulphur. Following the consumption of oxygen, microorganisms utilise a series of oxidants with progressively diminishing energy yields (NO_3^- > Mn^{2+} > Fe^{2+} > SO_4^{2-}; Froelich et al., 1979). As a major anion in modern day seawater (28 mM; Lowenstein et al., 2003), sulphate is often the most bioavailable electron acceptor that bacteria use to oxidise carbon, which can be described via the following reaction:

$$1. \qquad 2\,[CH_2O] + SO_4^{2-} \qquad \Rightarrow \qquad 2\,HCO_3^- + H_2S$$

Modern seawater is well oxygenated, and so this process (bacterial sulphate reduction; BSR) normally only occurs beneath the SWI in sediment pore fluids. The alkalinity and reduced sulphur that are by-products of reaction 1 commonly result in the respective precipitation of diagenetic carbonate and pyrite. However, in SEDEX systems BSR is thought to occur above the SWI, with progressive sulphate reduction leading to the development of an H_2S-bearing (euxinic) water column. In this model, the precipitation of base metal sulphides is strictly syn-sedimentary, occurring from the water column following the hydrothermal venting of metal-bearing fluids. The

development of euxinic conditions is therefore considered to be a prerequisite for effective mineralisation in SEDEX systems. In the Selwyn Basin model, the Macmillan Pass deposits represent vent proximal systems (Figure 1.3A), whereas other Selwyn Basin deposits (e.g. Howards Pass) where a vent complex has not been identified are considered vent distal (Goodfellow et al. 1993). In vent distal deposits, hydrothermal fluids are transported away from the vent, either in the water column or via a brine pool to the site of mineralisation (Figure 1.3B).

1.2.2. Evidence for euxinic conditions in the Selwyn Basin

Historically, the major stable isotopes of sulphur (^{32}S = 95.02%, ^{34}S = 4.21%) have proven to be powerful tracers of geochemical processes operating in the sulphur cycle (Harrison and Thode, 1958; Thode et al., 1961; Kaplan and Rittenberg, 1964; Ohmoto and Rye, 1979; Ohmoto and Goldhaber, 1997; Seal et al., 2000; Canfield, 2001; Seal, 2006; Bottrell and Newton, 2006). During BSR, bacteria preferentially metabolise sulphate bearing the lighter isotope, ^{32}S (Kaplan and Rittenberg, 1964). Therefore a diagnostic feature of sulphides precipitated during BSR is ^{34}S-depletion, which can be reported as an isotope ratio using δ-notation:

$$2. \qquad \delta^{34}S = 1000 \text{ x } [\, (^{34}S \,/^{32}S)_{sample} - (^{34}S \,/^{32}S)_{VCDT} \,] \, / \, (^{34}S \,/^{32}S)_{VCDT}$$

In equation 2, the difference between the unknown (sample) and standard (Vienna Canyon Diablo Troilite; VCDT) is reported in per mil units (‰). The difference between values of $\delta^{34}S_{\text{-sulphide}}$ and $\delta^{34}S_{\text{-sulphate}}$ can then be expressed in epsilon notation:

$$3. \qquad \varepsilon^{34}S = \delta^{34}S_{sulphate} - \delta^{34}S_{sulphide}$$

The magnitude of sulphur isotopic fractionation during BSR is commonly large ($\varepsilon^{34}S$ = +16 to +42‰; Habicht and Canfield, 1997), and in normal marine environments, sulphides such as pyrite are characterised by negative $\delta^{34}S$ values.

For pyritic and barite-bearing mudstones in the Selwyn Basin, Goodfellow and Jonasson (1984) report a secular sulphur isotope curve through the Paleozoic, reconstructing reduced sulphur and seawater sulphate from the respective pyrite and barite records. However, it is important to highlight some sedimentological interpretations that profoundly influenced the interpretation of isotopic data in this study: organic rich mudstones are interpreted to have formed via slow, pelagic processes during periods of basin stagnation and anoxia, supported by limited evidence of clastic input and an absence of any biogenic activity; as a corollary, diagenetic pore fluids are assumed to have been in open communication with overlying seawater; therefore, sulphur isotope analyses of pyrite and barite precipitated in this environment are believed to record information about sulphur cycling in the water column. Goodfellow and Jonasson (1984) reported unusually positive $\delta^{34}S$ values in both pyrite and barite hosted in these organic rich mudstones, and argued that co-variation between $\delta^{34}S_{sulphide}$ and $\delta^{34}S_{sulphate}$ is best explained by the quantitative reduction of seawater sulphate, during which $\delta^{34}S_{sulphide}$ values approach initial $\delta^{34}S_{sulphate}$ values for the Late Devonian (approximately +24‰; Claypool et al., 1980). The development of $\delta^{34}S_{barite}$ values that exceed +24‰ was considered evidence of an evolved, depleted sulphate reservoir, controlled by closed system Rayleigh fractionation processes in the water column. In this model, the production of reduced sulphur is considered to be a single step process. Together, the records of $\delta^{34}S_{pyrite}$ and $\delta^{34}S_{barite}$ values are used as the primary evidence for basin-wide euxinia and the

formation of a metal trap for Selwyn Basin SEDEX systems.

The implication of using SEDEX as a term to define a CD-type deposit is there has to be clear evidence that water column sulphide precipitation was an important process. For this reason, only when referring to the conventional model for Selwyn Basin CD-type mineralisation will the term SEDEX be used; otherwise the non-genetic terminology of Leach et al. (2010) is preferred, which qualifies this style of mineralisation as CD-type.

1.2.3. Origin of Late Devonian barite

Barite ($BaSO_4$) is highly insoluble (log K = $10^{-9.96}$; Bowers et al. 1984), such that barite dissolution only occurs in extremely low sulphate concentrations. The precipitation of barite can occur directly from seawater, from diagenetic pore fluids or via hydrothermal processes (for a review, see Hanor, 2000; Griffith and Paytan, 2012), which can be distinguished through textural and isotopic analysis (e.g. Paytan et al., 2002; Johnson et al., 2009).

The occurrence of barite in Selwyn Basin CD-type systems is largely restricted to the Late Devonian. Stratiform barite is a major component of the Macmillan Pass and Gataga Districts, whilst also occurring independently of sulphide mineralisation (barren barite). In the conventional model for SEDEX mineralisation in the Selwyn Basin, the source of barium is assumed to be hydrothermal in origin, with barite precipitating from seawater following exhalation of Zn-Pb-Ba bearing fluids; it is suggested that barren barite deposits are a distal expression of a SEDEX system (Goodfellow and Lydon, 2007). In a restricted water mass, as is suggested for the

Selwyn Basin, widespread barite precipitation would have required long-lived hydrothermal activity to provide a continuous barium source.

At the Red Dog CD-type Zn-Pb deposit in Alaska, there are massive enrichments of barite in the host rock (Kelley and Jennings, 2004). The paragenetic relationship between barite, base metal sulphides and carbonate is complex (e.g. Kelley et al., 2004). Notably, there is both textural and isotopic evidence that barite is a pre-hydrothermal phase, and that some of the sulphide precipitation at Red Dog occurred via replacement of barite (Johnson et al., 2004). Therefore barite formation may be a potentially important precursor to base metal mineralisation in some CD-type systems.

Accumulation of barite has been suggested to occur in low temperature, diagenetic environments (e.g. Torres et al., 2003). In these systems, barium solubility is enhanced in sulphate depleted, methane-rich diagenetic pore fluids, which develop during the methanogenic breakdown of organic matter (Torres et al., 1996). Depending on the flow regime of these barium rich fluids, accumulations of barite can occur as mounds on the seafloor (e.g. Greinert et al., 2002) or as stratiform enrichments within the sediment (e.g. Torres et al. 2003). In these systems, the source of barium is associated with decaying organic matter, and is remobilised via fluid flow at relatively shallow levels within sedimentary basins, independently of hydrothermal activity.

1.3. Hydrothermal Fluid Geochemistry in CD-type Systems

There are only a limited number of studies that have directly analysed basic fluid chemistry in CD-type systems (Gardner and Hutcheon, 1985; Samson and Russell, 1987; Ansdell et al., 1989; Leach et al., 2004; Rajabi et al., 2014). At Macmillan Pass,

the studies of Gardner and Hutcheon (1985) and Ansdell et al. (1989) focused on the vent complex, which forms the primary conduit of fluid upflow, and is well preserved beneath the overlying bedded mineralisation.

In these earlier fluid inclusion studies at the Jason (Gardner and Hutcheon, 1985) and Tom (Ansdell et al. 1989) deposits, a wide range of temperature (157°C to 335°C) and salinity (5-18 wt. % NaCl) data is reported for some of the major gangue mineral phases (quartz, ankerite). These studies also reported CO_2-bearing fluid inclusion assemblages, but disagreed upon the relationship between CO_2 and mineralisation. Gardner and Hutcheon (1985) suggested the CO_2 was of primary origin, although they did not specify its origin, and Ansdell et al. (1989) argued that CO_2-bearing inclusions post-dated the hydrothermal event, and formed during a later, tectonic event.

Salinity is considered to be the master variable for Pb and Zn solubility in crustal fluids (Yardley, 2005), although at temperatures in excess of 250°C base metal solubility can be enhanced even at relatively modest salinities (Tornos and Heinrich, 2008). Previous studies at Macmillan Pass provide no constraints on fO_2 and ΣS, which are also important parameters for metal transport (Seward and Barnes, 1997). The lack of data on fluid temperature and salinity, and constraints on parameters such as fO_2 and ΣS, means there remains major uncertainty over the metal transporting capacity of the hydrothermal fluid at Macmillan Pass, and in CD-type systems in general. Some authors have used thermodynamic models to evaluate metal transport and deposition in CD-type fluids (e.g. Cooke et al., 2000; Tornos and Heinrich, 2008), however the applicability of these models is directly linked to input parameters provided by fluid inclusion data and mineralogical information.

Using temperature and salinity constraints of earlier fluid inclusion studies (Gardner and Hutcheon, 1985; Samson and Russell, 1987; Ansdell et al., 1989), Cooke et al. (2000) modeled the solubility of base metals and barium in SEDEX fluids. Cooke et al. (2000) compared the SEDEX systems in the Paleoproterozoic McArthur Basin, where the basin-fill contains relatively oxidising lithologies, and the Selwyn Basin, where organic rich mudstones represent more reducing lithologies. In their study, Cooke et al. (2000) conclude that two sub-types of SEDEX deposit should be defined according to the redox state of the mineralising fluid: Selwyn-type deposits are produced by reduced (aH$_2$S > aSO$_4{}^{2-}$) fluids in which co-transportation of base metals and barium occurs in a moderately saline (~10 wt.% NaCl), high-temperature (>250°C) and acidic (pH = 4) fluid; McArthur-type deposits are produced by lower temperature (~150°C) oxidised fluids (aH$_2$S < aSO$_4{}^{2-}$) incapable of transporting barium, developed in evaporite-bearing basins dominated by more oxidised syn-rift clastics (e.g. McArthur Basin).

Tornos and Heinrich (2008) presented a convincing argument for the development of base metal enriched fluids in a Late Devonian shale basin; in their model, saline brines in equilibrium with shales developed into mildly reducing but sulphur-deficient, moderately acidic, ore-forming fluids at temperatures greater than >250°C. Contrary to the common assumption that metals are supplied from early rift-stage clastics such as continental red-beds (Metcalfe et al., 1994; Goodfellow et al., 1993), Tornos and Heinrich (2008) suggest that shales themselves provide the metal source, citing evidence of a correlation of metal ratios between fluid and source rock.

In CD-type systems with barite as a major component (e.g. Macmillan Pass, Red Dog), the relationship of the sulphate phase and the base metal sulphides has some

important implications for hydrothermal fluid geochemistry. Where barium solubility is enhanced in reducing fluids, base metal solubilities are greater in more oxidising fluids. Indeed, Cooke et al. (2000) suggest that to maintain co-transportation of barium and base metals in hydrothermal fluids, high temperatures and acidity are required. This model operates implicitly under the assumption that barium and base metals originate from the same source and are coevally precipitated (Goodfellow and Jonasson, 1984). It also means that sulphur must be sourced locally (i.e. seawater), as co-transportation of barium and base metals will be inhibited if high concentrations of either oxidised or reduced sulphur are in the fluid.

1.3.1. Alteration in CD-type systems

Attempts to evaluate alteration in CD-type deposits have been developed mostly through acquisition of bulk geochemical data from surrounding lithologies (e.g. Large et al. 1998; 2000). These studies have developed alteration indices that quantify hydrothermal input on the basis of a suite of elements considered to be hydrothermal in origin (e.g. Pb, Zn, As, Mn, Tl). The application of these data is dependent upon accurate knowledge of stratigraphic location relative to the hydrothermal system, to enable comparison of un-mineralised to mineralised strata. The value of these data partly relates to how far away a hydrothermal system can be recognised by its alteration footprint. In many CD-type systems this is not straightforward, owing to the homogeneity of mudstones and difficulties associated with correlation of lithological units with few defining characteristics. Further complications may also arise due to the absence of a known point source, i.e. vent complex, in the deposit architecture of most CD-type systems.

1.4. Objectives

For CD-type base metal deposits, which are commonly fine grained and challenging to interpret, models of ore formation can be one-dimensional. For example, in the Selwyn Basin SEDEX model, a direct causal relationship between periods of basin stagnation and mineralisation is invoked, which implies water column chemistry as the driving factor in metallogenesis (Goodfellow and Jonasson, 1984; Turner, 1992; Goodfellow and Lydon, 2007). This is an elegant model, which attempts to explain the uneven distribution of SEDEX systems in the context of evolving ocean chemistry; however, some aspects require re-evaluation, specifically, with respect to recent work on the sedimentology of fine-grained clastic rocks (Arthur and Sageman, 1994; Schieber et al., 2007; Schieber et al., 2010; Macquaker et al., 2010; Aplin and Macquaker, 2011), and the interpretation of sulphur isotopes in pyrite and barite in marine strata (Jørgensen et al., 2004; Johnson et al., 2009; Borowski et al., 2013). Furthermore, subsequent to many of the studies at Macmillan Pass have been numerous relevant studies on modern sediment-covered ridge-crest systems (Goodfellow and Blaise, 1988; Seewald et al. 1994; Cruse and Seewald, 2006). These studies provide a valuable framework in which to evaluate how hydrothermal systems may have evolved in ancient geologic samples, and specifically how hydrothermal fluids interacted with immature, organic-rich lithologies.

To resolve how a hydrothermal system evolves temporally and spatially with respect to a chemically reactive host rock requires a multi-dimensional approach, with the integration of different types of data. In the subsequent chapters of this thesis, attempts have been made to explore the following research areas.

1.4.1 The sedimentary environment and nature of the host rock

The fine-grained, organic rich mudstones that form a large proportion of Selwyn Basin stratigraphy are widely regarded as having been deposited via pelagic processes, with stagnation and reduced oxygenation of the water column contributing towards enhanced organic matter preservation. This interpretation forms a major line of support for the restricted, euxinic model, and subsequent interpretation of sulphur isotope data. However, models for the deposition of organic rich mudstones have expanded in scope and detail since the original work in the Selwyn Basin was carried out in the 1980s. Indeed, mudstones can preserve major differences in composition and sedimentology, reflecting a broad range of depositional environments (Aplin and Macquaker, 2011). For example, some studies have described rapid mudstone deposition via non-pelagic processes, which are not restricted to deep marine environments (Schieber et al. 2007; Macquaker et al. 2010). Similarly, organic matter preservation can occur in a variety of settings, of which stagnant, restricted basins are non-unique environments (Arthur and Sagemann, 1994).

There is an important coupling between sedimentology and geochemistry, and the accurate interpretation of one data set cannot be made without the other. For example, at a first order, the open or closed nature of sulphur isotope fractionation can be linked to sedimentation rate (Goldhaber and Kaplan, 1975). Rapid sedimentation events lead to periodic closures of pore fluid networks, producing closed system sulphur isotope fractionation on a local scale, whereas low sedimentation rates enhance connectivity between pore fluids and seawater. Sulphides precipitated in the latter environment may record information useful for interpreting sulphur cycling in the water column.

A comprehensive understanding of sedimentology and geochemistry enables more

accurate reconstructions of paleo-environments. In turn, this allows for the characterisation of ambient conditions in the basin, where un-mineralised strata that are coeval with the hydrothermal system can be identified; this is important for developing a more robust framework for the evaluation of hydrothermal alteration.

1.4.2. Fluid geochemistry in CD-type systems

In all hydrothermal systems, constraining the origin and geochemical evolution of fluids is key for understanding the source, transport and deposition of metals. In CD-type systems, there are only a limited number of deposits where vent complexes are preserved, and which contain samples amenable to fluid inclusion analysis. Indeed, the restricted database of fluid geochemistry has been cited as one of the major limitations in our understanding of CD-type systems (Wilkinson, 2014).

The fluid inclusions in CD-type systems are generally small (< 10μm), making reliable, accurate measurements challenging to obtain. Existing temperature and salinity constraints are broad (157°C to 335°C, 2.6 to 18 wt. % NaCl equivalent; Gardner and Hutcheon, 1985; Ansdell et al. 1989) and lacking in petrographic context, while important parameters such as fO_2, total sulphur content (ΣS) and pH remain ambiguous. There is clear motivation for revisiting these older studies, to provide better petrographic context for new and existing fluid inclusion data, and to supplement them with additional geochemical data that may help to address the following aspects of fluid geochemistry in these systems:

1. Where are the metals coming from?
2. What is the nature of alteration?
3. What is the redox state of the fluid?

4. Can we better constrain fluid temperature, salinity and role of CO_2 in the system?

5. How might these fluids compare to fluids in modern day sediment covered vent systems?

1.4.3. The geochemical controls on metal deposition

In sediment-hosted base metal systems, both high sulphur concentrations and high rates of sulphate reduction are critical for the development of an effective metal trap. The original source of sulphur in CD-type systems is generally regarded to be seawater sulphate (Ohmoto and Goldhaber, 1997). Therefore the concentration of sulphate in seawater, which has changed through geologic time (Lowenstein et al. 2003), is an important, but previously ignored factor for these systems. It is possible to highlight the problems associated with the conventional model for SEDEX mineralisation at Macmillan Pass, using a simple mass balance approach (e.g. Ohmoto et al., 1988),

The combined geological resource of Tom and Jason is approximately 25 Mt of mineralisation grading at 7% Zn and 5% Pb (Goodfellow and Lydon, 2007). The total Pb and Zn content in the mudstones (3 Mt), as galena and sphalerite, corresponds to approximately 0.7 Mt of sulphur – this is a conservative estimate considering pyrite has not been included in the calculation. To then account for this sulphur budget in terms of Late Devonian seawater sulphate (~7 mM; Horita et al., 2002) requires >3 km^3 seawater, assuming 100% reduction. Considering that at the Jason deposit, Gardner and Hutcheon (1985) suggest a water depth of ~500m, sulphur replenishment from at least 1.5-2km away from the vent is required to satisfy the mass balance of the system. Furthermore, application of this model to older Selwyn Basin systems, which

are far greater in size (e.g. Howards Pass; 100 Mt @ 5% Zn and 2% Pb; Goodfellow and Lydon, 2007), implies euxinia on an even broader scale. Therefore it seems unlikely that the stratigraphic accumulation of sulphides in any Selwyn Basin system could have been produced predominantly via water column precipitation.

There are also problems associated with the sulphur isotope data that constrain the secular sulphur isotope curve of Goodfellow and Jonasson (1984), including: (1) the interpretation of pyrite and barite data assumes co-variation produced by a single step process (BSR in the water column); however, $\delta^{34}S_{sulphide}$ and $\delta^{34}S_{sulphate}$ values do not necessarily adhere to this trend; (2) samples of pyrite and barite do not always come from the same stratigraphic location, which has in part been used to explain (1) by Goodfellow and Turner (1988); (3) poor stratigraphic control on samples; (4) a wide range of data constrain the curve for any one time period (see Goodfellow and Jonasson, 1984). This has led to debate over the application of the euxinic basin model to explain stratiform styles of mineralisation in CD-type systems (Eldridge et al., 1988; Goodfellow and Turner, 1988). Indeed, it is highly likely that these systems are more complex; for example, the isotopic data that form the foundation for the euxinic basin model was acquired from mineral separates of pyrite and barite (Goodfellow and Jonasson, 1984). However these systems often contain multiple phases of sulphides (e.g. Eldridge et al. 1988), perhaps with contrasting isotopic signatures, which would explain the large range in $\delta^{34}S$ values that are encountered.

It is necessary, therefore, to evaluate alternative mechanisms of sulphide and barite precipitation. The development of micro-analytical techniques such as secondary ion mass spectrometry (SIMS) provides the opportunity to evaluate the isotopic evolution of complex, fine-grained samples (e.g. Eldridge et al. 1988). This will

almost certainly enable a more comprehensive understanding of sulphur cycling in these systems, at a greater temporal and spatial resolution, and ultimately avoid one-dimensional models and their associated problems.

1.5. Thesis Outline

In this thesis, multiple data sets have been integrated to address these research questions – these include: drill-core sampling; detailed petrographic analysis of all components of the deposit architecture (Tom and Jason); host rock major element chemistry; bulk rock pyrite sulphur isotope analysis; secondary ion mass spectrometry (SIMS) analysis of $\delta^{34}S$ values in pyrite and barite, and $\delta^{18}O$ values in barite; electron probe micro-analysis (EPMA) of various mineral phases (carbonates, silicates); laser ablation-inductively coupled plasma-mass spectrometry (LA-ICP-MS); analyses of $\delta^{18}O$, $\delta^{13}C$ and $^{87}Sr/^{86}Sr$ values for vent complex carbonate; fluid inclusion microthermometry and gas analysis; thermodynamic modeling of mineral stability and base metal solubility.

The chapters are organised in the following format, as manuscripts prepared for publication in peer-reviewed journals, which are either in preparation for submission, have been submitted (in review) or are accepted (in press).

Chapter 2. The importance of siliceous radiolarian bearing mudstones in the formation of sediment-hosted Zn-Pb±Ba mineralisation in the Selwyn Basin, Yukon, Canada).

The SiO₂ content of mudstones at Macmillan Pass preserve no obvious relationship with the hydrothermal activity at Macmillan Pass, and most likely represents an increased flux of biogenic silica. Radiolarians (30 to ~500μm) have been identified within the host rock, either replaced by sulphide or hydrothermal carbonate, or recrystallised to silica spheroids. They are identifiable with a hand lens and form distinctive 10cm thick radiolarian-rich beds (>50% radiolarians by volume) within the mineralised horizons and in barren, time equivalent strata, and therefore are a useful stratigraphic marker unit in otherwise homogenous, featureless fine-grained mudstones.

The presence of highly siliceous, carbonaceous mudstone units (with preserved radiolarians) suggests that in the Late Devonian there was a link between biological productivity in the water column, the resultant sedimentation and the CD-type deposits. These biosiliceous lithologies may be particularly favorable host rocks to CD-type mineralisation as: (1) high porosities during early diagenesis represent exploitable volume and enhance permeabilities in partially lithified sediments, which are important parameters for sub-seafloor replacement mineralisation; (2) they are organic rich due to their deposition in productive settings, and have a high capacity for the generation of sulphide via sulphate reduction. Therefore, we suggest there is a requirement for CD-type deposits to be associated with high biological activity and productivity in oceans, and sediments derived from those processes.

A modified version of this chapter has been accepted to Economic Geology (Scientific Communications):

Magnall, J.M., Gleeson, S.A. and Paradis, S., The importance of siliceous radiolarian

bearing mudstones in the formation of sediment-hosted Zn-Pb+-Ba mineralisation in the Selwyn Basin, Yukon, Canada).

Chapter 3. The role of diagenetic processes in the formation of shale hosted massive sulphide deposits - a sulphur and oxygen isotopic study of barite and pyrite from the Late Devonian Tom and Jason deposits, Selwyn Basin, Canada.

Highly positive $\delta^{34}S$ values in sulphide minerals are a common feature of sediment hosted massive sulphide deposits (SHMS). Often this is attributed to near quantitative consumption of seawater sulphate, and for Paleozoic strata of the Selwyn Basin (Canada) this is thought to occur during bacterial sulphate reduction (BSR) in a euxinic water column. In this study, we document the textural and isotopic relationship between barite, pyrite and hydrothermal sulphides using a variety of petrographic techniques and in-situ isotopic microanalysis (secondary ion mass spectrometry; SIMS) of barite and pyrite. These data are supplemented by bulk rock pyrite analyses of $\delta^{34}S$ values (n = 37) from drill-core samples of un-mineralised (barren) mudstone, to provide a means by which to evaluate the mass balance of sulphur in the host rock.

There are three generations of barite, with overlapping ranges in $\delta^{34}S$ and $\delta^{18}O$ values (+23.5 to +34.0‰ and +16.4 to +18.3‰ respectively) consistent with an origin from modified Late Devonian seawater. We propose that barite formed following remobilisation of productivity-derived barium within the sediment, and precipitated within diagenetic pore fluids close to the sediment water interface. Two generations of

pyrite are texturally associated with barite: framboidal pyrite (*py-I*), which has negative $\delta^{34}S$ values (-23 to -28‰; *n* = 9)*,* and euhedral pyrite (*py-II*), which preserves more enriched in $\delta^{34}S$ values (+8 to +26‰; *n* = 86). It is reasoned that stratiform pyrite and barite developed along diagenetic redox fronts, where the isotopic relationships ($\delta^{34}S_{pyrite} \approx \delta^{34}S_{barite}$) can only be explained by sulphate reduction coupled with anaerobic methane oxidation (AOM-SR). Importantly, hydrothermal sulphides (pyrite, sphalerite and galena) all post-date this diagenetic barite-pyrite assemblage, and textural and mineralogical evidence indicates barite replacement to be an important process during mineralisation. Neither the textures nor the documented isotopic relationships can be produced by processes operating in a euxinic water column, which represents a major departure from the conventional model for SEDEX mineralisation at Macmillan Pass. The positive $\delta^{34}S$ values in sulphides, a common feature of CD-type systems both in the Selwyn Basin and throughout the geologic record, may reflect AOM-SR and thus form an important, but previously unidentified, process in these systems.

A modified version of this chapter in review with Geochimica et Cosmochimica Acta:

Magnall, J.M., Gleeson, S.A., Stern, R.A., Newton, R.J., Poulton, S.W., and Paradis, S., The role of diagenetic processes in the formation of shale hosted massive sulphide deposits - a sulphur and oxygen isotopic study of barite and pyrite from the Late Devonian Tom and Jason deposits, Selwyn Basin, Canada.

Chapter 4. Vent Complex Geochemistry in Sediment-Hosted Massive

Sulphide (SHMS) Systems.

Two main paragenetic stages are preserved in the vent complexes of the Tom and Jason CD-type deposits: (1) disseminated ankerite alteration of the organic-rich mudstone host rock and crosscutting stockwork ankerite veining (± pyrobitumen, pyrite and quartz) and (2) main stage massive sulphide (galena-pyrrhotite-pyrite ± chalcopyrite-sphalerite) and siderite (± barytocalcite and quartz) mineralisation. Mineral separates of vent complex sulphides were targeted for sulphur isotope analysis ($\delta^{34}S_{VCDT}$); trace and rare earth elements (REEs) in carbonate were analysed *in situ* using LA-ICP-MS; fluid inclusion microthermometry was performed on samples of ankerite, quartz and barytcalcite, and the volatile content of fluid inclusions in quartz was analysed via incremental crush fast scan mass spectrometry. The petrographic framework and fluid inclusion data were then used as a basis for thermodynamic modeling of base metal solubility and fluid pH, fO_2 and ΣS content.

The two vent complexes record the interaction of a hot (>250°C), acidic (pH ≤ 4.5), metal bearing fluid with an organic rich host rock, resulting in the local thermal degradation of organic matter coupled with the release of volatile components (CO_2, CH_4, C_1-C_4 hydrocarbons, N_2) into the fluid and precipitation of sulphides during thermochemical sulphate reduction. There is evidence of steep thermal and redox gradients, developed locally during interaction of the hydrothermal fluid with the chemically reactive, immature host rock and associated mixing with diagenetic fluids. In this respect, similar processes to fluid rock interaction at modern day sediment covered ridge axis (Guaymas Basin) are recorded in the two Late Devonian CD-type systems. Using this framework, it is possible to model the metal transporting capacity of the deep fluid, which even at modest salinities was high (>100ppm Zn and Pb),

owing to the combined effects of high temperature, low pH (≤ 4) and fO$_2$ ($>10^{-36}$).

A modified version of this chapter has been prepared for submission to Geochimica et Cosmochimica Acta:

Magnall, J.M., Gleeson, S.A., Blamey, N.F. and Paradis, S., Vent Complex Geochemistry in Sediment-Hosted Massive Sulphide (SHMS) Systems.

Chapter 5. Mineralising processes in sediment hosted Zn-Pb-Ba systems – deposit genesis at Macmillan Pass.

In previous chapters, the application of micro-analytical techniques and thermodynamic modeling of mineral assemblages has documented geochemical gradients (temperature, fO$_2$, ΣS) on a local scale. How this relates to deposit scale processes is evaluated in Chapter 5, with the aim of producing a new model for CD-type mineralisation at Macmillan Pass. This has been achieved through the modeling of δ^{18}O and δ^{13}C values in carbonate from the vent complex, and other components of the deposit architecture, which supports derivation of carbon from the host rock. Furthermore, the modeling approach produces results that are consistent with a hot ($>250°$C) fluid, and ^{87}Sr/^{86}Sr values preserved in ankerite provide evidence of a fluid that interacted with old radiogenic lithologies, most likely basal rift clastics to the Selwyn Basin.

Replacement textures in the bedded mineralisation are also evaluated to determine what formed the metal trap for sulphides in the bedded mineralisation. Petrographic evidence of sub-seafloor replacement mineralisation is presented, along

with a mass balance argument in support of barite replacement. Therefore the formation of barite is reasoned to provide an effective means by which to pre-enrich the host rock in sulphur, and is a key component of the host rock at Macmillan Pass. Barite precipitation occurred prior to the main hydrothermal event, and enhanced fluid circulation in the basin during the onset of hydrothermal activity mobilised barium in reducing fluids associated with organic rich sequences in the stratigraphy. Main stage hydrothermal activity is characterised by a limited number of pulses of hot, metal rich fluid, which entered a shallow diagenetic setting in which sediments were partially consolidated.

A modified version of this chapter has been prepared for submission to Economic Geology:

Magnall, J.M., Gleeson, S.A., Creaser, R.A., Paradis, S., Mineralising processes in sediment hosted Zn-Pb-Ba systems – deposit genesis at Macmillan Pass.

Chapter 6. Conclusions

The results and interpretations presented in this thesis represent a marked departure from conventional models of CD-type mineralisation in the Selwyn Basin, which placed strong emphasis on water column chemistry, and specifically euxinia.

What I have attempted to achieve in this thesis, is to develop a more comprehensive assessment of how the sedimentology and chemistry of organic rich

sediments contribute to hydrothermal systems through time and space. This short chapter provides a synthesis of some of the important results of preceding chapters, and aims to place them into a broad context, with comments directed towards future work.

Figures

Figure 1.1 Map showing the geographical extent of the Selwyn Basin in western North America, highlighting the location of major sediment-hosted base-metal districts (modified from Colpron and Nelson, 2009). The Kechika Trough forms a southeastern extension of the Selwyn Basin, where it is truncated by the Tintina fault. The local geology of MacMillan Pass (modified from Abbott and Turner, 1991) and location of the Tom and Jason deposits are below.
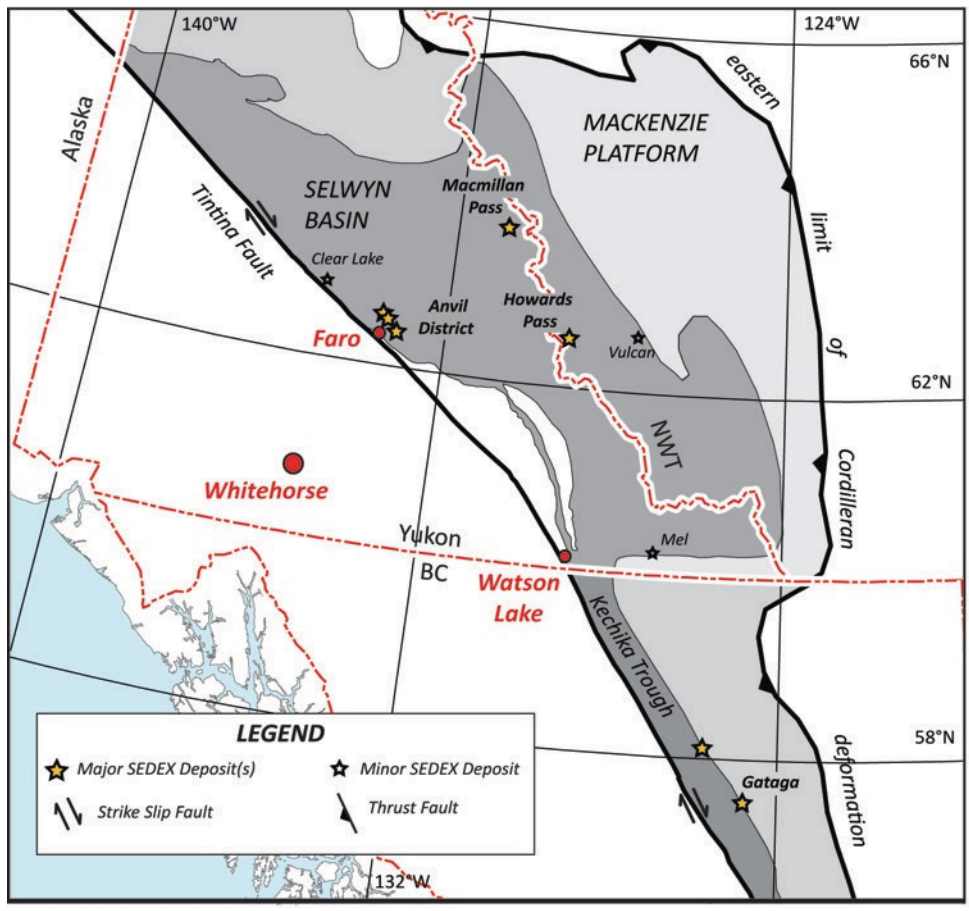
Figure 1.2 Stratigraphic column for the Selwyn Basin, compiled mostly from studies produced at Macmillan Pass. Black dots represent ages provided by conodont biostratigraphy (Dawson and Orchard, 1982; Irwin and Orchard, 1991). Stars indicate the three major mineralising events in Selwyn Basin stratigraphy. Compiled from Carne (1979), Large (1980), Abbott and Turner (1991), Gordey and Anderson (1993) and Turner et al. (2011).

Period	Epoch	Group	Formation		Lithology
MISSISSIPPIAN	LOWER		Tsichu Fm.		Quartzarenite
DEVONIAN	UPPER	EARN GROUP	Prevost Fm.		Greywacke
				Macmillan Pass District ★	Siliceous Mudstone
	MIDDLE		Portrait Lake Fm.		Silty Mudstone, Sandstone, Conglomerate
	LOWER				Siltstone
SILURIAN	UPPER	ROAD RIVER GROUP	Steel Fm.		Siliceous dolomitic mudstone
	LOWER		Duo Lake Fm.	**Howards Pass District** ★	Siliceous mudstone, chert and minor limestone
ORDOVICIAN	UPPER				
	MIDDLE				
	LOWER		Rabbitkettle Fm.		Silty Limestone
CAMBRIAN			Gull Lake Fm.	**Anvil District** ★	Siltstone and minor limestone conglomerate
PROTEROZOIC		HYLAND GROUP	Narchilla Fm.		Shale and siltstone
			Yusezyu Fm.		Gritty sandstone and shale

Figure 1.3. The Selwyn Basin model for SEDEX mineralisation. A – vent proximal deposit (e.g. Macmillan Pass, Tom and Jason deposits). B – vent distal deposit (e.g. Howards Pass deposits). Modified from Goodfellow and Lydon (2007).

A — Hydrothermal Plume Model

O₂

H₂S

Plume

Vent Distal

Vent Proximal

Bedded Sulfides

Replacement Zone

Vent Complex

Alteration

Footwall Mudstones

B — Brine Pool Model

Brine Pool

32
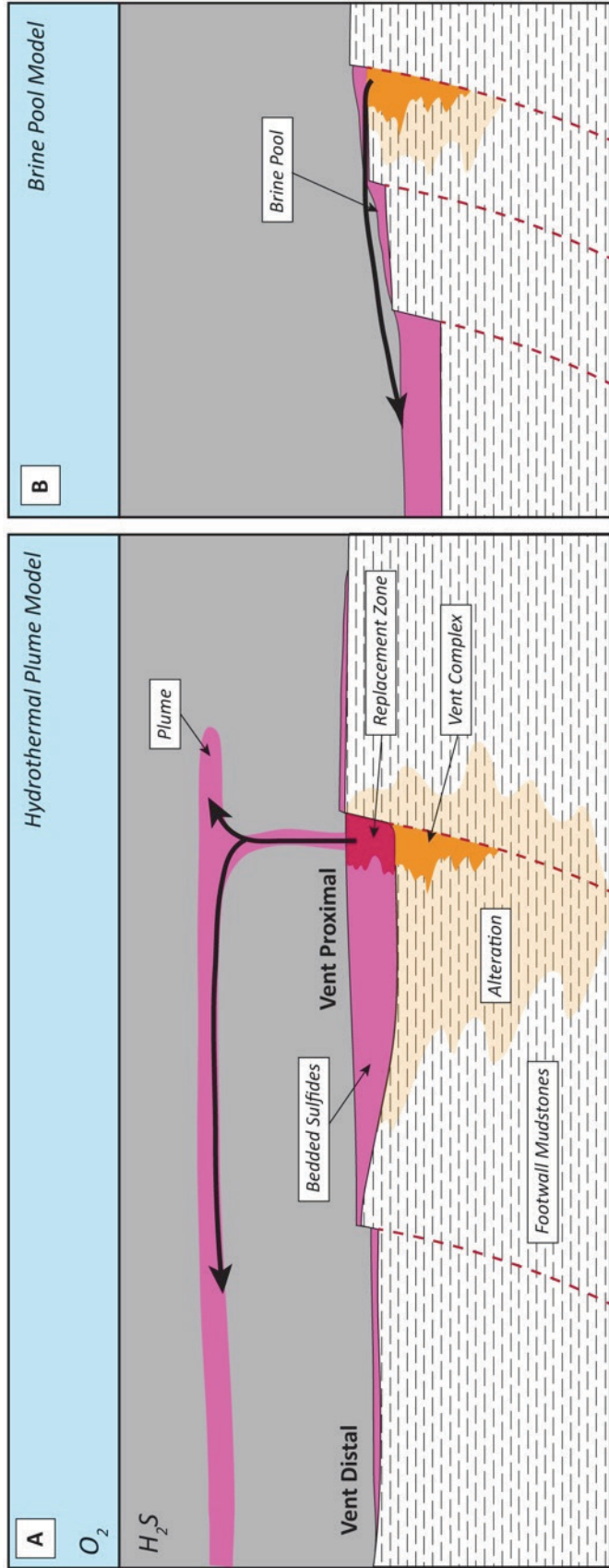
References

Ansdell K. M., Nesbitt B. E. and Longstaffe F. J. (1989) A Fluid Inclusion and Stable Isotope Study of the Tom Ba-Pb-Zn Deposit, Yukon Territory, Canada. *Econ. Geol.* **84**, 841–856.

Aplin A. C. and Macquaker J. H. S. (2011) Mudstone diversity: Origin and implications for source , seal , and reservoir properties in petroleum systems. *Am. Assoc. Pet. Geol. Bull.* **12**, 2031–2059.

Appold M. S. and Wenz Z. J. (2011) Composition of Ore Fluid Inclusions from the Viburnum Trend, Southeast Missouri District, United States: Implications for Transport and Precipitation Mechanisms. *Econ. Geol.* **106**, 55–78.

Arthur M. A. and Sageman B. B. (1994) Marine black shales: depositional mechanisms and environments of ancient deposits. *Annu. Rev. Earth Planet. Sci.* **22**, 499–551.

Borowski W. S., Rodriguez N. M., Paull C. K. and Ussler W. (2013) Are [34]S-enriched authigenic sulfide minerals a proxy for elevated methane flux and gas hydrates in the geologic record? *Mar. Pet. Geol.* **43**, 381–395.

Bottrell S. H. and Newton R. J. (2006) Reconstruction of changes in global sulfur cycling from marine sulfate isotopes. *Earth-Science Rev.* **75**, 59–83.

Brown T. J., Wrighton C. E., Raycraft E. R., Shaw R. A., Deady E. A., Rippingale J., Bide T. and Idoine N. (2015) *British Geological Survey – World mineral production (2009-2013).*, NERC.

Canfield D. E. (2001) Isotope fractionation by natural populations of sulfate-reducing bacteria. *Geochim. Cosmochim. Acta* **65**, 1117–1124.

Carne R. C. and Cathro R. J. (1982) Sedimentary exhalative (sedex) zinc-lead-silver deposits, northern Canadian Cordillera. *Can. Min. Metall. Bull.* **75**, 66–78.

Claypool G. E., Holser W. T., Kaplan I. R., Sakai H. and Zak I. (1980) The age curves of sulfur and oxygen isotopes in marine sulfate and their mutual interpretation. *Chem. Geol.* **28**, 199–260.

Conliffe J., Wilton D. H. C., Blamey N. J. F. and Archibald S. M. (2013) Paleoproterozoic Mississippi Valley Type Pb-Zn mineralization in the Ramah Group, Northern Labrador: Stable isotope, fluid inclusion and quantitative fluid inclusion gas analyses. *Chem. Geol.* **362**, 211–223.

Cooke D. R., Bull S. W., Large R. R. and McGoldrick P. J. (2000) The Importance of Oxidized Brines for the Formation of Australian Proterozoic Stratiform Sediment-Hosted Pb-Zn (Sedex) Deposits. *Econ. Geol.* **95**, 1–18.

Dawson K. M. and Orchard M. J. (1982) Regional metallogeny of the northern Cordillera: biostratigraphy, correlation and metallogenic significance of bedded barite occurrences in eastern Yukon and western District of Mackenzie. *Geol. Surv. Canada, Pap. 82-1C*, 31–38.

Eisbacher G. H. (1985) Late proterozoic rifting, glacial sedimentation, and sedimentary cycles in the light of Windermere deposition, Western Canada. *Palaeogeogr. Palaeoclimatol. Palaeoecol.* **51**, 231–254.

Eldridge C. S., Walshe J. L., Compston W., Williams I. S., Both R. A., Ohmoto H., Goodfellow W. D. and Turner R. J. W. (1988) Sulfur isotope variability in sediment-hosted massive sulfide deposits as determined using the ion microprobe SHRIMP: I. An example from the Rammelsberg Orebody – a reply. *Econ. Geol.* **84**, 443–449.

Farquhar J., Nanping W., Canfield D. E. and Oduro H. (2010) Connections between Sulfur Cycle Evolution, Sulfur Isotopes, Sediments, and Base Metal Sulfide Deposits. *Econ. Geol.* **105**, 509–533.

Froelich P. N., Klinkhammer G. P., Bender M. L., Luedtke N. A., Heath G. R., Cullen D., Dauphin P., Hammond D. and Hartman B. (1979) Early oxidation of organic matter in pelagic sediments of the eastern equatorial Atlantic: suhoxic diagenesis. *Geochim. Cosmochim. Acta* **43**, 1075–1090.

Gabrielse H. (1967) Tectonic evolution of the northern Canadian Cordillera. *Can. J. Earth Sci.* **4**, 271–298.

Gardner H. D. and Hutcheon I. (1985) Geochemistry, Mineralogy, and Geology of the Jason Pb-Zn Deposits, Macmillan Pass, Yukon, Canada. *Econ. Geol.* **80**, 1257–1276.

Goodfellow W. D. (1987) Anoxic Stratified Oceans as a Source of Sulphur in Sediment-Hosted Stratiform Zn-Pb Deposits (Selwyn Basin, Yukon, Canada). *Chem. Geol.* **65**, 359–382.

Goodfellow W. D. (2007) Base metal metallogeny of the Selwyn Basin, Canada. In *Mineral Deposits of Canada: A Synthesis of Major Deposit-Types, District*

Metallogeny, the Evolution of Geological Provinces, and Exploration Methods Geological Association of Canada, Mineral Deposits Division, Special Publication. pp. 553–579.

Goodfellow W. D., Cecile M. P. and Leybourne M. I. (1995) Geochemistry, petrogenesis, and tectonic setting of lower Paleozoic alkalic and potassic volcanic rocks, Northern Canadian Cordilleran miogeocline. *Can. J. Earth Sci.* **32**, 1236–1254.

Goodfellow W. D. and Jonasson I. R. (1986) Environment of formation of the Howards Pass (XY) Zn-Pb deposit, Selwyn Basin, Yukon. In *Mineral Deposits of Northern Cordillera* (ed. J. A. Morin). The Canadian Institute of Mining and Metallurgy. pp. 19–50.

Goodfellow W. D. and Jonasson I. R. (1984) Ocean stagnation and ventilation defined by ^{34}S secular trends in pyrite and barite, Selwyn Basin, Yukon. *Geology* **12**, 583–586.

Goodfellow W. D. and Lydon J. W. (2007) Sedimentary Exhalative (SEDEX) Deposits. In *Mineral Deposits of Canada: A Synthesis of Major Deposit-Types, District Metallogeny, the Evolution of Geological Provinces, and Exploration Methods* pp. 163–183.

Goodfellow W. D. and Turner R. J. W. (1988) Sulfur isotope variability in sediment-hosted massive sulfide deposits as determined using the ion microprobe SHRIMP: I. An example from the Rammelsberg Orebody – a discussion. *Econ. Geol.* **84**, 451–452.

Gordey S. P. and Anderson R. G. (1993) *Evolution of the northern cordilleran miogeocline, Nahanni map area (105I), Yukon and Northwest Territories.* Memoir 428., Geological Survey of Canada, Memoir 428.

Greinert J., Bollwerk S. M., Derkachev A., Bohrmann G. and Suess E. (2002) Massive barite deposits and carbonate mineralization in the Derugin Basin, Sea of Okhotsk: precipitation processes at cold seep sites. *Earth Planet. Sci. Lett.* **203**, 165–180.

Griffith E. M. and Paytan A. (2012) Barite in the ocean - occurrence, geochemistry and palaeoceanographic applications. *Sedimentology* **59**, 1817–1835.

Habicht K. S. and Canfield D. E. (1997) Sulfur isotope fractionation during bacterial sulfate reduction in organic-rich sediments. *Geochim. Cosmochim. Acta* **61**, 5351–61.

Harrison A. G. G. and Thode H. G. (1958) Mechanism of the bacterial reduction of sulphate from isotope fractionation studies. *Trans. Faraday Soc.* **54**, 84–92.

Horita J., Zimmerman H. and Holland H. D. (2002) Chemical evolution of seawater during the Phanerozoic : Implications from the record of marine evaporites. *Geochim. Cosmochim. Acta* **66**, 3733–3756.

Irwin S. E. B. and Orchard M. J. (1991) Upper Devonian–Lower Carboniferous conodont biostratigraphy of the Earn Group and overlying units, northern Cordillera. In *Ordovician to Triassic Conodont Paleontology of the Canadian Cordillera* (eds. M. J. Orchard and A. D. McCracken). Geological Survey of

Canada, Bulletin 417. pp. 185–213.

Johnson C. a., Emsbo P., Poole F. G. and Rye R. O. (2009) Sulfur- and oxygen-isotopes in sediment-hosted stratiform barite deposits. *Geochim. Cosmochim. Acta* **73**, 133–147.

Johnson C. A., Kelley K. D. and Leach D. L. (2004) Sulfur and Oxygen Isotopes in Barite Deposits of the Western Brooks Range, Alaska, and Implications for the Origin of the Red Dog Massive Sulfide Deposits. *Econ. Geol.* **99**, 1435–1448.

Jørgensen B. B., Böttcher M. E., Lüschen H., Neretin L. N. and Volkov I. I. (2004) Anaerobic methane oxidation and a deep H_2S sink generate isotopically heavy sulfides in Black Sea sediments. *Geochim. Cosmochim. Acta* **68**, 2095–2118.

Kaplan I. R. and Rittenberg S. C. (1964) Microbiological Fractionation of Sulphur Isotopes. *J. Gen. Microbiol.* **34**, 195–212.

Kelley K. D., Dumoulin J. A. and Jennings S. (2004) The Anarraaq Zn-Pb-Ag and Barite Deposit, Northern Alaska: Evidence for Replacement of Carbonate by Barite and Sulfides. *Econ. Geol.* **99**, 1577–1591.

Kelley K. K. and Jennings S. (2004) A Special Issue Devoted to Barite and Zn-Pb-Ag Deposits in the Red Dog District, Western Brooks Range, Northern Alaska. *Econ. Geol.* **99**, 1267–1280.

Large R. R., Bull S. W., McGoldrick P. J., Walters S., Derrick G. M. and Carr G. R. (2005) Strata-Bound and Stratiform Zn-Pb-Ag Deposits in Proterozoic Sedimentary Basins, Northern Australia. *Econ. Geol.* **100**, 931– 963.

Leach D. L., Bradley D. C., Huston D., Pisarevsky S. A., Taylor R. D. and Gardoll J. (2010) Sediment-Hosted Lead-Zinc Deposits in Earth History. *Econ. Geol.* **105**, 593–625.

Leach D. L., Marsh E., Emsbo P., Rombach C. S., Kelley K. K. and Anthony M. (2004) Nature of Hydrothermal Fluids at the Shale-Hosted Red Dog Zn-Pb-Ag Deposits, Brooks Range, Alaska. *Econ. Geol.* **99**, 1449–1480.

Leach D. L., Sangster D. F., Kelley K. D., Large R. R., Garven G., Allen C. R., Gutzmer J. and Walters J. (2005) Sediment-Hosted Lead-Zinc Deposits: A Global Perspective. *Econ. Geol.* **100**, 561–607.

Leach D. and Sangster D. F. (1993) Mississippi Valley-type lead-zinc deposits. In *Mineral Deposit Modeling* (eds. R. V. Kirkham, W. D. Sinclair, R. I. Thorpe, and J. M. Duke). Geological Association of Canada. pp. 289–314.

Lowenstein T. K., Hardie L. a., Timofeeff M. N. and Demicco R. V. (2003) Secular variation in seawater chemistry and the origin of calcium chloride basinal brines. *Geology* **31**, 857.

Lyons T. W., Gellatly A. M., Mcgoldrick P. J. and Kah L. C. (2006) Proterozoic sedimentary exhalative (SEDEX) deposits and links to evolving ocean chemistry. *Geol. Soc. Am. Mem.* **198**, 169–184.

Macquaker J. H. S., Bentley S. J. and Bohacs K. M. (2010) Wave-enhanced sediment-gravity flows and mud dispersal across continental shelves: Reappraising sediment transport processes operating in ancient mudstone successions.

Geology **38**, 947–950.

Nelson J. and Colpron M. (2007) Tectonics and metallogeny of the British Columbia, Yukon and Alaskan Cordillera, 1.8 Ga to the present. *Miner. Depos. Canada A Synth. Major Depos. Dist. Metallog. Evol. Geol. Prov. Explor. Methods* **2703**, 755–791.

Nelson J. L., Survey B. C. G., Box P. O., Govt S. P., Columbia B., Colpron M., Piercey S. J., Road R. L., Dusel-bacon C., Park M. and Murphy D. C. (2006) Paleozoic tectonic and metallogenetic evolution of pericratonic terranes in Yukon , northern British Columbia and eastern Alaska 1. *GAC Spec. Pap.* *45*, 323–360.

Nelson J., Paradis S., Christensen J. and Gabites J. (2002) Canadian Cordilleran Mississippi Valley-Type Deposits : A Case for Devonian-Mississippian Back-Arc Hydrothermal Origin. *Econ. Geol.* **97**, 1013–1036.

Ohmoto H. and Goldhaber M. B. (1997) Sulfur and Carbon Isotopes. In *Geochemistry of Hydrothermal Ore Deposits* (ed. H. L. Barnes). John Wiley & Sons. pp. 517–612.

Paytan A., Mearon S., Cobb K. and Kastner M. (2002) Origin of marine barite deposits: Sr and S isotope characterization. *Geology* **30**, 747.

Rajabi A., Rastad E., Canet C. and Alfonso P. (2014) The early Cambrian Chahmir shale-hosted Zn–Pb deposit, Central Iran: an example of vent-proximal SEDEX mineralization. *Miner. Depos.*

Samson I. M. and Russell M. J. (1987) Genesis of the Silvermines zinc-lead-barite

deposit, Ireland; fluid inclusion and stable isotope evidence. *Econ. Geol.* **82**, 371–394.

Schieber J., Southard J. B. and Schimmelmann A. (2010) Lenticular Shale Fabrics Resulting from Intermittent Erosion of Water-Rich Muds--Interpreting the Rock Record in the Light of Recent Flume Experiments. *J. Sediment. Res.* **80**, 119–128.

Schieber J., Southard J. and Thaisen K. (2007) Accretion of mudstone beds from migrating floccule ripples. *Science* **318**, 1760–3.

Seal R. R. (2006) Sulfur Isotope Geochemistry of Sulfide Minerals. *Rev. Mineral. Geochemistry* **61**, 633–677.

Seal R. R., Alpers C. N. and Rye R. O. (2000) Stable Isotope Systematics of Sulfate Minerals. *Rev. Mineral. Geochemistry* **40**, 541–602.

Singer D. A. (1995) World Class Base and Precious Metal Deposits – A Quantitative Analysis. *Econ. Geol.* **90**, 88–104.

Stoffell B., Appold M. S., Wilkinson J. J., McClean N. A. and Jeffries T. E. (2008) Geochemistry and Evolution of Mississippi Valley-Type Mineralizing Brines from the Tri-State and Northern Arkansas Districts Determined by LA-ICP-MS Microanalysis of Fluid Inclusions. *Econ. Geol.* **103**, 1411–1435.

Thode H. G., Monster J. and Dunford H. B. (1961) Sulphur isotope geochemistry. *Geochim. Cosmochim. Acta* **25**, 159–174.

Tornos F. and Heinrich C. (2008) Shale basins, sulfur-deficient ore brines and the

formation of exhalative base metal deposits. *Chem. Geol.* **247**, 195–207.

Torres M. E., Bohrmann G., Dubé T. E., Poole F. G., Poole, Forrest G. and Poole F. G. (2003) Formation of modern and Paleozoic stratiform barite at cold methane seeps on continental margins. *Geology* **31**, 897–900.

Torres M. E., Brumsack H. J., Bohrmann G. and Emeis K. C. (1996) Barite fronts in continental margin sediments: a new look at barium remobilization in the zone of sulfate reduction and formation of heavy barites in diagenetic fronts. *Chem. Geol.* **127**, 125–139.

Turner R. J. W. (1992) Formation of Phanerozoic stratiform sediment , hosted zinc-lead deposits : Evidence for the critical role of ocean anoxia. *Chem. Geol.* **99**, 165–188.

Wilkinson J. J. (2003) On diagenesis, dolomitisation and mineralisation in the Irish Zn-Pb orefield. *Miner. Depos.* **38**, 968–983.

Wilkinson J. J. (2014) Sediment-Hosted Zinc–Lead Mineralization: Processes and Perspectives. In *Treatise on Geochemistry: Second Edition* Elsevier Ltd. pp. 219–249.

Yardley B. W. D. (2005) Metal Concentrations in Crustal Fluids and Their Relationship to Ore Formation. *Econ. Geol.* **100**, 613–632.

Chapter 2. The importance of siliceous radiolarian bearing mudstones in the formation of sediment-hosted Zn-Pb+-Ba mineralisation in the Selwyn Basin, Yukon, Canada).

2.1. Introduction

The Paleozoic Selwyn Basin, Canada, is host to multiple Clastic-Dominated (CD) –type deposits (Leach et al., 2010), which collectively have a total known tonnage of 55Mt (Pb + Zn; Taylor et al., 2009). This endowment represents a significant accumulation of base metal sulphides, making the Selwyn Basin the third most fertile sedimentary basin discovered in the geological record, behind the Proterozoic Mt. Isa-McArthur Basin (112Mt) and Curnamona Craton (75Mt; Broken Hill) (Goodfellow and Lydon, 2007). These deposits are typically hosted by siliceous, organic-rich, mud- and siltstones, and form laterally extensive (>100s meters), tabular ore bodies. In the Selwyn Basin the mudstone host-rocks have been interpreted as pelagic, deep marine deposits, formed during periods of basinal restriction with limited clastic input (Goodfellow, 2007). The mudstones commonly appear homogenous and featureless in the field, are poorly exposed and are located within the Cordilleran fold and thrust belt, making the mapping, logging and correlation of important basinal events challenging.

Mudstones typically comprise detrital and biogenic components (Aplin and Macquaker, 2011), and although often featureless, it is possible to derive useful geologic information via detailed petrographic (Macquaker et al., 2007) and geochemical characterization (Harris et al., 2013). Radiolarians, which can form an important biogenic component of mudstones, are siliceous, planktonic organisms that

occur from the Lower Cambrian to present (Anderson, 1983). The availability of nutrients, not silica, controls the proliferation of radiolarians, and so they are particularly abundant within strata formed in high productivity settings (e.g. upwelling zones; De Wever and Baudin, 1996). Radiolarian tests can range in size from 30μm to 2mm with a skeleton composed of opal-A synthesized from dissolved silica, which also provides a framework for structurally bound organic carbon (De Wever and Baudin, 1996; De Wever et al., 2001). Although not strictly primary producers, radiolarians are most abundant in the photic zone (upper 200m), and due to the absence of a silica compensation depth, they can be preserved at a wide range of depths (Anderson, 1983).

This Chapter documents the presence of a distinctive unit containing high abundances of radiolarians, located in the mineralised strata at the Tom and Jason deposits (Macmillan Pass district), and also in un-mineralised (barren) strata. This association suggests that oceanic productivity and sedimentation is broadly time-equivalent with hydrothermal activity. This unit is also useful as a marker bed in barren rocks. This is significant, as large sections of the stratigraphy are featureless in outcrop, and are thus challenging to map and correlate. We suggest that the high Si content of these rocks is derived predominantly from biogenic silica, and that it had an important role in facilitating sub-surface fluid flow.

2.2. Geological Background

The Selwyn Basin comprises an ocean-ward thickening sequence of clastic sedimentary rocks deposited along the continental margin of Laurentia (ancestral North America)

between the Neoproterozoic and Late Devonian (Gabrielse, 1967). The onset of basinal sedimentation was initiated during rifting associated with the continental breakup of Rodinia (~760 Ma), and led to passive margin sedimentation (Eisbacher, 1985; Gordey and Anderson, 1993). Time equivalent strata are also preserved in the Kechika Trough, which forms a southeastwardly extension of the Selwyn Basin (MacIntyre, 1998). The sedimentary environment changed in the Late Devonian-Mississippian, as thick accumulations of coarse clastic sedimentary rocks were deposited over basinal strata (Gordey and Anderson, 1993). This change in sedimentology has been attributed to regional extension in a distal back-arc setting, produced during slab roll-back (Nelson et al., 2002; Nelson et al., 2006). Subsequent Jurassic-Cretaceous accretionary deformation then led to the incorporation of strata into the northern Cordilleran fold and thrust belt (Nelson and Colpron, 2007). Selwyn Basin strata form part of the *inner belt* (basinal facies of Ancestral North America), characterized by regional-scale folds and thrusts, slaty cleavage and tight isoclinal folding; platformal carbonates form the *outer belt* (platform facies of Ancestral North America) and represent the eastern most extent of deformation (Gordey et al., 2010).

Three major periods of CD-type mineralisation have been recognised in the Selwyn Basin and Kechika Trough (Figure 2.1), hosted by Cambrian, Silurian and Upper Devonian strata. The oldest mineralisation is located in the Anvil district, and is hosted in the Cambrian Mount Mye Formation, which comprises poly-deformed phyllites and schists that are time-equivalent to the Gull Lake Formation (Pigage, 1991). Carbonaceous and siliceous mudstones of the Ordovician-Silurian Road River Group are the host to the Zn-Pb deposits of the Howard's Pass district (Morganti, 1979). Lastly, Upper Devonian strata preserve hydrothermal activity in the Selwyn Basin and Kechika Trough (Pigage, 1986; Paradis et al., 1998). At Macmillan Pass,

massive sulphide mineralisation (Tom, Jason Zn-Pb deposits) is hosted in the carbonaceous and siliceous mudstones of the Earn Group (Goodfellow and Rhodes, 1991). The Earn Group in this area is relatively undeformed and has been subject to sub-greenschist metamorphism; therefore, the units contain well preserved primary hydrothermal and sedimentary features. As a result, the model for Selwyn Basin-type deposits (see Goodfellow and Lydon, 2007) has been largely developed from work at Macmillan Pass.

2.3. Sampling and Methods

Ten drill-cores from the Tom and Jason camps were logged, and changes in lithology, sedimentary facies, hydrothermal alteration and paragenetic stages of mineralisation were recorded in detail. For this study, samples from above and below the ore horizon in two of the most characteristic drill-holes at Tom (TYK-1, TYK-5) and a regional, un-mineralised drill-hole between Tom and Jason (76-17) are described (see Figure 2.1 for drill-hole locations). Transmitted and reflected light petrography was used to determine textural and mineralogical relationships in mineralised and un-mineralised samples. Un-mineralised mudstone samples, with no evidence of veining or alteration, were obtained from TYK-5 (n = 18) and 76-17 (n = 19) and analyzed for major element oxides at ACME Laboratories, Vancouver. Bulk rock powders were analyzed via lithium metaborate / tetraborate fusion-XRF. Total organic carbon (TOC) was analyzed on the same bulk rock powders at Geomark Laboratories, Texas.

2.4. Results

At Macmillan Pass, the Zn-Pb mineralisation is hosted by a siliceous mudstone that is hard and dark grey to black in color (Figure 2.2A). Apart from subtle, graded (silt to mud) sub-centimeter beds it is relatively homogenous. Radiolarians are disseminated within this siliceous mudstone in all drill-holes; they are most commonly preserved as microcrystalline quartz spheroids (<0.5mm), and can be difficult to distinguish from quartz silt unless remnants of the fine skeletal structure are present (Figure 2.2B and C). Notably, high abundance beds (<10cm thick) with >50% (by volume) radiolarians are present in the mudstone units at Tom and Jason, and in the regional drill-hole (76-17). In these beds, where some radiolarians have been replaced by carbonate and weathered, the mudstone has a distinctive spotty appearance (Figure 2.2D). Within the mineralised strata at Tom and Jason there is evidence of abundant radiolarians preserved in the host rock; commonly, the basic skeletal outline has been partially preserved by an early generation of pyrite, which is then overprinted by base-metal sulphides (Figure 2.2E and F). The morphology of the preserved radiolarians are of the taxonomic order Spumellaria (Anderson, 1983). Radiolarians are 50-150μm in diameter, and have fine concentric shells around a central capsule with delicate spines that radiate outward (rhizopodia; De Wever et al. 2001).

The siliceous mudstone overlies a package of coarser siltstone, sandstone, diamictites and major conglomerate beds, consistent with previous detailed studies by Abbott and Turner (1991). The diamictite bed, and underlying sedimentary sequence (conglomerates, silt-laminated mudstones), can be used to broadly correlate between drill-holes at Tom and Jason, as is shown between TYK-5 and 76-17 (Figure 2.3). TYK-5 and TYK-1 are located relatively close to each other (<250 meters), although the

absence of the diamictite and conglomerate beds from TYK-5 may be linked to a combination of fault displacement and lateral variability in the deposition of these sequences. The mineralised strata in TYK-1 and TYK-5 are, therefore, considered to be correlative.

The stratigraphic correlation provides a framework in which to assess the composition of the mudstones, and compare samples from a setting that is distal to mineralisation (76-17) with those that are more proximal (TYK-5). All mudstones are SiO_2-enriched (67 to 83 wt.% SiO_2) relative to the North American Shale Composite (NASC = 60 to 64 wt. % SiO_2; Gromet et al., 1984). In Figure 2.3, the organic carbon content (TOC) and SiO_2 content (normalized to Al_2O_3) of the samples from 76-17 and TYK-5 are presented alongside the drill-hole logs. TOC values range between 2 to 5 wt. % and SiO_2 / Al_2O_3 between 7 and 14, both of which are largely consistent between the two drill-holes. Further major element chemistry for these samples is presented in Figure 2.4 and Tables A1 and A2 (appendix A). In Figure 2.4A, three important trends are apparent: (1) 76-17 has a uniform K_2O / Al_2O_3 ratio, the molar proportions of which are consistent with muscovite; (2) the K_2O / Al_2O_3 ratio of TYK-5 is markedly lower than 76-17, particularly for samples in close proximity to mineralisation (Figure 2.4B); and (3) a trend towards increasing CaO and MgO is likely representative of increasing carbonate content. In terms of SiO_2, there is a negative correlation with TiO_2 (Figure 2.4C).

2.5. Discussion

2.5.1. Exploration implications and the origin of silica

At Macmillan Pass, the radiolarian-rich unit serves as a marker, which, supported by stratigraphic relationships, can be used to correlate between mineralised and un-mineralised strata. This is particularly valuable when working with fine-grained, recessive and deformed units, in which alternative stratigraphic constraints (e.g. radiometric geochronometers, biostratigraphy, geochemistry) are unavailable and may not always provide the same resolution. These mudstones are also highly siliceous, which may in part reflect the biogenic input of radiolarians. However, it can be challenging to demonstrate, without ambiguity, the link between biogenic processes and silica content, considering silica may also be sourced via detrital and hydrothermal inputs. Along with clay minerals and minor feldspar and lithic components, quartz silt is a major detrital component of mudstones deposited in marine settings (Aplin and Macquaker, 2011). Assessment of detrital input commonly involves normalization to proxy elements such as Ti and Al (for discussion, see Van Der Weijden, 2002). In 76-17, uniform K_2O / Al_2O_3 ratios are consistent with detritally-sourced muscovite (Figure 2.4A, B). However, SiO_2 / Al_2O_3 is uncorrelated with K_2O / Al_2O_3 (Figure 2.4B), and negatively correlated with TiO_2 (Figure 2.4C), providing evidence that in these samples, a substantial proportion of silica has a non-detrital origin.

Hydrothermal alteration is another potential source of silica in carbonaceous mudstones (e.g. Slack et al., 2004). The identification of siliceous mudstones within both barren (76-17) and mineralised (TYK-5) stratigraphic sequences provides a useful framework for evaluating hydrothermal alteration and associated input of silica.

Hydrothermal alteration can be assessed using a variety of major element indices (e.g. Böstrom, 1973; Nesbitt and Young, 1982; Large and Mcgoldrick, 1998). Using the chemical index of alteration (CIA, defined in Figure 4A; Nesbitt and Young, 1982), the samples at Macmillan Pass fall mostly within a range typical of un-altered mudstones (CIA = ~70). However, in TYK-5, lower K_2O / Al_2O_3 ratios in samples proximal to the mineralised interval (Figure 2.4B) indicate the loss of potassium relative to samples from 76-17. Such potassium loss likely occurred as the host rock buffered an acidic hydrothermal fluid (Yardley, 2005), and it represents subtle alteration that is not recorded by other proxies (e.g. Böstrom, 1973; Nesbitt and Young, 1982; Large and Mcgoldrick, 1998). Importantly, this alteration is not correlated with silica content, and provides convincing evidence that hydrothermal input was not a major source of silica in these samples.

Therefore, the major source of silica in these samples was biogenic in origin. This is consistent with Harris et al. (2013), who proposed biogenic activity as the source of silica in Upper Devonian (Frasnian-Fammenian) mudstones from the Permian Basin (Texas), and which preserve comparable TOC (median = 4.9 wt. %) and SiO_2 / Al_2O_3 (median = 12) contents to samples from Macmillan Pass. Furthermore, a model in which siliceous organisms (e.g. radiolarians) formed an important biogenic flux to the mudstones at Macmillan Pass is consistent with Schieber et al. (2000), who cautioned that the high quartz content in mudstones observed throughout the Paleozoic may actually represent high fluxes of productivity-derived silica. Indeed, recent models of the global silica cycle now suggest that highly productive continental margin settings form a major sink for biogenic silica deposition (DeMaster, 2002; Tréguer and De La Rocha, 2013).

2.5.2. Siliceous mudstones as a host rock

Siliceous radiolarian-rich units are a common feature of strata hosting base metal deposits in the Selwyn Basin. Similar to the deposits at Macmillan Pass (this study), radiolarians have been identified in the siliceous mudstones hosting the Cirque deposit of the Gataga district (McClay, 1991) and also the chert hosting the Howard's Pass deposits (Morganti, 1979). At Macmillan Pass therefore, the role of biogenic silica in the host rock and any impact on the hydrothermal system warrants evaluation from a physical and chemical perspective.

The TOC content of the Macmillan Pass mudstones, consistently greater than 2 wt.%, is higher than average marine mudstones (approximately 0.5 wt.%; Aplin and Macquaker, 2011). Multiple variables contribute to the preservation of organic carbon in marine sediments and sedimentary rocks (see Arthur and Sageman, 1994); however, the level of organic matter preservation observed at Macmillan Pass has been interpreted to represent enhanced primary productivity during the Late Devonian. This is also supported by the preservation of high abundance radiolarian beds, typically produced during seasonal blooms of intense biological productivity (De Wever and Baudin, 1996).

Recognising evidence of productivity in otherwise featureless mudstones represents an important step for identifying potential host rocks for CD-type deposits. Whether by biogenic or abiogenic pathways, organic carbon is a powerful reductant of sulphate, and it forms an important constituent of sediments deposited in highly productive settings (Arthur and Sagemann, 1994). Biosiliceous, carbonaceous mudstones formed in highly productive settings, therefore, have a high capacity to reduce sulphate and generate sulphide, and thus provide the chemical "trap" necessary

to form a massive sulphide deposit.

In modern day environments, sediments rich in biogenic silica are deposited along highly productive continental margin settings (e.g. the Peruvian upwelling zone; Scholz et al., 2011), and recent models of the global silica cycle suggest these settings form a major sink for biogenic silica deposition (DeMaster 2002; Tregeur and De La Rocha, 2013). Dynamic and seasonal processes are characteristic in these environments, including high fluxes of biogenic detritus, variable organic concentrations and extreme redox gradients (Böning et al., 2004; Scholz et al., 2011). Importantly, unconsolidated biosiliceous sediments can retain high porosities during shallow burial (>70% at 500m; Isaacs et al., 1982), and fluid flow regimes in the shallow subsurface can be dynamic (Davies et al., 2006; Davies et al., 2008). The possibility that partially lithified siliceous sediment, rich in radiolarians, can facilitate fluid flow is an interesting idea, considering the role mudstones often form as impermeable barriers (Aplin and Macquaker, 2011). Indeed, sulphide preservation of radiolarian tests (Figure 2.2E and F), and mudstone alteration both fifteen meters above and below the mineralised interval in TYK-5 (Figure 2.4B), lends support to a model in which some component of hydrothermal fluid flow occurred in the subsurface away from the primary vent. Although high porosities do not necessarily produce high permeabilities, the opaline silica framework in partially lithified biosiliceous sediments forms both a more permeable and chemically reactive medium than a lithified mudstone (Davies et al. 2008). Furthermore, enhanced porosities in fluid saturated pore space could potentially be exploited during sub-seafloor replacement. The infiltration and interaction of hydrothermal fluids with partially lithified, sulphur-rich sediments is likely to be an important aspect in the development of all CD-type systems, particularly considering the physical and chemical heterogeneities that exist in sediment shortly

after deposition (see Aller, 2014). At Macmillan Pass, we would argue that radiolarian-rich units within siliceous mudstones facilitated sub-seafloor fluid flow and preserved volume that was exploited by sub-seafloor replacement processes. The deposition of these lithologies in a productive environment provided the host rock with some of the necessary prerequisites (organic matter) for effective massive sulphide mineralisation.

2.6. Conclusions

The association of radiolarian-rich mudstones with CD-type base-metal mineralisation at Macmillan Pass, and elsewhere in the Selwyn Basin, represents a simple, field-recognisable stratigraphic marker for these deposits in the Late Devonian. This study demonstrates some of the useful interpretations that can be made using careful petrography of these challenging rocks and major element geochemistry. Abundant radiolarians point to highly productive conditions that may have been operational on a seasonal basis, and which also represent a high flux of biogenic silica to the mudstones deposited in the Late Devonian at the time of mineralisation. Biosiliceous lithologies host CD-type deposits throughout the Paleozoic in the Selwyn Basin, and we suggest that these units played an important role in the mineralising process; they facilitated the effective migration of hydrothermal fluids in the subsurface, and their organic carbon content meant they had a high capacity for the generation of sulphide via sulphate reduction. These factors should both be included as exploration criteria when identifying potential host rocks for sediment-hosted base-metal deposits in any sedimentary basin.

Figures

Figure 2.1. The local geology of MacMillan Pass (modified from Abbott and Turner, 1991) and location of the Tom and Jason deposits are below. The drill holes sampled for this study are indicated by the hexagonal markers (76-17, TYK-1 and TYK-5).
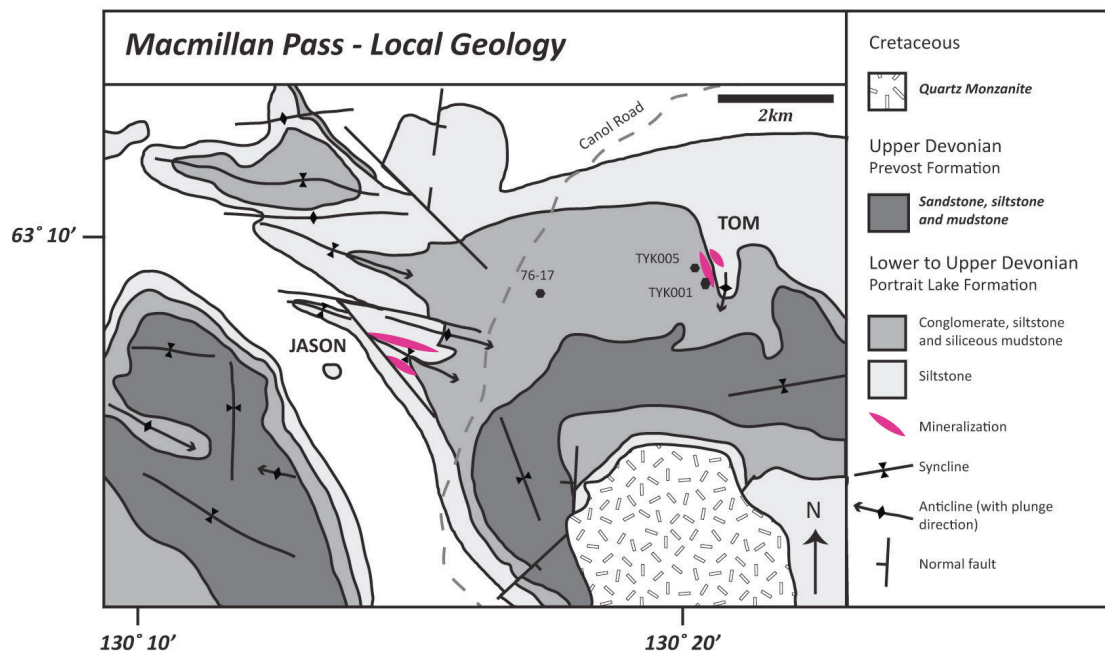
Figure 2.2. A – hand sample of typical mudstone from 76-17 (280m), with disseminated radiolarians preserved by diagenetic iron carbonate. B – a photograph of a sample from 76-17; radiolarian tests are clearly preserved by milky-white quartz, whereas those in the upper half of the image have been weathered out. C – thin section photomicrograph of silicified radiolarian tests (Tom deposit). Note the difference in scale compared to C. D - hand sample from a radiolarian-rich bed form 76-17 (285m), where radiolarians preserved by diagenetic carbonate have been weathered out resulting in a distinctive pockmarked appearance. E - photomicrograph from a bed containing abundant silicified radiolarians (silica spheroids) within the stratabound mineralisation at Tom. F - Radiolarians overprinted by multiple generations of sulphides in the stratabound mineralisation at Tom. Note the delicate skeletal structure that is preserved by the early generation of pyrite and preferentially replaced by later galena. Abbreviations; Py = pyrite, Gn = galena, Sp = sphalerite.
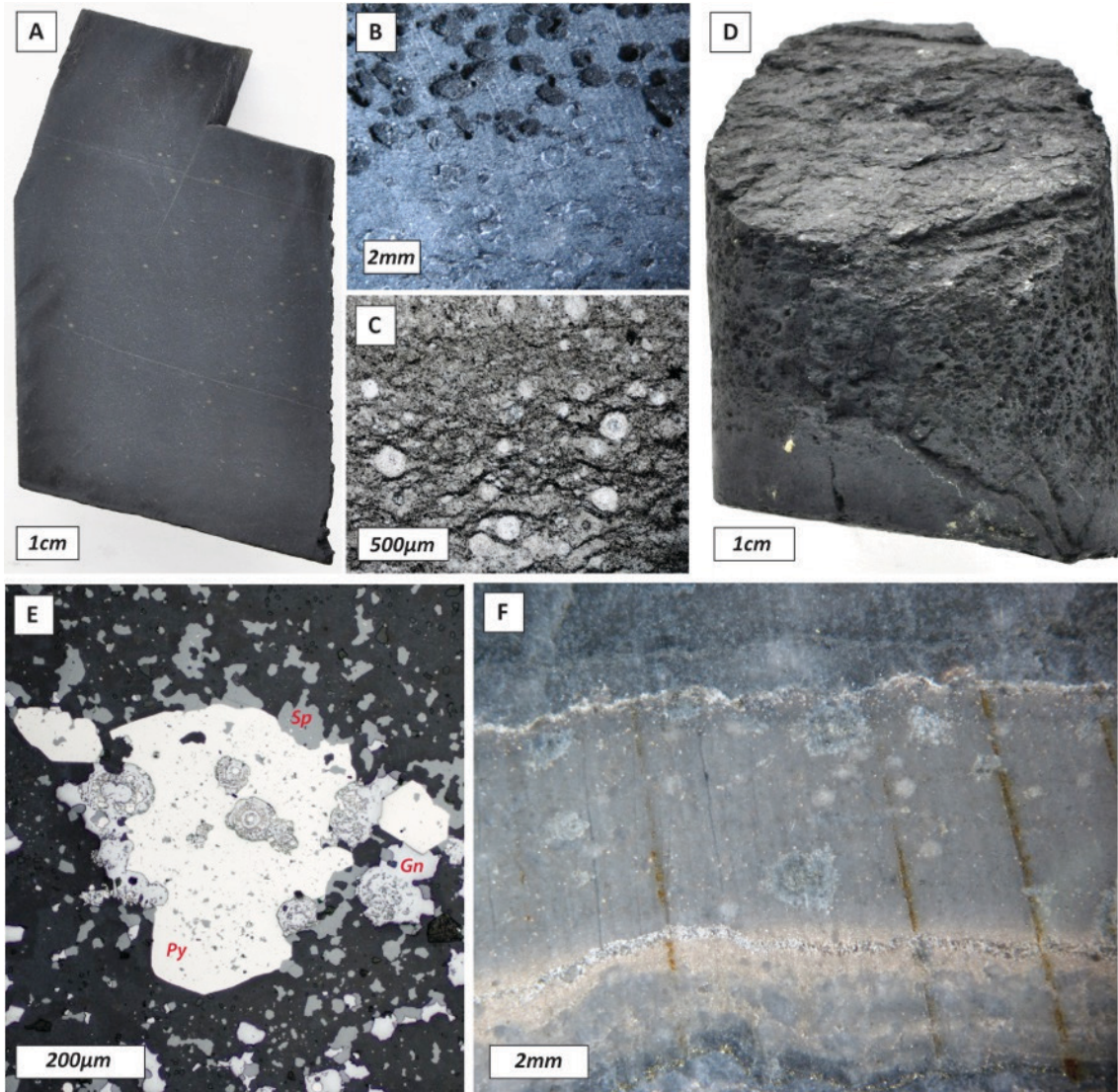
Figure 2.3. Sedimentary logs for drill-holes TYK-1, 76-17 and TYK-5. The dashed grey line between TYK-1 and 76-17 represents the correlation of a diamictite bed, and the black horizon in 76-17 (285m) represents the high abundance radiolarian unit; remnants of these beds have been identified in the mineralised strata at Tom and Jason but are too small (<10cm) to present in the logs. Total organic carbon (TOC; wt. %) and SiO_2 / Al_2O_3 data are presented for 76-17 and TYK-5.
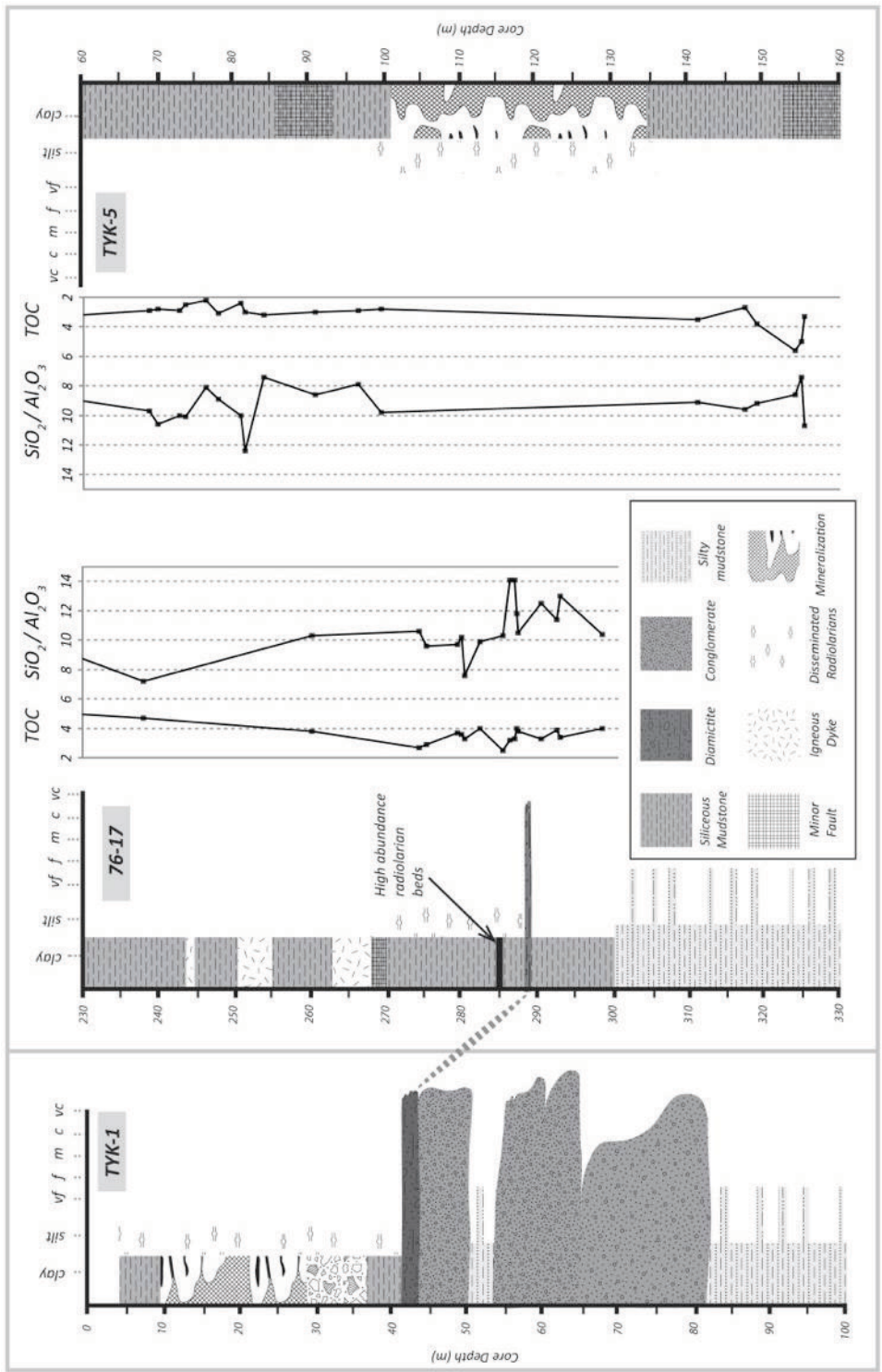
Figure 2.4. A – ternary plot of Al_2O_3—K_2O—$CaO+MgO$. Chemical index of alteration (CIA = [Al_2O_3 / (Al_2O_3+CaO+Na_2O+K_2O)] x 100; Nesbitt and Young, 1982) is represented by the size of the sample symbols, and number of samples corresponding with a CIA range is denoted in parentheses in the key. The three trends discussed in the text are highlighted with numbers and arrows. B – SiO_2 vs. K_2O (Al_2O_3 normalised) plot. The black line (0.29) represents the molar proportions (K_2O and Al_2O_3) for muscovite. Samples from TYK-5 all plot below 0.25, and samples <15m above or below mineralisation plot below 0.2. C – SiO_2 / Al_2O_3 vs. TiO_2 plot. A negative correlation for all samples supports a non-detrital origin for SiO_2.
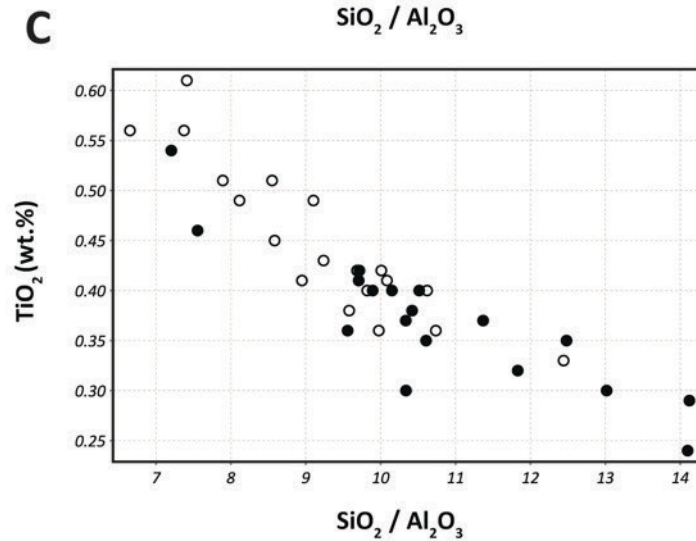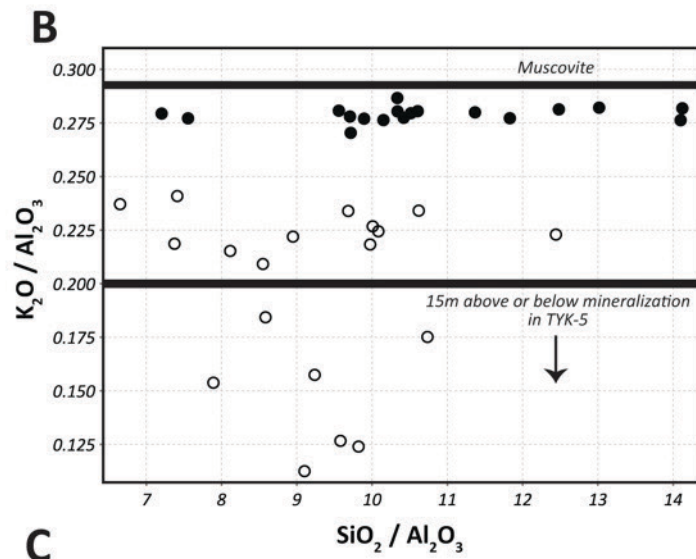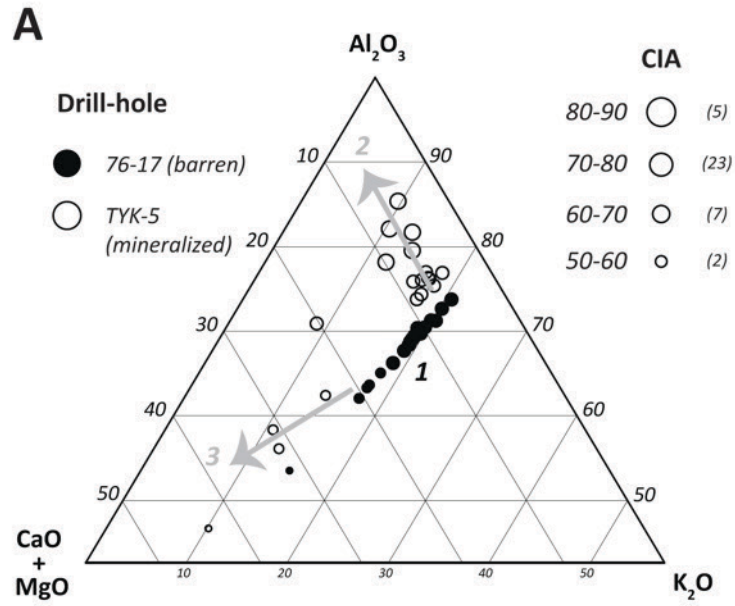
References

Abbott J. G. and Turner R. J. (1991) Character and paleotectonic setting of Devonian stratiform sediment-hosted Zn, Pb, Ba deposits, Macmillan Fold Belt, Yukon. In *Geological Survey of Canada Open File 2169* (eds. J. G. Abbott and R. J. Turner). pp. 99–136.

Aller R. C. (2014) Sedimentary Diagenesis, Depositional Environments, and Benthic Fluxes. In *Treatise on Geochemistry* Elsevier Ltd. pp. 293–334.

Anderson R. O. (1983) *Radiolaria*., New York Springer-Verlag.

Aplin A. C. and Macquaker J. H. S. (2011) Mudstone diversity : Origin and implications for source , seal , and reservoir properties in petroleum systems. *Am. Assoc. Pet. Geol. Bull.* **12**, 2031–2059.

Arthur M. A. and Sageman B. B. (1994) Marine black shales: depositional mechanisms and environments of ancient deposits. *Annu. Rev. Earth Planet. Sci.*

Böning P., Brumsack H.-J., Böttcher M. E., Schnetger B., Kriete C., Kallmeyer J. and Borchers S. L. (2004) Geochemistry of Peruvian near-surface sediments. *Geochim. Cosmochim. Acta* **68**, 4429–4451.

Böstrom K. (1973) The origin and fate of ferromanganoan active ridge sediments. *Stock. Contrib. to Geol.* **27**, 147–243.

Davies R. J., Goulty N. R. and Meadows D. (2008) Fluid flow due to the advance of

basin-scale silica reaction zones. *Geol. Soc. Am. Bull.* **120**, 195–206.

Davies R. J., Huuse M., Hirst P., Cartwright J. and Yang Y. (2006) Giant clastic intrusions primed by silica diagenesis. *Geology* **34**, 917.

DeMaster D. J. (2002) The accumulation and cycling of biogenic silica in the Southern Ocean: revisiting the marine silica budget. *Deep Sea Res. Part II Top. Stud. Oceanogr.* **49**, 3155–3167.

Eisbacher G. H. (1985) Late proterozoic rifting, glacial sedimentation, and sedimentary cycles in the light of windermere deposition, Western Canada. *Palaeogeogr. Palaeoclimatol. Palaeoecol.* **51**, 231–254.

Gabrielse H. (1967) Tectonic evolution of the northern Canadian Cordillera. *Can. J. Earth Sci.* **4**, 271–298.

Goodfellow W. D. (2007) Base metal metallogeny of the Selwyn Basin, Canada. In *Mineral Deposits of Canada: A Synthesis of Major Deposit-Types, District Metallogeny, the Evolution of Geological Provinces, and Exploration Methods* Geological Association of Canada, Mineral Deposits Division, Special Publication. pp. 553–579.

Goodfellow W. D. and Lydon J. W. (2007) Sedimentary Exhalative (SEDEX) Deposits. In *Mineral Deposits of Canada: A Synthesis of Major Deposit-Types, District Metallogeny, the Evolution of Geological Provinces, and Exploration Methods* pp. 163–183.

Goodfellow W. D. and Rhodes D. (1991) Geological setting, geochemsitry and origin of

the Tom stratiform Zn-Pb-Ag-barite deposits. In *Geological Survey of Canada Open File 2169* (eds. J. G. Abbott and R. J. Turner). pp. 177–239.

Gordey S. P. and Anderson R. G. (1993) *Evolution of the northern cordilleran miogeocline, Nahanni map area (105I), Yukon and Northwest Territories.* Memoir 428., Geological Survey of Canada, Memoir 428.

Gordey S. P., Macdonald J. D., Turner E. C. and Long D. G. F. (2010) Structural Geology of the Central Mackenzie Mountains. In *Geology of the central Mackenzie mountains of the North Canadian Cordillera, Sekwi Mountain (105P), Mount Eduni (106A), and northwestern Wrigley Lake (95M) map-areas, Northwest Territories* (eds. E. Martel, E. C. Turner, and B. J. Fischer). NWT Geoscience Office. pp. 215–250.

Gromet L. P., Haskin L. a., Korotev R. L. and Dymek R. F. (1984) The "North American shale composite": Its compilation, major and trace element characteristics. *Geochim. Cosmochim. Acta* **48**, 2469–2482.

Harris N. B., Mnich C. a., Selby D. and Korn D. (2013) Minor and Trace Element and Re-Os Chemistry of the Upper Devonian Woodford Shale, Permian Basin, West Texas: Insights into Metal Abundance and Basin Processes. *Chem. Geol.* **356**, 76–93.

Isaacs C. M., Survey U. S. G., Road M. and Park M. (1982) Influence of rock composition on kinetics of silica phase changes in the Monterey Formation , Santa Barbara area , California.

Large R. R. and Mcgoldrick P. J. (1998) Lithogeochemical halos and geochemical

vectors to stratiform sediment hosted Zn – Pb – Ag deposits, 1. Lady Loretta Deposit, Queensland. *J. Geochemical Explor.* **63**, 37–56.

Leach D. L., Bradley D. C., Huston D., Pisarevsky S. A., Taylor R. D. and Gardoll J. (2010) Sediment-Hosted Lead-Zinc Deposits in Earth History. *Econ. Geol.* **105**, 593–625.

MacIntyre D. G. (1998) *Geology, geochemistry and mineral deposits of the Akie River area, northeast British Columbia.*,

Macquaker J. H. S., Taylor K. G. and Gawthorpe R. L. (2007) High-Resolution Facies Analyses of Mudstones: Implications for Paleoenvironmental and Sequence Stratigraphic Interpretations of Offshore Ancient Mud-Dominated Successions. *J. Sediment. Res.* **77**, 324–339.

McClay K. R. (1991) Deformation of stratiform Zn-Pb (-barite) deposits in the northern Canadian Cordillera. *Ore Geol. Rev.* **6**, 435–462.

Morganti J. M. (1979) The geology and ore deposits of the Howards Pass area, Yukon and Northwest Territories: the origin of basinal sedimentary stratiform sulphide deposits. University of British Columbia.

Nelson J. and Colpron M. (2007) Tectonics and metallogeny of the British Columbia, Yukon and Alaskan Cordillera, 1.8 Ga to the present. *Miner. Depos. Canada A Synth. Major Depos. Dist. Metallog. Evol. Geol. Prov. Explor. Methods* **2703**, 755–791.

Nelson J. L., Survey B. C. G., Box P. O., Govt S. P., Columbia B., Colpron M., Piercey S.

J., Road R. L., Dusel-bacon C., Park M. and Murphy D. C. (2006) Paleozoic tectonic and metallogenetic evolution of pericratonic terranes in Yukon , northern British Columbia and eastern Alaska 1. *GAC Spec. Pap. 45*, 323–360.

Nelson J., Paradis S., Christensen J. and Gabites J. (2002) Canadian Cordilleran Mississippi Valley-Type Deposits : A Case for Devonian-Mississippian Back-Arc Hydrothermal Origin. *Econ. Geol.* **97**, 1013–1036.

Nesbitt H. W. and Young G. M. (1982) Early Proterozoic climates and plate motions inferred from major element chemistry of lutites. *Nature* **299**, 715–717.

Paradis S., Nelson J. L. and Irwin S. E. B. (1998) Age constraints on the devonian shale-hosted Zn-Pb-Ba deposits, Gataga District, Northeastern British Columbia, Canada. *Econ. Geol.* **93**, 184–200.

Pigage L. C. (1991) Field guide Anvil Pb-Zn-Ag District, Yukon Territory, Canada. In *Geological Survey of Canada Open File 2169* (eds. J. G. Abbott and R. J. W. Turner). pp. 177–244.

Pigage L. C. (1986) Geology of the Cirque barite-zinc-lead-silver deposits, northeastern British Columbia. In *Mineral Deposits of Northern Cordillera* (ed. J. A. Morin). Canadian Institute of Mining and Metallurgy. pp. 71–86.

Schieber J., Krinsley D. and Riciputi L. (2000) Diagenetic origin of quartz silt in mudstones and implications for silica cycling. *Nature* **406**, 981–5.

Scholz F., Hensen C., Noffke A., Rohde A., Liebetrau V. and Wallmann K. (2011) Early diagenesis of redox-sensitive trace metals in the Peru upwelling area – response

to ENSO-related oxygen fluctuations in the water column. *Geochim. Cosmochim. Acta* **75**, 7257–7276.

Slack J. F., Kelley K. D., Anderson V. M., Clark J. L. and Ayuso R. a. (2004) Multistage hydrothermal silicification and Fe-Tl-As-Sb-Ge-REE enrichment in the Red Dog Zn-Pb-Ag district, northern Alaska: Geochemistry, origin, and exploration applications. *Econ. Geol.* **99**, 1481–1508.

Taylor R. D., Leach D. L., Bradley D. C. and Psarevsky S. A. (2009) *Compilation of mineral resource data for Mississippi Valley-type and CD sediment-hosted lead-zinc deposits.*,

Tréguer P. J. and De La Rocha C. L. (2013) The world ocean silica cycle. *Ann. Rev. Mar. Sci.* **5**, 477–501.

Van Der Weijden C. H. (2002) Pitfalls of normalization of marine geochemical data using a common divisor. *Mar. Geol.* **184**, 167–187.

De Wever P. and Baudin F. (1996) Palaeogeography of radiolarite and organic-rich deposits in Mesozoic Tethys. *Geol. Rundschau* **85**, 310–326.

De Wever P., Dumitrica P., Caulet J. P., Nigrini C. and Caridroit M. (2001) *Radiolarians in the sedimentary record.*, Taylor and Francis.

Chapter 3. The role of diagenetic processes in the formation of shale hosted massive sulphide deposits - a sulphur and oxygen isotopic study of barite and pyrite from the Late Devonian Tom and Jason deposits, Selwyn Basin, Canada.

3.1. Introduction

The distribution of clastic-dominated (CD) Pb-Zn deposits (Leach et al., 2005; 2010) in the geological record has led to the suggestion that secular changes in ocean chemistry impart a fundamental control on ore genesis (Goodfellow and Jonasson, 1984; Turner et al., 1992; Lyons et al., 2006; Farquhar et al., 2010). In essence, these deposits represent anomalous accumulations of reduced sulphur in marine strata, the origin of which is widely accepted to be seawater sulphate (Ohmoto and Goldhaber, 1997). The mechanism of seawater sulphate reduction, therefore, is a fundamental component of metallogenesis.

In marine strata, bacterial sulphate reduction (BSR) is the most important geochemical pathway for sulphide production, and produces a large kinetic fractionation due to the preferential selection, by bacteria, of sulphate molecules containing ^{32}S and ^{16}O (Kaplan and Rittenberg, 1964). Bacterial sulphate reduction commonly occurs in the diagenetic environment, beneath the sediment water interface (SWI) where chemical, physical and biological processes continue to affect unconsolidated sediment post-deposition (see detailed reviews by Berner, 1980; Emerson and Hedges, 2003; Aller and Brook, 2014). Typically, pyrite forms a dominant sink for sulphide produced via BSR (Raiswell, 1982). In the Paleozoic,

evidence of BSR is typically recorded by ^{34}S-depleted pyrite (Canfield, 2004). It is, however, possible to produce a wide range of isotopic compositions during BSR, and the magnitude of the sulphur isotope fractionation is dependent on a number of factors, including sulphate reduction rate, substrate type and concentration (Canfield, 2001), sulphate diffusion and the isotopic composition of diffusional fluxes (Jørgensen, 1979; Jørgensen et al., 2001; Jørgensen and Kasten, 2006), reaction reversibility (Rees, 1973; Brunner and Bernasconi, 2005) and sedimentation rate (Goldhaber and Kaplan, 1975).

Positive δ^{34}S values are a characteristic feature of sulphides in CD-type deposits (Lyons et al., 2006). These isotopic compositions, when present in marine sediments in un-mineralised settings, are thought to represent periods of severe sulphate limitation commonly driven by BSR; such conditions may develop on a variety of scales, from within the cell membranes of sulphate reducing microorganisms (Habicht and Canfield, 1997), up to more regional scales within the water column (e.g. Newton et al., 2011). It is also possible to produce positive δ^{34}S values in the diagenetic environment (Jørgensen et al., 2004), and it was recently suggested that stratigraphic accumulations of pyrite, with positive δ^{34}S values, may be diagnostic of sulphate reduction near the sulphate-methane transition zone (Borowski et al. 2013). However, constraining diagenetic processes remains a challenge for many CD-type systems, as hydrothermal processes often overprint and destroy many early textures.

In the Selwyn Basin, Canada, there are three major base metal events hosted in organic rich mudstones (Figure 1.1; 1.2; 3.1). Stratiform accumulations of pyrite, barite, galena and sphalerite (e.g. Figure 3.2) have been used to infer syn-sedimentary precipitation from the water column, thereby invoking venting of Pb-Zn-Fe ± Ba rich

hydrothermal fluids above the SWI (Goodfellow and Lydon, 2007). For this reason, these deposits were originally referred to as sedimentary exhalative (SEDEX; Carne and Cathro, 1982), although clastic dominated (CD-type) has since been suggested as a non-genetic term (Leach et al., 2010). In the SEDEX model, a key component of mineralisation is the presence of a metal trap (i.e. reduced sulphur) in the water column; this requires the development of euxinic conditions, and accumulation of H_2S in the water column during near quantitative sulphate reduction during BSR. Precipitation of barite and pyrite from a restricted water column therefore provides the current explanation for their textural appearance (stratiform) and associated isotopic properties (positive $\delta^{34}S$ values) (Goodfellow and Jonasson, 1984; Goodfellow, 1987).

This model, herein referred to as the *Selwyn Basin model*, has some important implications for CD-type (or SEDEX) metallogenesis in the region: (1) to account for the accumulation of millions of tons of massive sulphide in a hydrothermal deposit, euxinic conditions, concomitant with hydrothermal activity, must have prevailed for long timescales (>5Ma; Turner, 1992), (2) in a restricted basin model, the short oceanic residence time of barium (10kyr; Paytan and Griffith, 2007) predicates a hydrothermal source of barium to sustain barite precipitation, and (3) for the Zn-Pb-(Ba) deposits in the Selwyn Basin, this implies co-transportation of barium and base metals in the hydrothermal fluid, the solubility constraints of which have been an important topic of discussion (Cooke et al., 2000).

The Late Devonian deposits at Macmillan Pass (Figure 1.1; 2.1) are the youngest, least deformed examples of Selwyn Basin CD-type mineralisation. The Macmillan Pass deposits are also host to abundant barite, which provides a record of the isotopic composition of sulphate ($\delta^{34}S_{sulphate}$). This is particularly important, for to a certain

extent the value of the sulphide sulphur ($\delta^{34}S_{sulphide}$) record depends on how the $\delta^{34}S_{sulphate}$ reservoir evolves. Previous studies employed mineral separate analysis, in which barite and pyrite were extracted from barren and mineralised mudstones in stratigraphic sequences hosting CDtype deposits in the Selwyn Basin (Goodfellow and Jonasson, 1984; Goodfellow, 1987). However, petrographic work now indicates a more complex paragenesis, including multiple generations of both barite and pyrite (Magnall et al. 2014). This means isotopic data obtained from this type of bulk analysis is likely derived from a mixture of sources. Furthermore, the presence of stratiform barite independent of sulphide mineralisation (e.g. Cecile et al., 1983; Fernandes, 2011), has led some to question whether or not the barium is hydrothermal in origin (Torres et al., 2003).

In recent years, the development of high-precision sulphur isotope micro-analytical techniques by secondary ion mass spectrometry (SIMS) enables more detailed isotopic characterisation of complex samples (e.g. Kozdon et al., 2010). Importantly, where minerals (e.g. pyrite) are multi-generational, a combination of bulk rock and SIMS data provides a powerful tool with which to assess the relative contribution (mass balance) of different sources of sulphur. Here, we (1) provide a comprehensive petrographic framework within which to interpret isotopic data, (2) present $\delta^{34}S$ and $\delta^{18}O$ values in barite and $\delta^{34}S$ values in pyrite, to constrain the environment of mineral formation within the system at Macmillan Pass, and (3) rigorously evaluate the evidence for euxinia, and propose alternative processes for the cycling of sulphur in these systems.

3.2. Regional Geology – The Selwyn Basin

The Selwyn Basin, Canada, contains clastic rocks deposited in a passive margin setting along the western margin of North America between the late Neoproterozoic and late Devonian (Gordey and Anderson, 1993). The Paleozoic stratigraphy is dominated by organic-rich mudstones interpreted to represent deep-marine, pelagic sedimentation during periods of limited clastic input (Goodfellow, 2007). These mudstones are host to three major periods of CD-type mineralisation (see Figure 3.1) during the Cambrian (Anvil District; Pigage, 1986), Silurian (Howard's Pass District; Morganti, 1979) and Late Devonian (Macmillan Pass District; Gardner and Hutcheon, 1985; Ansdell et al., 1989). During the late Devonian-early Mississippian, Selwyn Basin strata were deformed during collision with an island arc, and incorporated into the Cordilleran fold and thrust belt (Nelson et al., 2002).

The most well preserved examples of Selwyn Basin CD-type mineralisation are located at Macmillan Pass. In contrast to older mineralised districts (e.g. Anvil, Howard's Pass), the metamorphic grade of Macmillan Pass strata is sub-greenschist facies and the majority of deformation is localized around fault zones. Thus, many of the primary sedimentary and hydrothermal features are preserved. The mudstones are rich in organic carbon, radiolarians and silica, and are locally pyritic and sometimes subtly bedded (Chapter 2). In terms of hydrothermal features, the Tom and Jason deposits are unique in that the complete deposit architecture is preserved, with a well-defined feeder zone (hydrothermal vent) and overlying sulphides. The assumption of the conventional SEDEX model is that mineralisation was syn-sedimentary, and therefore the deposits are considered to be of equivalent age as the host rock.

The age constraints on the sulphur isotope curve (Figure 3.1) of Goodfellow and Jonasson, (1984) and Goodfellow (1987), are provided by conodont biostratigraphy (Dawson and Orchard, 1982) and stratigraphic correlations (Gordey et al. 1982). For Macmillan Pass, this places the Tom and Jason deposits within Middle Devonian Eifelian-Givetian strata. Irwin and Orchard (1991) have since compiled additional conodont biostratigraphy for Macmillan Pass strata, and more accurately constrained the age of mudstones hosting the Tom and Jason deposits to between the Lower *hassi* through Lower *rhenana* conodont zones, corresponding to a Frasnian age. Stratiform barite mineralisation can be split into two major intervals according to conodont zones, of which the Cathy prospect (Eifelian to early Frasnian) is older than Tom and Jason strata, but younger deposits (Gary, Pete, Jeff) are overlapping in age (Irwin and Orchard, 1991). The δ^{34}S composition of global seawater during the late Devonian has been studied in some detail, and the range preserved in carbonate-associated sulphate (CAS) during the Frasnian is between 20‰ and 25‰ (John et al., 2010; Chen et al., 2013). During the early part of the Frasnian, the CAS record is relatively stable; however, analyses across the Frasnian-Fammenian reveal large shifts (from +30‰ down to +10‰) in the δ^{34}S values of seawater sulphate (Chen et al., 2013).

3.3. Samples and analytical methods

Samples were collected from drill-core located at the Tom and Jason deposits (Macmillan Pass, Yukon Territory; see Figures 1.1; 2.1). A total of 10 drill-holes were logged and sampled, and over 400 mineralised samples were collected. Care was taken to sample the least deformed examples of mineralisation, which preserve primary mineralogical relationships, and in particular, examples of stratiform barite, pyrite and

ore-forming sulphides (Figure 3.2). Paragenetic relationships were assessed in detail under binocular microscope, and key samples were prepared as thin sections. Transmitted and reflected light petrography, and backscattered electron (BSE) imagery were used to assess key mineralogical relationships. Un-mineralised (barren) mudstone samples were obtained from two drill-holes (76-17, n = 18; TYK-5, n = 19). TYK-5 is a drill-hole that intersects 40 metres of mineralised strata at the Tom deposit, and 76-17 is a barren drill-hole located between the Tom and Jason deposits, and has been correlated with strata at Tom (for more detail, see Chapter 2). These samples display no visible indication of hydrothermal alteration, and although pyritic, they contain no other major sulphide phases. The barren mudstones are dark in colour and siliceous, and from the same sedimentary sequence described in the study of Goodfellow and Jonasson (1984).

3.3.1. Secondary ion mass spectrometry (SIMS)

Sample preparation, pre-analysis imaging and isotopic analysis were performed at the Canadian Centre for Isotopic Microanalysis (CCIM), University of Alberta. Sample discs were isolated from polished thin sections using diamond core bits ranging between 2 and 3 mm diameter. The discs (n = 40) were cast in epoxy, along with pre-polished pieces of in-house barite and pyrite reference materials (RM's) to form two standard 25 mm mounts (M1269 and M1270). The mounts were coated with 7nm Au and imaged using a scanning electron microscope (SEM; Zeiss EVO MA15), operating at 20 kV and 3 nA beam current. Once imaged, mounts were coated with additional Au to bring the total to 30nm.

Sulphur isotope ratios ($^{34}S/^{32}S$) and oxygen isotope ratios ($^{18}O/^{16}O$) were

determined using an IMS-1280 multi-collector ion microprobe. The isotopic composition of sulphur and oxygen are reported in terms of standard δ-notation, in reference to the composition of Vienna Canyon Diablo Troilite (VCDT) for sulphur (1), and Vienna Standard Mean Ocean Water (V-SMOW) for oxygen (2);

1. $\delta^{34}S = 1000\ x\ [\ (^{34}S/^{32}S)_{sample} - (^{34}S/^{32}S)_{VCDT}\ ]\ /\ (^{34}S/^{32}S)_{VCDT}$

2. $\delta^{18}O = 1000\ x\ [\ (^{18}O/^{16}O)_{sample} - (^{18}O/^{16}O)_{VSMOW}\ ]\ /\ (^{18}O/^{16}O)_{VSMOW}$

Key analytical conditions and parameters are summarized in Table 3.1. The primary beam used focused 20 keV ^{133}Cs+ ions to form a probe 10 − 15μm diameter. Negative secondary ions were extracted into the mass analyzer, and automated tuning of the secondary preceded each analysis. Isotopes of interest ($^{32}S^-$, $^{34}S^-$, $^{16}O^-$, $^{18}O^-$) were analyzed simultaneously in Faraday cups. The analytical protocol interspersed analyses of unknowns with the reference materials (RM's) in a 4:1 ratio. A total of 176 analyses of pyrite were performed, and 184 $\delta^{34}S$ and 121 $\delta^{18}O$ analyses of barite. Instrumental mass fractionation (IMF) was determined for the analytical sessions from utilizing all the replicate analyses of the RM's. Final uncertainties are typically ±0.15 − 0.25 ‰ at 95% confidence interval (2σ), and propagate within-spot counting errors, between-spot errors (geometric effects) and between-session errors. Errors do not include the absolute uncertainty in the composition of the RMs (Table 3.1) of ±0.2 − 0. 5 ‰. No orientation-related biases have been found for SIMS analysis of pyrite or barite at CCIM (e.g. Kozdon et al., 2010).

3.3.2. Bulk rock $\delta^{34}S_{pyrite}$ analysis

A chromous chloride extraction of pyrite sulphur was made using the technique of Canfield et al. (1986). The isotopic composition of the extracted sulphide, as Ag_2S, was analysed on an Isoprime mass spectrometer coupled to an Elementar Pyrocube elemental analyser. Samples were wrapped in tin cups and combusted with oxygen (N5.0) at 1150°C in a stream of helium. The resulting gases passed over tungstic oxide at the same temperature. Water was removed from the gas stream using phosphorus pentaoxide on an inert carrier (Sicapent) and excess oxygen was removed by passing the gas over copper wires held at 850°C. SO_2 was separated from other gases using a temperature controlled adsorption/desorption column. The $\delta^{34}S$ was derived using the integrated mass 64 and mass 66 signals from the sample relative to those in a pulse of independently introduced reference gas (N3.0). All solid reagents were sourced from Elemental Microanalysis, UK, and all gases from BOC, UK. Calibration to the international scale was performed using IAEA-S3 and an in house seawater sulphate standard isotopically indistinguishable from NBS-127. Assigned values for these standards were -32.06 ‰ and +20.3 ‰ respectively. Errors (1σ) are reported as 0.17‰ and 0.4‰ for samples from 76-17 and TYK-5 respectively.

3.4. Results

3.4.1. Mineralogical paragenesis

The mineralogical paragenesis is presented in Figure 3.3, which has been split in to three stages, two of which precede hydrothermal input (i.e. Zn-Pb-Fe sulphides). The

barren mudstone samples from 76-17 and TYK-5 only contain pyrite from stages 1 and 2, and no barite; mineralised samples contain all 3 paragenetic stages. Key features of the paragenesis will now be described in chronological order (see Figure 3.3).

Stage 1. One of the earliest features preserved in these samples are pyritised radiolarian tests, which can be locally enriched in barium (Figure 3.4A and B). Framboidal pyrite (py-1) is a distinctive early phase, with framboid diameters mostly greater than 7μm (often >20μm) (Figure 3.4C). An early generation of barite (brt-I) forms small (<25μm), interstitial, anhedral crystals that typically occur as patchy replacements of quartz within the mudstone (Figure 3.4D). The temporal relationship between py-I and brt-I is hard to distinguish.

Stage 2. Euhedral pyrite (py-II) post-dates py-I in all samples (e.g. Figure 3.4C and 3.5A) and is present in two main forms, as either stratiform accumulations (py-IIa; Figure 3.2 and Figure 3.5A) or as solitary, disseminated crystals (py-IIb; Figure 3.5A and B). Separating py-IIa and py-IIb temporally within stage 2 has not been possible. Brt-II forms more equant, euhedral crystals (>25μm; Figure 3.5B), which often occur as discontinuous stratiform enrichments in association with py-IIa (Figure 3.2). There can be a continuum of textures between brt-I and brt-II, and the patchy brt-I enrichments (stage 1) sometimes develop into the more monominerallic, stratiform brt-II. Py-IIb also commonly occurs intergrown with brt-II (Figure 3.5B). Barite-III (brt-III) is present as irregular veinlets that crosscut mudstone laminae and earlier barite generations, but which also appear as feeder veins linked to the formation of brt-I and brt-II (Figure 3.5C). Euhedral, monoclinic celsian crystals provide a useful marker phase in the paragenesis, often occurring on the top of mudstone laminations, along organic-rich horizons (e.g. Figure 3.5B), and as overgrowths of py-I (Figure

76

3.5D) and intergrown (but out of textural equilibrium) with brt-II (e.g. Figure 3.4D).

Stage 3. A simple mineral assemblage, comprising pyrite, sphalerite, galena and witherite, characterizes the hydrothermal input in the mineralised samples. Pyrite (py-III) forms large sub- to anhedral replacements and overgrowths of earlier barite (Figure 5E), and witherite forms an accessory phase to sphalerite (Figure 3.5E). Galena is the last phase in the paragenesis, and occurs as anhedral, interstitial crystals that overprint earlier barite and pyrite mineralisation along stratiform horizons (Figure 3.5F).

3.4.2. SIMS – sulphur and oxygen isotopes

The δ^{34}S values for both barite and pyrite are summarised in Figure 3.6 (see appendix B for full compilation). Pyrite-I has a distinctive isotopic signature, with δ^{34}S values that range between -30.0‰ and -20.8‰. The subsequent generations of pyrite (py-II + III) overlap in isotopic composition, despite being distinct texturally, with δ^{34}S values that range between +3.0‰ and +25.7‰. Compared to pyrite, barite has a narrower range of δ^{34}S values (between +23.5‰ and +34‰), with the three generations of barite overlapping in isotopic composition. However, there are large isotopic variations (3-4‰) recorded on a very small scale (<50μm), within barite of the same generation. The δ^{18}O values of barite are between +16.4‰ to +18.3‰, and are presented in a cross plot with δ^{34}S values in Figure 3.7.

For brt-II and py-II, there are some important isotopic relationships to highlight: the δ^{34}S composition of py-IIa (+17.4‰ to +25.7‰) approaches the δ^{34}S composition of brt-II (+23.7‰ to +30.6‰) when they are in close proximity (Figure 3.8), and for

py-IIb, which is intergrown with brt-II, the median difference in isotopic composition between $\delta^{34}S$-barite and $\delta^{34}S$-pyrite values is +16.0‰.

3.4.3. Bulk rock $\delta^{34}S$-pyrite values

The $\delta^{34}S$ values of sulphur extracted from barren mudstone samples (drill-holes 76-17 and TYK-5) can be assumed to originate from pyrite, owing to the absence of hydrothermal sulphides (i.e. sphalerite, galena). The bulk rock $\delta^{34}S$-pyrite values (Figure 3.6) have a broad distribution, from -15.6‰ to +8.7‰ (*n = 37*). The results from the two different drill-holes form two broad populations: in 76-17, $\delta^{34}S$ values are between -15.6‰ and -0.7‰, whereas in TYK-5, values are between -5.3‰ and +8.7‰. Although these samples were obtained from the same stratigraphic interval as those analyzed by Goodfellow and Jonasson, (1984), our data extend to much lower $\delta^{34}S$ values (-15.6 to +8.7‰; this study, *versus* +22.0‰ to +33.8‰; Goodfellow and Jonasson, 1984).

3.5 – Discussion

3.5.1. $\delta^{34}S$ and $\delta^{18}O$ values in barite – constraints on formational environment

It is possible to draw comparisons between values of $\delta^{34}S_{barite}$ (this study) and the Late Devonian record of $\delta^{34}S_{CAS}$ (e.g. John et al. 2010; Chen et al., 2012), to assess differences in the $\delta^{34}S$ composition of seawater sulphate. The underlying assumption being that the lowest $\delta^{34}S_{barite}$ values represent the closest approximation of seawater sulphate, and any trend toward more positive values indicates modification of the

sulphate reservoir (e.g. Cecile et al. 1983). As noted by Chen et al. (2012), low seawater sulphate concentrations (7mM relative to 28mM in modern oceans; Lowenstein et al. 2003) in the Late Devonian may have resulted in a global seawater sulphate budget more sensitive to inputs and outputs, producing high spatial and temporal variability in the isotopic record. However, the lowest $\delta^{34}S_{barite}$ values (+24‰, n = 6; Figure 3.6) do broadly overlap with current records of un-modified Frasnian seawater (+20‰ to +25‰; John et al., 2010; Chen et al., 2013), providing some indication that when barite precipitated, the sulphate reservoir in the Selwyn Basin was not restricted from the global ocean. The majority of the data fall around a median $\delta^{34}S_{barite}$ value (~ +27‰), and so barite likely precipitated from seawater that underwent minor modification via BSR, but importantly, not near-quantitative reduction as argued by Goodfellow and Jonasson (1984). The range of $\delta^{34}S_{barite}$ values could readily have been produced in open system conditions, where sulphate-resupply outcompeted sulphate consumption (BSR) in diagenetic pore fluids well connected with the overlying water column. The small scale isotopic variability preserved in Brt-I is consistent with the development of localized pore fluid microniches, in which the nature of Rayleigh fractionation varied according to transient changes in the rate of sulphate diffusion vs. consumption (Widerlund et al., 2012).

Notably, there is no convincing evidence that barite from later paragenetic stages (e.g. brt-III) has a more modified sulphur isotope composition (see Figure 3.6). The overlap in $\delta^{34}S$ values between different barite generations suggests that precipitation occurred from similar diagenetic fluids. In addition, the observation of barite veins is consistent with studies that have documented barite dissolution and barium mobilization in sulphate deficient pore fluids that develop during diagenesis (Torres et

al., 1996; Dickens, 2001). Re-precipitation of barite then occurs along diagenetic redox fronts, at the intersection of diffusional gradients between reducing, barium-bearing fluids and sulphate-rich pore fluids (Torres et al., 2003). This diagenetic model would contrast distinctly with the traditional model for barite precipitation in the Selwyn Basin, which involves hydrothermal venting of barium, and barite precipitation in the water column (Goodfellow, 2007). Notably, there is limited petrographic evidence to support water column barite precipitation; barite predates all hydrothermal input (as represented by py-III, sphalerite and galena), and following the criteria outlined by (Paytan et al., 2002), the barite described in this study is typical of barite precipitated beneath the SWI ($>5\mu m$ in diameter).

In Figure 3.7, the $\delta^{18}O$ values of barite are presented together with $\delta^{34}S$ values. The relatively narrow range in $\delta^{18}O$ values (+16.4‰ to +18.3‰) extends to more positive values than the results presented by Gardner and Hutcheon (1985) at the Jason deposit (median $\delta^{18}O$ value = +14.5‰, n = 17). Indeed, the results from Gardner and Hutcheon (1985) are closer to estimates of Frasnian seawater sulphate (grey box; Figure 7).

The processes governing variability in $\delta^{18}O_{sulphate}$ values for records of seawater sulphate are complex. Unlike sulphur, which is affected only by a kinetic fractionation during sulphate reduction, a combination of factors may contribute to $\delta^{18}O_{sulphate}$ values. Early work highlighted equilibrium oxygen isotope exchange, between sulphate-enzyme complexes and H_2O, as the main process controlling $\delta^{18}O_{sulphate}$ values during BSR (Fritz et al., 1989). However, the positive correlation between $\delta^{34}S$ and $\delta^{18}O$ values from pore fluid sulphate analysis has been used as evidence of kinetic isotope effects, which are dependent on sulphate reduction rates (Aharon et al., 2000). Yet

there does appear to be an upper limit to which $\delta^{18}O$ values increase (e.g. Turchyn et al., 2006), recently explained by equilibrium isotope-exchange between BSR reaction intermediaries (e.g. SO_3^-) and ambient water (Antler et al., 2013). In this study, $\delta^{18}O_{barite}$ values have a narrow distribution (+16.3‰ to +18.3‰), with a slight enrichment in $\delta^{18}O$ values relative to coeval seawater sulphate (+10‰ to +16‰; John et al. 2010). If the analyses of Gardner and Hutcheon (1985) are evaluated with the data from this study, there is a two-part trend, whereby an initial increase in $\delta^{18}O$ values (with little change in $\delta^{34}S$ values) is followed by a sharp increase in $\delta^{34}S$ values (across a narrow $\delta^{18}O$ range). This two-part trend is also consistent with a compilation of $\delta^{18}O—\delta^{34}S$ values in barite produced by Johnson et al. (2009). Whereas kinetic effects are responsible for $\delta^{34}S_{barite}$, it is likely that equilibrium exchange is controlling the narrow range observed in the $\delta^{18}O_{barite}$ composition.

3.5.2. Origin of barium

In the *Selwyn Basin model*, barium is leached from the basement and / or feldspathic clastic rocks within the sedimentary pile by hydrothermal fluids, similar to hydrothermal barite in modern day settings (Californian continental margin, Hein et al., 2007). In this model, Zn, Pb and Ba share a common source, and are co-transported by the hydrothermal fluid before exhalation into the water column. However, this model imposes important geochemical constraints on the hydrothermal fluid, as the mutual solubilities of barite and base metal sulphides are sensitive to changes in temperature, pH and fO$_2$ (Cooke et al., 2000).

Collectively, the petrographic and isotopic evidence presented here do not support

the *Selwyn Basin model*; barite precipitation predates hydrothermal input and isotopic evidence suggests precipitation occurred in an open system diagenetic setting. Therefore, the processes responsible for barium transport and barite precipitation were likely decoupled from the processes responsible for Zn and Pb sulphide formation. Hydrothermal activity cannot be discounted as the original source of barium, and is estimated to contribute to 1/3 of the modern day barium seawater budget (Hanor, 2000). However, there is no evidence that the Selwyn Basin was restricted from global oceanic circulation, thus the Selwyn Basin barium budget was likely derived from a global hydrothermal flux related to mid-ocean ridge systems. The important consideration, therefore, is how barium in seawater was concentrated into diagenetic fluids.

The host rock of the Tom and Jason deposits was deposited in a highly productive depositional setting (Chapter 2). Previous studies have proposed a correlation between barium enrichment in mudstones and paleo-productivity (Schmitz, 1987; Dymond and Collier, 1996; Paytan and Griffith, 2007), and there is evidence of an association between discrete barite particles (<1µm) and planktonic organisms in modern day oceanographic settings (Dehairs et al., 1980; Bishop, 1988). In turn, this has been replicated in laboratory experiments, in which barite precipitation has been biologically mediated (Gonzalez-Muñoz et al., 2012). These features are rarely observed in the geological record (see Stamatakis and Hein, 1993), due to the diagenetic remobilization of barium after pore water sulphate depletion. However, we have documented barium particules in the skeletal framework of radiolarians preserved by hydrothermal sulphides at MacMillan Pass (Figure 3.4A and B). We suggest, therefore, that this observation supports a biologically mediated flux of barium to the sediments, which was then concentrated below the SWI in reducing pore

fluids before barite precipitation occurred along diagenetic redox fronts. In the following section, the formation of sulphides in this environment will be discussed.

3.5.3. $\delta^{34}S$ values in pyrite

At least four major generations of pyrite have been identified at Macmillan Pass, with distinctive end-member $\delta^{34}S$ values preserved in py-I and py-II (see Figure 3.5). It seems likely, therefore, that previous analyses (Goodfellow and Jonasson, 1984; Goodfellow, 1987) contained reduced sulphur from different sources, perhaps representing different processes. Indeed, the distribution of sulphur isotope values bears resemblance to Irish-type systems, where ore-forming sulphides preserve end member $\delta^{34}S$ compositions that are distinctly negative (bacteriogenic) and positive (hydrothermal sulphur) (see Anderson et al., 1998; Barrie et al., 2009). The sources and cycling of sulphur within the system should therefore be apparent from the coupling of textural and mineralogical relationships with isotopic data. This will be explored in the following section.

Py-I (framboidal pyrite): This generation of pyrite is disseminated throughout both the un-mineralised and mineralised mudstones at Macmillan Pass. Framboidal textures are thought to form in aqueous solutions, in which the precursors to pyrite formation, iron monosulphides, are supersaturated, i.e. sulphide production < iron supply (Raiswell, 1982; Passier et al., 1997). These conditions could have developed with slow rates of BSR, which is consistent with the large fractionation observed between Late Devonian seawater sulphate and the isotopic composition recorded in py-I (Goldhaber and Kaplan, 1975). As with $\delta^{34}S_{barite}$, the range of $\delta^{34}S_{py-I}$ values we report are mutually consistent with precipitation from the same diagenetic fluids

modified by BSR, and an isotopic fractionation ($\varepsilon^{34}S$) of 49‰. This isotopic relationship is representative of environmental settings in which sulphate resupply outcompetes sulphate consumption (open system conditions). Py-I could have formed in a ventilated, euxinic water column, however this is a non-unique explanation, and the size of the majority of framboids (>7μm in diameter) supports a diagenetic origin in which sulphate was bacterially reduced (Wilkin et al. 1996).

Py-II (euhedral pyrite): The euhedral crystal habit of py-II contrasts with py-I framboids, and likely represents a decrease in the level of pore fluid supersaturation with respect to Fe monosulphide precursors (Raiswell, 1982; Passier et al., 1997). This type of pyrite is commonplace in diagenetic environments that are limited in terms of pore water sulphate and Fe (Raiswell, 1982). Texturally, py-II forms the clearest paragenetic relationship with barite (brt-II), either as stratiform accumulations (py-IIa Figure 3.2) or intergrown with brt-II (py-IIb; Figure 3.5B). This mineral assemblage clearly pre-dates hydrothermal input, and importantly, py-IIa records the highest $\delta^{34}S$ values. As the $\delta^{34}S$ values of py-IIa approaches the values reported by Goodfellow and Jonasson (1984), this pyrite could represent the dominant component of some of their analyses. Operating under the assumption of SEDEX processes, Goodfellow and Jonasson (1984) may have targeted stratiform pyrite, although this is not clear from their limited sample descriptions.

3.5.4. $\delta^{34}S$ relationship between py-II and brt-II

The $\delta^{34}S$ composition of py-I records a bacteriogenic source of reduced sulphur. However the isotopic relationship between py-II and brt-II (see Figure 3.8), whereby $\delta^{34}S_{pyrite}$ values approach relatively un-modified seawater sulphate $\delta^{34}S_{barite}$ values is

difficult to reconcile within the parameters of the Selwyn Basin *model* (BSR and water column euxinia). Alternative pathways of sulphate reduction, capable of producing positive $\delta^{34}S$ values in sulphide proximal to a relatively un-modified source of seawater sulphate, must therefore be considered.

It is possible to produce enriched $\delta^{34}S_{sulphide}$ values during thermochemical sulphate reduction (TSR; Machel et al., 1995). Above 110°C and in the presence of a reductant (e.g. organic matter), sulphate is reduced with an associated kinetic fractionation that scales with temperature (Kiyosu and Krouse, 1990). Therefore it is necessary to consider whether py-II formed during an early (pre Zn-Pb) hydrothermal event, in which sulphate was utilized from either pore fluids or barite dissolution. Using the experimentally derived equation of Kiyosu and Krouse (1990), the isotopic relationship between brt-II and py-IIa ($\varepsilon^{34}S = <10‰$) would require temperatures in excess of 250°C. Alternatively, it may be that the entire budget of sulphate was utilized during TSR, in which case $\delta^{34}S_{sulphide}$ could approach $\delta^{34}S_{sulphate}$ values. However, carbonate is an important by-product of TSR (see Machel et al. 1995; Machel, 2001), and is absent within the py-II and brt-II assemblage in Stage 2 (see Table 2). It is also unlikely that the temperatures required for TSR could be sustained close to the SWI, as hydrothermal fluids entering a diagenetic environment would rapidly cool upon interaction with seawater saturated sediment.

High $\delta^{34}S$ values can also be produced during diagenesis, and a low temperature, non-hydrothermal origin for this isotopic relationship is consistent with the presence of py-II in the barren mudstone samples (Figure 3.3A and B). As pore fluid sulphate is exhausted with depth during organic matter consumption via BSR, any remaining labile organic matter will continue to degrade via methanogenesis (Froelich et al.,

1979; Jørgensen and Kasten, 2006);

$$3. \quad 2\,CH_2O \Rightarrow CO_2 + CH_4$$

Reaction (3) may proceed via either biogenic (e.g. Joye et al., 2004) or thermogenic (e.g. Cruse and Seewald, 2006) processes, and both represent important pathways in the sedimentary carbon cycle (Jørgensen and Kasten, 2006). The methane, and other short-chain alkanes produced during reaction (3) accumulate within diagenetic pore fluids. Through advection and diffusion, this methane encounters sulphate-bearing pore fluids at shallower sediment depths. Where methanic and sulphate-bearing fluids interact, anaerobic oxidation of methane (AOM) proceeds according to reaction (4) (Barnes and Goldberg, 1976; Reeburgh, 1976);

$$4. \quad CH_4 + SO_4{}^{2-} \Rightarrow HCO_3{}^- + HS^- + H_2O$$
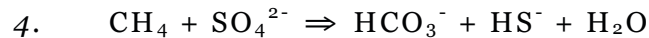
This reaction produces a sharp redox boundary, called the sulphate-methane transition zone (SMTZ; Iversen and Jørgensen, 1985), and represents an important mechanism for suppression of methane emissions into the ocean and atmosphere (Reeburgh, 2007). The location of the SMTZ within the sediment is dependent upon competing fluxes of downward diffusing sulphate (from seawater) and upward diffusing methane (methanogenesis), which in modern day environments may occur between 1.5 meters (Iversen and Jørgensen, 1985; Niewöhner et al., 1998) and deeper than 8 meters below the SWI (e.g. Borowski et al. 2013). Notably, the methane-rich, sulphate-poor fluids below the SMTZ are highly effective at mobilising barium (Torres et al., 1996). These fluids, which form a source reservoir for methane or cold seeps, are capable of producing diagenetic barite enrichments when they interact with sulphate bearing pore fluids above the SMTZ (Torres et al., 2003; Arndt et al., 2009; Henkel et al., 2012).

AOM is effective in reducing the downward diffusing sulphate flux in near quantitative proportions (Niewöhner et al., 1998), and is thus capable of producing high $\delta^{34}S$ values in sulphides (Jørgensen et al., 2004; Borowski et al., 2013). The respective stratiform accumulations and isotopic composition of py-IIa and brt-II (Figure 7) could reflect the preservation of a relict SMTZ. The reduced sulphur produced during reaction (4), in the presence of reactive iron, is capable of promoting the formation of authigenic pyrite (Jørgensen et al., 2004). Certainly, stratiform pyrite (and mineralogical precursors) has been recognized in diagenetic settings (e.g. Kasten et al. 1998), and in studies of modern day sapropels pyrite typically accumulates along centimeter thick horizons (Passier et al. 1997). It is reasonable, therefore, that post compaction these horizons may appear on a much finer scale (e.g. Figure 3.2 and 3.7).

The $\delta^{34}S$ values of py-IIb may also provide further support for the presence of a relict SMTZ. Py-IIb typically occurs as idiomorphic crystals intergrown with brt-II, located above stratiform enrichments of py-IIa. If the py-IIa—brt-II assemblage represents the presence of a relict SMTZ, the base of the overlying sulphate reduction zone should be characterized by diminishing sulphate concentrations (Jørgensen and Kasten, 2006). Considering the low solubility of barite (log K = -9.96 at 25°C; Bowers et al. 1984), the presence of celsian intergrown with brt-II suggests sulphate concentrations may have depleted between formation of Stage 1 and Stage 2. At sulphate concentrations less than 200μM, the isotopic fractionation associated with sulphate reduction is greatly reduced ($\varepsilon^{34}S$ = <10‰; Habicht and Canfield, 2002; Crowe et al., 2014; Zhelezinskaia et al., 2014). The precipitation of barite would lead to diminished pore fluid sulphate, which may be an important factor for the $\delta^{34}S$ values of py-IIb. Indeed, in some of our samples, there are examples of core to rim increases in

$\delta^{34}S_{py-IIb}$ values that may record gradual sulphate depletion during mineral growth (e.g. Kohn et al. 1998). If the isotopic relationship between brt-II—py-IIb is to have been controlled by sulphate concentrations $<200\mu M$, it is necessary to evaluate the solubility of barite in such conditions.

3.5.5. Barite and pyrite solubility

The low solubility of barite (log K = -9.96 at 25°C; Bowers et al. 1984) means that it remains stable into the stability field of pyrite; at low temperature (<100°C) this corresponds with an fO_2 in the range of 10^{-70} to 10^{-75}, and is supported by the textural equilibrium between barite and pyrite in Stage 2 (Figure 3.5B). The sulphate limitation responsible for producing the $\delta^{34}S$ values of py-II was likely caused by a combination of AOM (py-IIa) and barite precipitation (py-IIb). The evidence for open system BSR preserved by $\delta^{34}S_{barite}$ suggests the SMTZ may have been operating closer to the SWI than in modern day systems (<1.5 metres), consistent with recent modeling of barium cycling and penetration depth of the SMTZ as a function of sulphate concentration (Arning et al., 2015). A schematic of this model, and how it produced stage 1 and stage 2 of the paragenesis is presented in Figure 3.9.

Considering the independent evidence for low seawater sulphate in Late Devonian oceans (7mM; Lowenstein et al., 2003) it is not unexpected to find evidence for diminished sulphate penetration below the SWI. It is also worth speculating about two important effects that low sulphate concentrations would have on the flux of productivity derived barium: (1) low sulphate concentrations would enable a larger seawater barium budget, and (2) a greater proportion of organic matter, and therefore, barium, would escape BSR and become susceptible to re-mineralisation via

methanogenesis. The latter (2) may be highly speculative, considering the multiple variables that are responsible for organic matter preservation (Arthur and Sageman, 1994). However, it is perhaps noteworthy that during the Cretaceous, which forms another low point in seawater sulphate during the Paleozoic (Lowenstein et al., 2003; Lowenstein et al., 2014), extensive organic matter accumulation is recorded in marine strata (Stein et al., 1986), along with evidence of barite accumulation (Torres et al., 1996; Arndt et al., 2009). The abundance of barite in Late Devonian strata (Jewell, 1994; Canet et al., 2014), therefore, may at least in part be explained by low seawater sulphate, and the effect that this had on barium cycling during early diagenesis.

3.5.6. Mixed diagenetic signatures – bulk rock pyrite $\delta^{34}S$ values

The *Selwyn Basin model* was supported by $\delta^{34}S$ values in pyrite from un-mineralised mudstone samples, in which BSR was considered to produce the vast majority of reduced sulphur. However, having documented multiple generations of diagenetic pyrite in the mineralisation at Macmillan Pass, with contrasting sources of reduced sulphur (BSR and AOM-SR), it is necessary to reconsider the interpretation of these previous analyses. All generations of diagenetic pyrite (py-I, py-IIa and py-IIb) have been identified in un-mineralised mudstones (Figure 3.3) from drill-holes 76-17 and TYK-5. Although TYK-5 does intersect ~40 meters of massive sulphide, the mudstones from either drill-hole have no evidence of hydrothermal input in the form of Zn-Pb sulphides (sphalerite and galena), and there is only subtle evidence of hydrothermal alteration (Chapter 2). Thus, it is possible to make a simple calculation of the relative contribution of each diagenetic pyrite generation to the bulk rock signature.

A binary mixing model was used to assess the relative contributions of py-I and

py-II to the reduced sulphur budget of the host mudstones. In 76-17, to account for bulk rock isotopic composition (between 25th and 75th percentiles), py-II contributes 45-65% of the reduced sulphur budget; for TYK-5, this value is greater, between 65 and 85% (see Table 3.2). One possible explanation for the extreme values reported by Goodfellow and Jonasson (1984) is their samples contained abundant py-IIa. More importantly, it is clear that compared to 76-17, py-II contributes a larger proportion of reduced sulphur to samples from TYK-5. Thus, the hydrothermal system likely impacted, albeit subtly, upon diagenetic processes.

3.5.7. Implications for mineralisation at Macmillan Pass

Our data do not support a model of quantitative sulphate reduction in a euxinic water column. In contrast, the textural and isotopic evidence we present support a model in which mineralisation occurred beneath the SWI. Thus, the absence of the metal trap in the water column presents an interesting question – what alternative sources of reduced sulphur were available for the hydrothermal system? Hydrothermal pyrite py-III spans a wide range of $\delta^{34}S$ values (+3.0‰ to +18.6‰), which overlap with py-IIb, but also extend to lower and higher values, forming a distribution that probably represents mixing of reduced sulphur from multiple sources.

Considering the textural evidence for barite dissolution (Figure 3.5E and F), one potential sulphur source would be the utilization of barite-sulphur by the hydrothermal fluid. This would represent an interesting mechanism by which to promote massive sulphide mineralisation in a diagenetic system that shows evidence of sulphur limitation (*section 3.5.4*). Figure 3.5E provides an example of a mineral assemblage that is commonplace in the mineralisation at Tom and Jason, involving witherite-

pyrite-sphalerite associated with barite dissolution. Barite displays retrograde solubility at temperatures greater than 100°C, thus, conditions for barite dissolution would have been most favourable as the hydrothermal fluid cooled below 100°C upon entering a shallow, diagenetic environment. However, in order to produce reduced sulphur from barite-derived sulphate there must also have been a reductant present.

In modern day hydrothermal systems in organic-rich sediments, thermogenic degradation of organic matter proceeds, according to reaction (3), to produce short-chain alkanes (methane, ethane, propane and butane; Adams et al., 2013). Hydrothermal fluids contain increased concentrations of these hydrocarbon gases, and SR coupled with AOM is enhanced <90°C (Wankel et al., 2012). Although TSR may have been operating at the higher temperatures (~250°C; Gardner and Hutcheon, 1985; Ansdell et al., 1989) in the hydrothermal vents at Tom and Jason, to dissolve barite and reduce sulphate will have required lower temperatures (<100°C), which is more consistent with AOM-SR. The overlap in isotopic composition of py-III with py-II supports a model involving a common source of reduced sulphur.

The discrepancy in bulk rock $\delta^{34}S$ composition between TYK-5 and 76-17 may represent intensified diagenetic fluid flow in sediments proximal to the hydrothermal system. A thermal anomaly produced by hydrothermal activity, would have led to increased convection of diagenetic fluids; combined with thermogenic degradation of organic matter, an intensification of methane oxidation (e.g. Cruse and Seewald, 2006) accounts for the increased contribution of py-II to the bulk sulphur budget in TYK-5. Indeed, it has been demonstrated that rates of sulphate reduction coupled with AOM (AOM-SR) increase with temperature, leading to enhanced cycling of short-chain alkanes in organic-rich sediments impacted by hydrothermal activity (Adams et al.,

2013). It is entirely plausible that the extensive accumulation of barite closer to the hydrothermal system represents a combination of these two factors.

In overarching terms, we have presented evidence that highlights the range of processes that may be operating in these systems. It is unlikely that one single factor (e.g. euxinia) formed the metal trap for CD-type deposits in basins such as the Selwyn Basin, but rather it is a combination of factors that contributed to their formation. Certainly, we argue that it is more reasonable to concentrate sulphur in a host rock via multiple diagenetic pathways (barite precipitation, BSR, AOM-SR), than it is to achieve this exclusively in the water column.

3.6. Conclusions

A common feature of Sediment Hosted Massive Sulphide (SHMS) deposits is the preservation of stratiform sulphides with positive $\delta^{34}S$ values. In the conventional model for Selwyn Basin SEDEX deposits (*Selwyn Basin model*), stratiform mineralisation forms following water column precipitation of barite, pyrite and Zn-Pb sulphides (sphalerite, galena). The source of reduced sulphur, and the isotopic characteristics of barite and sulphides, is controlled by the near quantitative reduction of seawater sulphate and the development of euxinic conditions. In this study, we have identified multiple generations of barite (brt-I, II, III) and pyrite (py-I, IIa, IIb ± III) in both stratiform mineralisation (Tom, Jason deposits) and un-mineralised mudstones from Late Devonian Selwyn Basin strata (Macmillan Pass, YT). It is therefore clear that the use of isotopic data obtained via micro-analytical techniques (*secondary ion mass spectrometry*; SIMS) is required, in tandem with bulk techniques, to fully assess the

cycling of sulphur in these systems.

In contrast to the *Selwyn Basin model*, the petrographic and isotopic data (δ^{34}S; barite, pyrite) produced from stratiform features in mineralised samples from Macmillan Pass support a diagenetic origin (i.e. formation beneath the sediment water interface; SWI). The δ^{34}S values of three generations of barite overlap (+23.5‰ to +34.0‰) and there is no evidence to suggest the sulphate source (i.e. seawater) underwent near quantitative sulphate reduction. Furthermore, barite pre-dates all evidence of hydrothermal input (Zn-Pb-Fe sulphides). Together, this rules out a hydrothermal origin for barite, and precipitation from a restricted, euxinic water column. This conclusion raises an interesting problem, concerning what forms the metal 'trap' for base metals in such mineralised systems.

We find that in the textural and isotopic relationship between barite (brt-II) and pyrite (py-IIa), there is evidence of sulphate reduction coupled with anoxic oxidation of methane (AOM-SR). This process is highly effective at reducing pore water sulphate (to H$_2$S), locally, in nearly quantitative proportions, thereby producing positive δ^{34}S$_{pyrite}$ values. Bulk rock δ^{34}S$_{pyrite}$ data, obtained from un-mineralised mudstone samples from two drill holes (TYK-5 and 76-17), suggest this process may have been intensified by hydrothermal convection of diagenetic fluids. Together, we argue that pre-existing barite enrichments and AOM-SR would have proven highly effective in concentrating sulphur beneath the SWI at Macmillan Pass. This is particularly important if consideration is given to the concentration of seawater sulphate during the Late Devonian. Indeed, secular changes in seawater sulphate and its role in methanogenesis may represent important variables in the distribution of CD-type and barite deposits in

the geologic record.

Tables and Figures

Table 1. Variables in the operating conditions for SIMS analysis of $\delta^{34}S_{pyrite}$, $\delta^{34}S_{barite}$ and $\delta^{18}O_{barite}$ values.

	$\delta^{34}S$-pyrite	$\delta^{34}S$-barite	$\delta^{18}O$-barite
Cs probe diameter (μm)	10	15	12
Beam Current (nA)	0.85	2.5	2.5
Electron gun used	no	yes	yes
Implantation raster (μm)	18 x 18	20 x 20	20 x 20
Entrance & field apertures (μm, mm)	122, 5x5	122, 5x5	122, 5x5
Field magnification	100x	100x	100x
Energy slit	Full open	Full open	Full open
Detectors	L'2 (FC, $10^{10}\Omega$), FC2 (FC, $10^{11}\Omega$)	L'2 (FC, $10^{10}\Omega$), FC2 (FC, $10^{11}\Omega$)	L'2 (FC, $10^{10}\Omega$), H'2 (FC, $10^{11}\Omega$)
Mass Resolution	2000, 2100	2000, 2100	1950, 2275
Secondary ions detected and mean counts/s	$^{32}S^- = 1*10^9$ $^{34}S^- = 4.5*10^7$	$^{32}S^- = 7*10^8$ $^{34}S^- = 3*10^7$	$^{16}O^- = 3.5*10^9$ $^{18}O^- = 7*10^6$
RM identity	S0322A pyrite	S0327 barite	S0327 barite
RM composition	$\delta^{34}S_{VCDT} = -0.2 \pm 0.2‰$	$\delta^{34}S_{VCDT} = +22.3 \pm 0.5‰$	$\delta^{18}S_{VSMOW} = +11.0 \pm 0.5‰$
Peak counting time	75 s	75 s	75 s
Standard deviation of RM analyses	0.04‰	0.05‰	0.07‰ − 0.11‰
Typical ±2σ of unknowns	± 0.17‰	± 0.18‰	± 0.24‰

Table 3.2. Summary of features for non-hydrothermal pyrite at Macmillan Pass, and their calculated contribution to the bulk rock signature in 76-17 and TYK-5.

	Morphology	$\delta^{34}S$ (‰)	Reduced S Pathway	Setting	% Contribution to 76-17	% Contribution to TYK-5
Py-I	Framboidal	-20.8 to -30.0	BSR	Below SWI	35-55	35-15
Py-IIa	Euhedral	+17.4 to +25.7	AOM-SR	Below SWI	45-65	65-85
Py-IIb	Euhedral	+6.9 to +15.7	AOM-SR / BSR	Below SWI		
G+J (1984)		+22 to +33.8	BSR	Water Column		

Figure 3.1. Lower Paleozoic Selwyn Basin stratigraphy with the secular sulphur isotope curve of Goodfellow and Jonasson (1984). The three CD-type mineral districts at Macmillan Pass (this study), Howards Pass and the Anvil District are denoted by stars in their respective stratigraphic positions. The stratigraphy is compiled from Gordey and Anderson (1993) and Turner et al. (2011). Sulphur isotope data for barite and pyrite are re-plotted from Goodfellow and Jonasson (1984).
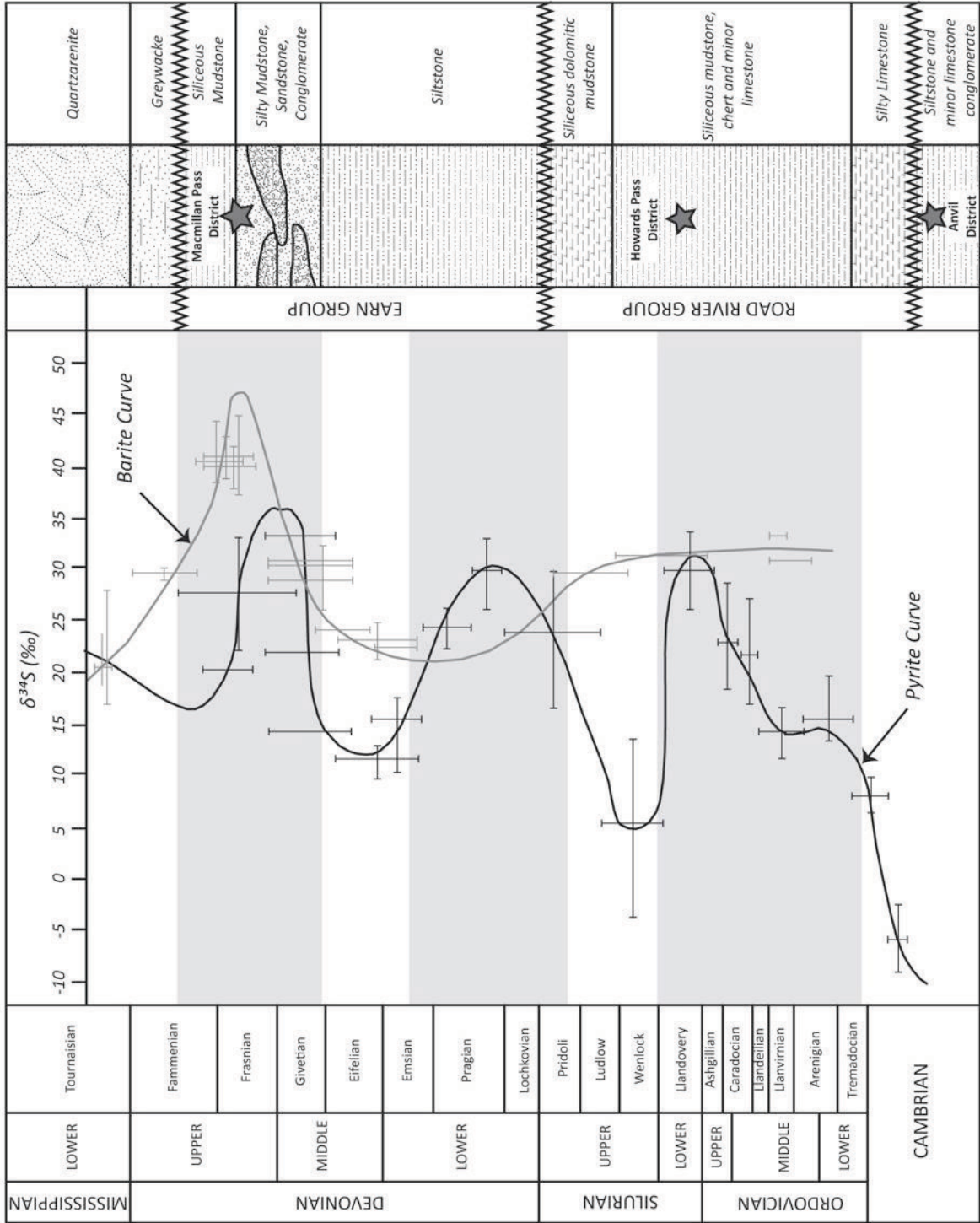
Figure 3.2. A - Hand sample of mineralisation from Jason (81-68A-69). Milky white layers are barite-rich, with varying degrees of sphalerite replacement (yellow) and interlaminated with pyrite. B – Hand sample of mineralisation from Jason (81-68A-127). Stratiform euhedral pyrite and replacement galena within a barite-rich mudstone.
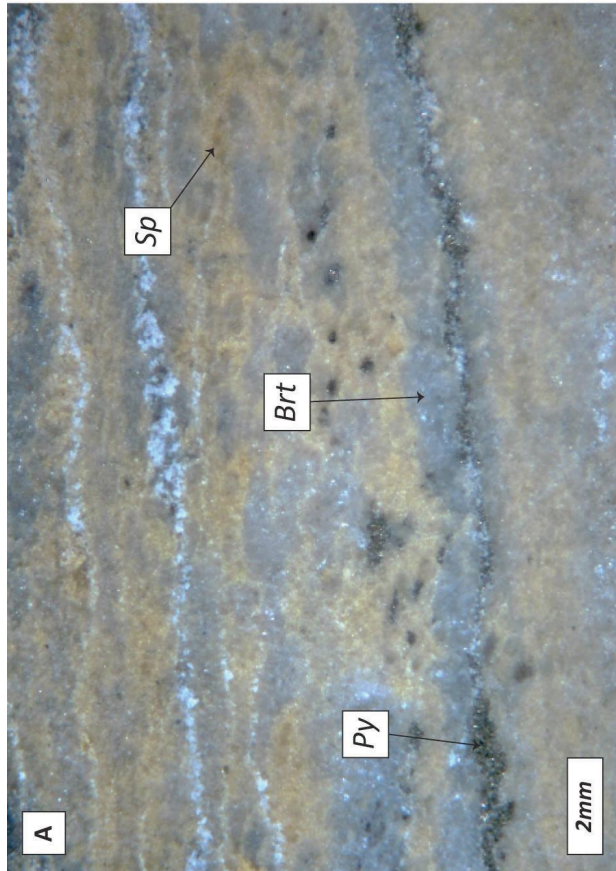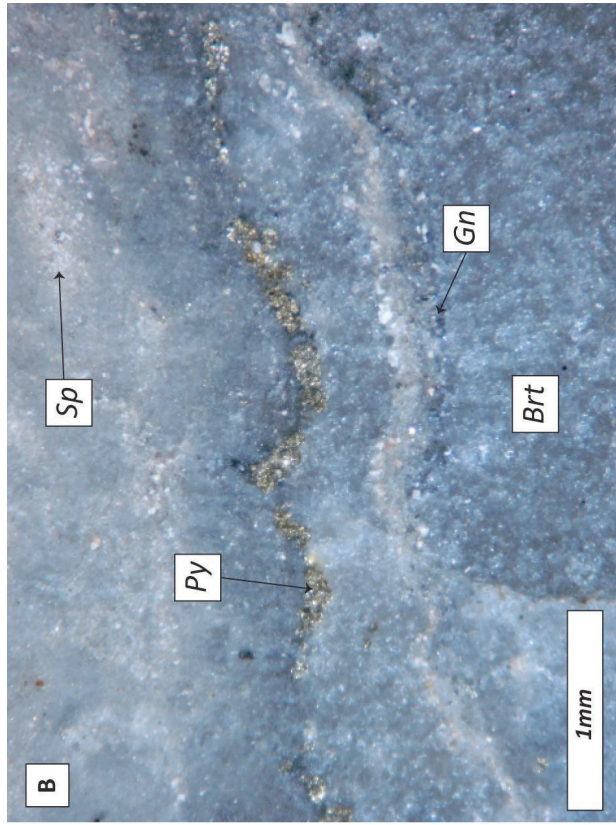
Figure 3.3. Mineralogical paragenesis for mineralised samples at Tom and Jason. Stages 1 and 2 predate the mineralisation (Stage 3).

				Stage 1
Barite-I	▬			- Microcrystalline (<25µm) barite (brt-I)
Pyrite-I	▬			- Framboidal (>7µm) pyrite (py-I)
				Stage 2
Barite-II		▬▪▪▪▪		- Stratiform barite (brt-II)
Celsian		▬▪▪▪▪		- Euhedral celsian intergrown with brt-II
Pyrite-IIa		▬▬		- Euhedral pyrite
Pyrite-IIb		▬▬		- stratiform accumulations (py-IIa)
				- idiomorphic within brt-II (py-IIb)
Barite-III		▪▪▪▪▬		- Vein barite (brt-III)
				Stage 3 (hydrothermal)
Pyrite-III			▬	- Sub- to anhedral pyrite (py-III)
Witherite			▬	- Assemblage of witherite (wth), sphalerite
Sphalerite			▬▪▪▪▪	(sp) and minor galena (gn) associated with
Galena			▪▪▪▬	barite dissolution

Figure 3.4. Petrography of barium and sulphide phases in bedded mineralisation at Tom and Jason. A – Electron probe X-ray image of sulphur. Green = sphalerite; red = pyrite; blue = galena. B - X-ray imaging of barium (white). Note the localized micron scale enrichments within the skeletal structure of the radiolarians. The larger, Ba-bearing, anhedral crystals at the bottom of the image do not contain sulphur, and are therefore likely barium carbonate. C - reflected light image of framboidal pyrite (py-I) overgrown by euhedral pyrite (py-IIb), in a siliceous mudstone with interstitial pyrobitumen. D - reflected light image of barite (brt-I) interstitial to microcrystalline quartz (qz). Barium feldspar (celsian; cn) occurs in the centre of the image, partially replaced by barite. Sphalerite (sp) occurs as interstital replacement of barite.
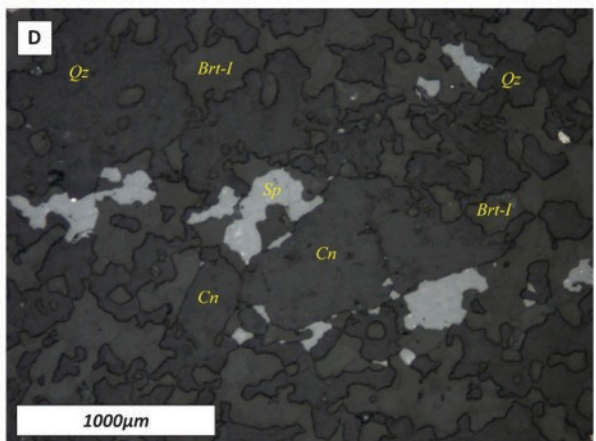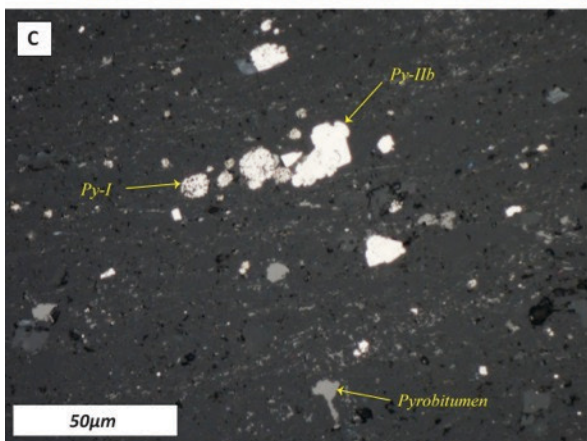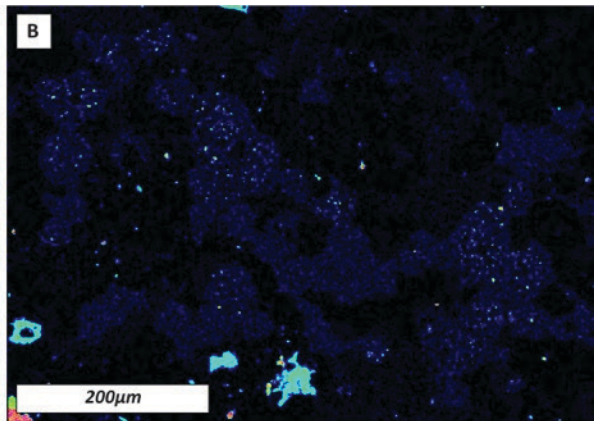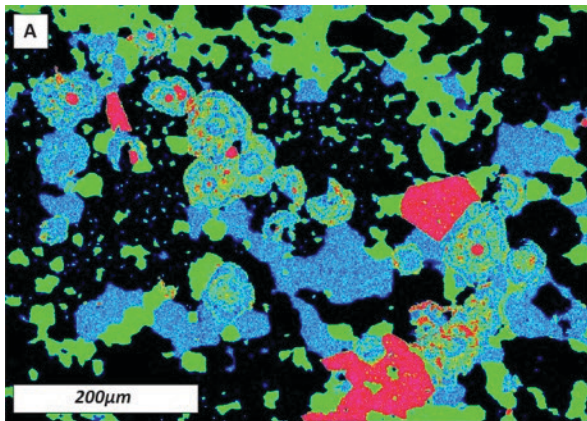
Figure 3.5. Petrography of stratiform barite and pyrite, overprinted by hydrothermal sulphides. A - Stratabound enrichment of py-IIa within a barren mudstone sample (reflected light image). B - Barium feldspar (celsian; cn) formed along a stratal horizon, with euhedral barite (brt-II) overlying and replacing it. Euhedral py-IIb crystals occur within brt-II and are both overprinted by subsequent sphalerite (sp) (reflected light image). C - Mudstone lamination with interstitial barite (brt-I), interlaminated with brt-II and cut by brt-III. Sphalerite replaces barite towards bottom of the image (reflected light image). D - Framboidal pyrite (py-I) and barite (brt-I) overprinted by later generation of pyrite (py-III); framboidal pyrite seems to provide a porous framework for the mineralising fluid to exploit, highlighted by the precipitation of galena (backscatter electron image). E – Py-III replacing barite in association with sphalerite (sp) and witherite (wth). F – Stratabound brt-II replaced by sphalerite (sp) and galena (gn).
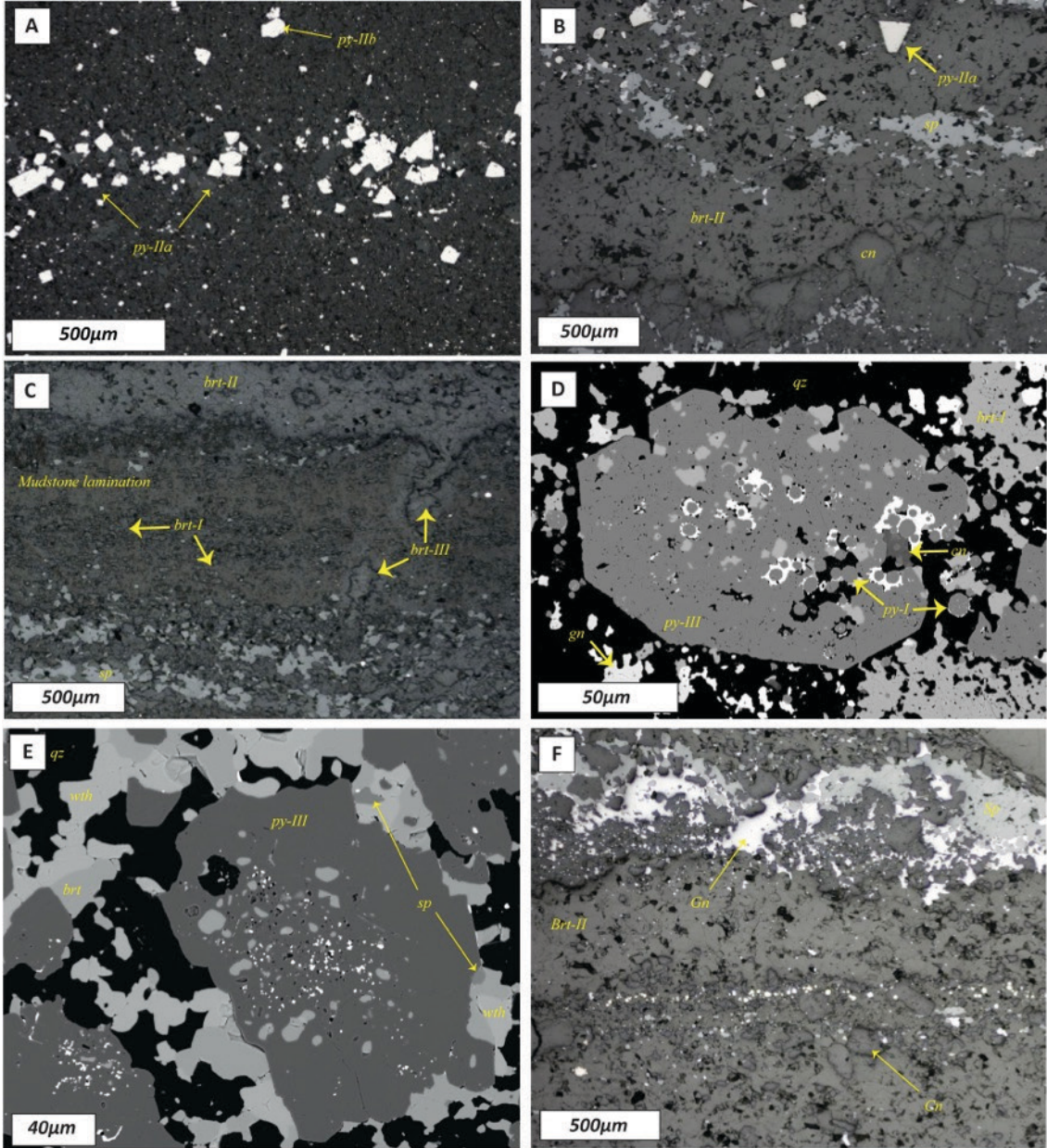
Figure 3.6. A box percentile plot (with distribution shape) for the compiled $\delta^{34}S$ values. Mineral phases are indicated below, along with percentile data. Black dots represent individual analyses, diamonds represent mean values, and solid horizontal lines represent median values.

	Brt-I	Brt-II	Brt-III	Py-I	Py-IIa	Py-IIb	Py-III	Bulk Pyrite (76-17)	Bulk Pyrite (TYK-5)
Mean	27.2	26.8	27.8	-24.7	21.0	11.1	10.4	-5.5	2.8
Median	27.4	26.7	28.3	-24.7	20.6	11.0	10.6	-4.1	3.1
25th	25.5	25.9	27.5	-26.8	19.5	10.1	9.0	-7.7	-0.6
75th	29.1	27.1	28.6	-22.4	22.2	11.7	12.8	-1.9	6.7
n	62	86	36	9	35	51	80	18	19
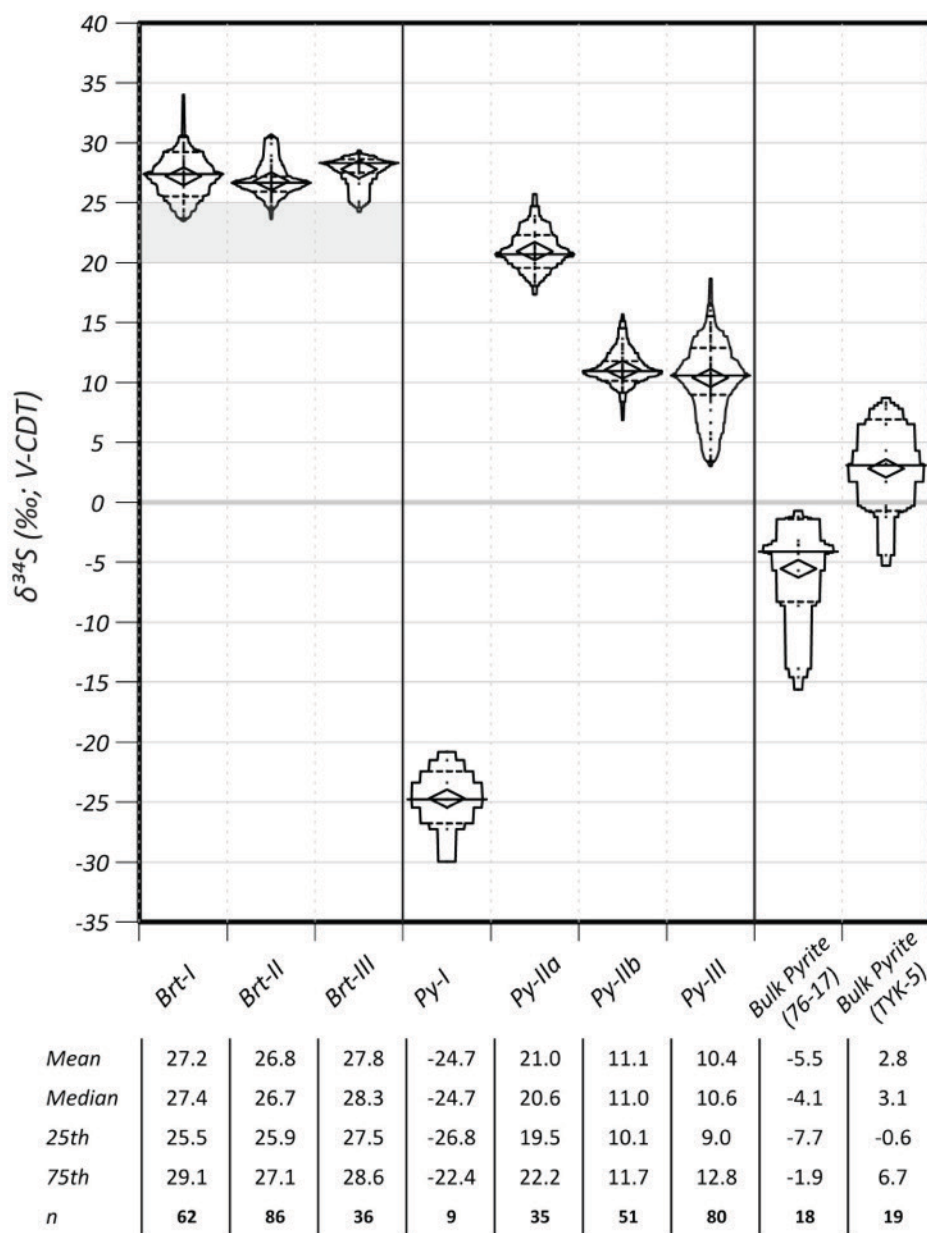
Figure 3.7. Plot of $\delta^{34}S$ vs $\delta^{18}O$ values for barite in Late Devonian strata at Macmillan Pass, including data from Gardner and Hutcheon (1985). Grey box shows the range in $\delta^{34}S$ and $\delta^{18}O$ compositions of Late Devonian seawater (John et al. 2010; Chen et al. 2013). Arrow depicts the evolution of $\delta^{34}S$ vs $\delta^{18}O$ values from a seawater origin.
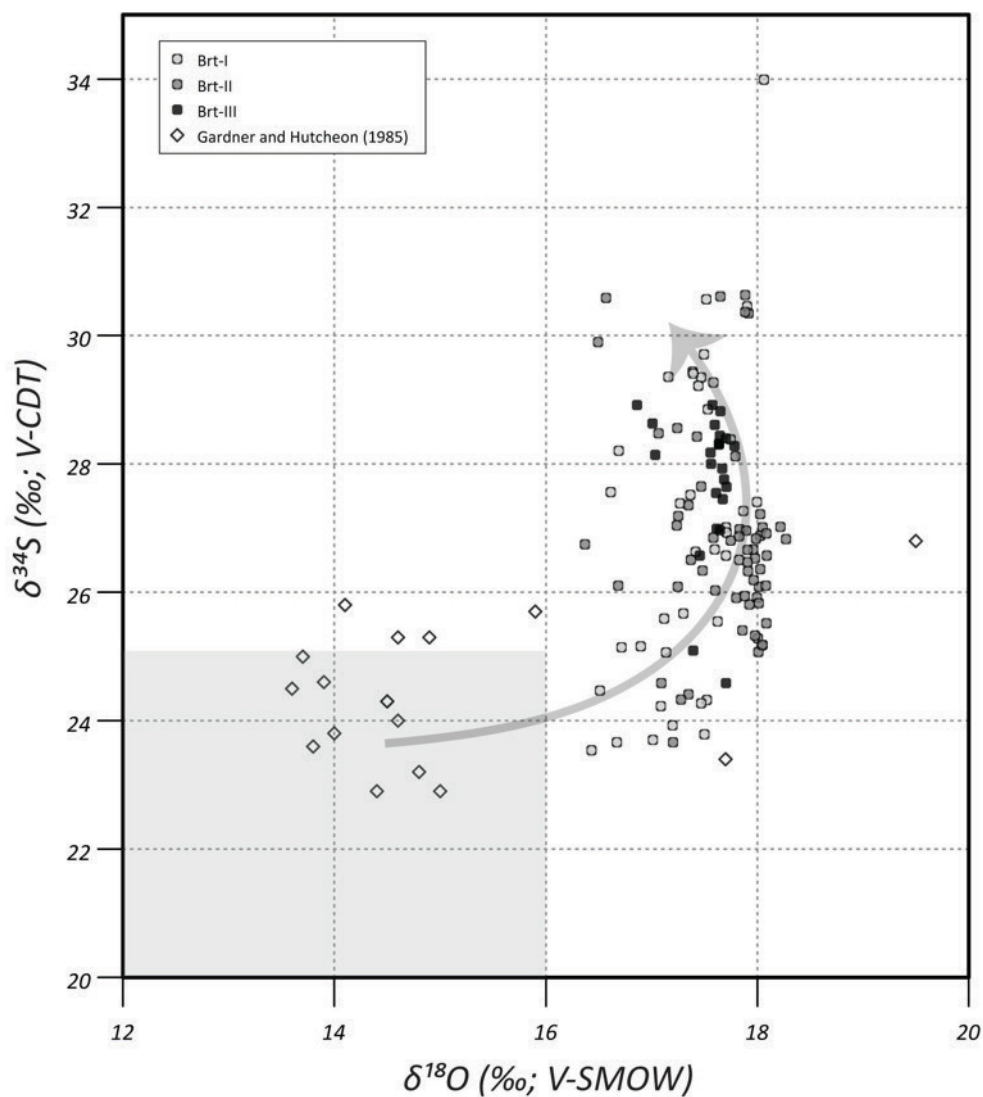
Figure 3.8. Example of stratiform pyrite and barite from bedded mineralisation at Jason. A - Stratiform pyrite (py-IIa) and barite (brt-II). Fine-grained, interstitial orange mineral is sphalerite. B - Backscatter electron images of area highlighted in red box (A). Isotopic analyses (SIMS) are marked by green (barite) and red (pyrite) circles, with results (δ^{34}S values) in white boxes.
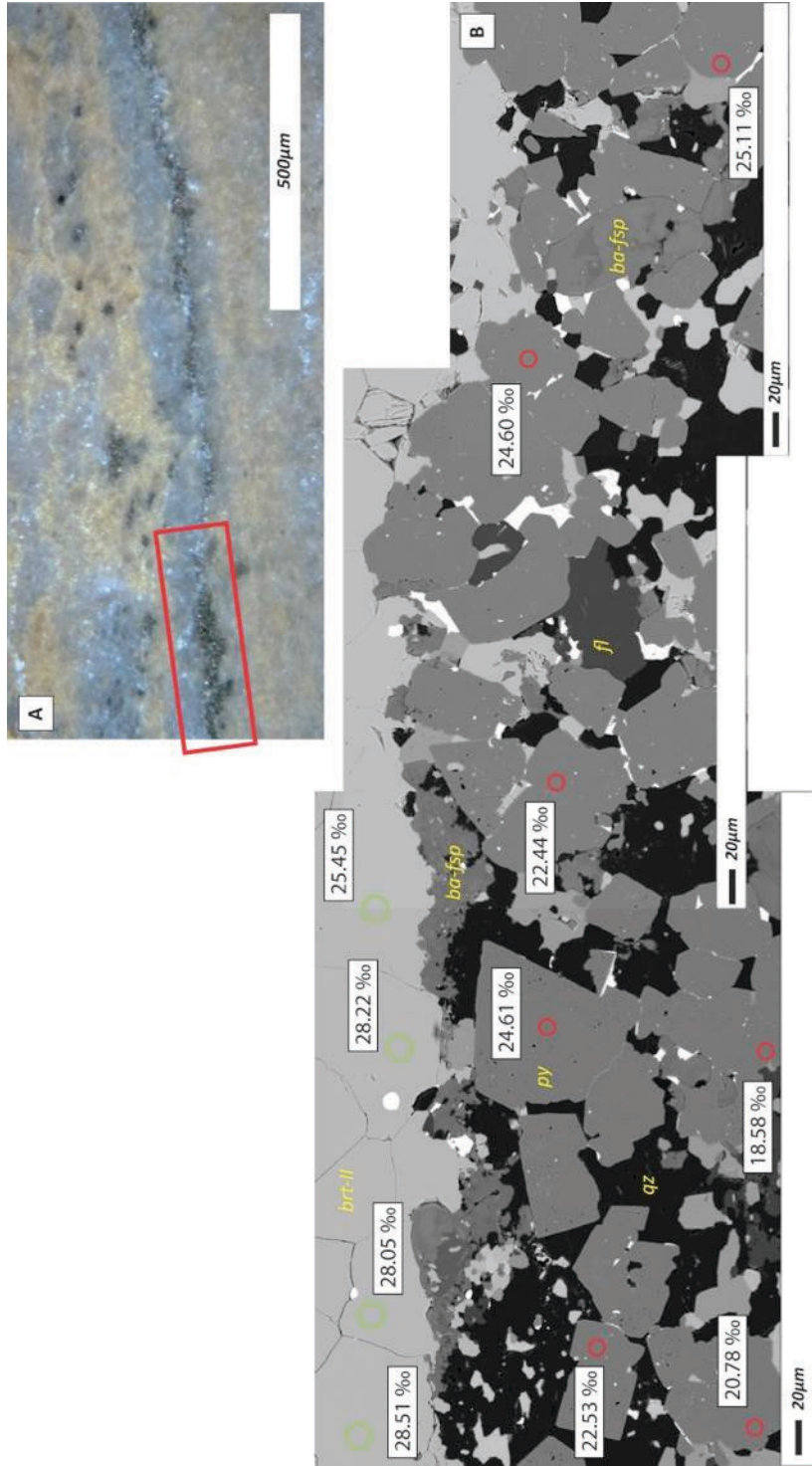
Figure 3.9. Schematic model for the formation of Stages 1 and 2 of the mineralogical paragenesis in the bedded mineralisation. The pore water profile of key geochemical parameters (e.g. SO_4^{2-}, Fe^{2+}, CH_4 and H_2S) are given on the left hand side.
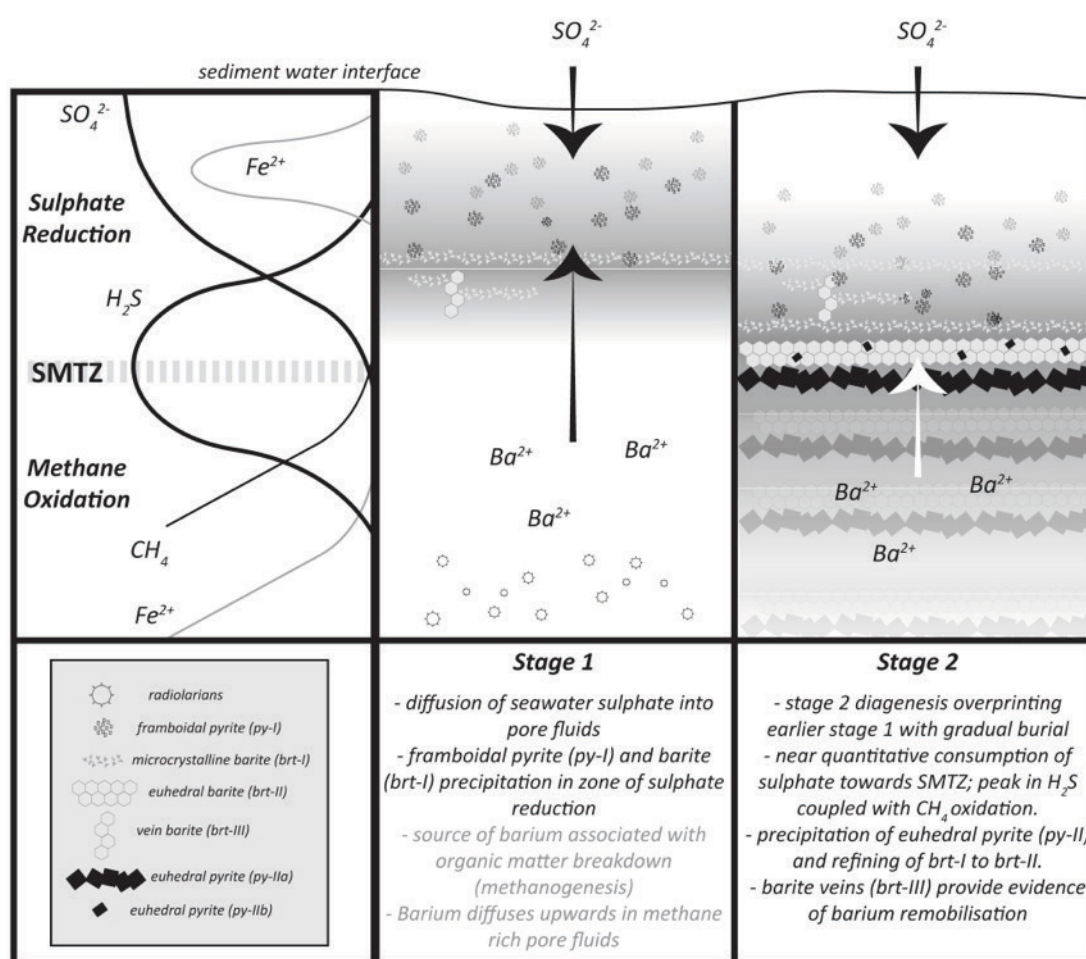
References

Adams M. M., Hoarfrost A. L., Bose A., Joye S. B. and Girguis P. R. (2013) Anaerobic oxidation of short-chain alkanes in hydrothermal sediments: potential influences on sulfur cycling and microbial diversity. *Front. Microbiol.* **4**, 1–11.

Aharon P., Fu B. and Rouge B. (2000) Microbial sulfate reduction rates and sulfur and oxygen isotope fractionations at oil and gas seeps in deepwater Gulf of Mexico. *Geochim. Cosmochim. Acta* **64**, 233–246.

Aller R. C. (2014) Sedimentary Diagenesis, Depositional Environments, and Benthic Fluxes. In *Treatise on Geochemistry* Elsevier Ltd. pp. 293–334.

Anderson I. K., Ashton J. H., Boyce A. J., Fallick A. E. and Russel M. J. (1998) Ore Depositional Processes in the Navan Zn-Pb Deposit, Ireland. *Econ. Geol.*

Ansdell K. M., Nesbitt B. E. and Longstaffe F. J. (1989) A Fluid Inclusion and Stable Isotope Study of the Tom Ba-Pb-Zn Deposit, Yukon Territory, Canada. *Econ. Geol.* **84**, 841–856.

Antler G., Turchyn A. V., Rennie V., Herut B. and Sivan O. (2013) Coupled sulfur and oxygen isotope insight into bacterial sulfate reduction in the natural environment. *Geochim. Cosmochim. Acta* **118**, 98–117.

Arndt S., Hetzel A. and Brumsack H.-J. (2009) Evolution of organic matter degradation in Cretaceous black shales inferred from authigenic barite: A

reaction-transport model. *Geochim. Cosmochim. Acta* **73**, 2000–2022.

Arning E. T., Gaucher E. C., van Berk W. and Schulz H.-M. (2015) Hydrogeochemical models locating sulfate-methane transition zone in marine sediments overlying black shales: A new tool to locate biogenic methane? *Mar. Pet. Geol.* **59**, 563–574.

Arthur M. A. and Sageman B. B. (1994) Marine black shales: depositional mechanisms and environments of ancient deposits. *Annu. Rev. Earth Planet. Sci.*

Barnes R. O. and Goldberg E. D. (1976) Methane production and consumption in anoxic marine sediments. *Geology* **4**, 297–300.

Barrie C. D., Boyce A. J., Boyle A. P., Williams P. J., Blake K., Wilkinson J. J., Lowther M., Mcdermott P. and Prior D. J. (2009) On the growth of colloform textures: a case study of sphalerite from the Galmoy ore body, Ireland. *J. Geol. Soc. London* **166**, 563–582.

Bishop J. K. B. (1988) The barite-opal-organic carbon association in oceanic particulate matter. *Nature*.

Borowski W. S., Rodriguez N. M., Paull C. K. and Ussler W. (2013) Are [34]S-enriched authigenic sulfide minerals a proxy for elevated methane flux and gas hydrates in the geologic record? *Mar. Pet. Geol.* **43**, 381–395.

Brunner B. and Bernasconi S. M. (2005) A revised isotope fractionation model for dissimilatory sulfate reduction in sulfate reducing bacteria. *Geochim. Cosmochim. Acta* **69**, 4759–4771.

Canet C., Anadón P., González-partida E., Alfonso P., Rajabi A., Pérez-segura E. and

Alba-aldave L. A. (2014) Paleozoic bedded barite deposits from Sonora (NW Mexico): Evidence for a hydrocarbon seep environment of formation. *Ore Geol. Rev.* **56**, 292–300.

Canfield D. E. (2001) Isotope fractionation by natural populations of sulfate-reducing bacteria. *Geochim. Cosmochim. Acta* **65**, 1117–1124.

Canfield D. E. (2004) The evolution of the earth surface sulfur reservoir. *Am. J. Sci.* **304**, 839–861.

Canfield D. E., Raiswell R., Westrich J. T., Reaves C. M. and Berner R. a. (1986) The use of chromium reduction in the analysis of reduced inorganic sulfur in sediments and shales. *Chem. Geol.* **54**, 149–155.

Cecile M. P., Shakur M. A. and Krouse H. R. (1983) The isotopic composition of western Canadian barites and the possible derivation of oceanic sulphate δ34S and δ18O age curves. *Can. J. Earth Sci.* **20**, 1528–1535.

Chen D., Wang J., Racki G., Li H., Wang C., Ma X. and Whalen M. T. (2013) Large sulphur isotopic perturbations and oceanic changes during the Frasnian-Famennian transition of the Late Devonian. *J. Geol. Soc. London* **170**, 465–476.

Cooke D. R., Bull S. W., Large R. R. and McGoldrick P. J. (2000) The Importance of Oxidized Brines for the Formation of Australian Proterozoic Stratiform Sediment-Hosted Pb-Zn (Sedex) Deposits. *Econ. Geol.* **95**, 1–18.

Crowe S. A., Paris G., Katsev S., Jones C., Kim S.-T., Zerkle A. L., Nomosatryo S., Fowle D. A., Adkins J. F., Sessions A. L., Farquhar J. and Canfield D. E. (2014) Sulfate

was a trace constituent of Archean seawater. *Science (80-.).* **346**, 735–739.

Cruse A. M. and Seewald J. S. (2006) Geochemistry of low-molecular weight hydrocarbons in hydrothermal fluids from Middle Valley, northern Juan de Fuca Ridge. *Geochim. Cosmochim. Acta* **70**, 2073–2092.

Dehairs F., Chesselet R. and Jedwab J. (1980) Discrete suspended particles of barite and the barium cycle in the open ocean. *Earth Planet. Sci. Lett.* **49**, 528–550.

Dickens G. R. D. (2001) Sulfate profiles and barium fronts in sediment on the Blake Ridge : Present and past methane fluxes through a large gas hydrate reservoir. *Geochim. Cosmochim. Acta* **65**, 529–543.

Dymond J. and Collier R. (1996) Particulate barium fluxes and their relationships to biological productivity. *Deep Sea Res. Part II* **43**, 1283–1308.

Emerson S. and Hedges J. (2003) Sediment Diagenesis and Benthic Flux. In *Treatise on Geochemistry* (eds. H. D. Holland and K. K. Turekian).

Farquhar J., Nanping W., Canfield D. E. and Oduro H. (2010) Connections between Sulfur Cycle Evolution, Sulfur Isotopes, Sediments, and Base Metal Sulfide Deposits. *Econ. Geol.* **105**, 509–533.

Fernandes N. A. (2011) Geology and Geochemistry of Late Devonian-Mississippian Sediment-Hosted Barite Sequences of the Selwyn Basin, NWT and Yukon, Canada. University of Alberta.

Fritz P., Basharmal G. M., Drimmie R. J., Ibsen J. and Qureshi R. M. (1989) Oxygen isotope exchange between sulphate and water during bacterial reduction of

sulphate. *Chem. Geol. Isot. Geosci. Sect.* **79**, 99–105.

Froelich P. N., Klinkhammer G. P., Bender M. L., Luedtke N. A., Heath G. R., Cullen D., Dauphin P., Hammond D. and Hartman B. (1979) Early oxidation of organic matter in pelagic sediments of the eastern equatorial Atlantic: suhoxic diagenesis. *Geochim. Cosmochim. Acta*.

Gardner H. D. and Hutcheon I. (1985) Geochemistry, Mineralogy, and Geology of the Jason Pb-Zn Deposits, Macmillan Pass, Yukon, Canada. *Econ. Geol.* **80**, 1257–1276.

Goldhaber M. B. and Kaplan I. R. (1975) Controls and consequences of sulfate reduction rates in recent marine sediments. *Soil Sci.* **119**, 42–55.

Gonzalez-Muñoz M. T., Martinez-Ruiz F., Morcillo F., Martin-Ramos J. D. and Paytan A. (2012) Precipitation of barite by marine bacteria: A possible mechanism for marine barite formation. *Geology* **40**, 675–678.

Goodfellow W. D. (1987) Anoxic Stratified Oceans as a Source of Sulphur in Sediment-Hosted Stratiform Zn-Pb Deposits (Selwyn Basin, Yukon, Canada). *Chem. Geol.* **65**, 359–382.

Goodfellow W. D. (2007) Base metal metallogeny of the Selwyn Basin, Canada. In *Mineral Deposits of Canada: A Synthesis of Major Deposit-Types, District Metallogeny, the Evolution of Geological Provinces, and Exploration Methods* Geological Association of Canada, Mineral Deposits Division, Special Publication. pp. 553–579.

Goodfellow W. D. and Jonasson I. R. (1984) Ocean stagnation and ventilation defined by 34-S secular trends in pyrite and barite, Selwyn Basin, Yukon. *Geology* **12**, 583–586.

Goodfellow W. D. and Lydon J. W. (2007) Sedimentary Exhalative (SEDEX) Deposits. In *Mineral Deposits of Canada: A Synthesis of Major Deposit-Types, District Metallogeny, the Evolution of Geological Provinces, and Exploration Methods* pp. 163–183.

Habicht K. S. and Canfield D. E. (1997) Sulfur isotope fractionation during bacterial sulfate reduction in organic-rich sediments. *Geochim. Cosmochim. Acta* **61**, 5351–61.

Hanor J. S. (2000) Barite-Celestine Geochemistry and Environments of Formation. *Rev. Mineral. Geochemistry* **40**, 193–275.

Hein J. R., Zierenberg R. a., Maynard J. B. and Hannington M. D. (2007) Barite-forming environments along a rifted continental margin, Southern California Borderland. *Deep Sea Res. Part II* **54**, 1327–1349.

Henkel S., Mogollón J. M., Nöthen K., Franke C., Bogus K., Robin E., Bahr A., Blumenberg M., Pape T., Seifert R., März C., de Lange G. J. and Kasten S. (2012) Diagenetic barium cycling in Black Sea sediments – A case study for anoxic marine environments. *Geochim. Cosmochim. Acta* **88**, 88–105.

Iversen N. and Jørgensen B. B. (1985) Anaerobic methane oxidation rates at the sulfate-methane transition in marine sediments from Kattegat and Skagerrak

(Denmark). *Limnol. Oceanogr.* **1985**, 944–955.

Jewell P. W. (1994) Paleoredox Conditions and the Origin of Bedded Barites along the Late Devonian North American Continental Margin. *J. Geol.* **102**, 151–164.

John E. H., Wignall P. B., Newton R. J. and Bottrell S. H. (2010) $\delta^{34}S_{CAS}$ and $\delta^{18}O_{CAS}$ records during the Frasnian–Famennian (Late Devonian) transition and their bearing on mass extinction models. *Chem. Geol.* **275**, 221–234.

Jørgensen B. B., Böttcher M. E., Lüschen H., Neretin L. N. and Volkov I. I. (2004) Anaerobic methane oxidation and a deep H_2S sink generate isotopically heavy sulfides in Black Sea sediments. *Geochim. Cosmochim. Acta* **68**, 2095–2118.

Jørgensen B. B. J. (1979) A theoretical model of the stable sulfur isotope distribution in marine sediments. *Geochim. Cosmochim. Acta* **43**, 363–374.

Jørgensen B. B. J. and Kasten S. (2006) Sulfur Cycling and Methane Oxidation. In *Marine Geochemistry* (eds. H. D. Schulz and M. Zabel).

Jørgensen B. B. J., Weber A. and Zopfi J. (2001) Sulfate reduction and anaerobic methane oxidation in Black Sea sediments. *Deep. Res. I* **48**, 2097–2120.

Joye S. B., Boetius A., Orcutt B. N., Montoya J. P., Schulz H. N., Erickson M. J. and Lugo S. K. (2004) The anaerobic oxidation of methane and sulfate reduction in sediments from Gulf of Mexico cold seeps. *Chem. Geol.* **205**, 219–238.

Kaplan I. R. and Rittenberg S. C. (1964) Microbiological Fractionation of Sulphur Isotopes. *J. Gen. Microbiol.* **34**, 195–212.

Kiyosu Y. and Krouse R. H. (1990) The role of organic and acid the in the sulfur abiogenic isotope reduction effect. *Geochem. J.* **24**, 21–27.

Kozdon R., Kita N. T., Huberty J. M., Fournelle J. H., Johnson C. a. and Valley J. W. (2010) In situ sulfur isotope analysis of sulfide minerals by SIMS: Precision and accuracy, with application to thermometry of ~3.5Ga Pilbara cherts. *Chem. Geol.* **275**, 243–253.

Leach D. L., Bradley D. C., Huston D., Pisarevsky S. A., Taylor R. D. and Gardoll J. (2010) Sediment-Hosted Lead-Zinc Deposits in Earth History. *Econ. Geol.* **105**, 593–625.

Leach D. L., Sangster D. F., Kelley K. D., Large R. R., Garven G., Allen C. R., Gutzmer J. and Walters J. (2005) Sediment-Hosted Lead-Zinc Deposits: A Global Perspective. *Econ. Geol.* **100**, 561–607.

Lowenstein T. K., Hardie L. a., Timofeeff M. N. and Demicco R. V. (2003) Secular variation in seawater chemistry and the origin of calcium chloride basinal brines. *Geology* **31**, 857.

Lowenstein T. K., Kendall B. and Anbar A. D. (2014) The Geologic History of Seawater. In *Treatise on Geochemistry* Elsevier Ltd. pp. 569–629.

Lyons T. W., Gellatly A. M., Mcgoldrick P. J. and Kah L. C. (2006) Proterozoic sedimentary exhalative (SEDEX) deposits and links to evolving ocean chemistry. *Geol. Soc. Am. Mem.*

Machel H. G. (2001) Bacterial and thermochemical sulfate reduction in diagenetic

settings - old and new insights. *Sediment. Geol.* **140**, 143–175.

Machel H. G., Krouse H. R. and Sassen R. (1995) Products and distinguishing criteria of bacterial and thermochemical sulfate reduction. *Appl. Geochemistry* **10**, 373–389.

Nelson J., Paradis S., Christensen J. and Gabites J. (2002) Canadian Cordilleran Mississippi Valley-Type Deposits : A Case for Devonian-Mississippian Back-Arc Hydrothermal Origin. *Econ. Geol.* **97**, 1013–1036.

Newton R. J., Reeves E. P., Kafousia N., Wignall P. B., Bottrell S. H. and Sha J.-G. (2010) Low marine sulfate concentrations and the isolation of the European epicontinental sea during the Early Jurassic. *Geology* **39**, 7–10.

Niewöhner C., Hensen C., Kasten S., Zabel M. and Schulz H. D. (1998) Deep sulfate reduction completely mediated by anaerobic methane oxidation in sediments of the upwelling area off Namibia. *Geochim. Cosmochim. Acta* **62**, 455–464.

Passier H. F., Middelburg J. J., Lange G. J. De and Böttcher M. E. (1997) Pyrite contents, microtextures, and sulfur isotopes in relation to formation of the youngest eastern Mediterranean sapropel. *Geology* **25**, 519–522.

Paytan A. and Griffith E. M. (2007) Marine barite: Recorder of variations in ocean export productivity. *Deep Sea Res. Part II* **54**, 687–705.

Paytan A., Mearon S., Cobb K. and Kastner M. (2002) Origin of marine barite deposits: Sr and S isotope characterization. *Geology* **30**, 747.

Raiswell R. (1982) Pyrite texture, isotopic composition and the availability of iron. *Am.*

J. Sci.

Reeburgh W. S. (1976) Methane consumption in cariaco trench waters and sediments. *Earth Planet. Sci. Lett.* **28**, 337–344.

Reeburgh W. S. (2007) Oceanic methane biogeochemistry. *Chem. Rev.* **107**, 486–513.

Rees C. E. (1973) A steady-state model for sulphur isotope fractionation in bacterial reduction processes. *Geochim. Cosmochim. Acta* **37**, 1141–1162.

Schmitz B. (1987) Barium, equatorial high productivity, and the northward wandering of the Indian continent. *Paleoceanography* **2**, 63–77.

Stamatakis M. G. and Hein J. R. (1993) Origin of barite in Tertiary marine sedimentary rocks from Lefkas Island, Greece. *Econ. Geol.* **88**, 91–103.

Stein R., Rullkötter J. and Welte D. H. (1986) Accumulation of organic-carbon-rich sediments in the Late Jurassic and Cretaceous Atlantic Ocean — A synthesis. *Chem. Geol.* **56**, 1–32.

Torres M. E., Bohrmann G., Dubé T. E., Poole F. G., Poole, Forrest G. and Poole F. G. (2003) Formation of modern and Paleozoic stratiform barite at cold methane seeps on continental margins. *Geology* **31**, 897–900.

Torres M. E., Brumsack H. J., Bohrmann G. and Emeis K. C. (1996) Barite fronts in continental margin sediments: a new look at barium remobilization in the zone of sulfate reduction and formation of heavy barites in diagenetic fronts. *Chem. Geol.* **127**, 125–139.

Turchyn A. V., Sivan O. and Schrag D. P. (2006) Oxygen isotopic composition of sulfate in deep sea pore fluid: evidence for rapid sulfur cycling. *Geobiology* **4**, 191–201.

Turner R. J. W. (1992) Formation of Phanerozoic stratiform sediment , hosted zinc-lead deposits : Evidence for the critical role of ocean anoxia. *Chem. Geol.* **99**, 165–188.

Wankel S. D., Adams M. M., Johnston D. T., Hansel C. M., Joye S. B. and Girguis P. R. (2012) Anaerobic methane oxidation in metalliferous hydrothermal sediments: influence on carbon flux and decoupling from sulfate reduction. *Environ. Microbiol.* **14**, 2726–40.

Widerlund A., Nowell G. M., Davison W. and Pearson D. G. (2012) High-resolution measurements of sulphur isotope variations in sediment pore-waters by laser ablation multicollector inductively coupled plasma mass spectrometry. *Chem. Geol.* **291**, 278–285.

Zhelezinskaia I., Kaufman A. J., Farquhar J. and Cliff J. (2014) Large sulfur isotope fractionations associated with Neoarchean microbial sulfate reduction. *Science (80-.).* **346**, 742–744.

Chapter 4. Vent complex geochemistry in Clastic-Dominated (CD-type) massive sulphide systems of the Macmillan Pass district, Yukon, Canada

4.1 – Introduction

Mineralisation in Clastic Dominated-type (CD) systems typically occurs at or close to the sediment-water interface in sedimentary basins via non-magmatic processes (Leach et al., 2005; Wilkinson, 2014). The lack of evidence for magmatic input suggests CD-type deposits are genetically different from volcanogenic massive sulphide (VMS) deposits and modern vents at mid ocean ridge (MOR) systems. Whereas fluids exhaled from modern hydrothermal vent systems evolve via the convective circulation of seawater at spreading centers, fluids in CD-type systems have a more ambiguous origin (Wilkinson, 2014).

For CD-type systems in the geologic record, the hydrothermal vent complex is a key genetic feature, as it represents the primary conduit of fluid up-flow. As such, vent complexes should provide a record of fluid chemistry, and may preserve evidence of key geochemical processes. However, there are only a limited number of CD-type deposits where a hydrothermal vent complex is preserved, and even fewer where a clear relationship exists between vent and overlying sulphide mineralisation (e.g. Gardner and Hutcheon, 1985; Ansdell et al., 1989; Rajabi et al., 2014). This represents a major limitation for the characterisation of hydrothermal fluid geochemistry in CD-type systems (Wilkinson, 2014). The current state of knowledge relies, almost exclusively, upon a limited number of fluid inclusion studies from vent complexes

(Gardner and Hutcheon, 1985; Ansdell et al., 1989; Rajabi et al., 2014). Other studies that have analysed fluid inclusions from discordant veins associated with CD-type systems (Everett et al., 1999; Leach et al., 2004), however the relationship between these veins and the overlying bedded mineralisation is not clear. It is necessary to emphasize that in samples from CD-type systems, fluid inclusions are generally small (< 10μm), thus making reliable, accurate measurements challenging to obtain. Existing temperature and salinity constraints are broad (157°C to 335°C, 2.6 to 18 wt. % NaCl equivalent; Gardner and Hutcheon, 1985; Ansdell et al., 1989) and lacking in petrographic context, while parameters such as fO$_2$, total sulphur content (ΣS) and pH remain ambiguous. These parameters are all important controls on the solubility of Pb and Zn in crustal fluids (Yardley, 2005).

In modern settings (e.g. Guaymas Basin), experimental studies have shown that reaction of hot hydrothermal fluids with organic-rich sediments can result in the release of both CO$_2$, transition metals (Zn, Pb, Fe) and a suite of volatile components (Welhan and Lupton, 1987; Seewald et al., 1990; 1994; Cruse and Seewald, 2001, Cruse and Seewald, 2006). These systems are typically characterised by steep thermal and chemical gradients, where fluid chemistry is modified at a shallow level during interaction with chemically reactive sediments and their pore fluids. Tracing these interactions is challenging in geologic systems, primarily due to issues of preservation and the interpretation of transient geochemical signatures in the context of what are often complex mineralogical relationships. In CD-type systems, there have been attempts to reconstruct basic fluid composition and metal solubility via thermodynamic modeling (Cooke et al. 2000; Tornos and Heinrich, 2008). However, no attempt has been made to constrain how these systems evolve on a local scale and perhaps spatially and temporally in terms of interaction with the partially lithified

mudstone host rock.

The rare earth element (REE) composition of hydrothermal fluids provides a useful record of fluid chemistry and flow paths (Klinkhammer et al., 1994), and there is potential for equivalent information to be derived from the analysis of carbonates in hydrothermal systems (e.g. Bau and Moller, 1992), due to minimal fluid-mineral fractionation (Sholkovitz and Shen, 1995; Jakubowicz et al., 2015). Furthermore, micro-analytical techniques now afford the sampling of carbonates at a high spatial resolution (Jochum et al., 2012), and have been applied successfully to studies of authigenic carbonate (Himmler et al., 2010; Zhang et al., 2014; Jakubowicz et al., 2015), but have yet to be widely applied to hydrothermal systems (e.g. Fusswinkel et al., 2013). The analysis of volatile components in fluids from modern systems can also prove useful for evaluating the derivation and alteration of carbon (Welhan and Lupton, 1987; Cruse and Seewald, 2006; Cruse and Seewald, 2010), and in geologic systems there is potential to acquire equivalent information via quantitative analysis of volatile components in fluid inclusions (Blamey, 2012).

In this study, samples have been obtained from the vent complexes of two CD-type deposits (Tom, Jason) hosted in Upper Devonian strata of the Earn Group from the Selwyn Basin, Yukon Territory, Canada. There are two overarching objectives to this study: (1) evaluate the metal transport capacity of CD-type fluids, and (2) evaluate how organic rich mudstones contribute to fluid chemistry, and draw comparison to modern day sediment-covered ridge axis systems (e.g. Guaymas Basin). This has been achieved using two broad approaches: (1) petrography and fluid inclusion microthermometry form a framework for modeling the thermodynamic stability of mineral assemblages, in terms of temperature, pH, $f\text{O}_2$, ΣS and ΣC, which provide important constraints on

the composition of the fluid entering the vent, (2) sulphur isotope analysis of sulphides, *in situ* REE element analysis of carbonate (LA-ICP-MS), and fluid inclusion gas analysis are used to assess interaction with the host rock.

4.2 – Selwyn Basin Geology

The Selwyn Basin (Figure 1.1) contains clastic sedimentary rocks that were deposited between the Precambrian and Late Devonian along the western passive margin of ancestral North America (Gabrielse, 1967). The Windermere Supergroup (Hadrynian-Cambrian) forms a 4-6km thick basal sequence in the Selwyn Basin, comprising immature rift clastic sedimentary rocks deposited during erosion of the crystalline basement and breakup of Rodinia (~760 Ma; Eisbacher, 1985).

Subsequent deposition was dominated by carbonaceous mudstones, which form a major component of the Selwyn Basin stratigraphy. The carbonaceous mudstones are host to three major periods of CD-type metallogenesis (i.e., Cambrian, Silurian and Late Devonian) during the evolution of the Selwyn Basin (Goodfellow and Lydon, 2007). Alkalic to ultra-potassic volcanism (flows, dykes and tuffs) related to extensional tectonics are coincident, but not spatially associated with CD-type mineralisation during all three periods (Goodfellow et al. 1995; Goodfellow, 2007).

Island arc accretion during the Mesozoic led to the incorporation of passive margin strata into the Cordilleran fold and thrust belt, and Selwyn Basin strata are characterised by regional-scale folds and thrusts and accompanied by slaty cleavage and intense tight to isoclinal folding (Gordey et al., 2010). The Tom and Jason deposits have been tectonically deformed, however this deformation is mostly localized to the

hinge zones of folds.

At Macmillan Pass, the metamorphic grade is low (sub-greenschist), and many of the primary sedimentary and hydrothermal features are well preserved. Tom and Jason are hosted in equivalent strata, and the vent complexes form a relatively discrete feature in the deposit architecture, as a zone of stockwork style carbonate and sulphide veining (see Figure 4.1) that crosscut a mudstone sequence of less than 5 meters stratigraphic thickness. The vent complexes transition upwards through a zone of massive sulphide and minor barium carbonates (barytocalcite and witherite) into more bedded (stratiform and stratabound) sulphide and barite mineralisation, which can reach approximately 20 to 30 meters stratigraphic thickness.

4.3 – Samples and Analytical Techniques

4.3.1. Samples

The Jason deposit and host strata have been deformed into a tight, upright syncline (Figure 4.2A). Samples of the Jason vent complex were obtained from a drill-hole (86-86A) that intersects the vent complex at a low angle to bedding, meaning that broadly, Jason vent samples are from a relatively narrow stratigraphic sequence within the deposit architecture. At the Tom deposit, which is deformed into an anticline (Figure 4.2B), the sampled drill-holes (TYK001, TYK002, TU70-2, T91-14) intersected the host rock perpendicular to bedding, and samples were obtained from strata beneath, within and above the vent complex (e.g. Figure 2.3, TYK001; Chapter 2).

It was possible to collect a wide variety of samples from the Tom and Jason vent

complexes (n = 50), which preserve varying degrees of carbonate and sulphide alteration of the host rock (Figure 4.1). The suite of samples that were targeted for carbonate trace element analysis are characterised by: (1) carbonate and massive sulphide alteration, with minimal preservation of the original host rock, (2) stockwork style veining that crosscut earlier carbonate alteration, and (3) stock work veining (e.g. in 86A-35) where the host rock is relatively unaltered, and which probably represents mineralisation in a peripheral vent setting. Samples that were targeted for fluid inclusion analysis (microthermometry, gas mass spectrometry) were obtained from: (1) veins hosted in conglomerates beneath the vent complex at Tom, (2) quartz and ankerite veins from highly altered vent samples at both Tom and Jason, and (3) sulphide-bearing barytocalcite veins in samples from the vent to bedded mineralisation transition zone.

4.3.2. Petrography, mineralogy and major element chemistry

Transmitted and reflected light microscopy was used to evaluate the mineralogy and paragenesis of samples. Mineral chemistry was analysed using the JEOL 8900 electron probe micro-analyzer (EPMA) (University of Alberta, Electron Microprobe Laboratory). The electron beam was operated at an accelerating voltage of 15 kV, a probe current of 15nA and a beam diameter of 1μm. For ankerite and siderite, standardisation involved analysis of FeO on siderite; MgO and CaO on dolomite; SrO on strontianite and MnO on rhodonite.

4.3.3. Fluid inclusion microthermometry

Doubly polished, 70-100μm thick fluid inclusion wafers (n=30) were prepared by

Vancouver Petrographics and the Thin Section Laboratory (Earth and Atmospheric Sciences, University of Alberta). Minerals in equilibrium, or which displayed close paragenetic relationships with sulphide phases were targeted for fluid inclusion analysis. Fluid inclusions are described in terms of phases present at room temperature (L_W = liquid water, L_C = liquid CO_2, V = vapour). These fluid inclusions were classified as secondary, pseudo-secondary or primary (Roedder, 1984) and groups of inclusions considered to be coeval were treated as fluid inclusion assemblages and targeted for analysis. Microthermometry was performed using a Linkham THMSG600 heating/freezing stage (working range of -196 to 600°C). The stage was calibrated at -56.6°C, 0°C and 374.1°C using SynFlinc synthetic standards, with accuracy ±0.2°C.

4.3.4. Fluid inclusion gas analysis

Samples of quartz that were well constrained within the paragenesis were targeted for quantitative fluid inclusion gas analysis using the incremental crush fast scan method that is described by (2012) and Blamey et al. (2015). Samples were analysed at the Fluid Inclusion Gas Laboratory at New Mexico Tech. Calibration was conducted using atmosphere in addition to three water:gas standards. Samples were cleaned with KOH then rinsed with deionised water to remove organics. About 0.2g of sample was placed in crushers and subjected to 10^{-8} Torr vacuum overnight. The quartz was incrementally crushed *in vacuo* and the liberated gases are measured by a dual Pfeiffer Prisma quadrupole mass spectrometer system using the crush fast scan method, prior to the volatiles being removed by a turbo pump. The signals are then processed using the matrix inversion approach described by Isenhour and Jurs (1972). As explained by Blamey et al. (2015), several factors influence the precision and detection limit but

these are typically ±5% and <1ppm (±1 femto mol) respectively for organic species in aqueous-dominated fluid inclusions.

4.3.5. Sulphur isotopes

Mineral separates of pyrite, galena and sphalerite were obtained from disaggregated core samples under the binocular microscope. Analyses were performed at the Isotope Science Laboratory (University of Calgary). Samples were introduced to a quartz tube combustion reactor (T = 1050°C), and eluent gases transferred by a helium carrier stream through a gas chromotograph to achieve gas separation before subsequent mass spectrometry (see method of Grassineau et al., 2001). Analysis of the $^{34}S/^{32}S$ ratio is reported in the per-mil notation relative to the Vienna-Canyon Diablo Troilite standard (V-CDT), with precision and reproducibility typically better than ±0.3‰.

4.3.6. LA-ICP-MS of vent carbonate

Analysis of rare earth elements in carbonate was performed using in situ laser ablation coupled with sector field inductively coupled plasma-mass spectrometry (LA-SF-ICP-MS) at the Arctic resources laboratory, Canadian Centre for Isotopic Microanalysis (CCIM; University of Alberta). Samples were prepared as polished 70μm thick sections and ablated using a Resonetics M-50 LR laser system (193nm) coupled to a high-resolution sector-field Thermo Element XR. The mass spectrometer was operated in low mass resolution mode (M/ΔM=ca. 300). Samples were ablated with laser repetition rates of 10 Hz using a spot size of 75μm and energy density of 7 Jcm^{-2}. Ablated aerosols were entrained in a He cell gas flow (600 mL/min) and subsequently mixed with N2 (2 mL/min) and Ar (0.8 mL/min) prior to entering the SF-ICP-MS

torch. The SF-ICP-MS was operated at 1300W and a torch depth of 3.5 mm. Argon and helium gas flow, torch position and focusing potentials were optimized to achieve optimal signals on Co, La and Th and low oxide production rates (ThO/Th < 0.3%). Data processing was carried out using Iolite (Paton et al.; https://iolite-software.com/) with NIST612 as an external standard and MACS-3 as a secondary carbonate standard. Internal standardisation was based on the calcium content of the sample, as determined by EPMA. The results of the carbonate secondary standard (MACS-3) agree with the reference values within relative uncertainties of 5–10% or better at the 95% confidence level.

4.4. Results

4.4.1. Mineralogy and paragenesis

Figure 4.3 presents a paragenesis for the precipitation of key mineral phases in the Tom and Jason vent complexes. This provides an important framework for understanding fluid evolution within the context of the geochemical data. The paragenesis can be split into two stages, which are characterised by different types of iron carbonate: (1) ferroan dolomite (ankerite), is the dominant gangue mineral phase in the majority of vent samples (see Figure 4.1), and (2) siderite, which, although is a more minor phase relative to ankerite, is associated with sulphide precipitation.

Stage 1. There are two generations of ankerite in stage 1: (1) small, anhedral, interlocking crystals disseminated in the host rock (Figure 4.4A) and in discordant, vuggy veins, and (2) distinctive, well formed stockwork style veining that brecciated

the host rock, with more equant, euhedral ankerite crystals (size; Figure 4.4B). In back-scattered electron (BSE) imaging of ankerite disseminated in the mudstone, it is possible to distinguish two ankerite-forming events (ank-1a and ank-1b; Figure 4.4C), of which the crosscutting generation (ank-1b) has higher $FeCO_3$ contents. Pyrite is the only sulphide mineral that forms during Stage 1, and together with pyrobitumen and minor amounts of quartz (Figure 4.4B) completes the assemblage.

Stage 2. Siderite is associated with the main sulphide mineral assemblage, comprising galena, chalcopyrite, pyrrhotite, pyrite, sphalerite and minor arsenopyrite (Figure 4.4C, D and E). The Stage 2 assemblage clearly crosscuts and overprints Stage 1 in all samples (Figure 4.4B, C, D and E), and is associated with barium-carbonates (barytocalcite and witherite; Figure 4.4F) where the vent transitions into the overlying bedded mineralisation (Chapter 3). The evolution between Stage 1 and 2 can be either abrupt, with Stage 2 veins crosscutting Stage 1 ankerite, or more gradual, with the Stage 2 assemblages precipitating in vuggy pore space in Stage 1 ankerite (Fig 4.5). The quartz in Stage 2 is divided into two generations, Q1 and Q2, distinguished by their optical clarity; Q1 is milky and translucent, whereas Q2 is clear and associated most closely with the sulphide precipitation that is interstitial to Q1.

4.4.2. Fluid inclusions

The optical characteristics of the carbonate, high abundance of fluid inclusions (cloudiness), and their small size ($\leq 5\mu m$) meant that in ankerite, it was not possible to carry out a microthermometric study on many of the samples. However, some analyses were possible in rare transparent, inclusion-poor ankerite, in which primary inclusions could be identified (Figure 4.6A and B). The primary inclusion assemblage in Stage 1

ankerite is characterised by euhedral, two-phase (L_W + V) inclusions, formed along growth zones defined by the rhombohedral crustal structure of ankerite (Figure 4.6B). Homogenization temperatures (T_h) for two-phase aqueous fluid inclusion assemblages from Stage 1 and 2 are presented in Figure 4.6. Homogenization temperatures for Stage 1 inclusions in ankerite record fluid temperatures between 216 and 266°C (n = 8).

Stage 2 quartz and barytocalcite preserve an assemblage of 3-phase (L_W + L_C + V) carbonic and 2-phase (L_W + V) aqueous inclusions (Figure 4.6C). The Stage 2 inclusions can be slightly larger (~10μm) than the Stage 1 assemblage and are randomly distributed within quartz and barytocalcite crystals (Figure 4.6C and E). The Stage 2 assemblage has also been identified in crystals that are proximal to sulphide minerals (Figure 4.6C) and are, therefore, interpreted to represent phases associated with the mineralizing fluids. In Stage 2, T_h measurements from quartz (Qz = 172°C to 215°C; n = 14) and barytocalcite (ba-cc = 108°C to 136°C; n = 14) are lower than Stage 1. Salinity measurements were only possible in 6 inclusions from Stage 2 quartz, for which the final melting of ice (T_{fm}) occurred between -2°C and -3.5°C, corresponding with salinities of 3.4 to 5.7 wt. % NaCl (Bodnar, 1993).

The gas content of fluid inclusions hosted in quartz is summarized in Table 4.1. In some samples it was possible to distinguish two types of quartz within individual veins, milky (Q1) and clear (Q2). Fluid inclusions have extremely high CO_2 concentrations, with the weighted mean of analyses from individual samples is between 8.4 and 57.5 mol.% CO_2. There are general decreasing abundances of short chain hydrocarbons with increasing chain length (Figure 4.8A) and a negative correlation between N_2/Ar and Ar/He (Figure 4.8B). However there is no systematic correlation between Q1 and Q2,

and some of the samples preserve anomalous propane (C_3H_8) concentrations.

4.4.3. Major element chemistry of ankerite and siderite

A summary of major element chemistry for ankerite and siderite is presented in Table 4.2. There are varying amounts of Fe and Mg in both carbonate phases, and higher Fe/Mg ratios are generally observed later in the development of both Stage 1 ankerite (Figure 4.9A) and Stage 2 siderite (Figure 4.9B). In addition, there is an interesting switch from a positive to negative correlation between Fe and Mn in ankerite (Figure 4.9C).

4.4.4. Sulphide $\delta^{34}S$ values

Table 4.3 is a summary table of the results of sulphur isotope analysis of sulphide mineral separates from the Tom and Jason vent complexes (see Appendix F for complete table). In samples from the Jason vent, galena (n = 8) and sphalerite (n = 3) $\delta^{34}S$ values are between +16.6 and +19.1‰, and +18.5 and +19.1‰, respectively. Samples from the Tom vent preserve a broad, but generally lower, range of $\delta^{34}S$ values, with galena (n = 5) between +7.5 and +16.2‰, and pyrite (n = 7) between +9.5 and 19.5‰. Sphalerite at Tom (n = 3) was sampled from transitional vent samples, with $\delta^{34}S$ values between +10.6 and +12.1‰.

4.4.5. Rare earth elements and yttrium (REEs and Y)

The REE data are normalized (REE_N) to chondrite values, and presented in Figure 4.10 with data from the North American Shale Composite (NASC; Gromet et al., 1984),

seawater (Alibo and Nozaki, 1999) and modern hydrothermal fluids (Bau and Dulski, 1999). See Appendix E for the complete data set. In terms of overall REE abundance, the Macmillan Pass carbonate is enriched relative to seawater and modern hydrothermal fluids. The overall abundance of REEs in ankerite is more comparable to NASC, and in some cases, REE_N profiles are middle REE (MREE) and heavy REE (HREE) enriched. Relative to NASC, all samples display variable depletion in LREEs ($La_N/Lu_N \ll 1$); this is in notable contrast to modern vent fluids, which show progressive light REE (LREE) enrichment. As with modern vent fluids, samples preserve positive europium anomalies.

4.5. Discussion

The mineralogical paragenesis is the same at Tom and Jason (Figure 4.3), providing evidence of mutual processes and possibly even of a common source and composition for the hydrothermal fluid. Importantly, the distinct Stage 1 and 2 mineral assemblages are evidence that the physico-chemical conditions governing the precipitation of Stage 1 minerals changed to produce the massive sulphide mineralisation in Stage 2. How these mineral assemblages formed, and the geochemistry of the fluids from which they precipitated, will form the first part of the discussion.

4.5.1. Stage 1 mineral assemblage

The hydrothermal activity at Tom and Jason produced at least two ankerite-forming events (host rock alteration and later stockwork veining; Figure 4.1). Ankerite, also known as ferroan dolomite ($Ca(Fe_xMg_{1-x})(CO_3)_2$), is the most abundant mineral in the

Stage 1 assemblage. It is common, but not ubiquitous, gangue mineral in other CD-type systems (Leach et al. 2010). Ankerite has been documented in the Late Devonian Iberian Pyrite Belt (Sánchez-España et al., 2003), and also in the Paleoproterozoic McArthur and Mt Isa basins, where it occurs in discordant veins and as an alteration phase of the host rock (Rye and Williams, 1981; Large and McGoldrick, 1998).

A wide range of Fe concentrations are observed in the ankerite of Stage 1, which is consistent with partial substitution of Fe for Mg ($(Ca(Fe_xMg_{1-x})(CO_3)_2$, $0 \leq x \leq 0.7$; Reeder, 1983; Radha and Navrotsky, 2013). However, the Fe content of Macmillan Pass ankerite (14-27% $FeCO_3$) extends to higher concentrations than reported in other CD-type systems (<20% $FeCO_3$; Large and McGoldrick, 1998). The higher Fe content of Macmillan Pass ankerite could be a function of fluid rock interaction with pyrite in basinal strata, either at a shallow level in partially lithified sediments (e.g. Cruse and Seewald, 2001) or during equilibration with pyritic mudstones that dominate the Paleozoic Selwyn Basin stratigraphy. In terms of a paragenetic trend, Fe content generally increases through Stage 1. Iron and Mn typically co-vary in hydrothermal fluids (German and Von Damm, 2014), and this is partly observed in Figure 4.9C; the reversal in this trend is most likely evidence of the precipitation of pyrite part of the way through Stage 1.

Homogenization temperatures (L+V ➔ L = T_h) in fluid inclusions from ankerite provide broad constraints of 216 to 266°C for Stage 1 fluid flow in the Jason vent, and are consistent with those reported by Gardner and Hutcheon (1985). The preservation of pyrobitumen during Stage 1 is evidence that organic carbon present in the carbonaceous mudstone was altered by the hydrothermal system. Indeed, the mudstone is enriched in organic carbon (TOC = 2-5 wt. %; Chapter 2) and the

temperature measured in Stage 1 are within the thermal window of organic carbon maturation (Hunt, 1996). Hydrothermal organic carbon maturation has also been recognized in other CD-type systems (Broadbent et al., 1998; Cooke et al., 2003), as well as in other ore deposit types (Rasmussen and Buick, 2000; Wilson, 2000) and modern hydrothermal systems (Peter et al., 1991; Cruse and Seewald, 2006).

At Macmillan Pass, the interaction between hydrothermal fluids and organic rich sediments is an important consideration that has implications for fluid chemistry in the vent complexes. Experimental studies have shown that at temperatures approaching 300°C, release of H_2S occurs both during organic matter degradation and via pyrite-pyrrhotite transformation (Seewald et al., 1994). Furthermore, during high temperature alteration, organic rich sediments may contribute CO_2 and high concentrations of ore-forming metals (Fe, Mn, Zn and Pb) to solutions (Cruse and Seewald, 2001), as well as leading to thermochemical sulphate reduction (TSR; Machel, 2001) according to reaction 1:

The operation of TSR requires temperatures in excess of 110°C, a reductant (organic matter) and a source of sulphate (seawater, evaporites) (Machel, 1987). Considering the temperature constraints of the Stage 1 fluid (>250°C), reaction kinetics would be fast enough to enable rapid sulphide production and precipitation of base metal sulphides (Anderson and Thom, 2007; Thom and Anderson, 2007).

Considering the proximity to the seafloor of CD-type systems and the absence of evaporites in the Selwyn Basin stratigraphy, Late Devonian seawater is the likeliest source of sulphate (~24‰; John et al., 2010). Using the equation of Kiyosu and Krouse

(1990), the isotopic fractionation of Late Devonian seawater sulphate during TSR has been calculated at different temperatures and presented in Figure 4.11. Notably, the $\delta^{34}S$ values from galena and sphalerite in the Jason vent, which form a relatively narrow distribution, are broadly consistent with the temperature of the Stage 1 fluid. It is more difficult to make a comparable assessment of TSR in the Tom vent on the basis of $\delta^{34}S$ values. The $\delta^{34}S$ values preserved in galena and pyrite encompass a broader range, however they also represent different types of samples, in terms of stratigraphic position and style of alteration (as discussed in section 4.3.1). However, very few of the samples extend to the positive $\delta^{34}S$ values that are typical of Jason sulphides, which may indicate that temperatures were lower in the Tom vent.

4.5.2. Stage 2 mineral assemblage

The main sulphide-mineralising event occurs during Stage 2 (Figures 4.4 and 4.5). The transition to Stage 2 of the paragenesis can be either transitional or abrupt, with sulphides occurring as interstitial vuggy replacement of Stage 1 ankerite or within crosscutting veins.

Homogenization temperatures of Stage 2 quartz fluid inclusions (T_h = 172°C to 215°C) are lower relative to the Stage 1 fluid, and are even lower in fluid inclusions hosted by barytocalcite (T_h = 108°C to 136°C). Barytocalcite and witherite occur in samples that are transitional between vent and the overlying barite rich bedded mineralisation (also described in Chapter 3) and likely represent a shallow component of the vent, more proximal to the paleo-seafloor. This represents a steep vertical gradient over approximately 10 meters of stratigraphic thickness. The fluid responsible for the Stage 2 sulphide assemblage produced penetrative dissolution textures within

137

ankerite which at 200°C, requires a fluid with a pH less than 4.

There has been disagreement in previous fluid inclusion studies (Gardner and Hutcheon, 1985; Ansdell et al., 1989) regarding the origin of CO_2 in the fluids in the Tom and Jason vent complexes. Gardner and Hutcheon (1985) recognized CO_2 in primary inclusions from the vent complex, whereas Ansdell et al. (1989) argued that CO_2 was introduced via tectonic fluids during a younger deformation event. In this study, samples of quartz and barytocalcite from Stage 2 preserve 2-phase aqueous inclusions coexisting with 3-phase carbonic inclusions (Figure 4.6C).

Melting of solid CO_2 occurs at -56.6°C, therefore the inclusions in quartz contain pure CO_2. In terms of overall abundance, bulk analyses of the gas content of quartz hosted fluid inclusions indicate very high CO_2 concentrations (38.46 to 68.44 mol.%). The origin of this CO_2 is an interesting aspect of the Stage 2 assemblage, considering the thermal alteration of organic matter that is preserved in the Stage 1 assemblage (Figure 4.4G and H). In the study by Conliffe et al. (2013), high concentrations of CO_2 (up to 21 mol. %) are reported for fluid inclusions in an MVT system, where CO_2 generation is proposed to occur via TSR (see reaction 1). The abundance of CO_2 in the MacMillan Pass vent complexes is higher that documented by Conliffe et al. (2013) which may reflect the higher organic content of the host rocks at Macmillan Pass (Chapter 2).

Importantly, the high concentrations of CO_2 in the fluid inclusions at Macmillan Pass could provide evidence of a fluid trapped at high pressures (>1 kb; Shepherd et al. 1985), at depths greater than 3km of lithostatic overburden. However, previous work by Gardner and Hutcheon (1985) reported evidence of phase separation (boiling) in fluid inclusions from the Jason vent and argued that fluids were trapped at a maximum

pressure of 250 bars, which factored water depth (maximum 420m) and host rock tensile strength (100-200 bars). Indeed, this is more consistent with the steep thermal gradient (Figure 6) and evidence that mineralisation occurred in an early diagenetic environment (Chapter 3), both of which support a model whereby mineralisation occurred at lower pressures. If these lower pressure constraints (maximum 250 bars) are used at Tom and Jason, a correction of +25°C can be made to obtain a trapping temperature for the fluids (Potter, 1977).

To produce such high concentrations of CO_2 in a shallow environment would therefore have required the trapping two separate (immiscible) phases, i.e. aqueous liquid and vapour rich CO_2. Cathles and Schoell (2007) proposed when temperatures greater than 320°C are reached at depth in sedimentary basins, the breakdown of carbonate mineral phases results in generation of CO_2; in their conceptual model, Ca-aluminosilicates (and then Fe and Mg silicates) form a source of Ca (Fe and Mg) for carbonate precipitation when the CO_2-rich gas encounters fluids during upward migration in the basin. However, when the buffer capacity of the host rock is exceeded, it is possible to generate high concentrations of unbuffered CO_2. This may provide a possible mechanism by which to generate a flux of CO_2 in a basin with a steep thermal gradient.

Interestingly, the volatile content of the Tom and Jason vent fluids are similar to those presented by Gaboury (2013) for orogenic gold systems. Gaboury (2013) argues that the high CO_2 content can be generated via degradation of ethane (C_2H_6):

$$2. \qquad C_2H_6 + 2H_2O \leftrightarrow CO_2 + CH_4 + 3H_2$$
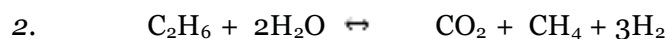
Importantly, the products of reaction (2) are favoured under oxidising conditions. Furthermore, short chain hydrocarbons can also be important for sulphate reduction (Joye et al., 2004), and so they may form an important contribution to the reduced sulphur budget of the hydrothermal systems at Macmillan Pass. If reaction (2) were occurring locally within the vent, it is possible that high concentrations of CO_2 could have been trapped immiscibly with the metal transporting fluid. Pressure release, such as during the failure of the host rock during the development of stockwork veins, may have been particularly important; were this to result in boiling (and the release of H_2), CO_2 generation via reaction (2) could be greatly enhanced.

4.5.3. Fluid inclusion volatile content

In this study, there is clear evidence of primary CO_2-bearing inclusions in barytocalcite that are closely associated with sulphide precipitation. Unfortunately, barytocalcite is restricted to minor veinlets, and there was not enough material to sample for gas analysis. However, it was possible to sample quartz in three samples (TYK1-7, TYK-9 and 86A-37) from Stage 2 of the paragenesis, for which there was a clear paragenetic relationship with ankerite (Stage 1) and sulphides (galena and sphalerite). The additional samples were obtained from quartz veins that crosscut carbonate altered conglomerates underlying the vent complex. We would strongly argue, therefore, that the CO_2 in the hydrothermal systems at Macmillan Pass is a primary feature.

The mudstone at Macmillan Pass is organic rich, and there is evidence that the mineralisation overlying the vent complex formed via sub-seafloor replacement processes (Chapter 3). In this regard, hydrothermal activity at Macmillan Pass may have similarities to modern day, sediment covered ridge axes such as found in the

Guaymas Basin. As discussed in the previous section, the thermal degradation of organic matter results in the release of volatile components such as CO_2, but also methane, other short chain hydrocarbons, and H_2S to solution (Shock et al., 2013).

There are some interesting aspects to the gas content of fluid inclusions from Macmillan Pass. Notably, samples from conglomerates underlying the vent complex preserve greater alkene contents (alkane/alkene < 1) than those hosted in the organic rich mudstones (alkane/alkene > 1). Indeed, redox equilibria between alkanes and alkenes buffers fO$_2$ (Blamey, 2012):

$$3. \qquad C_nH_{2n+2} + 0.5O_2 \qquad \leftrightarrow \qquad C_nH_{2n} + H_2O$$

Therefore, in a buffered system where alkenes are dominant relative to alkanes, the fluid is more oxidizing. The correlation between lithology and alkene vs. alkane content suggests there was a local control on fluid redox.

Hydrocarbons in sedimentary environments are most likely sourced from biogenic (e.g. Hinrichs et al., 2006) or thermogenic processes (Cruse and Seewald, 2006), the latter of which is associated with higher concentrations of longer chained alkanes. It is also possible to produce short chain hydrocarbons via abiogenic processes (Fischer-Tropsch synthesis; FTS), which involve the reduction of oxidized C-bearing species (CO_2, CO, HCO_3^- etc.) by H_2 produced during fluid rock interaction (McCollom and Seewald, 2007). The relative abundance of reaction products during FTS corresponds to a log-linear decrease in abundance with increasing C-number. However, similar distributions can be produced via thermogenic processes, with Cruse and Seewald (2006) noting that increasing C_1 / (C_2+C_3) ratios can be produced with increasing thermal stress, whereby degradation reactions transform longer chain hydrocarbons to

short chain products.

In Figure 4.8A, there is a general negative correlation between C_n and decreasing abundance, which is consistent with either FTS or thermogenic processes. However, only one sample (TYK1-9, Q2) preserves a straight-line trend. The thermogenic alteration of organic matter produces mostly alkanes, whereas FTS reactions produce both alkanes and alkenes (Blamey and Norman, 2002). The sample that preserves the most characteristic FTS C_1-C_4 distribution contains mostly alkanes, with only minor butene and propane.

A perplexing component in some of the profiles relates to anomalous propane concentrations, the origin of which is unknown. There have recently been reports of unusual sulphate reducers that preferentially utilize ethane (C_2H_6) over propane (Jaekel et al., 2013; Adams et al., 2013); therefore, it remains to be seen whether these anomalous profiles represent the influence of processes in the deeper biosphere. From these profiles alone it is not possible to distinguish between thermogenic and abiogenic processes, although the other evidence for organic matter alteration by TSR (section 4.5.2) suggests it was the former that was most important.

All samples, including those from veins in conglomerates underlying the vent complex, preserve a negative correlation between N_2/Ar and Ar/He (Figure 4.8B). Blamey and Norman (2002) explained this trend to correspond with volatiles related to calc-alkaline magmatism, whereby meteoric water, which has an air saturated N2/Ar value around 38, evolves towards magmatic values that exceed 100 (Giggenbach, 1996). However, in the absence of clear magmatic activity at Macmillan Pass, the enhanced N_2 content of these analyses can be more readily explained by organic carbon alteration. High Ar/He ratios in analyses of modern coral have been

142

attributed to the low concentration of He in air-saturated water (Azmy and Blamey, 2013). Therefore, the negative correlation between N_2/Ar and Ar/He could represent a hydrothermal fluid within components derived from mixing with meteoric water and also organic matter alteration. It is interesting to note that all samples fall on this trend, including the quartz veins beneath the vent complex, and those within the vent complex, which suggests their volatile content is linked by similar processes.

4.5.4. Mineral stability modeling

Notably, siderite, not ankerite is the main carbonate phase in Stage 2, and pyrrhotite is a major component of the sulphide assemblage. The precipitation of pyrrhotite represents a shift to more reducing conditions relative to the pyrite-bearing Stage 1 assemblage. Whether Stage 2 formed from a different pulse of hydrothermal fluid (relative to Stage 1), or during interaction of the hydrothermal system with an organic rich host rock is an important question to consider. How these mineral assemblages compare to predictions made by previous modeling (e.g. Cooke et al. 2000) and studies conducted in modern day sediment-covered ridge systems (Guaymas Basin; Cruse and Seewald, 2001) will provide valuable information about the geochemistry of fluids responsible for CD-type systems. Thermodynamic modeling can be a valuable tool for evaluating the geochemical conditions over which minerals are stable. The mineral assemblages that are preserved during Stage 1 and 2 may therefore record information about the fluids from which they precipitated, and how fluid chemistry evolved during hydrothermal activity.

Stage 1. The Stage 1 assemblage is relatively simple, and the constraints on fluid temperature (216 to 266°C) and the relative timing of ankerite and pyrite precipitation

are useful modeling parameters. The fluid was also likely to have been acidic, considering the level of the host rock alteration that is observed in most samples. This is supported by potassium loss from mudstones proximal to mineralisation (Chapter 2), which suggests a fluid buffered by the muscovite-kaolinite mineral assemblage (Yardley, 2005). For a fluid between 225 and 275°C and chloride content of 0.1 m (7 wt.% equiv. NaCl), this corresponds with a pH between 4.2 and 4.3 (Yardley, 2005).

A hydrothermal fluid with a sulphur budget buffered by a pyrite-pyrrhotite mineral assemblage ($\Sigma S = 10^{-2.8}$; Tornos and Heinrich, 2008) will not precipitate pyrite at temperatures greater than 275°C, and may require either cooling and / or the addition of reduced sulphur to precipitate sulphides. As iron content increases, ankerite precipitation becomes more endothermic (Radha and Navrotsky, 2013); this, together with the fluid inclusion microthermometric data provides evidence of cooling during Stage 1. In Figure 4.12 a pH—log$f$O$_2$ diagram shows the stability of Fe-bearing minerals at 250°C (see figure caption for modeling details). Pyrite is the only Fe-sulphide phase present in the Stage 1 assemblage, which according to Figure 12 provides constraints on the fO$_2$ of the fluid entering the vent to be between 10^{-35} and 10^{-40} at 275°C to 225°C. This fO$_2$ is consistent with the estimations made of hydrothermal fluids from the Guaymas Basin (Cruse and Seewald, 2001), and means that in the Stage 1 fluid, carbon will have been present as oxidized species (CO_2, HCO_3^-) and not as CH_4.

Stage 2. In Stage 2, siderite becomes the stable Fe-carbonate in the vent complex and there is a further trend towards decreasing temperatures (<250°C to ~100°C). Cooke et al. (2000) suggest that the occurrence of siderite is a distinguishing feature of Australian CD-type systems, commenting that it is absent in Selwyn Basin systems. In

their detailed account of siderite stability, Cooke et al. (2000) also suggest that in fluids above 300°C siderite is stable in both relatively oxidizing (pyrite-hematite) and also reducing (pyrite-magnetite) assemblages, whereas at <200°C stability is limited to more oxidizing conditions. Therefore, if all other parameters are equal (Fe, ΣC, ΣS), at temperatures <200°C it is fO_2 that provides the dominant control on whether siderite coexists with pyrite. Cooke et al. (2000) argue that the absence of siderite in Selwyn Basin CD-type deposits is evidence that the fluids responsible were more reducing than in the Australian systems. However, in the vent complexes at Tom and Jason, siderite is clearly present in a Stage 2 vein assemblage with pyrrhotite and pyrite (Figure 4.4C, E and F), which formed at temperatures less than 220°C (Figure 4.7). Furthermore, siderite also occurs as a transitional phase between Stage 1 and 2 (Figure 4.6). Therefore it is also necessary to consider how changing ΣC and ΣS impact siderite stability. It is possible to enhance the stability of siderite in low sulphur fluids (ΣS budget $< 10^{-3.5}\,m$). This is lower than the concentration of sulphur expected in fluids buffered by a pyrite-pyrrhotite assemblage (e.g. Tornos and Heinrich, 2008), and would imply the Macmillan Pass fluids did not equilibrate with reducing lithologies during ascent from deep within the basin.

However, it may be more relevant to evaluate the effects of increasing CO_2 on siderite stability, as the analyses of Stage 2 quartz indicate CO_2 derived from the host rock was an important, but variable component of the vent fluid. Considering the evidence of TSR in the vent complexes, it is therefore likely that the ΣC budget of the MacPass fluids evolved to higher concentrations during alteration of organic matter. Indeed, high concentrations of dissolved CO_2 (0.5 m) have been documented in modern fluids, produced via decarboxylation reactions during the alteration of organic

rich sediments at high temperature (Seewald et al. 1990; Seewald et al. 1994). In Figure 4.12, it is shown that a zone of siderite stability can be produced along the pyrite-magnetite boundary in fluids with an increased ΣC budget ($0.5m$).

There is abundant evidence that pyrrhotite, not pyrite, becomes the stable Fe-sulphide phase during Stage 2. In Figure 4.12, magnetite is stable before pyrrhotite with decreasing fO_2. However, with decreasing temperatures the stability field of magnetite is limited to a more alkali pH (>7) and siderite is no longer stable. The pyrite-pyrrhotite transition in Stage 2 is consistent with experimental work that has produced more reducing fluids during sediment alteration at high temperature (Seewald et al. 1990). This feature in the vent complexes at Macmillan Pass likely represents the consumption of SO_4^{2-} during TSR.

4.5.4. Metal transport

Salinity provides the most important control on the solubility of base metals in hydrothermal fluids (Yardley, 2005). The number of salinity measurements produced in this study indicates that, at least for the Stage 2 fluid, salinity was relatively low (<6 wt. % NaCl equiv.), broadly consistent with the earlier studies of Gardner and Hutcheon (1985) and Ansdell et al. (1989).

Base metal solubility negatively correlates with H_2S, and so transport of Pb and Zn in fluids associated with reducing lithologies (e.g. pyritic mudstones) has formed a key topic of debate (Cooke et al. 2000; Tornos and Heinrich, 2008). In the thermodynamic models of Cooke et al. (2000) and Tornos and Heinrich (2008), there is general consensus that base metal transport in reducing fluids ($H_2S > SO_4^{2-}$) requires high temperatures (>250°C), acidity (pH < 4.5) and moderate salinities (9 wt. % NaCl).

146

The temperature (≤275°C) and salinity (<6 wt. % NaCl equiv.) of the Macmillan Pass fluids are broadly consistent with the models of Cooke et al. (2000) and Tornos and Heinrich (2008), and at greater depths in the basin may have been hotter and more saline, considering the effects of cooling and dilution upon mixing with diagenetic fluids.

For the Macmillan Pass fluids, the unmodified composition of fluids entering the vent complex is probably best represented by the Stage 1 mineral assemblage. Considering the predominance of pyritic mudstones in the stratigraphy of the Selwyn Basin, it is reasonable to assume that the redox state (log–fO_2) of the fluid was close to the pyrite-pyrrhotite-magnetite (PPM) mineral buffer (Yardley, 2005; Tornos and Heinrich, 2008). Importantly, pyrite is the only Fe-sulphide phase present in Stage 1, which limits the fO_2 of the Stage 1 fluid, to between 10^{-36} and 10^{-33} at 275°C (Figure 4.12). In the fO_2 window defined by the Stage 1 assemblage, it is clear that even with modest salinity these fluids were capable of transporting in excess of 100 ppm of Pb and Zn. Sulphide precipitation occurred during fluid cooling, pH increase and interaction with reduced sulphur generated by TSR. There is no evidence that fluids at Macmillan Pass were highly saline (>10 wt. % NaCl equiv.), as with metal-rich basinal brines (e.g. Carpenter et al. 1974). Rather, a combination of high temperature (≤275°C), low pH (<4.5) and fO_2 (>10^{-36}) combined to maintain enhanced base metal solubilities.

4.5.5. Summary – evolving geochemical conditions

In summary, the development of Stage 1 and 2 mineral assemblages occurred during fluid cooling, from ~275°C to 175°C, and temperatures decreased further still at

shallow levels of the vent (~100°C). Along with temperature, alteration of organic carbon in the carbonaceous mudstones provided a first order control on the development of mineral assemblages during Stages 1 and 2. Evidence of TSR (pyrobitumen, CO_2-rich fluid inclusions, sulphur isotopes) is consistent with temperatures in excess of 250°C during Stage 1, and likely led to the buildup of H_2S, forming an important pathway of sulphide precipitation during Stage 2. It is important to highlight that the transition between Stage 1 and 2 mineral assemblages, particularly with respect to siderite and pyrrhotite, reflects the interaction of the hydrothermal fluid with organic rich mudstones. It is therefore useful to evaluate the REE composition of ankerite and siderite to further assess the evidence for fluid rock interaction and and to assess what other components were derived locally from the host rock.

4.5.6. Rare earth elements and yttrium content

The REE composition of ankerite and siderite enables further evaluation of inputs into the vent complex. The range of ankerite sample types (host rock dominant, host rock alteration and stockwork veining) should allow evaluation of the source of REEs, i.e. hydrothermal, host rock or seawater modified to varying degrees during diagenesis and development of the hydrothermal system.

In most analyses of ankerite, there is a broadly defined positive correlation between total REE abundance (ΣREE) and Y/Ho ratios (Figure 4.13). The similar geochemical behavior of Y and Ho means that most igneous and clastic rocks preserve chondritic Y/Ho ratios (26-28; Bau and Möller, 1992). Super-chondritic Y/Ho ratios are characteristic of seawater, due to the preferential complexation of REEs over Y by

organic matter and Fe-oxides (Y/Ho = 44-78; Bau and Dulski, 1995). By corollary, the low abundance of REEs in seawater (10^{-12} mol kg^{-1}; Elderfield and Greaves, 1982) increases in diagenetic pore fluids when these organic and Fe-oxide complexes break down (Haley et al., 2004). Therefore, carbonates precipitating in diagenetic environments are enriched in REEs (e.g. Himmler et al., 2010; Zhang et al., 2014; Jakubowicz et al., 2015) compared to carbonates precipitated directly from seawater (e.g. Sholkovitz and Shen, 1995), but both will preserve super-chondritic Y/Ho ratios.

It is possible that REEs in ankerite are sourced partly from host rock contamination, considering the destructive nature of Stage 1 alteration. Relative to seawater, organic rich mudstones are enriched in REEs (e.g. NASC; Gromet et al. 1984), and ablation of any remnant host rock would contaminate the ankerite analyses. However ΣREE abundance is negatively correlated with Ti (Figure 4.13A), which can be considered a proxy for host rock input, and so host rock contamination is not considered important.

Alternatively, it is possible that the hydrothermal fluid became enriched in REEs during fluid-rock interaction with underlying strata. However, unless the hydrothermal fluid equilibrated with underlying mudstones at unreasonable W/R ratios ($>10^5$ to 10^6), it is unlikely to have inherited high concentrations of REEs (Michard and Albarède, 1986; Bau, 1991). Relative to pristine seawater, modern vent fluids are enriched in REEs (Figure 4.10A), and do not approach the concentrations that are encountered in diagenetic pore fluids. The most plausible explanation for the positive correlation between ΣREE and Y/Ho, therefore, involves diagenetic fluid input into the vent complexes at Macmillan Pass. The permeability of the host rock at Macmillan Pass was likely to have been high, considering the partially lithified state

during the development of hydrothermal activity (Chapter 2). This will have enhanced the potential for entrainment and mixing of diagenetic fluids into the hydrothermal system.

4.5.7. Rare earth element fractionation

The fractionation of REEs occurs due to differences in mass and ionic radii, which results in systematic behavior through complexation or ionic substitution during co-precipitation (Elderfield and Greaves, 1982; Bau et al., 1992). This predictable behavior means that collectively, normalised REE data can reveal valuable information concerning fluid composition and flow history. For example, the positive Eu-anomalies, LREE enrichment and chondritic Y/Ho ratios that characterize modern vent fluids provide evidence of high-temperature seawater alteration of plagioclase (Klinkhammer et al., 1994; Bau and Dulski, 1999; Douville et al., 1999). However, the Y+REE$_N$ profiles in carbonates presented in this study contrast with modern day vent fluids (Figure 4.10A). Despite large positive Eu-anomalies, there are varying degrees of LREE depletion and enrichments in the MREEs above NASC. The origin of these features will now be evaluated to derive further information about the geochemistry of the hydrothermal fluid.

LREE depletion and MREE enrichment in ankerite and siderite: compared to all other reference reservoirs, the Y+REE$_N$ are characterised by varying degrees of LREE depletion (see Figure 4.10B to E). Fractionation of LREEs can reflect carbonate speciation, and therefore pH, as carbonate ions (CO_3^{2-}) preferentially complex the HREEs (Bau et al., 1992). As a result, an acidic fluid will become enriched in HREEs and depleted in LREEs during fluid-rock interaction, and this will be inherited by any

subsequent carbonate phase precipitated.

Many samples also preserve subtle enrichments in MREEs, relative to HREEs (TYK2-20a, 86A-37 and 86A-35). This is a characteristic feature of REEs sourced from Fe-rich anoxic pore fluids (Johannesson and Zhou, 1999; Haley et al., 2004; Himmler et al., 2010; Birgel et al., 2011; Jakubowicz et al., 2015). As with the ΣREE and Y/Ho systematics discussed in the previous section, the REE fractionation trends inherit features of the hydrothermal fluid, which was likely acidic (LREE depletion), and also input from diagenetic fluids (MREE enrichment).

Positive Eu-anomalies: unlike the other trivalent REEs, europium is redox-sensitive and can be reduced to its more soluble divalent form in either strongly reducing fluids or at temperatures above 250°C (Sverjensky, 1984). This results in positive anomalies above the neighboring (Sm, Gd) trivalent REEs (see Figure 4.10). In modern vent fluids Eu-anomalies are produced through fluid-mineral exchange during dissolution and recrystallisation of plagioclase feldspar (in basalt), which is enriched in europium (Klinkhammer et al. 1994). The Eu-anomalies in ankerite are smaller compared to modern vent fluids (see Figure 4.10A), and in the absence of other features such as LREE enrichment, basalt alteration can be ruled out for the MacPass vent fluids.

It is possible that the Eu-anomalies developed during fluid rock interaction with feldspars in the immature rift clastics in the basal sequence of the Selwyn Basin. Indeed, similar lithologies are often postulated to be the source of Pb in CD-type systems (Everett et al., 1999). In this case, fluid circulation would span to far greater depths in the basin than with MOR systems. This may provide explanation for the absence of LREE enrichment, which is characteristic of plagioclase alteration in MORB. Alternatively, it is possible to produce positive Eu anomalies in highly

reducing, anoxic pore fluids (Jacubowicz et al. 2015). Considering the evidence presented for diagenetic input, it may not be possible to distinguish between the two sources of Eu-enrichment.

Y+REEs in Siderite: siderite samples, like the ankerite samples, (see Figure 4.9F), have LREE depletion and positive Eu-anomalies. In general, the $Y+REE_N$ siderite profiles are relatively similar to ankerite, but are depleted overall in Y+REE abundance. This is probably associated with the limited acceptance of Y+REEs into a non Ca-bearing mineral (Bau and Möller, 1992).

Stage 1 to Stage 2 Transition: interestingly, the ankerite analyses with the highest REE concentrations are situated proximal to Stage 2 veins. The clearest example of this is 86A-39, which preserves a large MREE bulge above NASC (Figure 4.10D). There are two important conclusions to draw from this: (1) it provides evidence that the Stage 2 event may have altered the trace and REE systematics of Stage 1 ankerite, and is perhaps not unexpected considering the metastability of dolomite and its susceptibility to recrystallise during fluid-mineral interaction (Warren, 2000); (2) samples with the strongest diagenetic signature (MREE bulge) occur proximally to Stage 2 mineral assemblages, therefore diagenetic input may have been a factor during the evolution of Stage 1 to Stage 2.

To summarise, the acidic nature of the fluids entering the vent is further supported by LREE fractionation. However there is also good evidence that the hydrothermal fluid derived much of its REE budget from organic matter in the host rock, and the lowest REE abundances are found in ankerite hosted in samples that are least altered (86A-35). Therefore the Y+REEs preserve evidence of some mixing component between a hydrothermal fluid and diagenetically modified seawater. This is consistent with the

volatile content of the fluid inclusions, and further supports the evidence of there being a local control on the evolution of mineral assemblages in the vent complex.

4.6. Conclusions

This study provides an example of how geochemical interactions between hydrothermal fluids and recently deposited sediments can be traced in CD-type systems from the geologic record. Importantly, we have shown that components derived from the organic-rich mudstone at a shallow basinal level impart a first order control on mineralogical evolution, and are comparable to processes operating at modern day sediment-covered ridge-crest hydrothermal systems (e.g. Guaymas Basin). Specifically, the thermogenic alteration of organic carbon and associated thermochemical sulphate reduction provide important sources of carbon (CO_2, CH_4, C_1-C_4 hydrocarbons) and H_2S respectively, which at Macmillan Pass has resulted in the formation of Fe carbonates and massive sulphide mineralisation. However, although the fluid entering the vent complex was reducing ($H_2S > SO_4^{2-}$), enhanced base metal solubility (1000-3000 ppm Zn, 300-1000 ppm Cu and 80-200 ppm Pb) was maintained in a high temperature (>275°C), acidic (pH < 4.5), and relative reducing ($fO_2 > 10^{-36}$) fluid. The most reducing mineral assemblages, where pyrite was subordinate to pyrrhotite and siderite was stable rather than ankerite, developed during interaction of the hydrothermal fluid with the organic-rich mudstone in a shallow subseafloor setting. Therefore these mineral assemblages cannot be used as a basis when calculating base metal solubilities in the fluid entering the vent complex. Sulphide precipitation occurred following the generation of reduced sulphur via TSR, with sulphate derived from seawater. This corresponds with the $\delta^{34}S$ values in

sulphides, which are consistent with fluid inclusion temperature constraints for the Stage 1 fluid and the associated kinetic fractionation of sulphur isotopes during TSR. Super-chondritic Y/Ho ratios and enhanced REE abundance in ankerite provide further evidence for the input of diagenetically modified seawater into the vent.

Tables and Figures

Table 4.1. Fluid inclusion gas analyses for quartz mineral separates from the Tom and Jason vent complexes. Data are reported in mole % as burst size weighted mean of the samples.

	TYK1-7	TYK1-9 (Q2)	TYK1-11 (Q1)	82-86A-22 (Q2)	82-86A-37 (Q2)	TYK1-9 (Q1)	TYK1-11 (Q2)	TY71-13 (Q2)
n	8	8	10	10	10	9	7	8
H_2 (mol. %)	0.000	0.001	0.000	0.001	0.000	0.000	0.001	0.000
He	0.000	0.000	0.000	0.000	0.000	0.000	0.000	0.000
CH_4	0.295	0.095	0.228	0.413	1.031	0.145	0.163	0.209
H_2O	74.15	91.16	53.68	40.66	58.38	78.29	75.83	69.46
N_2	0.379	0.384	0.534	1.208	1.022	0.352	0.398	0.667
H_2S	0.000	0.001	0.001	0.000	0.001	0.000	0.000	0.000
Ar	0.000	0.003	0.001	0.002	0.004	0.001	0.000	0.002
CO_2	24.98	8.35	45.18	57.54	39.40	21.06	23.46	29.28
SO_2	0.000	0.000	0.000	0.000	0.000	0.000	0.000	0.000
C_2H_4	0.096	0.000	0.000	0.000	0.000	0.136	0.132	0.219
C_2H_6	0.022	0.006	0.038	0.069	0.044	0.000	0.000	0.000
C_3H_6	0.001	0.000	0.000	0.000	0.000	0.011	0.005	0.001
C_3H_8	0.074	0.002	0.337	0.109	0.115	0.000	0.005	0.156
C_4H_8	0.001	0.000	0.001	0.001	0.001	0.001	0.000	0.001
C_4H_{10}	0.001	0.000	0.000	0.000	0.001	0.000	0.000	0.001
Benzene	0.001	0.000	0.001	0.000	0.001	0.000	0.000	0.001
Mols Gas	1.19E-08	4.26E-10	1.99E-08	8.41E-09	1.31E-08	6.99E-09	6.43E-09	1.60E-08
CO_2 / CH_4	84.8	88.1	198.4	139.4	38.2	145.4	144.2	140.2
N_2/Ar	892.7	213.4	541.1	462.0	806.8	830.8	652.6	367.1
Ar/He	1.3	95.6	1.6	8.5	21.2	6.4	1.4	6.7

Table 4.2. Summary of ankerite and siderite major element chemistry obtained via EPMA analysis.

		$FeCO_3$ wt. %	$MgCO_3$ wt. %	$CaCO_3$ wt. %	$MnCO_3$ wt. %
		Ankerite			
TU70-2	Mean	25.08	24.60	48.61	1.38
(n = 32)	St. Dev.	2.23	2.71	0.38	0.59
86A-35	Mean	21.27	28.16	49.29	1.19
(n = 36)	St. Dev.	2.18	2.19	0.28	0.08
86A-39	Mean	21.27	28.16	49.29	1.19
(n = 47)	St. Dev.	2.18	2.19	0.28	0.08
TYK2-20a	Mean	20.98	28.14	48.43	1.92
(n = 29)	St. Dev.	2.76	2.76	1.07	0.95
86A-37	Mean	24.27	25.04	49.16	1.32
(n = 20)	St. Dev.	2.12	2.49	0.24	0.28
		Siderite			
TU70-2	Mean	93.80	4.03	1.25	0.86
(n = 32)	St. Dev.	4.88	3.81	0.94	0.37
86A-39	Mean	89.37	3.27	3.24	3.82
(n = 6)	St. Dev.	1.24	1.88	1.29	1.92
86A-37	Mean	88.22	6.95	3.56	1.21
(n = 10)	St. Dev.	6.97	4.60	2.35	0.44

Table 4.3. Summary of δ^{34}S values (‰; VCDT) in mineral separates from the Tom and Jason vent complexes.

| Deposit | Vent Sulphides δ^{34}S (‰; V-CDT) | | | | | | | |
| | Tom | | | | Jason | | | |
Mineral	n	min	median	max	n	min	median	max
Galena	5	7.7	10.8	15.9	8	16.6	17.5	19.0
Sphalerite	3	10.6	10.7	12.5	3	18.6	19.0	19.0
Pyrite	7	9.6	12.1	19.3				

Figure 4.1. Hand samples from the Tom and Jason vent complexes. The variable colouration (bright orange versus pale orange) is due to how freshly cut samples were when the image was taken. A –Sample 86A-31 from Jason, with stockwork style ankerite veining crosscutting altered host rock. B – Sample TYK2-17 from Tom, with thick ankerite veins crosscutting highly altered host rock. C –Sample 86A-35 from a marginal vent setting at Jason, with more discrete stockwork style ankerite veins crosscutting unaltered host rock.

Figure 4.2. The deposit geology of Tom and Jason. Approximate locations of drill-hole collars and plunge direction for drill-cores are denoted by the labeled arrows. A – Geology of the Jason deposit, adapted from Turner (1989). B – Geology of the Tom deposit, adapted from McClay and Bidwell (1986).
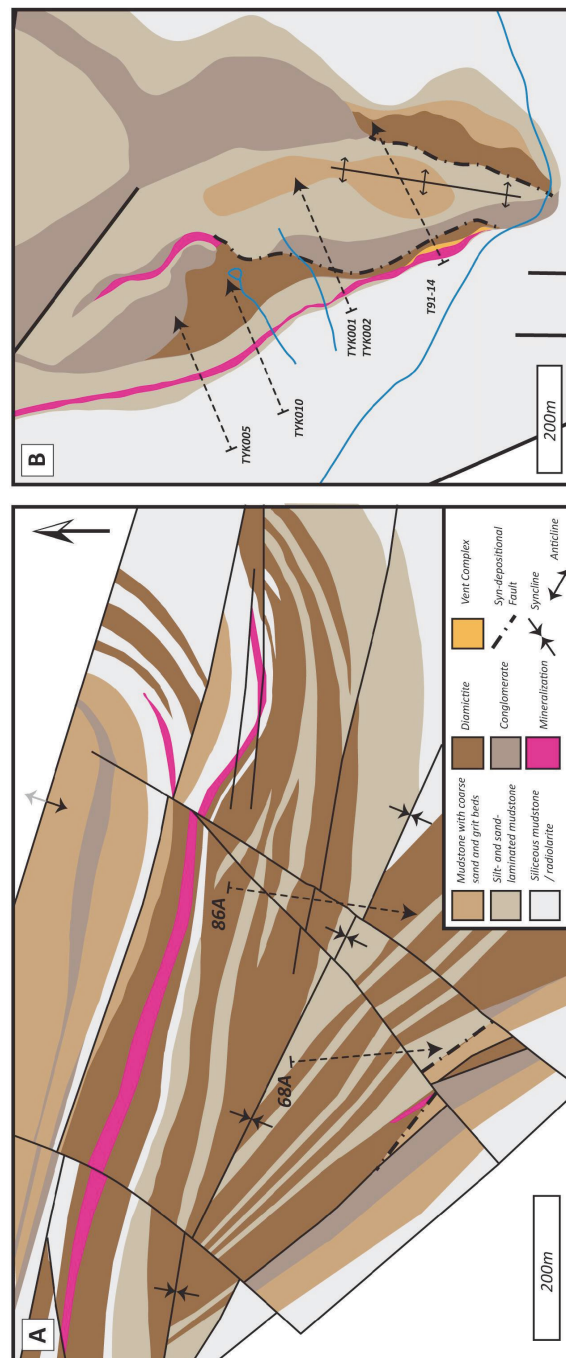
Figure 4.3. The mineralogical paragenesis for vent mineralisation at Tom and Jason. The grey boxes denote minerals targeted for fluid inclusion analysis.
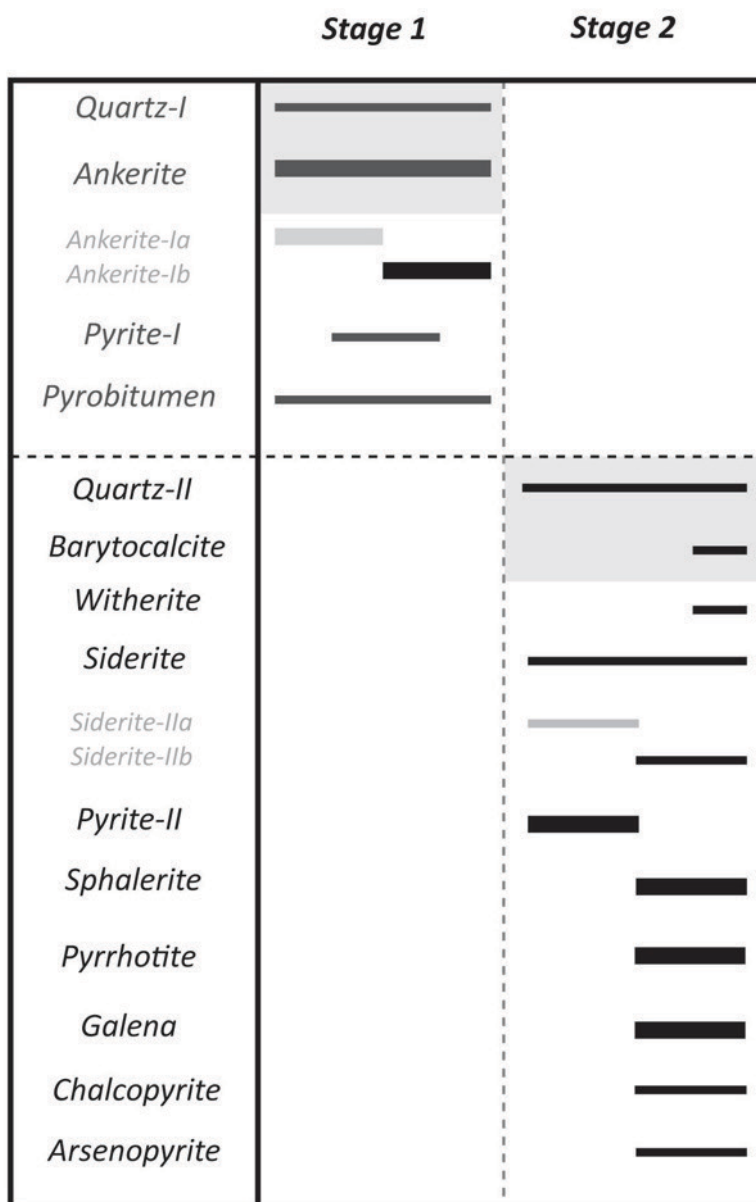
Figure 4.4. Petrography of the vent complexes at Tom and Jason. Mineral abbreviations as follows; pyrite (py), ankerite (ank), pyrobitumen (pyro), quartz (qz), siderite (sd), barytocalcite (ba-cc) sphalerite (sp), galena (gn) and chalcopyrite (ccp). A – Reflected light image of Stage 1 ankerite and pyrite (py-I) crosscut by Stage 2 pyrite (py-II). B – reflected light image of Stage 1 ankerite, quartz, pyrite and pyrobitumen. C – back scattered electron (BSE) image of Stage 2 vein assemblage consisting of siderite and pyrite (py-II) crosscutting Stage 1 ankerite. Notice the lighter, more Fe-rich ankerite (ank-Ib). D – reflected light image of Stage 2 vein assemblage consisting of chalcopyrite, pyrite (py-II), pyrrhotite and galena crosscutting Stage 1 ankerite (ank-1). E – BSE image of Stage 2 assemblage crosscutting Stage 1. F – BSE image of Stage 2 barytocalcite (ba-cc), Sd and Gn vein assemblage. G – reflected light image showing brecciation of Stage 1 pyrobitumen by Stage 2 mineralisation. H – reflected light image showing Stage 2 mineral assemblage overprinting pyrobitumen. Notice how pyrrhotite forms blebs within the galena.
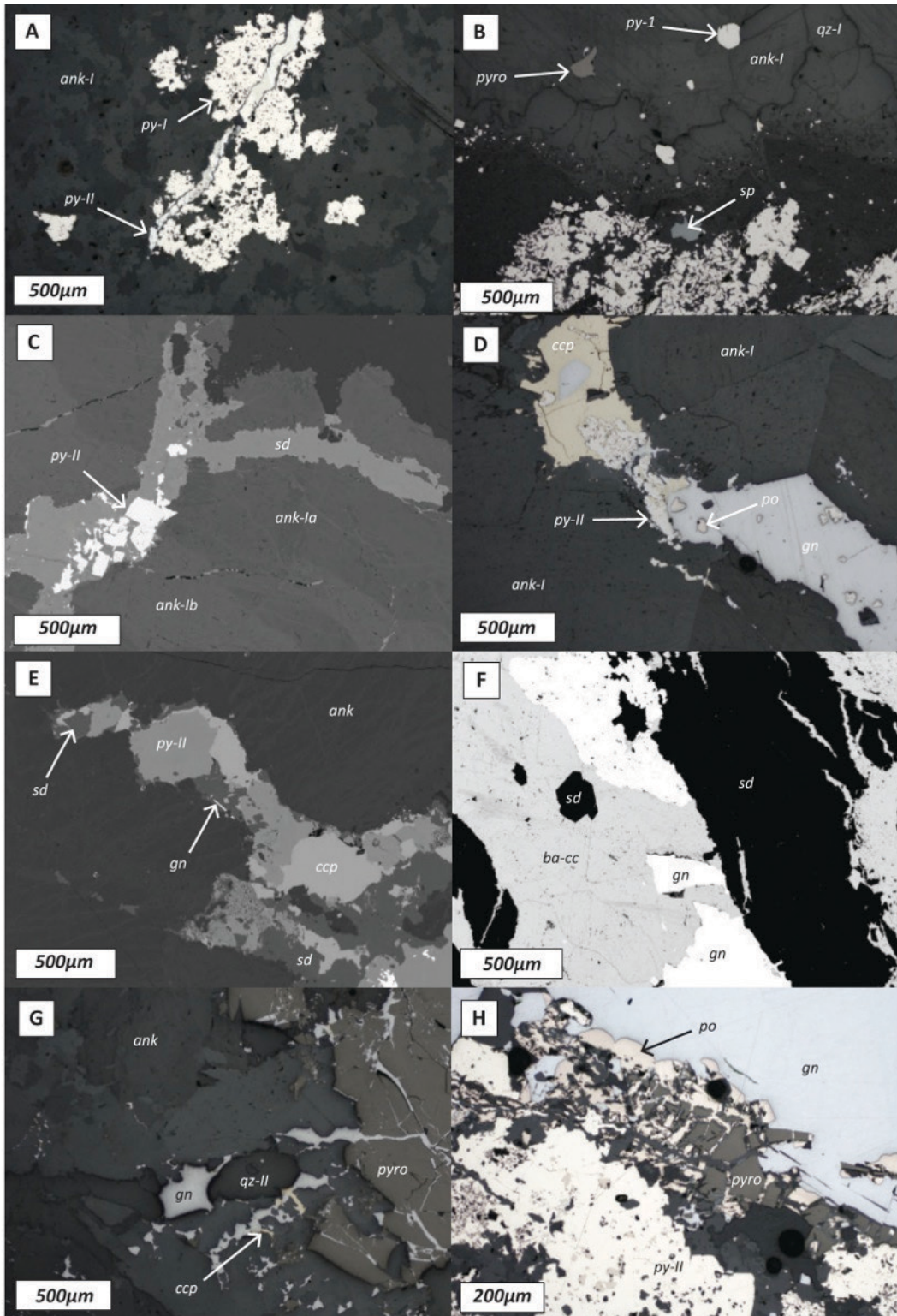
Figure 4.5. Transitional Stage 1 to Stage 2 texture. A – reflected light image of Stage 1 ankerite (ank) and pyrite (py-I) with Stage 2 siderite (sd) precipitating in vuggy pore space. B – BSE image of area highlighted in A, showing association of sphalerite (sp) with siderite.
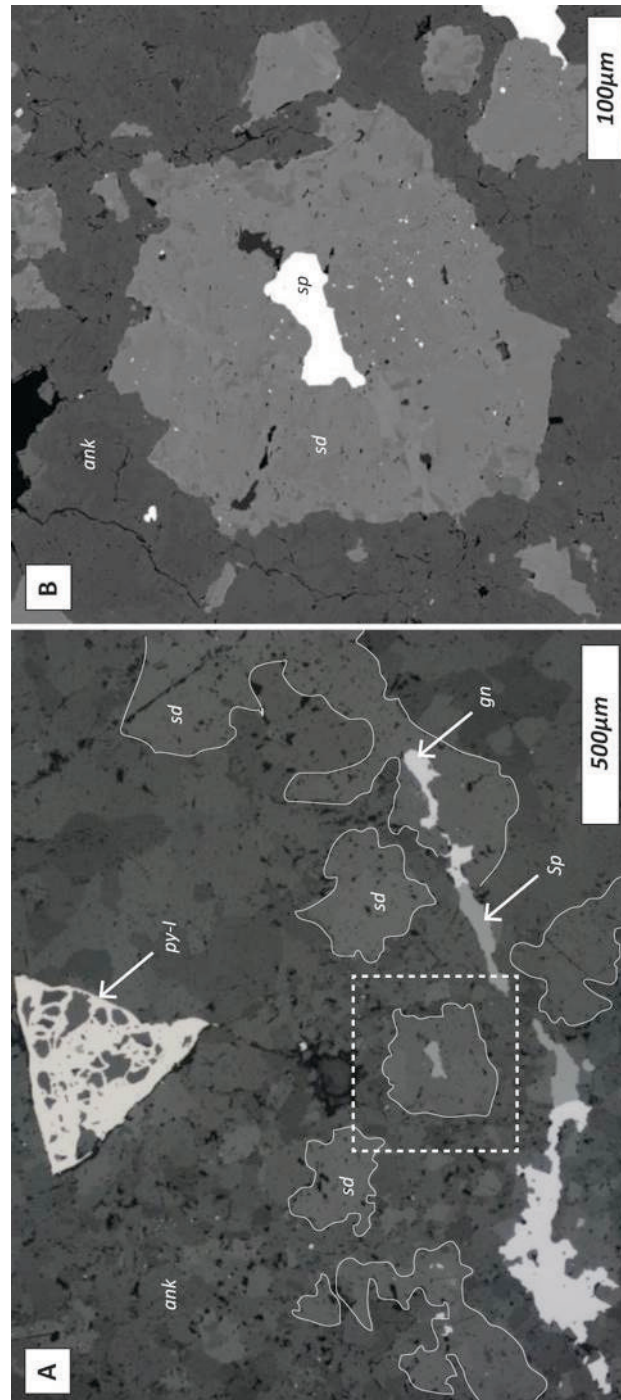
Figure 4.6. Fluid inclusions from the Tom and Jason vent complexes. A – image of a fluid inclusion wafer from sample 86A-22 (Jason deposit). The sample shows a clear crosscutting relationship of Stage 1 ankerite by a Stage 2 vein assemblage (quartz, qz; galena, gn). B – primary fluid inclusion assemblage in ankerite from area highlighted in A; red circles are fluid inclusions from which microthermometric data were obtained. C – fluid inclusion assemblage in quartz from area highlighted in A. D – primary fluid inclusion assemblage in ankerite (86A-22). E – fluid inclusion assemblage in bartyocalcite (ba-cal) from a Stage 2 vein also containing siderite (sd) and galena (gn). Sample from TU70-2. F – CO_2-rich inclusions coexisting with 2-phase inclusions in barite from a transitional vent sample (TYK2-14).
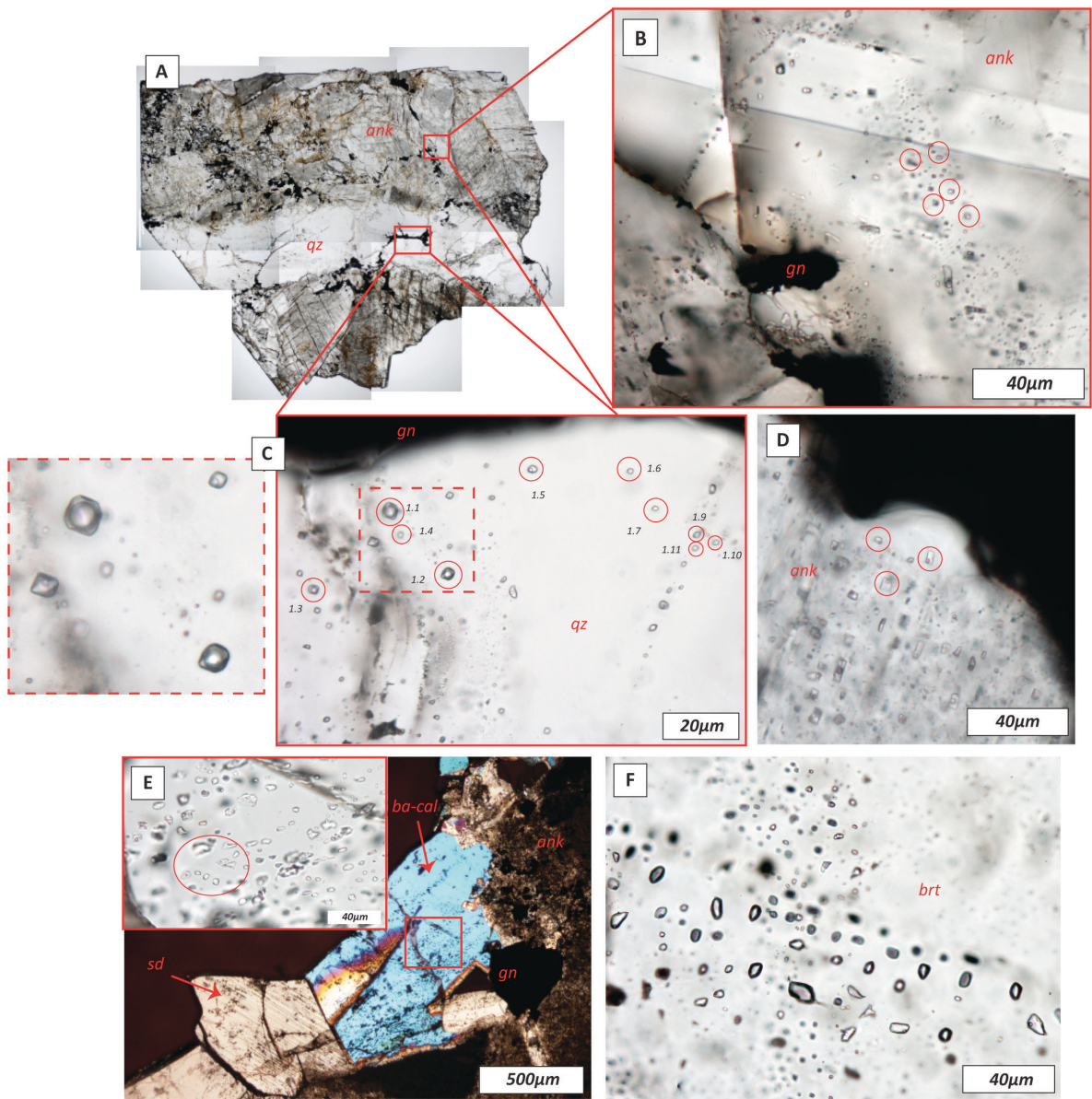
Figure 4.7. Homogenisation temperatures (T$_h$; °C) of fluid inclusions. Analyses of 2-phase inclusions hosted in Stage 1 ankerite and Stage 2 quartz and barytocalcite. Note the inverted y-axis. Range of temperatures from previous studies (Gardner and Hutcheon, 1985; Ansdell et al., 1989) denoted by grey bars.
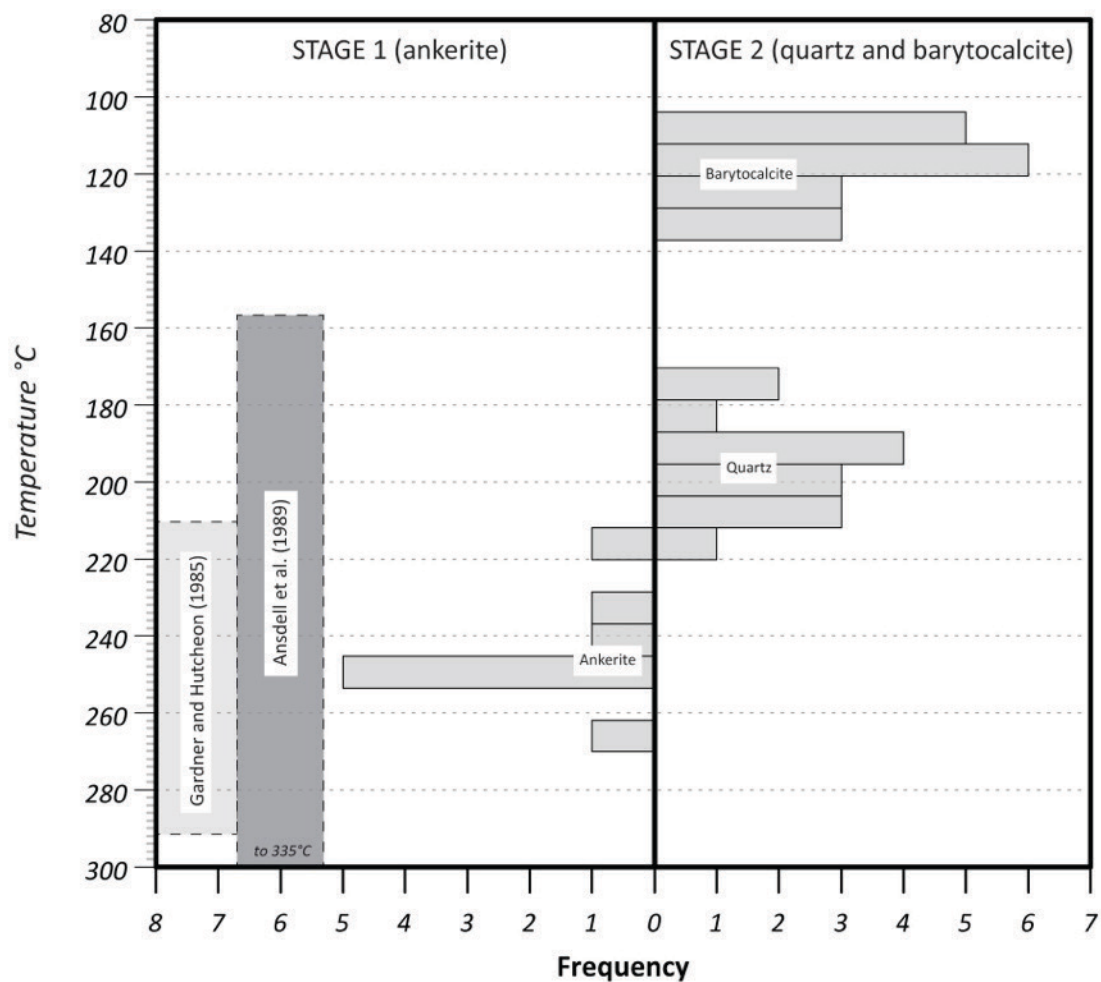
Figure 4.8. The volatile composition of fluid inclusions in quartz: A – The abundances of C_1 to C_4 short chain hydrocarbons (mol. %), B – N2/Ar vs. Ar/He (mol. %).
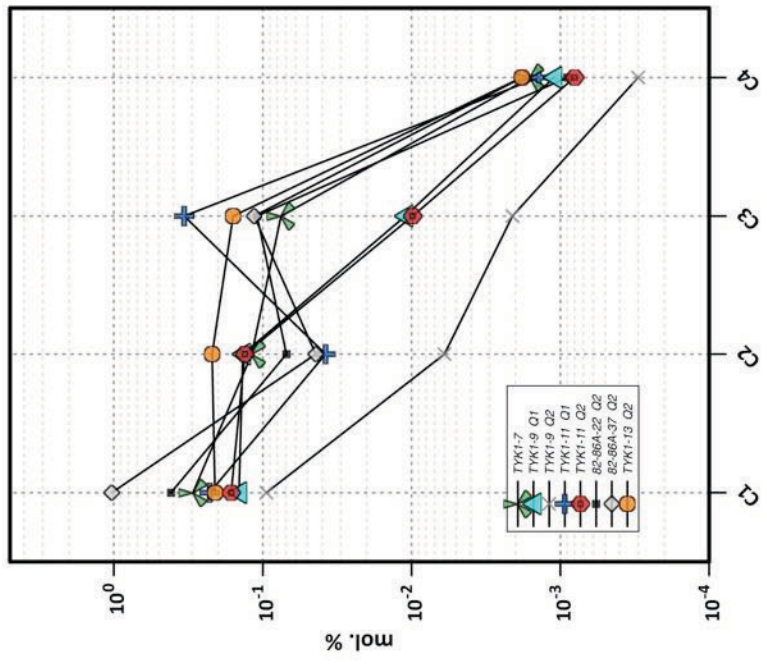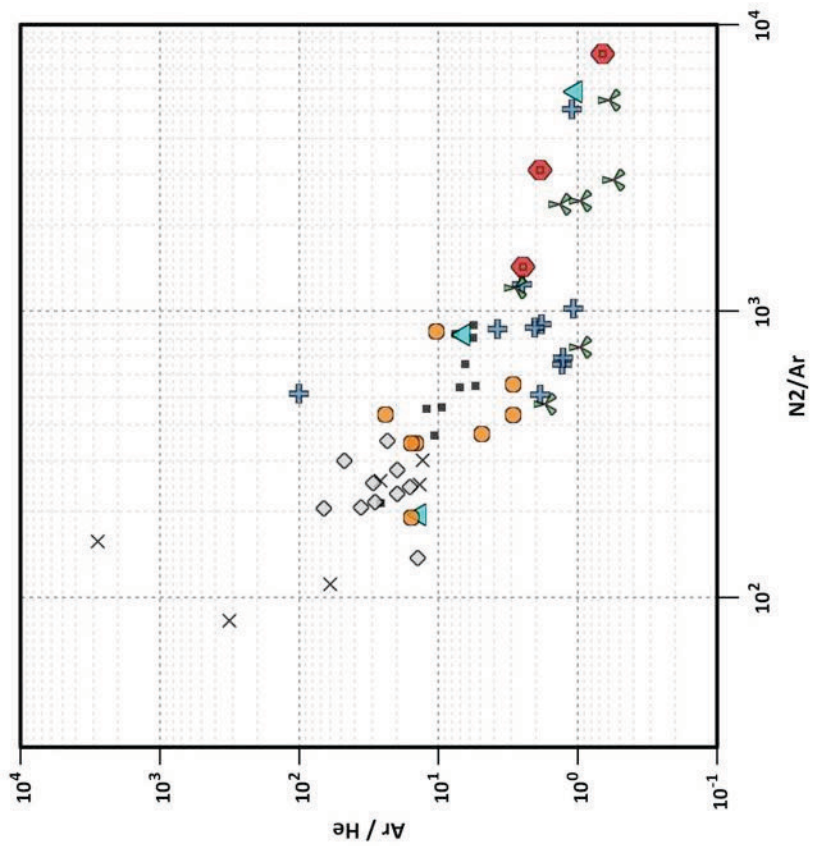
Figure 4.9. Cross-plots of carbonate major element chemistry (EPMA; wt. %). A – $FeCO_3$ vs. $MgCO_3$ for ankerite. B - $FeCO_3$ (wt. %) vs. $MgCO_3$ (wt. %) for siderite. $FeCO_3$ vs. $MnCO_3$ for ankerite.
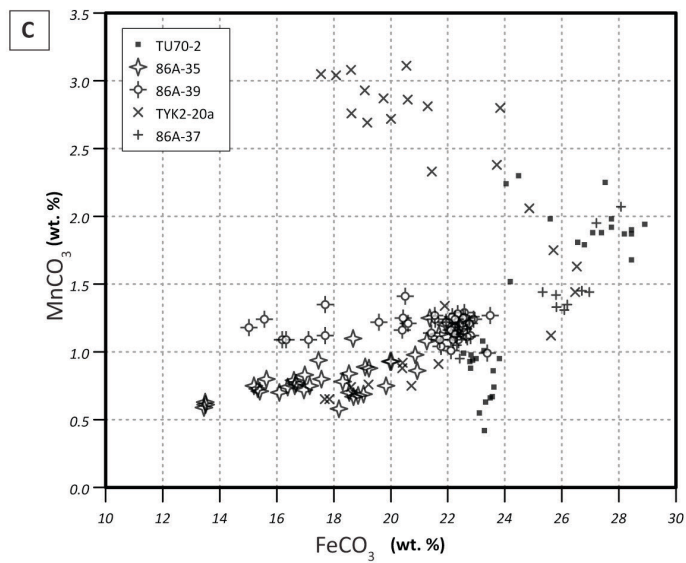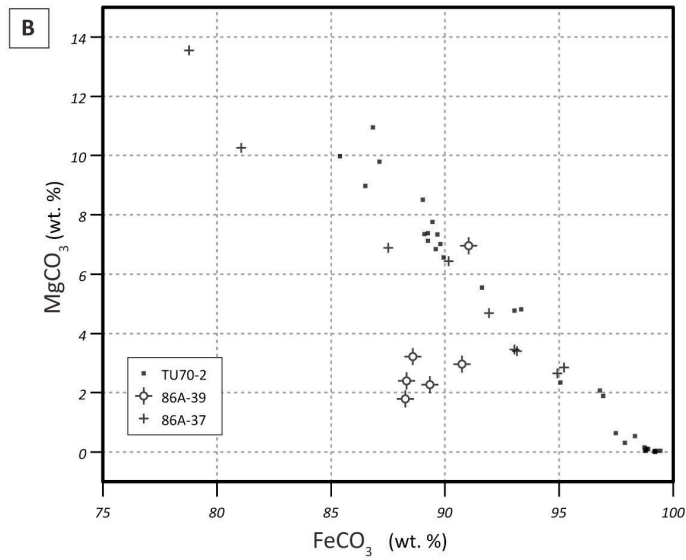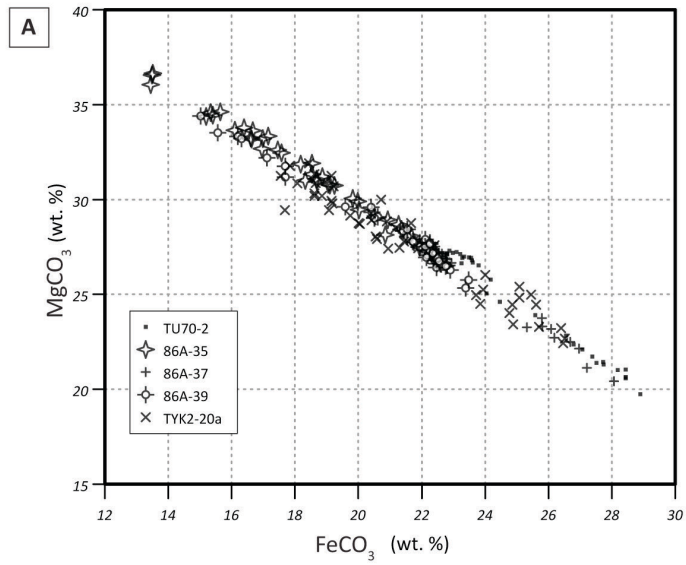
Figure 4.10. Chondrite normalised rare earth element profiles from LA-ICP-MS analysis of carbonates. A – Chrondrite-normalized REE data for seawater (blue line) (Alibo and Nozaki, 1999) and modern vent fluids (black line) (Bau and Dulski, 1999). B to F - chondrite-normalized plots of REE data from vent samples at Tom (TU70-2, TYK2-20a) and Jason (86A-35, 86A-37, 86A-39). Also included is the North American Shale Composite (NASC; Gromet et al. 1994; thick black line). Grey lines are analyses of ankerite-1a, orange lines are ankerite-1b and dark red is siderite.
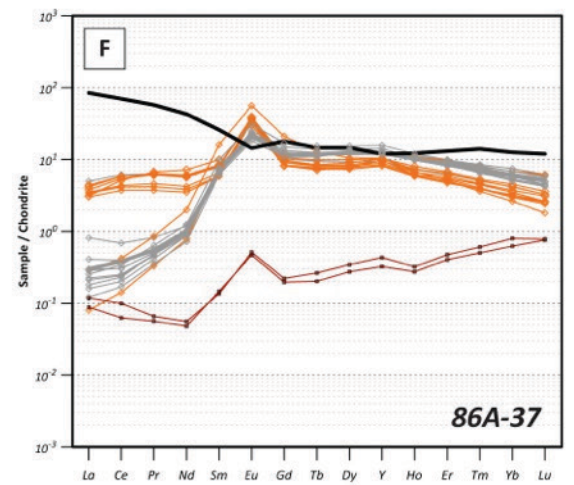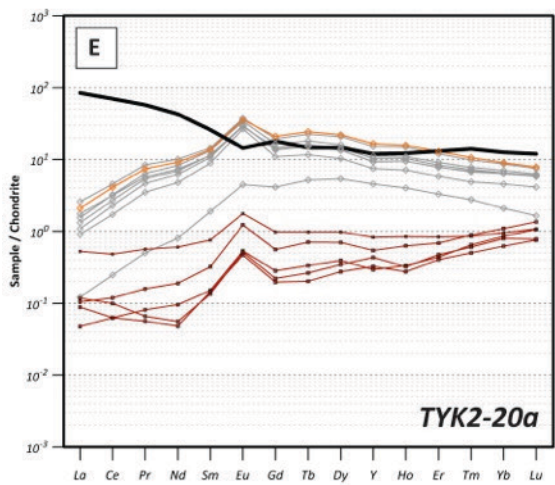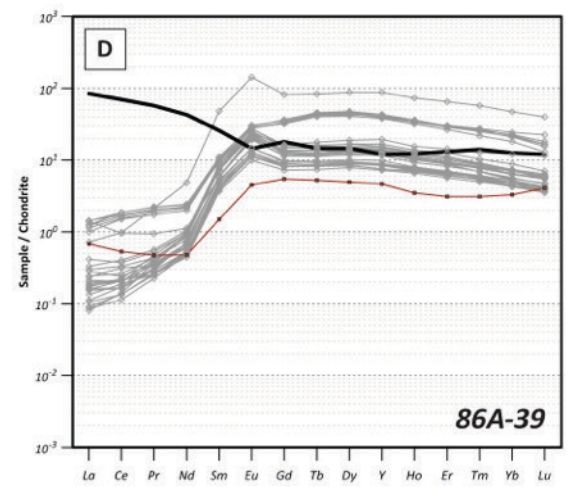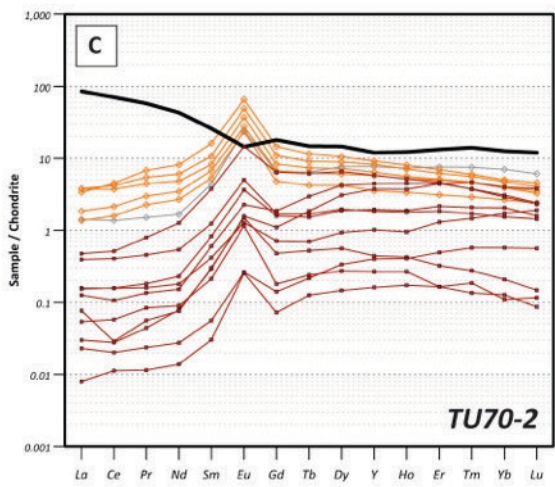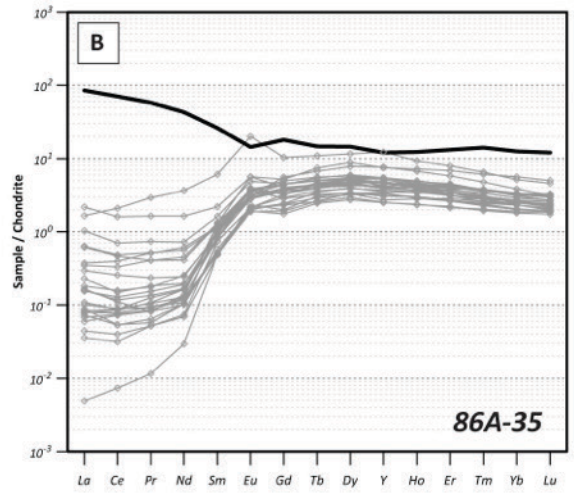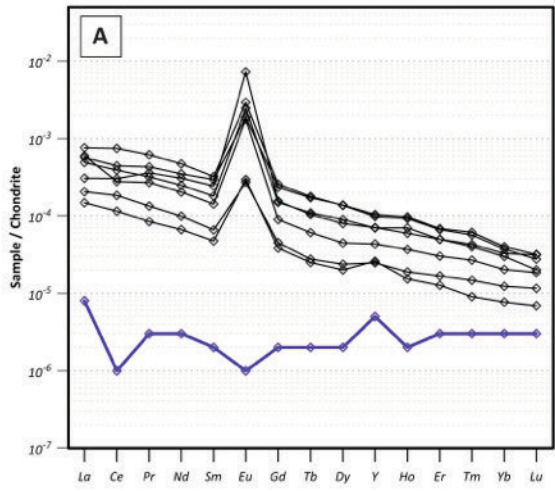
Figure 4.11. Box and whisker plot of $\delta^{34}S$ values (‰; V-CDT) for mineral separate analyses of sulphide minerals (pyrite, py; galena, gn; sphalerite, sp) from the Tom (Tv) and Jason (Jv) vent complexes. Boxes encompass 25th to 75th percentile with whiskers extending to outliers and horizontal line representing the median value. Assuming thermochemical sulphate reduction (TSR) of Late Devonian seawater sulphate ($\delta^{34}S$ = +24‰; John et al. 2010), theoretical $\delta^{34}S_{sulphide}$ lines have been calculated for different temperatures (degrees °C) using the equation of Kiyosu and Krouse (1990).
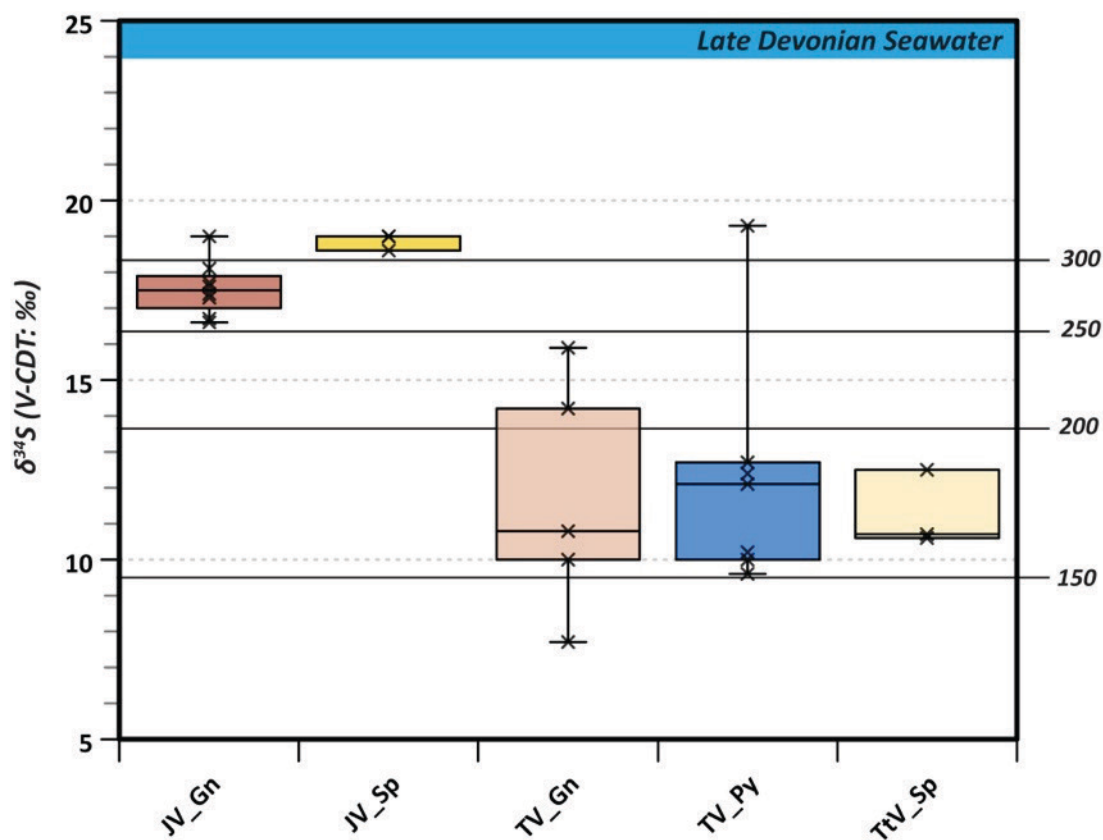
Figure 4.12. pH—log(fO_2) plot for the Stage 1 vent complex mineral assemblage. Calculated using Geochemists Workbench for a fluid with the compositional constraints of Cooke et al. (2000) at 250°C: aFe^{2+} = 10$^{-2.2}$, aH$_2$S = 10^{-3}, aCO$_{2(aq)}$ = 10$^{-0.6}$. The shaded area denoting the field of siderite stability was produced when recalculated with greater CO$_2$ content (aCO$_{2(aq)}$ = 10$^{-0.3}$). Solubility contours for Pb and Zn are shown, along with the pH of a fluid buffered by kaolinite-muscovite (at 6 wt. % NaCl equiv.).
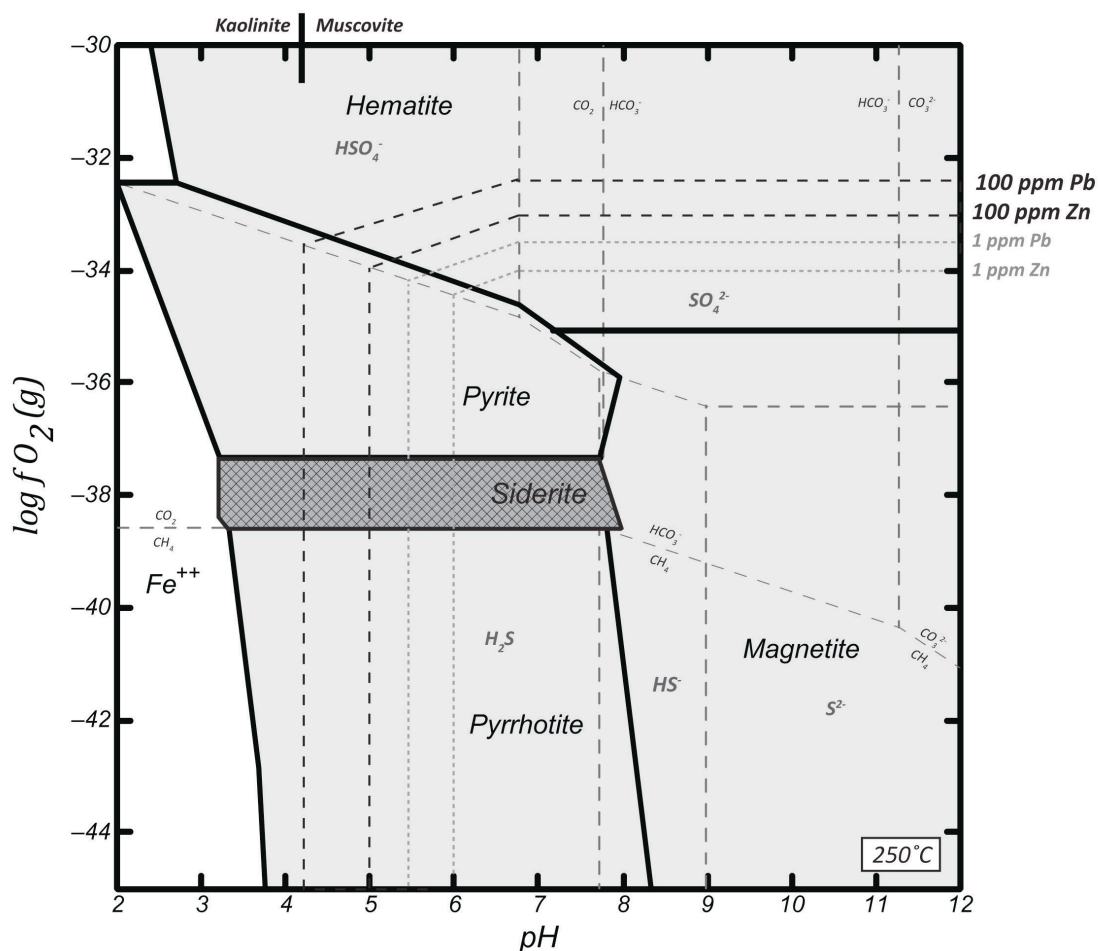
Figure 4.13. A – Ti (ppm) vs. ΣREE (ppm) for ankerite. B – ΣREE (ppm) vs. Y/Ho (ppm) for ankerite.
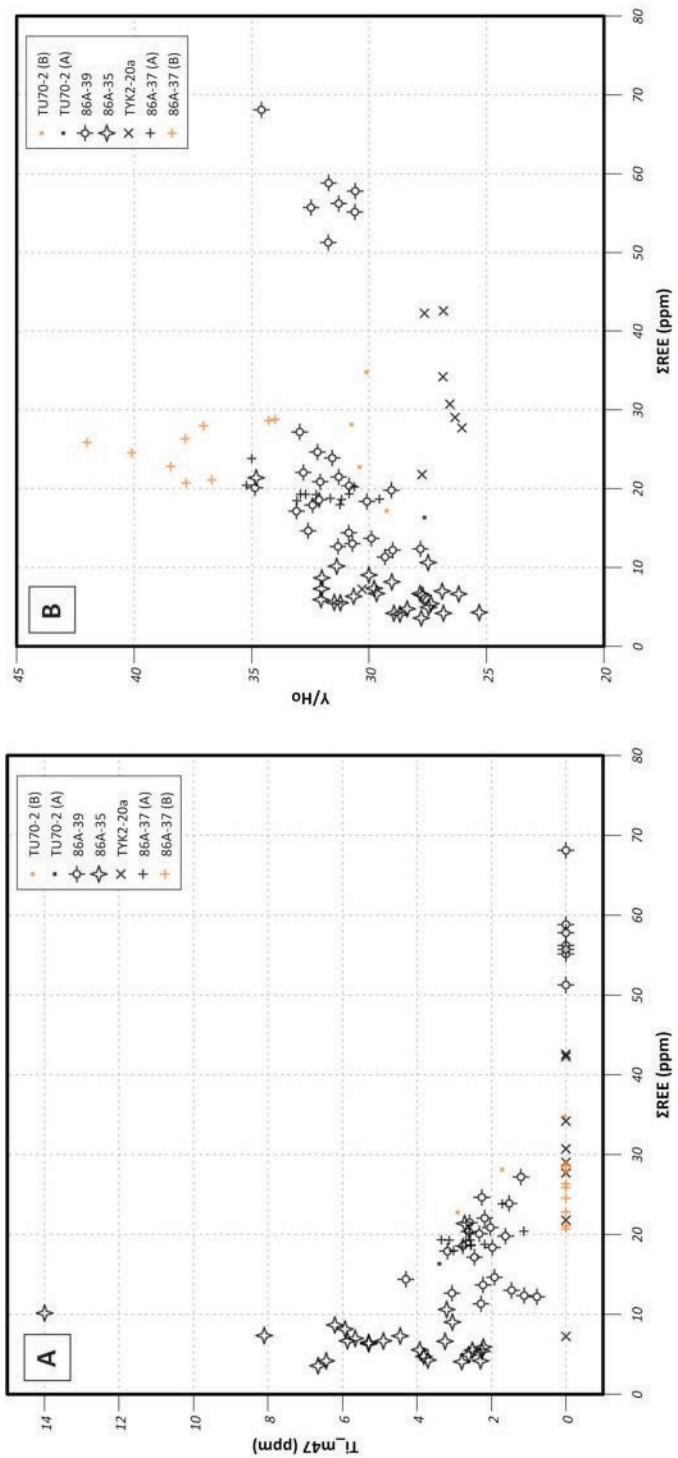
References

Adams M. M., Hoarfrost A. L., Bose A., Joye S. B. and Girguis P. R. (2013) Anaerobic oxidation of short-chain alkanes in hydrothermal sediments: potential influences on sulfur cycling and microbial diversity. *Front. Microbiol.* **4**, 1–11.

Alibo D. S. and Nozaki Y. (1999) Rare earth elements in seawater: Particle association, shale-normalization, and Ce oxidation. *Geochim. Cosmochim. Acta* **63**, 363–372.

Anderson G. M. and Thom J. (2007) The role of thermochemical sulfate reduction in the origin of Mississippi Valley-type deposits. II. Carbonate–sulfide relationships. *Geofluids*, 27–34.

Ansdell K. M., Nesbitt B. E. and Longstaffe F. J. (1989) A Fluid Inclusion and Stable Isotope Study of the Tom Ba-Pb-Zn Deposit, Yukon Territory, Canada. *Econ. Geol.* **84**, 841–856.

Azmy K. and Blamey N. J. F. F. (2013) Source of diagenetic fluids from fluid-inclusion gas ratios. *Chem. Geol.* **347**, 246–254.

Bau M. (1991) Rare-earth element mobility during hydrothermal and metamorphic fluid-rock interaction and the significance of the oxidation state of europium. *Chem. Geol.* **93**, 219–230.

Bau M. and Dulski P. (1995) Comparative study of yttrium and rare-earth element behaviours in fluorine-rich hydrothermal fluids. *Contrib. to Mineral. Petrol.* **119**,

213–223.

Bau M. and Dulski P. (1999) Comparing yttrium and rare earths in hydrothermal fluids from the Mid-Atlantic Ridge: implications for Y and REE behaviour during near-vent mixing and for the Y r Ho ratio of Proterozoic seawater. *Chem. Geol.*

Bau M., Moller P. and Möller P. (1992) Rare earth element fractionation in metamorphogenic hydrothermal calcite, magnesite and siderite. *Mineral. Petrol.* **45**, 231–246.

Birgel D., Feng D., Roberts H. H. and Peckmann J. (2011) Changing redox conditions at cold seeps as revealed by authigenic carbonates from Alaminos Canyon, northern Gulf of Mexico. *Chem. Geol.* **285**, 82–96.

Blamey N. J. F. (2012) Composition and evolution of crustal, geothermal and hydrothermal fluids interpreted using quantitative fluid inclusion gas analysis. *J. Geochemical Explor.* **116-117**, 17–27.

Blamey N. J. F., Parnell J., McMahon S., Mark D. F., Tomkinson T., Lee M., Shivak J., Izawa M. R. M., Banerjee N. R. and Flemming R. L. (2015) Evidence for methane in Martian meteorites. *Nat. Commun.* **6**, 7399.

Blamey N. and Norman D. (2002) New interpretations of geothermal fluid inclusion volatiles: Ar/He and N2/Ar ratios – a better indicator of magmatic volatiles, and equilibrium gas geothermometry. In *Twenty-Seventh Workshop on Geothermal Reservoir Engineering*

Bodnar R. J. (1993) Revised equation and table for determining the freezing point

depression of H_2O-NaCl solutions. *Geochim. Cosmochim. Acta* **57**, 683–684.

Broadbent C., Myers R. E. and Wright V. (1998) Geology and Origin of Shale-Hosted Mineralization at the Century Deposit, Queensland, Eromanga. *Econ. Geol.* **93**, 1264–1294.

Cathles L. M. and Schoell M. (2007) Modeling CO_2 generation, migration, and titration in sedimentary basins. *Geofluids* **7**, 441-450.

Conliffe J., Wilton D. H. C., Blamey N. J. F. and Archibald S. M. (2013) Paleoproterozoic Mississippi Valley Type Pb-Zn mineralization in the Ramah Group, Northern Labrador: Stable isotope, fluid inclusion and quantitative fluid inclusion gas analyses. *Chem. Geol.* **362**, 211–223.

Cooke D. R., Bull S. and Large R. R. (2003) Processes of ore formation in the stratiform sediment-hosted Zn-Pb deposits of Northern Australia: testing the Century model. *J. Geochemical Explor.* **78-79**, 519–524.

Cruse A. M. and Seewald J. S. (2006) Geochemistry of low-molecular weight hydrocarbons in hydrothermal fluids from Middle Valley, northern Juan de Fuca Ridge. *Geochim. Cosmochim. Acta* **70**, 2073–2092.

Cruse A. M. and Seewald J. S. (2010) Low-molecular weight hydrocarbons in vent fluids from the Main Endeavour Field, northern Juan de Fuca Ridge. *Geochim. Cosmochim. Acta* **74**, 6126–6140.

Cruse A. M. and Seewald J. S. (2001) Metal mobility in sediment-covered ridge-crest hydrothermal systems: *Geochim. Cosmochim. Acta* **65**, 3233–3247.

Douville E., Bienvenu P., Charlou J. L., Donval J. P., Fouquet Y., Appriou P. and Gamo T. (1999) Yttrium and rare earth elements in fluids from various deep-sea hydrothermal systems. *Geochim. Cosmochim. Acta* **63**, 627–643.

Eisbacher G. H. (1985) Late proterozoic rifting, glacial sedimentation, and sedimentary cycles in the light of Windermere deposition, Western Canada. *Palaeogeogr. Palaeoclimatol. Palaeoecol.* **51**, 231–254.

Elderfield H. H. and Greaves M. J. (1982) The rare earth elements in seawater. *Nature* **296**, 214–219.

Everett C. E., Wilkinson J. J. and Rye D. M. (1999) Fracture-controlled fluid flow in the Lower Palaeozoic basement rocks of Ireland: implications for the genesis of Irish-type Zn-Pb deposits. *Geol. Soc. London, Spec. Publ.* **155**, 247–276.

Fusswinkel T., Wagner T., Wenzel T., Wälle M. and Lorenz J. (2013) Evolution of unconformity-related MnFeAs vein mineralization, Sailauf (Germany): Insight from major and trace elements in oxide and carbonate minerals. *Ore Geol. Rev.* **50**, 28–51.

Gaboury D. (2013) Does gold in orogenic deposits come from pyrite in deeply buried carbon-rich sediments?: Insight from volatiles in fluid inclusions. *Geology* **41**, 1207-1210.

Gabrielse H. (1967) Tectonic evolution of the northern Canadian Cordillera. *Can. J. Earth Sci.* **4**, 271–298.

Gardner H. D. and Hutcheon I. (1985) Geochemistry, Mineralogy, and Geology of the

Jason Pb-Zn Deposits, Macmillan Pass, Yukon, Canada. *Econ. Geol.* **80**, 1257–1276.

Giggenbach W. F. (1996) Chemical Composition of Volcanic Gases. In *Monitoring and Mitigation of Volcano Hazards* Springer Berlin Heidelberg. pp. 221–256.

Gordey S. P., Macdonald J. D., Turner E. C. and Long D. G. F. (2010) Structural Geology of the Central Mackenzie Mountains. In *Geology of the central Mackenzie mountains of the North Canadian Cordillera, Sekwi Mountain (105P), Mount Eduni (106A), and northwestern Wrigley Lake (95M) map-areas, Northwest Territories* (eds. E. Martel, E. C. Turner, and B. J. Fischer). NWT Geoscience Office. pp. 215–250.

Grassineau N. V, Mattey D. P. and Lowry D. (2001) Sulfur isotope analysis of sulfide and sulfate minerals by continuous flow-isotope ratio mass spectrometry. *Anal. Chem.* **73**, 220–5.

Gromet L. P., Haskin L. a., Korotev R. L. and Dymek R. F. (1984) The "North American shale composite": Its compilation, major and trace element characteristics. *Geochim. Cosmochim. Acta* **48**, 2469–2482.

Haley B. A., Klinkhammer G. P. and McManus J. (2004) Rare earth elements in pore waters of marine sediments. *Geochim. Cosmochim. Acta* **68**, 1265–1279.

Himmler T., Bach W., Bohrmann G. and Peckmann J. (2010) Rare earth elements in authigenic methane-seep carbonates as tracers for fluid composition during early diagenesis. *Chem. Geol.* **277**, 126–136.

Hinrichs K.-U., Hayes J. M., Bach W., Spivack A. J., Hmelo L. R., Holm N. G., Johnson C. G. and Sylva S. P. (2006) Biological formation of ethane and propane in the deep marine subsurface. *Proc. Natl. Acad. Sci. U. S. A.* **103**, 14684–14689.

Hunt J. M. (1996) *Petroleum Geochemistry and Geology*., Freeman, New York.

Isenhour T. L. and Jurs P. C. (1972) *Introduction to computer programming for chemists*., Allyn & Baco.

Jaekel U., Musat N., Adam B., Kuypers M., Grundmann O. and Musat F. (2013) Anaerobic degradation of propane and butane by sulfate-reducing bacteria enriched from marine hydrocarbon cold seeps. *ISME J.* **7**, 885–95.

Jakubowicz M., Dopieralska J. and Belka Z. (2015) Tracing the composition and origin of fluids at an ancient hydrocarbon seep (Hollard Mound, Middle Devonian, Morocco): A Nd, REE and stable isotope study. *Geochim. Cosmochim. Acta* **156**, 50–74.

Jochum K. P., Scholz D., Stoll B., Weis U., Wilson S. a., Yang Q., Schwalb A., Börner N., Jacob D. E. and Andreae M. O. (2012) Accurate trace element analysis of speleothems and biogenic calcium carbonates by LA-ICP-MS. *Chem. Geol.* **318-319**, 31–44.

Johannesson K. H. and Zhou X. (1999) Origin of middle rare earth element enrichments in acid waters of a Canadian High Arctic lake. *Geochim. Cosmochim. Acta* **63**, 153–165.

John E. H., Wignall P. B., Newton R. J. and Bottrell S. H. (2010) $\delta^{34}S_{CAS}$ and $\delta^{18}O_{CAS}$

records during the Frasnian–Famennian (Late Devonian) transition and their bearing on mass extinction models. *Chem. Geol.* **275**, 221–234.

Joye S. B., Boetius A., Orcutt B. N., Montoya J. P., Schulz H. N., Erickson M. J. and Lugo S. K. (2004) The anaerobic oxidation of methane and sulfate reduction in sediments from Gulf of Mexico cold seeps. *Chem. Geol.* **205**, 219–238.

Kiyosu Y. and Krouse R. H. (1990) The role of organic and acid the in the sulfur abiogenic isotope reduction effect. *Geochem. J.* **24**, 21–27.

Klinkhammer G. ., Elderfield H., Edmond J. . and Mitra a (1994) Geochemical implications of rare earth element patterns in hydrothermal fluids from mid-ocean ridges. *Geochim. Cosmochim. Acta* **58**, 5105–5113.

Large R. R. and Mcgoldrick P. J. (1998) Lithogeochemical halos and geochemical vectors to stratiform sediment hosted Zn – Pb – Ag deposits, 1. Lady Loretta Deposit, Queensland. *J. Geochemical Explor.* **63**, 37–56.

Leach D. L., Marsh E., Emsbo P., Rombach C. S., Kelley K. K. and Anthony M. (2004) Nature of Hydrothermal Fluids at the Shale-Hosted Red Dog Zn-Pb-Ag Deposits, Brooks Range, Alaska. *Econ. Geol.* **99**, 1449–1480.

Leach D. L., Sangster D. F., Kelley K. D., Large R. R., Garven G., Allen C. R., Gutzmer J. and Walters J. (2005) Sediment-Hosted Lead-Zinc Deposits: A Global Perspective. *Econ. Geol.* **100**, 561–607.

Machel H. G. (2001) Bacterial and thermochemical sulfate reduction in diagenetic settings - old and new insights. *Sediment. Geol.* **140**, 143–175.

Machel H. G. (1987) Some aspects of diagenetic sulphate-hydrocarbon redox reactions Some aspects of diagenetic sulphate-hydrocarbon redox reactions. *Geol. Soc. London, Spec. Publ.* **36**, 15–28.

McCollom T. M. and Seewald J. S. (2007) Abiotic synthesis of organic compounds in deep-sea hydrothermal environments. *Chem. Rev.* **107**, 382–401.

Michard A. and Albarède F. (1986) The REE content of some hydrothermal fluids. *Chem. Geol.* **55**, 51–60.

Peter J. M., Peltonen P., Scott S. D., Simoneit B. R. T. and Kawka O. E. (1991) ^{14}C ages of hydrothermal petroleum and carbonate in Guaymas Basin, Gulf of California: implications for oil generation, expulsion, and migration. *Geology* **19**, 253–256.

Potter R.W. II. (1977) Pressure corrections for fluid inclusion homogenization temperatures based on the volumetric properties of the system $NaCl$-H_2O. *U.S. Geol. Surv. Jour. Res.* **5**, 602-608.

Radha A. V. and Navrotsky A. (2013) Thermodynamics of Carbonates. *Rev. Mineral. Geochemistry* **77**, 73–121.

Rajabi A., Rastad E., Canet C. and Alfonso P. (2014) The early Cambrian Chahmir shale-hosted Zn–Pb deposit, Central Iran: an example of vent-proximal SEDEX mineralization. *Miner. Depos.*

Rasmussen B. and Buick R. (2000) Oily old ores: Evidence for hydrothermal petroleum generation in an Archean volcanogenic massive sulfide deposit. *Geology* **28**, 731–734.

Reeder R. J. (1983) Crystal chemistry of the rhombohedral carbonates ed. R. J. Reeder. *Rev. Mineral.* **11**, 1–48.

Roedder E. (1984) Fluid inclusions. *Rev. Mineral.* **12**, 646p.

Rye D. M. and Williams N. (1981) Studies of the Base Metal Sulfide Deposits at McArthur River, Northern Territory, Australia: III. The Stable Isotope Geochemistry of the H.Y.C., Ridge, and Cooley Deposits. *Econ. Geol.*

Sánchez-España J., Velasco F., Boyce A. J. and Fallick A. E. (2003) Source and evolution of ore-forming hydrothermal fluids in the northern Iberian Pyrite Belt massive sulphide deposits (SW Spain): evidence from fluid inclusions and stable isotopes. *Miner. Depos.* **38**, 519–537.

Seewald J. S., Seyfried W. E. and Shanks W. C. (1994) Variations in the chemical and stable isotope composition of carbon and sulfur species during organic-rich sediment alteration: An experimental and theoretical study of hydrothermal activity at guaymas basin, gulf of california. *Geochim. Cosmochim. Acta* **58**, 5065–5082.

Shepherd T.J., Rankin A.H. and Alderton A.H. (1985) A Practical Guide to Fluid Inclusion Studies. Blackie and Son, Glastgow, 239 pp.

Shock E. L., Canovas P., Yang Z., Boyer G., Johnson K., Robinson K., Fecteau K., Windman T. and Cox A. (2013) Thermodynamics of Organic Transformations in Hydrothermal Fluids. *Rev. Mineral. Geochemistry* **76**, 311–350.

Sholkovitz E. and Shen G. T. (1995) The incorporation of rare earth elements in

modern coral. *Geochim. Cosmochim. Acta* **59**, 2749–2756.

Sverjensky D. a. (1984) Europium redox equilibria in aqueous solution. *Earth Planet. Sci. Lett.* **67**, 70–78.

Thom J. and Anderson G. M. (2007) The role of thermochemical sulfate reduction in the origin of Mississippi Valley-type deposits. I. Experimental results. *Geofluids*.

Warren J. (2000) Dolomite: occurrence, evolution and economically important associations. *Earth-Science Rev.* **52**, 1–81.

Welhan J. a. and Lupton J. E. (1987) Light hydrocarbon gases in Guaymas Basin hydrothermal fluids: thermogenic versus abiogenic origin. *Am. Assoc. Pet. Geol. Bull.* **71**, 215–223.

Wilkinson J. J. (2014) Sediment-Hosted Zinc–Lead Mineralization: Processes and Perspectives. In *Treatise on Geochemistry: Second Edition* Elsevier Ltd. pp. 219–249.

Wilson N. S. F. (2000) Organic petrology, chemical composition, and reflectance of pyrobitumen from the El Soldado Cu deposit, Chile. *Int. J. Coal Geol.* **43**, 53–82.

Yardley B. W. D. (2005) Metal Concentrations in Crustal Fluids and Their Relationship to Ore Formation. *Econ. Geol.* **100**, 613–632.

Zhang W., Guan P., Jian X., Feng F. and Zou C. (2014) In situ geochemistry of Lower Paleozoic dolomites in the north-western Tarim basin: Implications for the nature, origin, and evolution of diagenetic fluids. *Geochemistry, Geophys.*

Chapter 5. Mineralising processes in sediment hosted Zn-Pb-Ba systems – deposit genesis at Macmillan Pass.

5.1. Introduction

There are many challenges associated with interpreting the processes responsible for CD-type mineralisation: most models invoke mineralising processes that occur pre- to syn- compaction, resulting in complex, multi-generational textures that can be subjective to interpret; the host rock, commonly a fine-grained, organic rich mudstone, can be equally challenging to interpret, and recognising small-scale sedimentological features that aid paleo-environmental reconstruction and stratigraphic correlation can be difficult, both in outcrop and drill-core; thus, defining background, unaltered mudstones that represent ambient conditions may not be possible, which is problematic for any evaluation of hydrothermal alteration. This style of mineralisation has been described elsewhere, at major deposits that include McArthur River, Australia (Williams, 1978; Large et al., 1998), Mt. Isa, Australia (Large et al., 2005), Howards Pass, Canada (Goodfellow and Jonasson, 1986) and Red Dog, USA (Kelley et al., 2004), although debate commonly centers on the relative importance of syn-sedimentary (SEDEX) or more syn-diagenetic, replacement processes (e.g. Eldridge et al., 1993). For this reason, non-genetic terminology is preferred, and this style of mineralisation will be referred to as clastic dominated Pb-Zn type (CD-type; Leach et al., 2010).

Previous chapters have established how subsurface fluid flow could have been enhanced through immature, chemically reactive host rocks (Chapter 2), described alternative pathways of mineralisation that depart from the traditional model for water column euxinia (Chapter 3), and discussed how the hydrothermal fluid interacted with partially lithified sediments (Chapter 4). However, there are few unequivocal constraints regarding the source of the metals in CD-type systems and how fluid rock interaction can be traced at the deposit scale. In this study, we describe the mineralogy and paragenesis of all components of the Tom and Jason deposits (host rock, vent complex, alteration and bedded mineralisation), to provide a broader context and a more comprehensive synthesis of some of the new ideas surrounding CD-type mineralisation at Macmillan Pass. This has been supplemented with new isotopic data (C, O and Sr), which attempt to address outstanding questions, and is compiled with results from previous studies to present a new model for mineralisation at these localities.

5.2. Selwyn Basin Geology

The oldest exposed rocks in the Selwyn Basin are the 4-6 km thick Hadrynian-Cambrian Windermere Supergroup, which was deposited following the erosion of the sialic crystalline basement during the continental breakup of Rodinia (~760 Ma; Eisbacher, 1985). These lithologies include feldspathic conglomerate, sandstone and minor arkose, limestone and shale (Gordey, 1981). Overlying the Windermere Supergroup are fine-grained siltstones and limestones of the Gull Lake and Rabbitkettle Formations, followed by the Road River and Earn Groups (see stratigraphic column from Chapter 1; Figure 1.2). Mudstones comprise a major

proportion of the stratigraphy of the Selwyn Basin, and have been interpreted as deep-water facies deposited in an off-shelf passive margin environment (Gordey and Anderson, 1993).

Three episodes of extrusive and intrusive igneous activity have been identified during the evolution of the passive margin, with mafic volcanic flows, dykes and tuffs observed in Early Cambrian, Middle Ordovician, and Middle to Late Devonian strata (Goodfellow and Lydon, 2007). Alkalic and ultrapotassic volcanic rocks tend to be associated with syn-rift clastic rocks, and have been used as evidence for continental rifting (Goodfellow et al., 1995). In the Upper Devonian to Mississippian, slab rollback in a distal back-arc setting produced regional extension and resulted in thick accumulations of coarse clastic sediments over the basinal strata of the Selwyn Basin (Nelson et al., 2002; Nelson et al., 2006). This tectonic setting was important for volcanogenic massive sulphide (VMS) metallogenesis within allochthonous pericratonic terranes in the immediate back-arc and intra-arc settings (Galley et al., 2007). More distal back-arc settings formed the proposed environment of CD-type mineralisation (Nelson and Colpron, 2007).

The mid-Cretaceous to Tertiary (124-62 Ma) was a period of intrusive igneous activity, synchronous with island arc accretion and Cordilleran deformation (Nelson and Colpron, 2007). During Mesozoic deformation, passive margin strata of the Selwyn Basin were incorporated into the northern Cordillera fold and thrust belt. Basinal strata form the *inner belt*, and are characterised by slaty cleavage and intense tight to isoclinal folding, whereas platformal carbonates form the *outer belt* and represent the eastern most extent of deformation (Gordey et al., 2010).

5.2.1. The Selwyn Basin model

There are three major periods of CD-type metallogenesis preserved in Cambrian, Silurian and Late Devonian strata of the Selwyn Basin (Figure 1.2; Chapter 1). All deposits are hosted by fine-grained, carbonaceous mudstones, or metamorphic equivalents thereof, and the interpretation of sedimentology and geochemistry in these lithologies has directed previous paleo-environmental reconstructions in the Selwyn Basin (Goodfellow and Jonasson, 1984; Goodfellow and Jonasson, 1986; Goodfellow, 1987). Specifically, organic-rich, laminated mudstones, preserving no evidence of bioturbation, have been interpreted as being deposited via pelagic processes in an anoxic, deep marine environment (Goodfellow and Jonasson, 1984). In this setting, biological reduction of seawater sulphate is considered to have generated reduced sulphur and formed the metal trap. The preservation of δ^{34}S values that approach Late Devonian seawater sulphate in stratiform pyrite from Selwyn Basin mudstones led Goodfellow and Jonasson (1984) to conclude that pyrite precipitated from a euxinic water column during various stages of Selwyn Basin evolution.

The pyrite sampled by Goodfellow and Jonasson (1984) was interpreted to reflect ambient water column conditions for two main reasons: (1) stratiform pyrite was considered to be a water column precipitate (syn-sedimentary), and (2) the mudstone was considered to have been deposited via slow, pelagic processes, therefore diagenetic fluids remained as an open system with overlying seawater. Goodfellow and Jonasson (1984) produced a secular curve in δ^{34}S values in pyrite and barite, observing positive excursions broadly coincident with the three major periods of SEDEX metallogenesis. This was interpreted as evidence of near quantitative sulphate reduction in the water column and development of euxinic conditions, with basin scale closed system

189

Rayleigh fractionation producing the enriched $\delta^{34}S$ values in pyrite and barite.

In the Late Devonian CD-type systems (Macmillan Pass, Gataga District), stratiform barite is a major component of the bedded mineralisation. In these systems, barite and base metal sulphide precipitation are considered coeval, and stratiform barite occurrences with no base metal sulphides (barren barite), found more regionally, have been interpreted to either be distal expressions of a hydrothermal system or have formed during periods of basin ventilation (Goodfellow, 1987).

5.3. Macmillan Pass – Previous Work

There have been a number of geological and geochemical studies directed towards Macmillan Pass and specifically the deposits of Jason (Gardner, 1983; Gardner and Hutcheon, 1985; Bailes et al., 1986; Turner, 1986; Winn and Bailes, 1987; Turner et al., 1989) and Tom (Carne and Cathro, 1982; McClay and Bidwell, 1986; Ansdell et al., 1989; Goodfellow and Rhodes, 1991; Chapters 2-4 of this thesis). In the following section, work that is relevant to the new data presented in this study will be summarised.

5.3.1. Local geology

The Tom and Jason deposits are located 5 km away from each other (Figure 5.1), and are hosted by the Portrait Lake Formation within a sequence informally known as the Macmillan Pass Member (Abbott and Turner, 1991). The Macmillan Pass Member has been split into various subunits by different authors (see Figure 1), which include silt-laminated mudstone, pebble conglomerate and diamictite interbedded with sand-

and mud- stone and carbonaceous mudstone. Mineralisation at Tom is located at the top of the Macmillan Pass Member, within carbonaceous mudstones. A similar sequence is encountered at the Jason deposit, and previous workers suggest the two deposits formed broadly coevally (e.g. Turner, 1991). However, a combination of poor outcrop and abrupt facies changes can make stratigraphic correlations in the Macmillan Pass Member challenging. Therefore, use of previous stratigraphic nomenclature will be avoided when comparing the two deposits in this study. There have been no absolute age dating studies conducted on either the Tom or Jason deposits. Mudstones from the Macmillan Pass Member are considered deposited between the Lower *hassi* through Lower *rhenana* conodont zones, corresponding with a Frasnian age (Irwin and Orchard, 1991). As mineralisation has been considered syn-sedimentary (Goodfellow et al., 1993; Goodfellow and Lydon, 2007), this also forms the only constraint on the timing of hydrothermal activity at Macmillan Pass. Irwin and Orchard (1991) also identified two stratigraphic intervals hosting stratiform barite at Macmillan Pass; Eifelian to early Frasnian strata host the Cathy prospect, and equivalent strata to Tom and Jason are host to three separate barite deposits (Gary, Pete and Jeff).

The structural geology of the Macmillan Pass region is complex. Much of the work describing the paleo-tectonic setting is based upon regional 1:50,000 scale mapping produced by Abbott (1982). A series of normal faults have been identified in the Macmillan Pass region, and on the basis of local mapping and facies relationships are considered to be syn-depositional with the coarse clastics of the Macmillan Pass Member (Abbott and Turner, 1991). Mesozoic deformation then resulted in the formation of the Macmillan Fold Belt (MFB), which has been divided into three separate fault bounded blocks, characterised by different styles of deformation

(Abbott, 1982; Abbott and Turner, 1991). It has been suggested that the different structural trends are controlled by the geometry of pre-existing basement structures (Abbott and Turner, 1991), and that the syn-depositional faults may be reactivated structures (Goodfellow, 1987).

5.3.2. Deposit geology

The Jason and Tom deposits are located within the Central Block of the MFB, in which strata have been deformed by tight, upright folds and high angle reverse faults (Turner, 1986; Abbott and Turner, 1991). The Jason deposit has been deformed into a southeasterly plunging syncline (Figure 5.2A), which is offset by steeply dipping, east-southeasterly trending faults, parallel to the fold axial plane (Turner, 1986). Mineralisation is located on both north and south limbs of the fold, in three zones – the South, Main and End Zones, with the South Zone hosting the majority of the sulphide mineralisation (Turner, 1986; Turner, 1991). The Tom deposit is located within an anticline (Figure 5.2B), and mineralisation occurs in an East and West Zone (Goodfellow and Rhodes, 1991). The East Zone, which is located near the hinge of the anticline, is more intensely deformed than the West Zone (McClay and Bidwell, 1986).

Both the West Zone of Tom and the South Zone of Jason are hosted by siliceous, organic rich mudstones that overlie coarser clastic rocks of the Macmillan Pass Member. Hydrothermal breccia zones with stockwork style veining and massive sulphide mineralisation are preserved at both deposits, proximal to Late Devonian syn-depositional faults, and beneath the overlying mineralisation. These zones are considered to be the vent complexes, which formed the primary conduits of hydrothermal upflow at both deposits. Immediately overlying the vent complexes are

zones of massive sulphide mineralisation, which then transition into the bedded mineralisation. Previous studies (Goodfellow and Rhodes, 1991; Goodfellow and Lydon, 2007) have split the bedded mineralisation at Tom and Jason into different mineralogical and textural facies that are transitional in their location relative to the vent (vertically and laterally): pink facies mineralisation occurs proximally to the vent complex and is high grade, containing multiple generations of sphalerite; grey facies mineralisation occurs in a more vent-distal environment, where a greater proportion of host rock is preserved and sulphides appear more stratiform style; black facies mineralisation is the most vent-distal, and is dominated by the mudstone host rock with minor stratiform barite and sulphides.

Bedded sulphides at Jason vary in thickness from 3 to 18 meters (average 8m); along strike from the syn-despositional fault (and vent complex) mineralisation extends 200m, and down-dip from the fault 600m (Bailes et al., 1986). Proximal to the vent complex, the Tom West zone can reach up to 41m in thickness, whereas in vent distal settings, which may be up to 1200m from the vent, mineralisation thins to <1.5m (McClay and Bidwell, 1986).

5.3.3. Deposit geochemistry

The respective studies of Gardner and Hutcheon (1985) at Jason, and Ansdell et al. (1989) at Tom, presented fluid temperature (157°C to 335°C) and salinity (2.6 to 18 wt. % NaCl) data from analyses of fluid inclusions in vent carbonate and quartz. Fluid inclusion analyses in Chapter 3 provided further fluid constraints (Figures 4.5 and 4.6), with documentation of a steep thermal gradient between the deep (172 - 266°C) and shallow vent (108 - 136°C), low salinities (3.4 to 5.7 wt. % NaCl equiv.), and

convincing evidence that CO_2 is a primary feature of the hydrothermal fluid at both deposits. In Chapter 4, the manner in which hydrothermal fluid chemistry may have been altered during interaction with immature, organic rich mudstones was also documented; preservation of short chain hydrocarbons provides evidence of thermogenic organic matter alteration and input of diagenetic fluids was traced using analyses of rare earth elements in carbonates from the vent complex.

A number of studies have published $\delta^{34}S$ values for sulphides and barite at both the Tom and Jason deposits. In the secular curve for the Selwyn Basin, Goodfellow and Jonasson (1984) sampled pyrite from mudstones directly overlying mineralisation, which preserved positive $\delta^{34}S$ values (+22.0 to +33.8‰). In Chapter 3, two generations of pre-hydrothermal pyrite are described; *py-I*, which is framboidal, and preserves depleted $\delta^{34}S$ values (-30.0 to -20.8‰), and *py-IIa*, which occurs as stratiform aggregates of euhedral pyrite with much more enriched $\delta^{34}S$ values (+17.4 to +25.7‰). The $\delta^{34}S$ values in py-II approach the earlier results of Goodfellow and Jonasson (1984), however this pre-hydrothermal pyrite is also intergrown with stratiform barite, which preserves a relatively narrow range of $\delta^{34}S$ values (+23.5 to +34.0‰). Notably, in the mineralised drill-hole from which bulk pyrite was sampled in Chapter 3, there is a decrease in $\delta^{34}S$ values away (above and below) from mineralisation (Appendix A, Table A.1 and A.2).

The only $\delta^{34}S$ values for galena and sphalerite from the bedded mineralisation were presented by Gardner and Hutcheon (1985), who documented a relatively narrow range of $\delta^{34}S$ values in galena (+11.2‰ to +12‰) and sphalerite (+10.2‰ to +14.5‰), with more enriched $\delta^{34}S$ values in samples that are more transitional between vent and

bedded mineralisation (+17.7‰ to +22.5‰). The $\delta^{34}S$ values produced from analysis of hydrothermal pyrite (*py-III;* +3.0 to +18.6‰) in Chapter 3 broadly encompass es these previous results. Turner et al. (1989) report the only $^{87}Sr/^{86}Sr$ data for vent complex carbonate ($^{87}Sr/^{86}Sr$ = 0.7137 to 0.7221; n = 10) and stratiform barite ($^{87}Sr/^{86}Sr$ = 0.7129 to 0.7144; n = 9) in the overlying mineralisation at Jason.

Other isotopic constraints include a narrow range of $\delta^{13}C_{PDB}$ (-2.7 ± 0.3‰) and $\delta^{18}O_{\text{-VSMOW}}$ (+19.9 ± 0.2‰) values reported by Ansdell et al. (1989) for vent carbonates. Turner (1991) also reported $\delta^{13}C$ values, for siderite (-7.2 to -3.2‰; n = 19), ankerite (-9.1 to -1.6‰; n = 21) and barium carbonates (-10.3 to -8.4‰; n = 2), commenting that it is not possible to distinguish between derivation of carbon from the host rock or mantle degassing. Ansdell et al. (1989) also discussed alteration of the mudstone host rock in terms of bulk $\delta^{18}O$ values in the <2μm fraction of the host rock, which preserved no change, and the kaolinite / illite ratio, which increased in the host rock more proximal to mineralisation. This contrasts with earlier work at Jason (Longstaffe et al., 1982), which documented a halo of $\delta^{18}O$ values in <2μm fraction of the host rocks around the sulphide mineralisation. In Chapter 2, a stratigraphic correlation was made between the host rock to the Tom deposit in a distal and proximal setting. This helped to establish a biogenic origin for silica, coincident with enrichment in organic carbon (2-5 wt. %). A clear correlation was made between K_2O, Al_2O_3 and TiO_2, consistent with input from detrital muscovite, whereas mudstones sampled from a mineralised drill-hole preserved a decrease in the K_2O / Al_2O_3 ratio within 15 meters of mineralisation (above and below). In Chapter 2 this decrease in K_2O / Al_2O_3 is proposed to be evidence that an acidic hydrothermal fluid was buffered by the transformation of muscovite to illite and kaolinite.

5.3.4. Implications of recent work for the Selwyn Basin model

The work presented in Chapters 3 and 4 provides evidence that processes operating beneath the seafloor were important for the geochemical evolution of CD-type systems at Macmillan Pass. For example, a problematic feature of the euxinic basin model is the preservation of $\delta^{34}S$ values in barite that are consistent with relatively unmodified seawater sulphate. Previous explanations have suggested this to be a result of sampling barite and pyrite that are not stratigraphically equivalent (Goodfellow and Turner, 1988). However, in Chapter 3 it was shown that stratiform pyrite and barite approach isotopic equivalence ($\delta^{34}S_{pyrite} = \delta^{34}S_{barite}$) on a small scale, around a common $\delta^{34}S$ value of 24‰, consistent with Late Devonian seawater (Figure 3.8). The close, intergrown nature of stratiform pyrite and barite precludes the development of this isotopic relationship in a euxinic water column. Rather, it is more likely that this isotopic relationship represents the development of closed system sulphate reduction along a diagenetic redox front, such as during anaerobic oxidation of methane (AOM) (e.g. Borowski et al., 2013). Deeper within the system, evidence of an input of diagenetic fluids has been found in vent complex ankerite, and the fluid interaction with the host rock is interpreted to have formed a major control on mineralogical evolution within the vent complex (Chapter 4). However, the data supporting these ideas were obtained largely from micro-analytical techniques, the question of how relevant these processes were at the deposit scale remains unanswered. To assess this issue here we compile the previous data and introduce new petrographic and isotopic data to develop a deposit model for the MacMillan Pass deposits.

5.4. Samples

Detailed logging and sampling of the drill-core from the Tom and Jason deposits was carried out during summer field seasons in 2012 and 2013. Historical core and a recent drilling campaign by Hudbay Minerals expanded the drill-core available for sampling. A total of 300 samples were collected from 12 drill-holes at Tom, which intersected mineralisation from the West Zone as well as lithologies of the Macmillan Pass Member. The logs of 4 drill-holes that formed a continuous record through the Macmillan Pass Member and West zone mineralisation are presented in Figure 5.3. It was only possible to access historical core from the Jason deposit, and many of the drill-holes were incomplete or inaccessible, however it was possible to collect a comprehensive suite of samples (n = 180) from two drill-holes intersecting the South Zone mineralisation and vent complex. A barren, regional drill-hole (76-17), located between the two deposits (Figure 5.3) was also sampled and enabled a stratigraphic correlation of the un-mineralised background mudstone (Chapter 2; Figure 2.3).

5.5. Methodology

5.5.1. Petrography and EPMA

A suite of representative samples of all lithologies and mineralisation were evaluated in hand sample, and also under binocular microscope and using conventional reflected and transmitted light petrography. The JEOL 8900 (University of Alberta, Electron Microprobe Laboratory) was used for backscattered electron (BSE) imaging, wavelength dispersive spectroscopy (WDS) and electron dispersive

spectroscopy (EDS). These techniques were used to examine compositional zoning, textural relationships and major element mineral chemistry of barium feldspars. For WDS analyses, the electron beam was operated at an accelerating voltage of 15 kV, a probe current of 15 nA and a beam diameter of 5μm. Due to high Ba concentrations in the feldspars, standardisation of BaO was on Ba-niobate, and Na_2O on albite, K_2O on microcline, anorthite SiO_2, CaO, Al_2O_3 on anorthite, FeO on fayalite, MgO on diospide and MnO on willemite. Only those analyses producing totals ±2% of 100% and above the detection limit (3σ; see results) have been reported.

5.5.2. $\delta^{13}C_{PDB}$, $\delta^{18}O_{VSMOW}$ values and $^{87}Sr/^{86}Sr$ in vent ankerite

Analysis of $\delta^{13}C$ and $\delta^{18}O$ values in carbonate from host rock alteration, veining from the vent complex and bedded mineralisation were carried out at the Isotope Science Laboratory (University of Calgary). Samples from Tom (n = 16) and Jason (n = 10) were hand-picked under the binocular microscope, and mineral separates were ground to <50μm using an agate mortar and pestle. Samples were then digested with anhydrous phosphoric acid in a reaction vessel at 25°C to produce CO_2 introduced to the ion source of a VG 903, stable isotope ratio mass spectrometer. Internal standards were interspersed between samples sets of 20 to correct for instrumental drift and calibrate data against international reference materials, Vienna Pee Dee Belemnite (V-PDB) for $^{13}C/^{12}C$ and Standard Mean Ocean Water (SMOW) for $^{18}O/^{16}O$. Isotope ratios are reported in δ-notation in units of per-mil (‰) relative to the standards, with associated errors (1σ) of 0.2‰.

A subset of 11 samples was targeted for strontium isotope analysis. Sample dissolution and ion chromatography was conducted in a Class 100 cleanroom in the

Radiogenic Isotope Facility, Department of Earth and Atmospheric Sciences, University of Alberta, following the methods described in Buzon et al. (2007). Following sample preparation, Sr-bearing aliquots were diluted (2% HNO_3 solution) and aspirated into the ICP torch (DSN-100, Nu Instruments Inc.), and strontium isotope values were determined using a NuPlasma MC-ICP-MS instrument. Acquisition of strontium isotope data was in static, multi-collection mode using five Faraday collectors with 40 scans over 400 s. Prior to sample aspiration, a gas blank (and acid) was measured for 30 s, and following each analysis there was approximately 5 minutes of wash-out period. Accuracy and reproducibility were monitored by repeated analysis of NIST SRM 987, and the error (2σ) associated with individual analyses varied between 0.000013 and 0.000079.

5.6. Results

A summary of the mineralogical paragenesis for mineralisation in the bedded sulphides and vent complex has been presented in Chapters 3 (Figure 3.3) and 4 (Figure 4.2) respectively. In the following sections, an overview of the stratigraphy underlying the Tom and Jason deposits will be provided, followed by descriptions of the host rock, vent complex and the transition into the bedded mineralisation.

5.6.1. Stratigraphy underlying Tom and Jason

The Macmillan Pass Member underlying the Tom and Jason deposits comprises sand and silt laminated mudstones, and conglomerates (Figure 5.4). The mudstones, which both underlie and overlie the conglomerates, are dark grey to black and regularly

interbedded and interlaminated with coarse silt to fine sand, which can give them a pin-striped appearance (Figure 5.4A). Mudstone beds are typically planar, on a cm to sub-cm scale, with intervals of silt and sand that are finer (<1cm thick) and more irregular. Some samples have lenticular to flaser bedding, in which graded sand interbeds can be cross-laminated, and some sand beds are also boudinaged (Figure 5.4B). Conglomerates are a major component of the Macmillan Pass Member stratigraphic sequence, although there can be major lateral variability in thicknesses (e.g. TYK001 and T91-14; Figure 5.3). Individual beds are massive, and can be up to 10 meters thick, and preserve minor sand and grit interbeds. Clasts are rounded to sub-rounded, poorly sorted and mostly pebble sized (Figure 5.4C).

5.6.2. Host rock

The host rock is a black, homogenous, fine-grained, siliceous mudstone. It appears to be relatively featureless in drill-core, but with care, it is possible to identify certain sedimentological features that enable comparison between un-mineralised (barren) and mineralised mudstones (Figure 5.5). The mudstone is bedded, on a similar scale in both barren (Figure 5.5A) and mineralised samples (Figure 5.5B), with subtle cm-scale beds that grade upwards from fine quartz silt upward into more homogenous, clay-rich mudstone; within individual beds, sharp mm-scale laminations may be preserved (Figure 5.5C), which also contain wavy to lenticular laminations with ellipsoidal lenses (500µm) of quartz silt (~5µm) encased in a darker matrix of clay and organic material (Figure 5.5D). There is no evidence of any infaunal biological activity, although some beds contain high abundances of radiolarians, suggesting that deposition of this lithology occurred in a productive environment (Chapter 2). Two main generations of pyrite are preserved in the host rock, as disseminated framboids and euhedral crystals,

consistent with py-1 and py-II described in Chapter 3 (Figures 3.4 and 3.5).

5.6.3. Vent complex mineralisation and alteration

The vent complex forms a relatively discrete feature of the Tom and Jason deposits; in the drill-holes sampled from Tom, it reaches a maximum stratigraphic thickness of approximately 5 meters beneath the overlying bedded mineralisation (Figure 5.3). The extent of hydrothermal alteration and veining is spatially variable, perhaps controlled by proximity to the syn-depositional fault that formed the primary flow conduit for the hydrothermal fluids. Both vent complexes (Tom and Jason) are characterised by a two-stage paragenesis (Figure 4.2; Chapter 4), in which ankerite (Stage 1) is overprinted by subsequent Stage 2 massive sulphide mineralisation (Figure 5.6).

In many vent samples, there were at least two Stage 1 ankerite forming events: initial flooding of the host rock resulted in variable alteration of the immediate wall rock (Figure 4.1A Chapter 4), and is followed by a second pulse of fluid flow during which the host rock is brecciated and stockwork style ankerite veining develops (Figure 5.7A; Figure 4.1A, Chapter 4). Stage 1 mineralisation is also associated with the thermal alteration of organic matter in the host rock (pyrobitumen) and precipitation of pyrite. The sulphide mineralisation of Stage 2 can be destructive, with samples comprising greater than 30% massive sulphides (galena ± pyrite ± sphalerite ± pyrrhotite ± chalcopyrite) via the replacement of ankerite (Figure 5.6).

More subtle features are encountered on the margins of the vent complex, either laterally away from, beneath or above highly altered samples: in the peripheral (lateral) vent, minor stockwork style ankerite veins crosscut relatively unaltered host rock (Figure 5.7A); beneath the vent complexes, quartz-ankerite-sphalerite feeder veins

crosscut conglomerates (Figure 5.7B); above the vent complex, where there is a transition into the overlying bedded mineralisation, barite content increases and the relict bedded fabric of the host rock may be recognised (Figure 5.7C) – notably in these samples, barite dissolution is coupled with bartyocalcite and sulphide precipitation.

5.6.4. Bedded mineralisation

The bedded sulphide and barite mineralisation at Tom and Jason is fine-grained, stratiform to stratabound, and interbedded with varying proportions of the host rock. In terms of the overall deposit architecture, the vertical and lateral proximity to the vent complex forms a first order control on mineralogy and mineralisation style in the bedded sulphides. In general, proximity to the vent correlates with greater galena content and minimal host rock preservation (<20%). Well-preserved bedded textures may only be encountered with increasing vertical and lateral distance from the vent (Figure 5.8).

The scale at which observations are made can be an important factor when evaluating the bedded mineralisation. In hand sample, samples with stratiform textures appear comprised of a simple mineral assemblage (barite ± pyrite ± sphalerite ± galena). However, petrography at a higher resolution reveals there to be additional, minor mineral phases present (hyalophane, celsian, calcite, barytocalcite and witherite). Two general features of the mineralogical paragenesis of the bedded mineralisation are important to highlight: (1) hydrothermal sulphide precipitation is preceded by two generations of pyrite (py-I, II) and all occurrences of barite (brt-I, II, III), and (2) precipitation of hydrothermal sulphides is commonly associated with barite dissolution and the formation of barium carbonate phases such as barytocalcite

and witherite (Figure 5.9). Indeed, barite, which forms a major component of the bedded mineralisation, is commonly host to high concentrations of galena and sphalerite (Figure 5.10A), and where the interstitial replacement of barite is pervasive, monominerallic sulphide laminations can develop (Figure 3.2; Chapter 3).

It is also important to highlight the occurrence of stratiform textures that are associated with sulphide bearing veinlets; in Figure 5.11, an example of well-preserved stratiform mineralisation from the Tom deposit is presented. The irregular quartz-sphalerite-galena veinlet that crosscuts the laminated fabric of the host rock also precipitates sphalerite along a more stratiform horizon. Notably, this stratiform horizon contains abundant barium feldspar (celsian and hyalophane; mineral chemistry Table 5.1). In hand sample, barium feldspars can be distinguished as dark, monoclinic crystals within individual mudstone beds (Figure 5.8B), disseminated within barite (Figure 5.10A), or concentrated along the surfaces of mudstone beds (Figures 5.10B,C and 5.11C). The paragenetic relationship between celsian, hyalophane and other mineral phases is unclear; however, there are clear disequilibrium textures with barite, sulphides and carbonate (Figure 10A).

5.6.5. $\delta^{13}C_{-PDB}$, $\delta^{18}O_{-VSMOW}$ values and $^{87}Sr/^{86}Sr$ in vent ankerite

The respective $\delta^{13}C$ and $\delta^{18}O$ values at Jason are between -4.7 and -2.1‰ and +16 and +18.2‰, and at Tom, between -5 and -2-2‰ and +17.9 and +20.3‰ (Figure 5.12). The $^{87}Sr/^{86}Sr$ results are presented in Figure 5.13. The $^{87}Sr/^{86}Sr$ values range between 0.7131 and 0.7202, and are high relative to Late Devonian seawater (0.7079 to 0.7082; Denison et al., 1997).

5.7. Discussion

5.7.1. Host rock sedimentology

Mudstones in the bedded mineralisation at Tom and Jason preserve sedimentological features that include subtly graded beds, erosional basal surfaces and lenticular laminations. Notably, experimental work has shown that lenticular laminations form during the erosion and re-deposition of partially consolidated, water saturated mud clasts (Schieber et al., 2010). Therefore the association of lenticular laminations within laminated fabrics does not support pelagic sedimentation, rather higher energy sediment transport and deposition.

In terms of paleo-environmental reconstruction, without detailed facies analysis (e.g. Macquaker et al., 2007) in un-mineralised lithologies it is difficult to present a comprehensive model. However, there are similarities between the sedimentological features of the host rock and mudstones deposited in a ramp environment (e.g. Plint et al., 2012). Indeed, the deep-water, pelagic processes previously invoked (Goodfellow and Jonasson, 1984) are a non-unique explanation for the deposition of the host rock, and the evidence of biogenic input (biogenic silica, organic carbon; Chapter 2), is more supportive of a productive continental margin setting (e.g. Schieber et al., 2000).

It is possible that the mudstone beds preserving these features were deposited during anomalous sedimentation events, interspersed within longer periods of otherwise pelagic sedimentation, yet it is compelling that the lithologies underlying the host rock are higher energy deposits (conglomerates, sandstones, siltstone). Considering the tectonic activity associated with hydrothermal fluid flow, it is perhaps unsurprising to find evidence of high-energy deposition in the host rock. This is

particularly important for the syn-sedimentary model, where it has been suggested that low sedimentation rates (0.4cm yr^{-3}) would be an important factor in the generation of high Pb-Zn grades, to prevent dilution of ore-forming sulphides (Goodfellow and Jonasson, 1986). Furthermore, slow sedimentation rates have been used to invoke long-lasting periods of hydrothermal activity (>5 Ma; Turner, 1992).

A final aspect that is important to consider, involves the interaction between sedimentation rate and sulphur isotope fractionation (Goldhaber and Kaplan, 1975). For example, Goodfellow and Jonasson (1984) used slow sedimentation rates as criteria to invoke open system conditions between sediment pore fluids and the overlying water column; in turn, this supported a model in which δ^{34}S values in pyrite could be interpreted in terms of water column processes (i.e. euxinia). However, in rapidly deposited sediments, restriction of pore fluids from exchange with the overlying water column occurs much more rapidly, and adds a layer of complexity to the interpretation of δ^{34}S values (Goldhaber and Kaplan, 1975). The sedimentology of the host rock is an important factor to consider, one which can provide a foundation for the interpretation of geochemical data and mineralising textures. In the following section, hydrothermal processes at Macmillan Pass will be evaluated, starting with the source and evolution of the metal-rich fluids in the vent complex.

5.7.2. Metal source – strontium isotope composition of vent ankerite

The ^{87}Sr/^{86}Sr values preserved in vent complex ankerite (0.7131 to 0.7202) are higher than both Late Devonian seawater (^{87}Sr/^{86}Sr = 0.7080; Denison et al., 1997) and the Maximum Sr Isotope Ratio of Basinal Shale (MASIRBAS = 0.7120; Machel and Cavell, 1999). The upper constraint for ^{87}Sr/^{86}Sr values that MASIRBAS represents

incorporates the composition of strontium bound in carbonate from different mudstones within the Western Canadian sedimentary basin, and forms a useful approximation of the $^{87}Sr/^{86}Sr$ composition a fluid may attain through low temperature fluid rock interaction with such lithologies (Machel and Cavell, 1999). High $^{87}Sr/^{86}Sr$ values, greater than MASIRBAS, can be produced from the breakdown of Rb-rich minerals within mudstones (e.g. feldspars, micas), although this requires to high-grade metamorphic conditions (Machel and Cavell, 1999). At Macmillan Pass, the only feldspars to have been documented occur in mudstones of the bedded mineralisation overlying the vent complex.

To produce $^{87}Sr/^{86}Sr$ values above MASIRBAS, Machel and Cavell (1999) proposed that radiogenic strontium has to be sourced from extra-basinal sources, i.e. older basement lithologies that have accumulated radiogenic strontium. Indeed, the Hadrynian clastic rocks that form the basal rift sequence to the Selwyn Basin represent a potential source of radiogenic strontium. Furthermore, ionic substitution into feldspars (Pb, Ba) and muscovite (Zn) means that interaction with these lithologies could have produced metal enrichment in the fluids (Hemley and Hunt, 1992). Fluid rock interaction with basal rift sequences to the Selwyn Basin is also consistent with preliminary work conducted by Goodfellow and Jonasson (1986), who presented $^{87}Sr/^{86}Sr$ values (0.7140) in carbonate from the Active Member, host to mineralisation at the XY deposit (Howards Pass district). Interestingly, the $^{87}Sr/^{86}Sr$ values presented in this study are also similar to those presented for ore stage dolomite in MVT systems from the MacKenzie platform (Nelson et al., 2002; Gromek et al., 2012). This may be evidence that the fluids responsible for MVT and CD-type mineralisation in the Canadian Cordillera interacted with similar lithologies.

5.7.3. Fluid rock interaction in the vent complex – $\delta^{18}O$ and $\delta^{13}C$ of vent ankerite

Few studies have reported $\delta^{18}O$ and $\delta^{13}C$ values of vein samples from CD-type systems, largely due to an absence of appropriate sample material. Rye and Williams (1981) produced a study on discordant ankerite veins from the HYC deposit, and described co-variation of $\delta^{18}O$ and $\delta^{13}C$ values in terms of temperature dependent fractionation of a CO_2-bearing fluid over a gradient of 240°C to 170°C. At Macmillan Pass, analyses of fluid inclusions in ankerite provide evidence that the parental hydrothermal fluid may have been hotter, albeit overlapping with this temperature range (Gardner and Hutcheon, 1985; Ansdell et al. 1989; Chapter 4). Taylor (1987) warned that for systems hosted by organic rich mudstones, such as those in the Selwyn Basin, CH_4 could be the dominant carbon species in a hydrothermal fluid. However, the thermodynamic modeling of the Stage 1 mineral assemblage (Figure 4.11; Chapter 4), where pyrite (not pyrrhotite) is the stable mineral, is good evidence that CO_2 was the dominant carbon species in the Stage 1 fluid entering the vent complex (Chapter 4).

The samples of ankerite from the Jason and Tom vent complexes preserve separate positively correlated arrays of $\delta^{18}O$ and $\delta^{13}C$ values, albeit with greater scatter in the Tom samples, which are characterised by a higher range of $\delta^{18}O$ values (Figure 5.12). It is possible to produce the co-variation of $\delta^{18}O$ and $\delta^{13}C$ values in hydrothermal carbonates via a range of processes, which include: (1) two component fluid mixing (e.g. Schwinn et al., 2006), (2) CO_2 degassing and fractional crystallisation (e.g. Zheng, 1990), (3) fluid-rock interaction (e.g. Taylor, 1987), and (4) temperature dependent fractionation (e.g. Rye and Williams, 1981). In addition, the speciation of carbon (CH_4, H_2CO_3, HCO_3^-, CO_3^{2-}) exerts a further control on the magnitude of isotopic

fractionation (e.g. Spangenberg et al. 1996).

Before evaluating these different processes, it is important to highlight that the vent complex samples are characterised by varying degrees of hydrothermal input, preserved by varying degrees of ankerite alteration and stockwork style veining. Notably, samples from Jason were obtained from one drill-core (82-86A) and can be split into two groups, comprising ankerite from early host rock alteration and ankerite from subsequent stockwork style veining (e.g. Figure 4.1A, Chapter 4). In contrast, samples from Tom were obtained from a number of drill-cores, and represent a broader coverage of ankerite from the vent complex. Therefore the array of $\delta^{18}O$ and $\delta^{13}C$ values may be controlled by a combination of processes. For example, the composition of vein ankerite may record fluid-rock interaction, either with earlier hydrothermal alteration or diagenetic carbonate in the host rock. In addition, given the proximity of the vent complex to the seafloor and the evidence for diagenetic fluid input (Chapter 4) it is also possible that fluid mixing was an important process during hydrothermal evolution.

At Jason, co-variation of the $\delta^{18}O$ and $\delta^{13}C$ values is well defined (r^2 = 0.799), although the samples form two sub-groups within the overall trend: ankerite associated with early Stage 1 alteration is characterised by lower $\delta^{13}C$ values (-3.2 to -4.8‰), whereas those of the stockwork style veins have more positive $\delta^{18}O$ and $\delta^{13}C$ values. The samples from the Tom vent have a similar range of $\delta^{13}C$ values (-5 to -2.3‰) whilst extending to greater $\delta^{18}O$ values (+17.9 to +20.2‰). Due to these differences, samples from the Tom and Jason vents will be interpreted separately. Using the equations of Horita (2014), a series of temperature dependent fractionation curves have been calculated, with different starting fluid compositions, to evaluate

the role of temperature in the co-variation of the $\delta^{18}O$ and $\delta^{13}C$ values. Fractionation curves were calculated with the dominant C-bearing species as $H2CO_3$, and not HCO_3^-, considering the evidence for an acidic Stage 1 fluid (Chapter 4). However, it is clear that for samples from both Tom and Jason, co-variation of $\delta^{18}O$ and $\delta^{13}C$ occurs at a steeper gradient than the modeled temperature dependent fractionation trend for a H_2CO_3 bearing fluid (Figure 5.14).

The variety of sample types from which ankerite was sampled, in terms of alteration and stockwork style veining (which represent multiple ankerite forming events), means it is necessary to incorporate fluid rock interaction into this model. This has been attempted using the fluid rock interaction equation of Taylor (1987), across a temperature gradient that is consistent with fluid inclusion results for the Stage 1 fluid (Figure 4.6; Chapter 4). This model is most relevant for samples from the Jason vent, for which there are clear examples of Stage 1 ankerite alteration crosscut by subsequent stockwork style veining (see Figure 4.1A, Chapter 4). In the model presented in Figure 5.14, ankerite alteration occurs at high temperatures ($\leq 300°C$) and low fluid / rock ratios (0.01 to 1). These conditions represent the earliest ankerite forming event from a hydrothermal fluid with an initial fluid composition of -3‰ ($\delta^{13}C^{initial}$) and +9‰ ($\delta^{18}O^{initial}$). The samples characterised by stockwork style veining represent subsequent hydrothermal fluid input, which interacts with earlier carbonate phases at a fluid / rock ratios between 1 and 5. This model provides a good description of the co-variation in $\delta^{18}O$ and $\delta^{13}C$ values, and is consistent both with the fluid inclusion temperature constraints and the different styles of ankerite from Stage 1. If this model is applied to samples from the Tom vent, there is reasonable description of $\delta^{18}O$ and $\delta^{13}C$ co-variation if the initial fluid constraints are modified slightly ($\delta^{13}C^{initial} = -2.5‰$; $\delta^{18}O^{initial}$

= +10‰; 260°C to 210°C). A greater variety of samples was collected from the Tom deposit, which may explain why the trend is less clear when compared to Jason. Furthermore, the difference in δ^{34}S values of sulphides from the Tom and Jason vent complexes also support a lower temperature regime in the Tom vent (Figure 4.10; Chapter 4).

The initial δ^{13}C value of the hydrothermal fluid provides a record of the origin of carbon in the system. For example, carbon could have been sourced from three reservoirs: (1) marine carbonate, (2) organic matter, and (3) magmatic degassing. Organic matter is characterised by depleted δ^{13}C values (-25 ± 5‰) whereas marine carbonates in most sedimentary rocks preserve δ^{13}C values around 0‰; assuming a mole ratio of 4:1 (carbonate : organic carbon), this results in an average δ^{13}C value for the crust of -5‰ (Ohmoto and Goldhaber, 1997). Carbon dioxide derived from magmatic degassing retains δ^{13}C values mostly between -4 and -8‰ (Campbell and Larson, 1998).

A fluid with an initial δ^{13}C value of -3‰ is somewhat ambiguous to interpret, and it may be difficult to distinguish between crustal and magmatic carbon. However, the presence of pyrobitumen (organic carbon) in the Tom and Jason vent complexes and modeling of fluid rock interaction with early carbonate phases (inorganic carbon) is consistent with a crustal origin. There is also likely to have been a component of inorganic carbon in these fluids, derived from marine bicarbonate from diagenetic fluid input or perhaps via interaction with limestones sequences in the underlying stratigraphy (Figure 1.2; Chapter 1). The initial δ^{18}O value for the hydrothermal fluid is higher than seawater, and consistent with an evolved basinal fluid that has interacted

with sedimentary lithologies (Machel et al., 1995).

To summarise, in Chapter 4, a limited fluid inclusion microthermometry data set was presented, from which there was evidence that hot fluids (>250°C) entered the vent complex before undergoing cooling (<150°C). These results were obtained from a limited number of samples, and were restricted to minerals within vein assemblages. The modeling of $\delta^{18}O$ and $\delta^{13}C$ values in this section provides further evidence of a steep temperature gradient within the vent complexes at Tom and Jason, whilst also confirming the alteration of organic carbon in the host rock by the hydrothermal fluid.

5.7.4. Combined $^{87}Sr/^{86}Sr$, $\delta^{18}O$ and $\delta^{13}C$ values

The lowest $^{87}Sr/^{86}Sr$ values correspond with the lowest $\delta^{18}O$ and $\delta^{13}C$ values (Figure 5.15), in carbonate veinlets samples from the bedded mineralisation. In contrast, the highest $^{87}Sr/^{86}Sr$ values are preserved in two vent ankerite samples of stockwork style veining from Jason. Together, this provides some evidence of an isotopic gradient within the deposit architecture of the Tom and Jason deposits, controlled by decreasing temperatures and greater organic matter input in environments more proximal to seafloor; the $^{87}Sr/^{86}Sr$ values from the stockwork veining at Jason, which forms later in the Stage 1 paragenesis, are from samples with higher water rock ratios (see previous section) and a strontium budget dominated by the radiogenic hydrothermal input. This is also consistent with earlier studies by Turner et al. (1989), which describe a linear trend $^{87}Sr/^{86}Sr$ vs. 1/Sr (concentration) in barite and siderite, suggested as developing by mixing of a radiogenic strontium rich fluid with strontium poor, less radiogenic seawater.

5.7.5. Mineralisation pathways for the bedded sulphides

The majority of the ore in CD-type systems is located in the bedded sulphides, and in the conventional model for Selwyn Basin CD-type mineralisation, sulphide precipitation occurs in a euxinic water column. However, in Chapter 3 widespread euxinia was effectively ruled out as a metal trap, and so it is necessary to re-evaluate some of the textures and mineralogical relationships within the bedded mineralisation in the context of this work. Indeed, some of the more minor mineral phases, which include barium carbonates and barium feldspars, may record useful information in their respective isotopic composition and paragenetic relationships.

In Figure 5.11, a sample from the bedded mineralisation at Tom preserves an irregular discordant sulphide-bearing quartz veinlet that both crosscuts and offsets bedding before permeating along stratal horizons. Importantly, Figure 5.11 provides evidence of stratiform textures that develop beneath the sediment-water interface. The preservation of both brittle and ductile deformation features probably means the host rock was only partially lithified during hydrothermal fluid flow; these textures are similar to those that develop via soft sediment deformation processes in partially consolidated sediments from seismically active environments (e.g. El Taki and Pratt, 2012). Also preserved within these stratiform horizons is barium feldspar, which occur mostly as celsian, along with minor hyalophane. A number of authors have documented these mineral phases during their work on hydrothermal systems hosted in Selwyn Basin mudstones (Goodfellow and Jonasson, 1986; Ansdell et al., 1989; Turner, 1991; Orberger et al., 2005; Fernandes, 2011), although there have been differing interpretations regarding a diagenetic (Turner, 1991) or metamorphic-hydrothermal (Orberger et al. 2005) origin. The preferential formation of barium

feldspars on top of organic rich mudstone beds (Figure 5.10), and also between stratiform accumulations of barite and pyrite (Figure 3.8; Chapter 3), suggests a diagenetic origin. The development of highly reducing conditions, locally within pore fluids and perhaps in association with organic rich lamina, may account for the formation of barium feldspar rather than barite.

Barium carbonate and calcite present in the bedded mineralisation at Tom and Jason have received relatively little attention in previous studies, perhaps due to difficulties interpreting the fine-grained nature of many of the textures. However, it was possible to sample carbonate for analysis of $\delta^{13}C$ values (-12 and -20‰) from two veinlets at Tom, which crosscut the bedded mineralisation. Similar $\delta^{13}C$ values were reported by Jakubowicz et al. (2015) for carbonates formed in an ancient hydrocarbon seep. In this study, it was concluded that a proportion of carbon was derived from thermogenic methane, which is characterised by negative $\delta^{13}C$ values between -20 and -50‰ (McCollom and Seewald, 2007). The $\delta^{13}C$ values in this study are also similar to experimental results produced by Wankel et al. (2012), in which a dissolved inorganic carbon (DIC) flux representing seawater (3.4‰) was mixed with methane (-40‰), in a sediment core reactor. The result, following the anaerobic oxidation of methane, was a combined outflow of DIC with $\delta^{13}C$ values between -21 and -12‰. It is certainly worth speculating upon the possible role of thermogenic methane in sulphate reduction, having documented the role of anaerobic methane oxidation coupled with sulphate reduction during diagenesis (Chapter 3), and the production of short chain hydrocarbons during thermogenic alteration of organic matter in the vent (Chapter 4). Indeed, were thermogenic methane produced during hydrothermal alteration of organic rich sediments, fluid migration into overlying, partially lithified sediments,

could have resulted in the production of reduced sulphur (via methane oxidation).

Barium carbonate is also directly associated with barite replacement (Figure 5.9). This highlights an interesting aspect of barite replacement, which is mobilisation of barium during barite dissolution. Notably, the qualitative observation that barium carbonate is less abundant than sulphides in the bedded mineralisation raises an interesting question relating to mass balance, and whether it is possible to trace the extent of barium mobilisation. If this were possible, it may provide an indication of how much sulphur was derived from barite replacement, and formed a source of sulphur for the precipitation of sulphides in the bedded mineralisation.

5.7.6. The mass balance of barite replacement

During the replacement of barite by sulphides, mass transfer should result in barium being sequestered into other mineral phases. This occurs locally, with in situ precipitation of barium carbonates, but there is also evidence of a barium halo (of barium feldspars), correlated with subtle alteration (K_2O / Al_2O_3 < 0.2, Figure 2.4; Chapter 2) surrounding the bedded mineralisation at Tom, which may provide a proxy for evaluating the mass balance of the system. If the highest barium samples (~6.5 wt. %) contain barium sourced only from barite, dissolution would result in the release of 1.63 wt. % sulphur. Importantly, this does not factor in the sulphur associated with barium that was only mobilised only on a local scale, which precipitated as barytocalcite and witherite in-situ with sulphides. However, the sulphur represented by the broader barium remobilisation could still account for approximately 5 wt. % Zn or as much as 12 wt. % Pb (more likely a combination of the two). Considering the amount of unaltered barite that remains in the bedded mineralisation, it is worth

speculating that the CD-type deposits at Macmillan Pass could have been much bigger. If barite does form a major source of sulphur for CD-type systems, it may not be coincidental that one of the largest accumulations of barite discovered in the Paleozoic, in the Red Dog district (Kelley and Jennings, 2004), is also associated with world class CD-type mineralisation.

5.8. Conclusions – A model for replacement style mineralisation at Macmillan Pass

The data presented here and in preceding Chapters supports a model of replacement style mineralisation at Macmillan Pass. Firstly, alteration in samples from TYK005 at Tom occurs both above and below the bedded mineralisation. This is characterised by a negative correlation between increasing host rock barium content and decreasing K_2O / Al_2O_3 and bulk rock $\delta^{34}S$ values. Texturally, this is matched by greater disruption to the host rock fabric in samples that are proximal to the vent (e.g. Figure 5.8A). The longevity of hydrothermal activity in a replacement style CD-type system could be much shorter (e.g. Schardt et al. 2008) than one dominated by SEDEX processes (e.g. Turner, 1992). This is more consistent with the discrete nature of the hydrothermal vent, which likely formed from a limited number of well-defined fluid pulses within a relatively small stratigraphic section. This forms a marked contrast to a SEDEX model proposed for the HYC deposit, for which up to 10,000 discrete pulses of fluid flow have been implied to account for the formation of bedded mineralisation (Large et al., 1998).

In Figure 5.16, a schematic model for mineralisation at Macmillan Pass is

presented. In the Late Devonian strata at Macmillan Pass, there is evidence of high biogenic productivity (Chapter 2) and rapid sediment deposition (section 5.7.1; this chapter). The onset of hydrothermal activity, which developed with reactivation of a deep basin penetrating fault, promoted fluid flow at different levels of the basin. The circulation of basinal fluids was enhanced by fault-related permeability, resulting in the upflow of reducing, barium rich fluids into a shallow diagenetic setting where they precipitated as barite (Chapter 3). The development of minor, Late Devonian structures, associated with reactivation of older normal faults may explain the development of barren barite deposits elsewhere. At Tom and Jason, hydrothermal fluids, which acquired base metals from with older, basement derived lithologies from deeper in the basin (section 5.7.2), would have had a longer flow path and fluid ascent. This accounts for the pronounced two-stage paragenesis of the bedded mineralisation, in which early diagenetic assemblages (including barite) are widely overprinted by hydrothermal sulphides.

The hydrothermal fluid entering the vent complex was hot (>250°C) and interacted with a partially lithified host rock to produce carbonate from the alteration of organic matter and earlier diagenetic and hydrothermal carbonate. In Figure 5.17, the different sources of reduced sulphur are proposed in the context of the deposit architecture, from a compilation of $\delta^{34}S$ values from Chapters 3, 4 and previous studies (summarised in section 5.3.3). A key departure from previous models of CD-type mineralisation for the Selwyn Basin is the evidence in support of multiple sources of reduced sulphur, generated via processes operating in a sub-seafloor environment. Recognising these different processes (BSR, TSR, AOM-SR and barite replacement) highlights the diversity of processes operating in CD-type systems.

216

Tables and Figures

Table 5.1. EPMA major element oxide data for barium feldspars.

	SiO_2	Al_2O_3	FeO	MnO	MgO	BaO	CaO	Na_2O	K_2O	
	Celsian $BaAl_2Si_2O_8$									
N	66	66	10	5	45	66	27	66	66	
Mean (wt. %)	34.13	28.74	0.04	0.03	0.02	38.23	0.02	0.14	0.31	
Max	36.19	29.41	0.06	0.04	0.04	39.20	0.07	0.33	1.19	
Min	32.88	27.79	0.03	0.02	0.01	36.35	0.01	0.05	0.04	
% Std Dev	2.32	1.07	28.03	21.71	41.71	2.10	56.06	33.52	79.05	**TOTAL**
apfu	*2.03*	*2.02*	*0.00*	*0.00*	*0.00*	*0.89*	*0.00*	*0.02*	*0.02*	***4.98***
	Hyalophane $(K,Ba)Al(Si,Al)_3O_8$									
N	10	10	3	1	9	10	4	10	10	
Mean (wt. %)	48.99	23.06	0.04	0.03	0.03	20.49	0.03	0.25	6.55	
Max	49.79	23.87	0.06	0.03	0.05	22.04	0.06	0.34	6.97	
Min	47.64	22.63	0.03	0.03	0.01	19.35	0.01	0.13	5.82	
% Std Dev	1.52	1.44	30.07	0.00	36.95	4.55	72.17	25.52	5.37	**TOTAL**
apfu	*2.59*	*1.44*	*0.00*	*0.00*	*0.00*	*0.42*	*0.00*	*0.03*	*0.44*	***4.92***

Detection Limit (3σ)

%	0.012	0.010	0.023	0.020	0.009	0.034	0.011	0.011	0.010

217

Figure 5.1. The bedrock geology of the Macmillan Pass district. Adapted from McClay and Bidwell (1986).
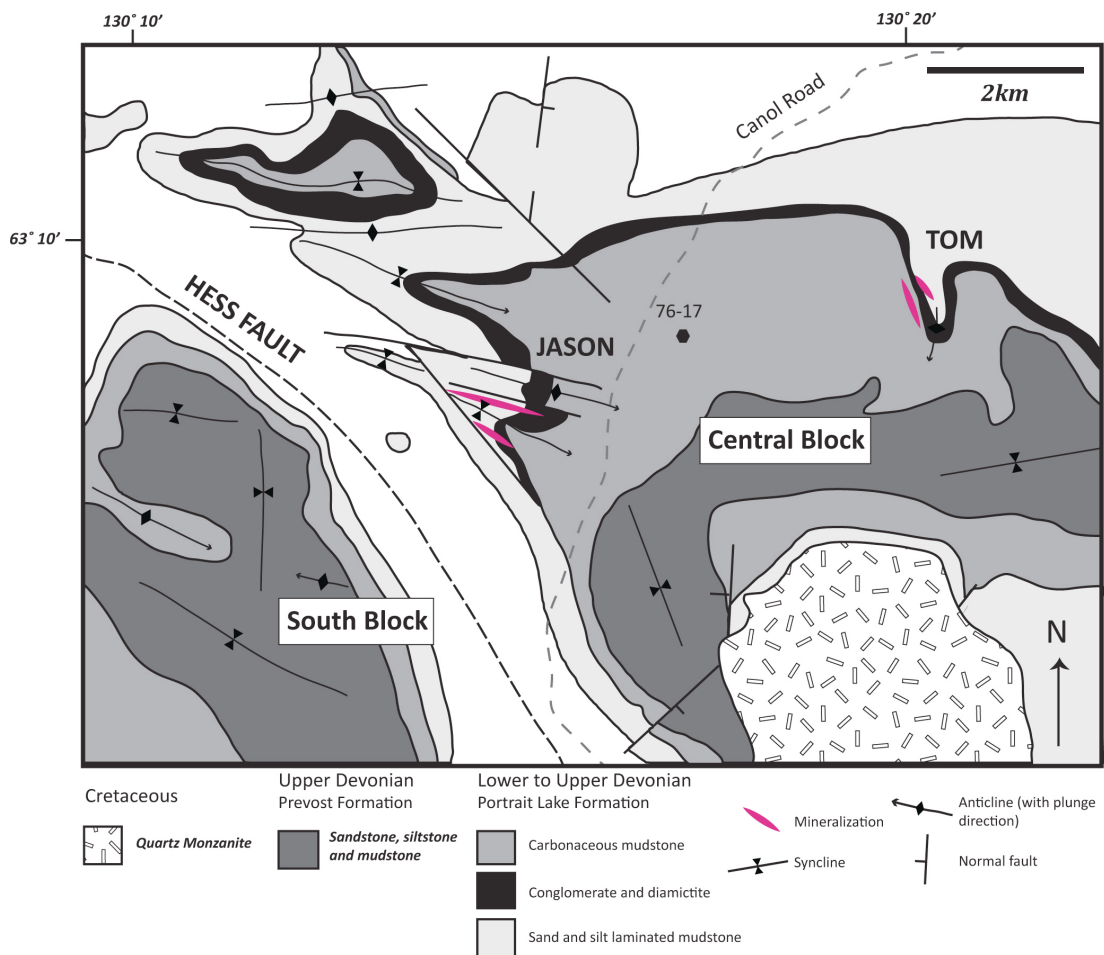
Figure 5.2. The deposit geology of Tom and Jason. Approximate locations of drill-hole collars and plunge direction for drill-cores are denoted by the labeled arrows. A – Geology of the Jason deposit, adapted from Turner (1989). B – Geology of the Tom deposit, adapted from McClay and Bidwell (1986).

Mudstone with coarse sand and grit beds
Silt- and sand-laminated mudstone
Siliceous mudstone / radiolarite
Diamictite
Conglomerate
Mineralization
Vent Complex
Syn-depositional Fault
Syncline
Anticline

200m

TYK005
TYK010
TYK001
TYK002
T91-14

86A
68A

200m

220
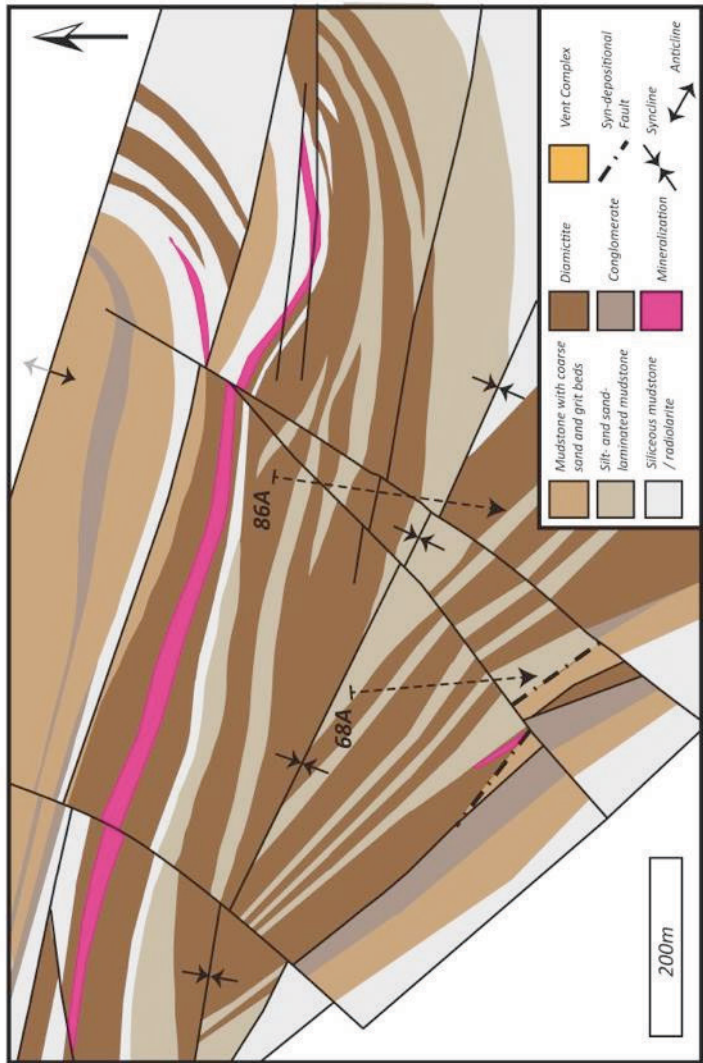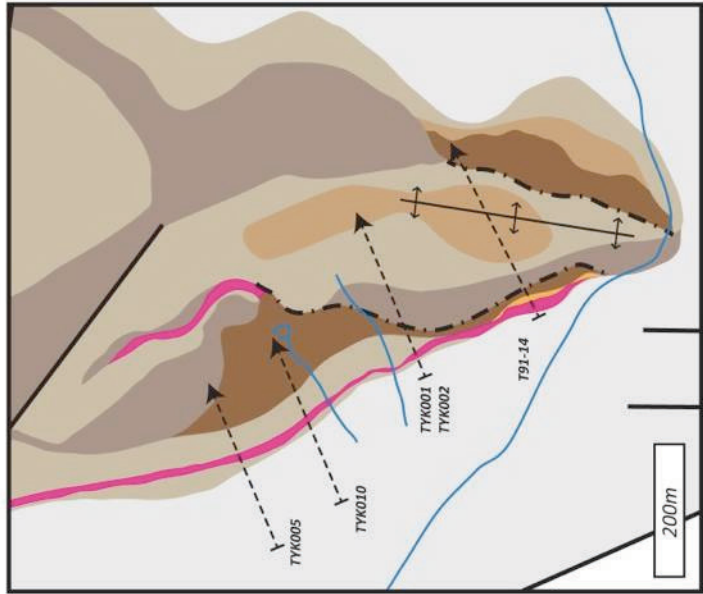
Figure 5.3. Lithological logs for drill-core that was sampled at Tom (DH-TYK005, TYK001 and T91-14) and drill-core from regional drill-hole between Tom and Jason (76-17; see location on Figure 5.1). A stratigraphic correlation (dashed line) has been made according to the common stratigraphic sequence that occurs beneath mineralisation (also described in Chapter 2).

Macmillan Pass Member

Legend:

Hydrothermal Vent

Mineralization

Igneous Dyke

Minor Fault

Silty mudstone

Conglomerate

Olistostrome

Siliceous Mudstone

Inferred Tom Horizon

Core Depth (m)

T91-14

TYK001

TYK005

76-17

222
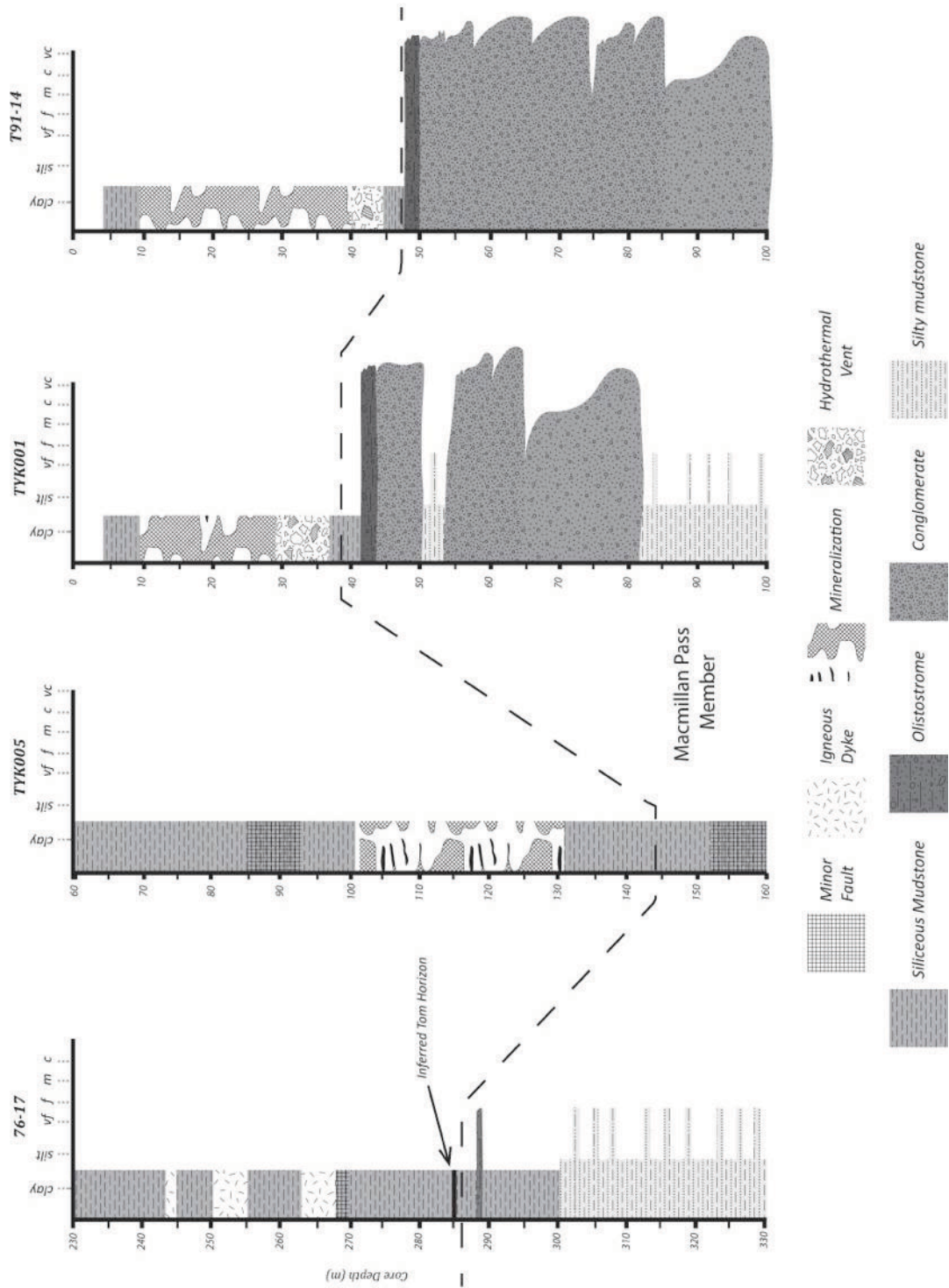
Figure 5.4. Hand sample photographs of the lithologies of the Macmillan Pass Member. A – Silt- and sand- laminated mudstone from DH-68A (600m). Notice the stratiform pyrite that has formed along one of the laminations. B – Mudstone with silt- and sand- interbeds from DH-68A (635m). The main sand contains ripples draped in mud, and the bed below is boudinaged. Towards the top of the sample there is an upward transition from lenticular to flaser bedding. C – Ankerite veined conglomerate from beneath the vent complex at Tom (DH-TYK002; 123.4m).
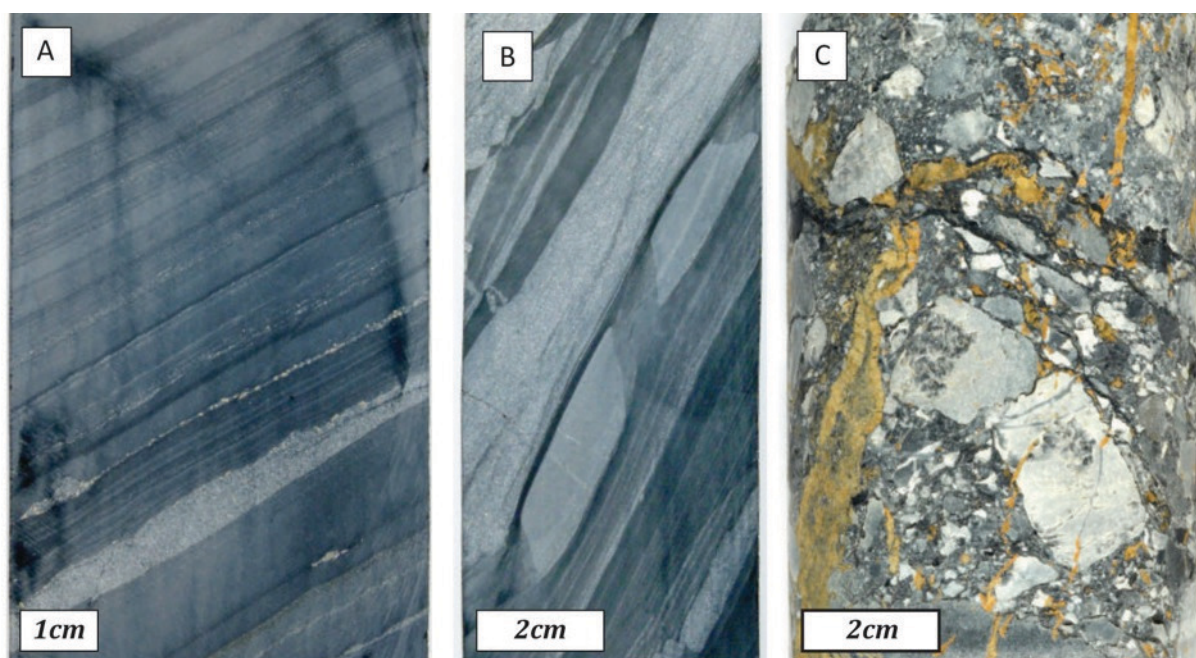
Figure 5.5. Examples of barren and mineralised carbonaceous mudstone from Macmillan Pass. A – A barren mudstone from close to the correlated hydrothermal event horizon in the regional drill-hole (DH-76-17; 282 meters). B – Bedded mineralisation from the Tom deposit (DH-T91-14; 13 meters) with well-preserved host rock beds. C – Cropped photograph of a thin section from the sample in B. Notice the sharp, graded bedding of the host rock. D – Photomicrograph (transmitted light) of lenticular laminations in a bed from the thin section in C.
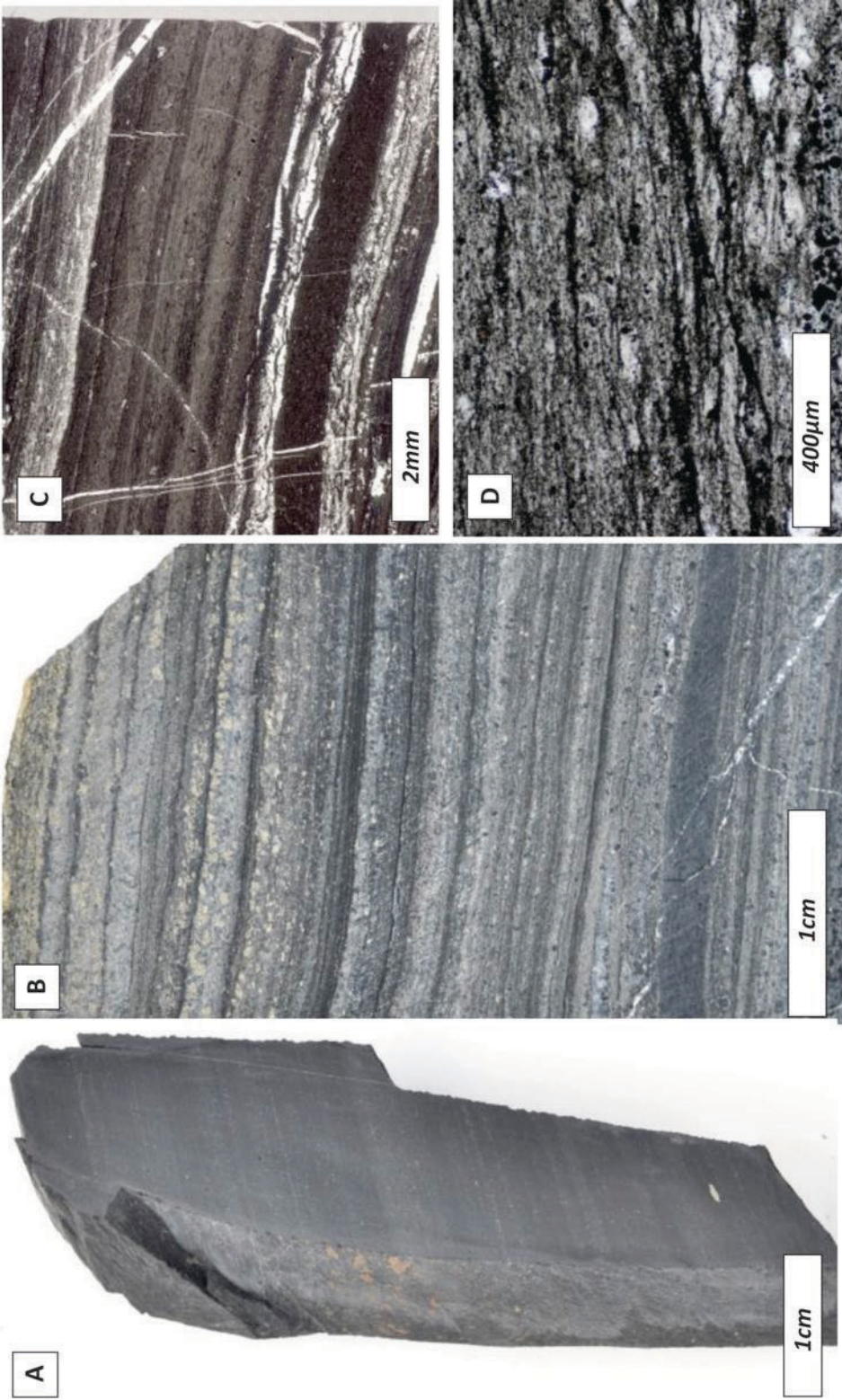
Figure 5.6. Binocular stereoscope photographs of Stage 2 sulphides replacing Stage 1 carbonate in vent complex samples from Jason. A – Sample from DH-86A (711m), with widespread sulphide replacement of ankerite (ank). Notice the black, altered organic matter (pyrobitumen; py-bit) towards the bottom right hand side of the sample. B – A higher resolution image of the sample in A, showing a common replacement texture of ankerite by galena (gn) and pyrrhotite (po).

B

po

gn

ank

1mm

A

po

gn

ank

py-bit

1cm

227
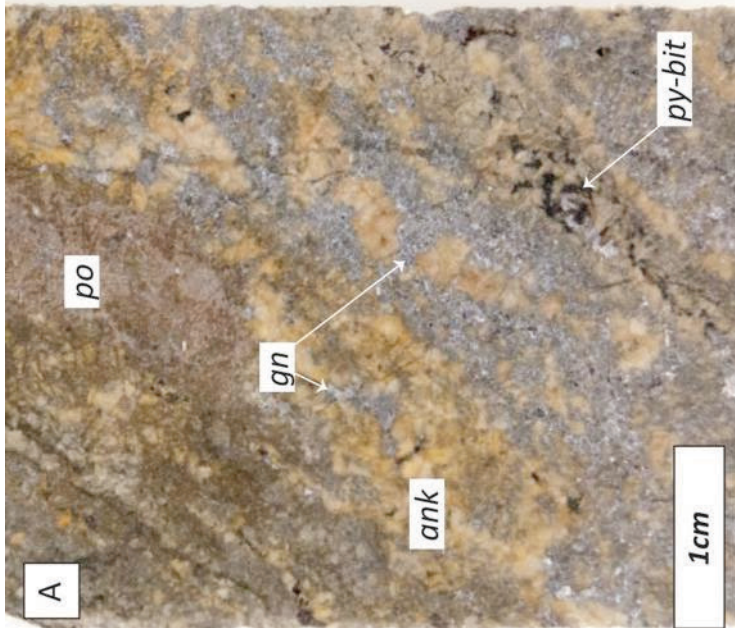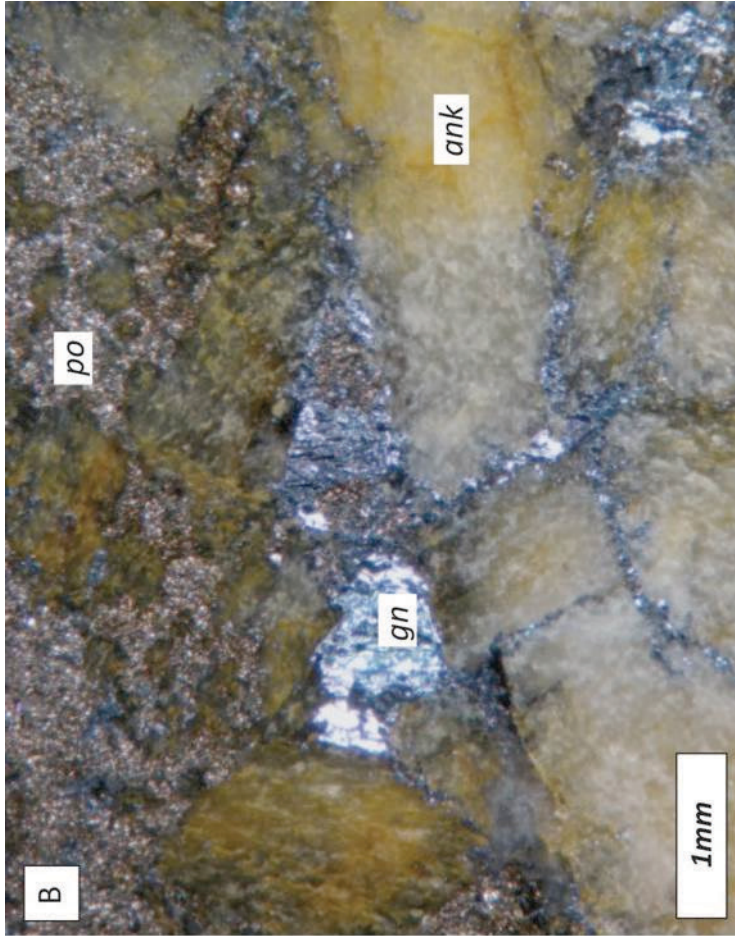
Figure 5.7. Hand sample photomicrographs of hydrothermal veining from marginal vent samples. A – Mudstone crosscut by ankerite veins from directly beneath the vent complex at Tom (DH-T91.14; 44 meters); B – Sample from DH-TYK001 (44m) of conglomerate directly underlying the vent complex at Tom, with a quartz-ankerite-sphalerite vein margined by a stylolite. C – Vent complex ankerite veining overprinting barite from the bedded mineralisation (DH-TYK002; 44m).
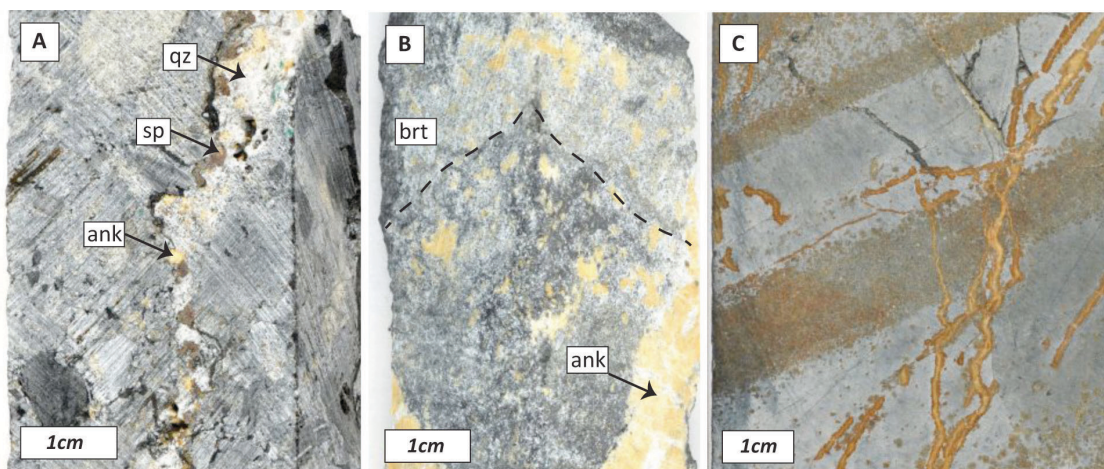
Figure 5.8. Photographs of bedded mineralisation, showing the textural transition upwards from the vent complex at Tom (DH-TYK002). A – Sample from 28.6m, with clear disruption to the laminated fabric of the rock. Preservation of the host rock is limited to the fine, dark grey laminations, and the dominant mineralogy is barite (light grey to white), barytocalcite and witherite (chalk white) and sphalerite (orange). B – Sample from 25.4m, with greater host rock preservation than A. The dark grey crystals in the mudstone bed are barium feldspar. C – Sample from 19m, with fine, crinkly laminations of host rock between more diffuse barite laminations.
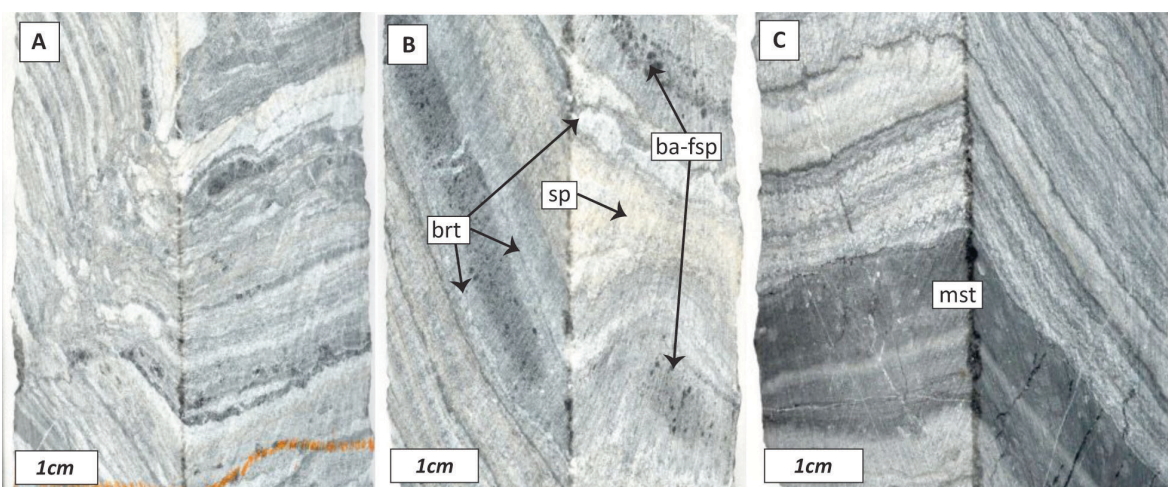
Figure 5.9. Sphalerite replacing barite, with associated barytocalcite. A – Cropped photograph of thin section in crossed polarised light, showing barytocalcite (ba-cc) halo around sphalerite (sp), within barite (brt). B – Reflected light photomicrograph of area highlighted by red box in A, showing sphalerite as an interstitial phase concentrated in a band within barite. C – Cross polarised photomicrograph of B, with barytocalcite identifiable by its anomalous birefringence.

231
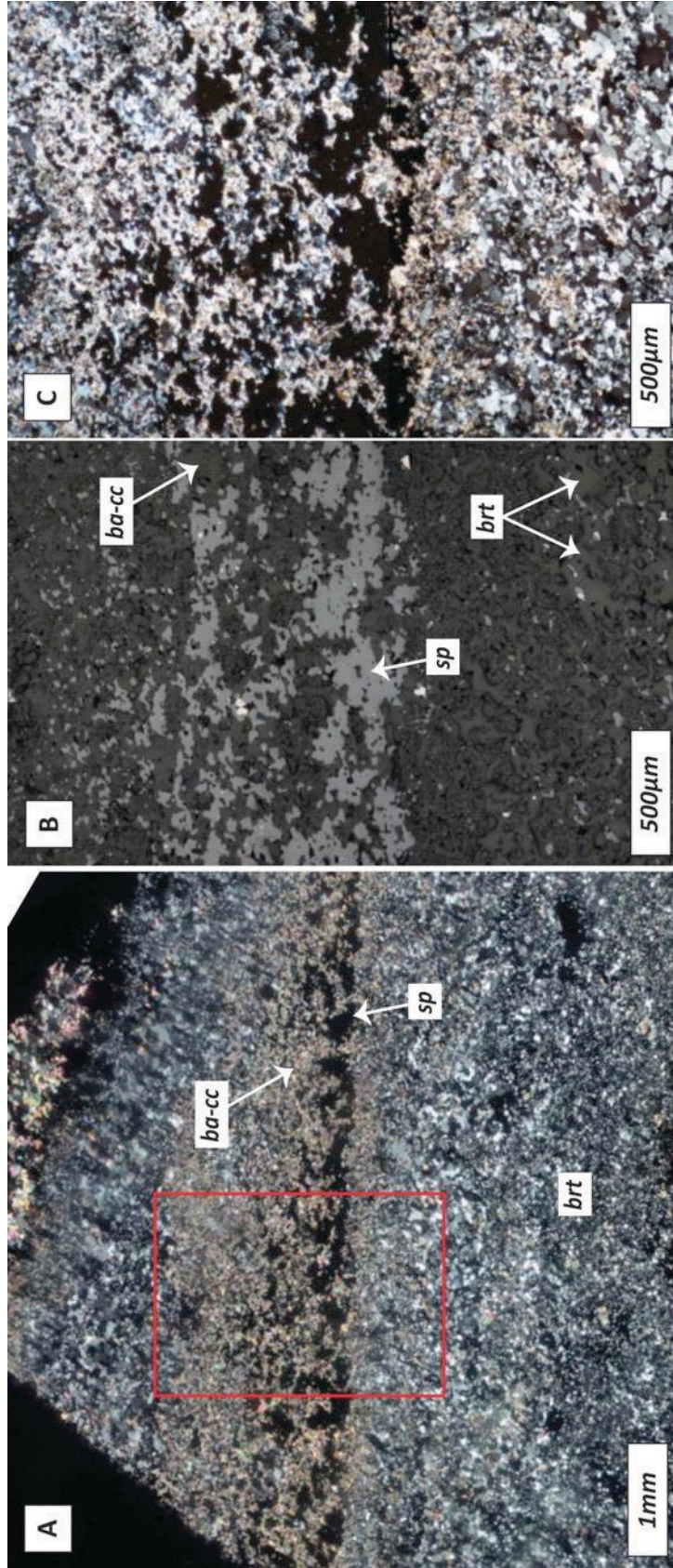
Figure 5.10. Photomicrographs of barium feldspars and sulphide replacement of barite. A – Galena (gn) interstitial to barite (brt), with celsian (cn) in disequilibrium with both phases (reflected light). B – Celsian crystals concentrated along the top of a mudstone bed, beneath stratiform barite and overprinted by sphalerite (sp) (reflected light). C – Cross polarised image of B.
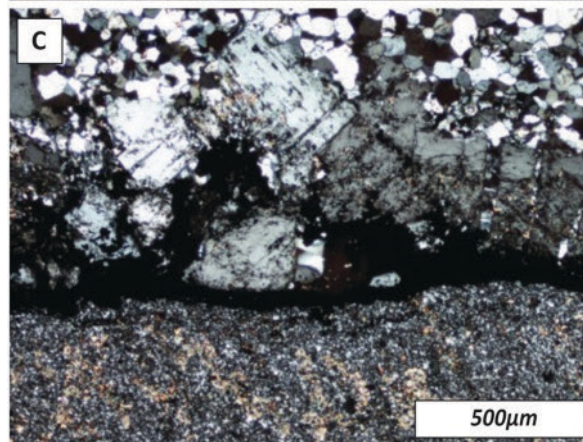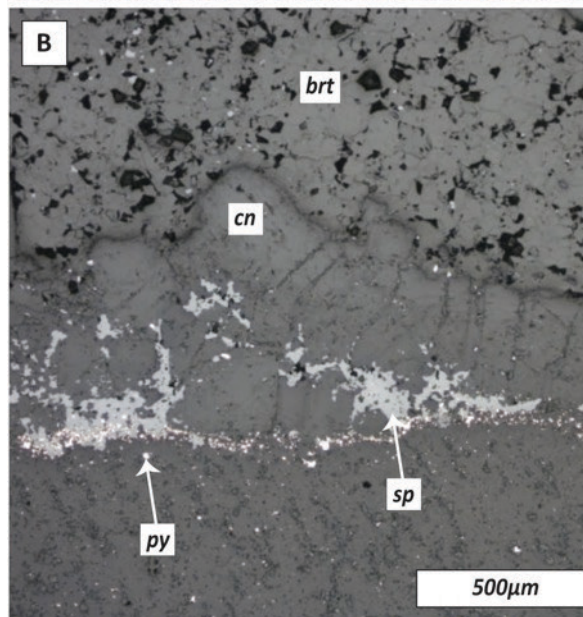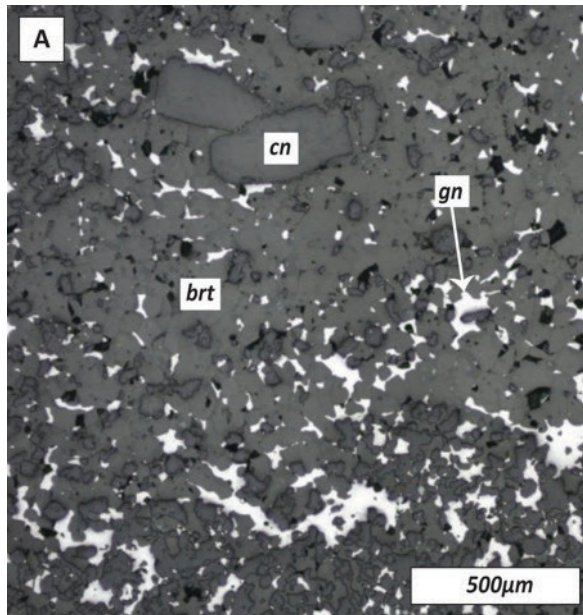
Figure 5.11. Replacement style veinlet in bedded mineralisation at Tom. A – Hand sample from DH-T91-14 (13 meters) showing well-preserved stratiform textures crosscut by an irregular veinlet. B – Annotated photograph of a thin section made from hand sample in A. Red dotted line highlights the veinlet, which crosscuts beds before developing along a stratiform horizon. C – Photomicrograph of white box from B (reflected light). Sphalerite precipitation concentrated along a stratiform horizon, overprinting earlier formed minerals such as celsian (cn).
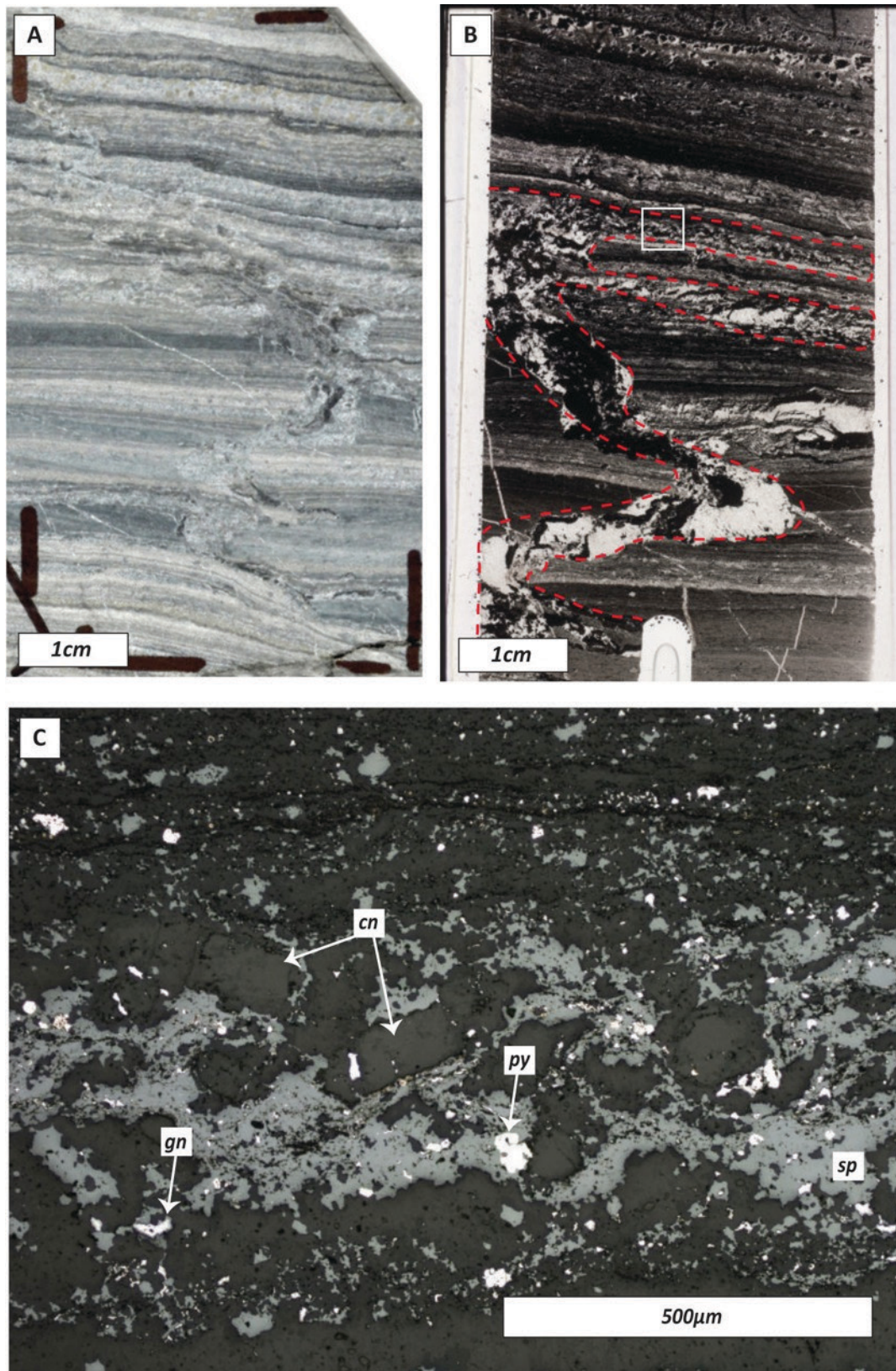
Figure 5.12. $\delta^{18}O$ vs. $\delta^{13}C$ values of carbonate samples from the Tom and Jason deposits. Samples of alteration and vent veining from Tom and Jason are ankerite, in contrast with barytocalcite from veinlets in the bedded mineralisation.
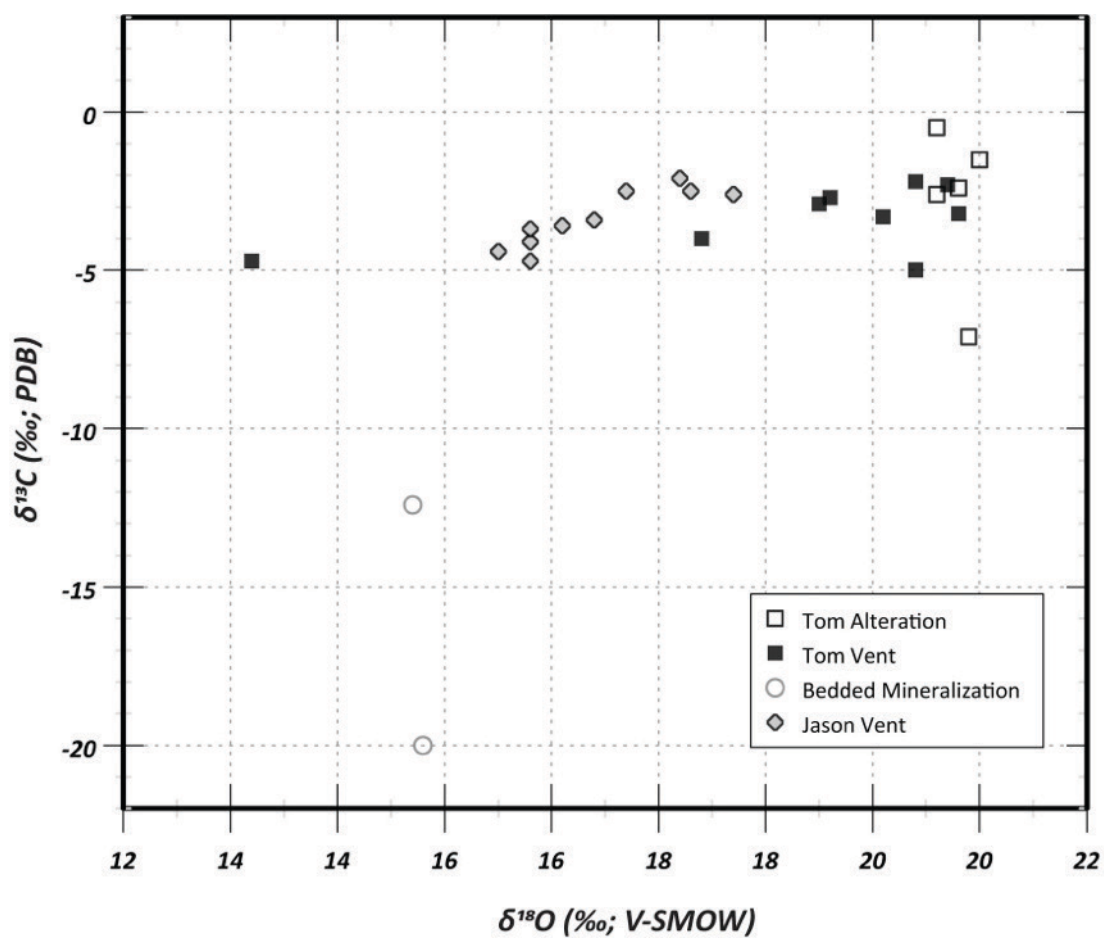
Figure 5.13. Histogram of ^{87}Sr/^{86}Sr values for carbonates at Tom and Jason. Includes ankerite from the Tom and Jason vent complexes and two samples of barytocalcite from veinlets in the bedded mineralisation at Tom. Dots represent individual samples from Jason and Tom, and the blue bar represents the ^{87}Sr/^{86}Sr value of Late Devonian seawater (Denilson et al. 1997).
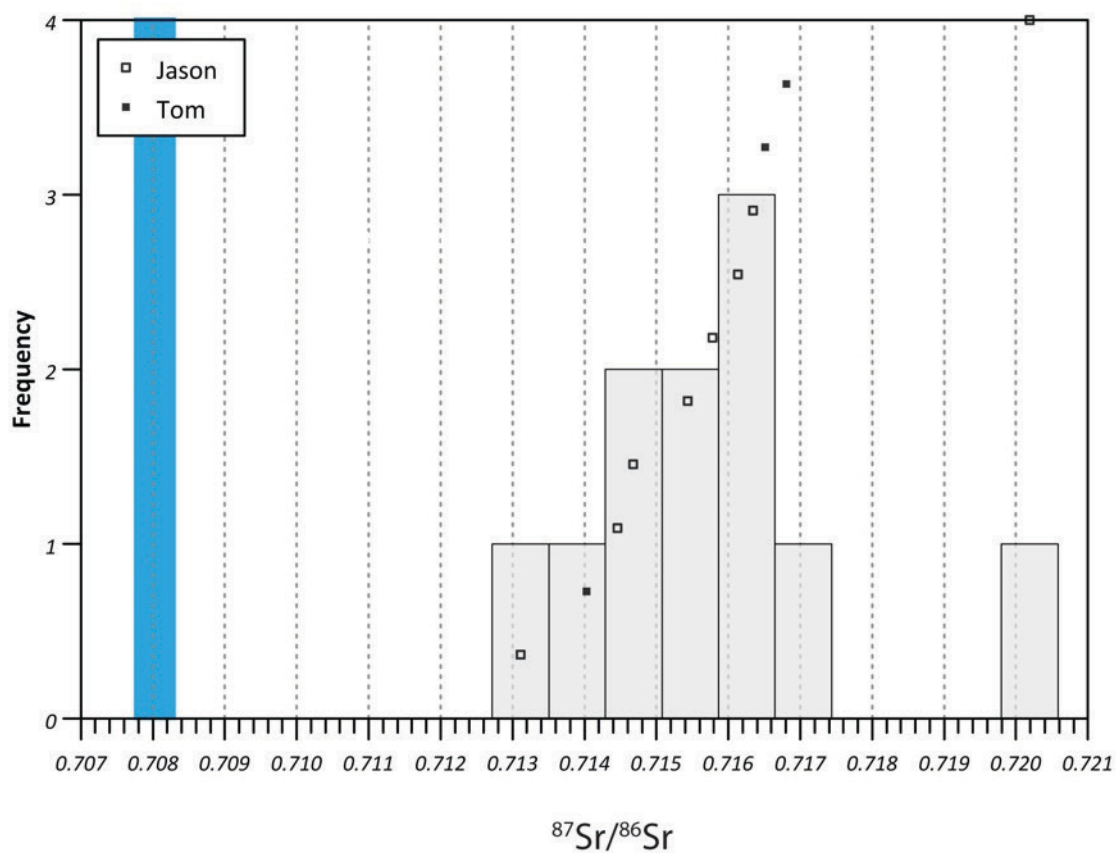
Figure 5.14. Modeling of fluid rock interaction for $\delta^{18}O$ vs. $\delta^{13}C$ values from ankerite in the Tom and Jason vent complexes. The initial fluid compositions, with respect to $\delta^{18}O$ vs. $\delta^{13}C$ values, are labeled in the boxes, with fractionation curves for temperature dependent model (linear) and a combined temperature dependent–fluid rock interaction (curvilinear) model. Equations of Horita (2014) and Taylor (1987) were used in the modeling. The data from the Jason vent (alteration and veining) are particularly well described by the combined model.
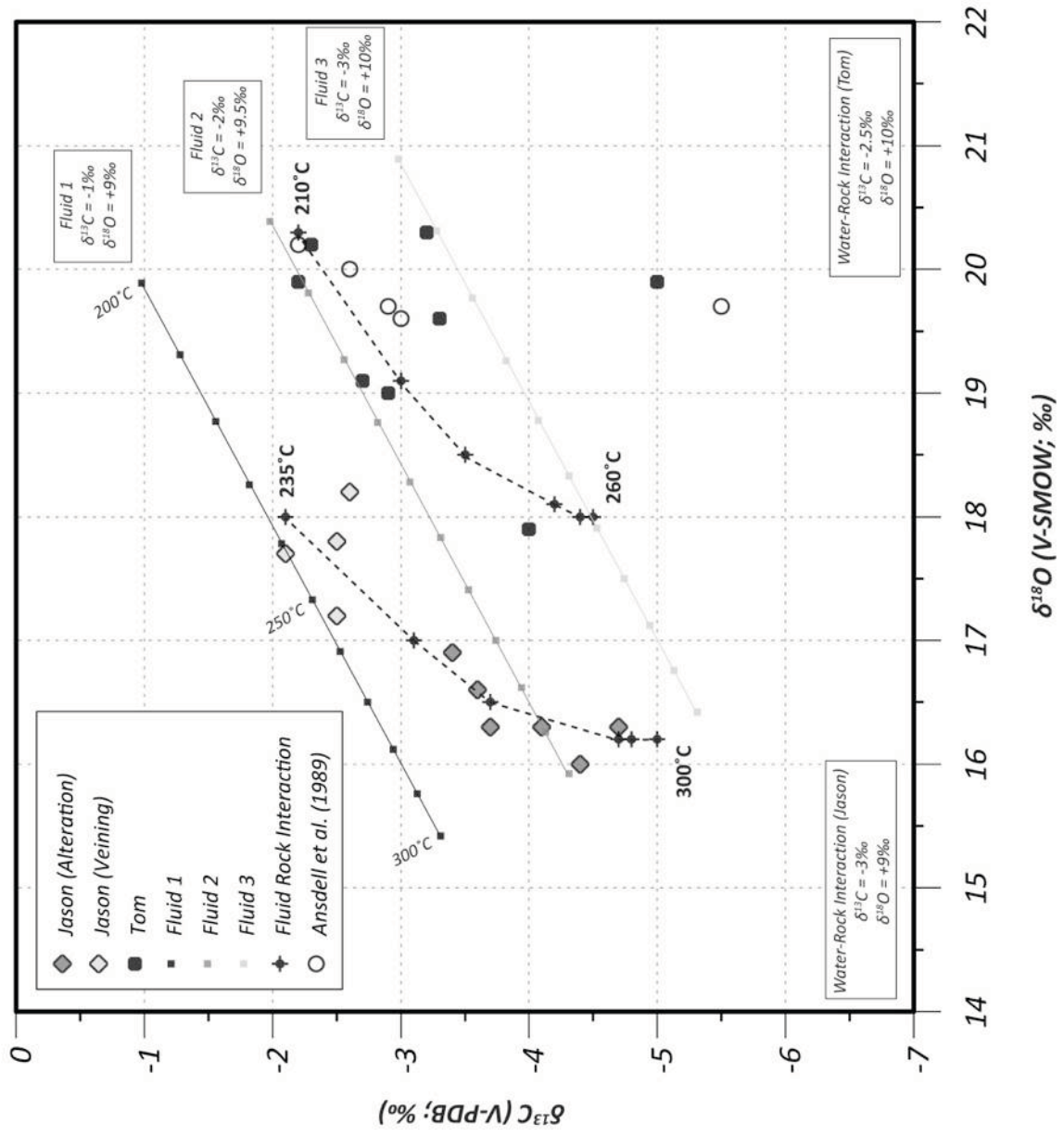
Figure 5.15. δ^{13}C values vs. ^{87}Sr/^{86}Sr cross plot.
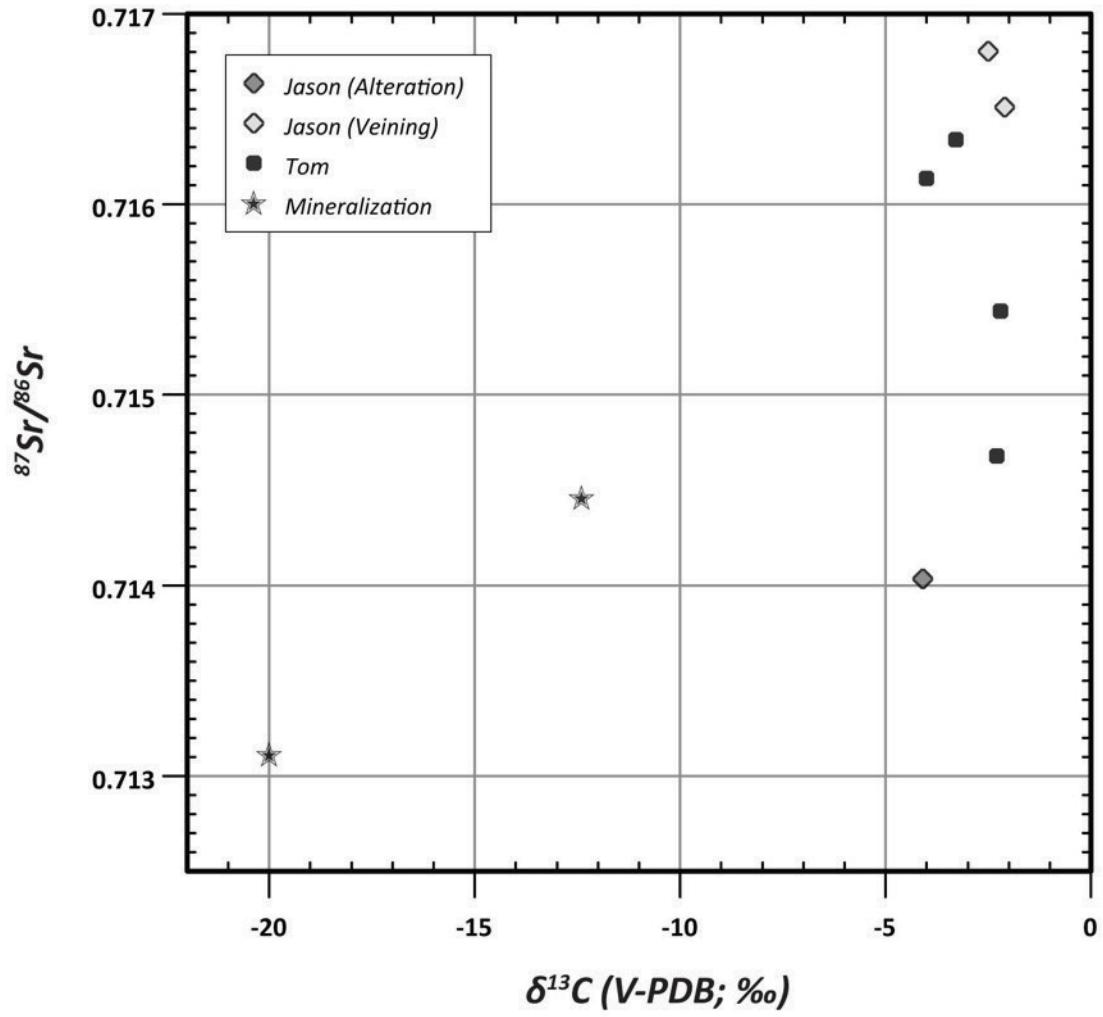
Figure 5.16. Schematic model for the development of CD-type mineralisation at Macmillan Pass. Metals are sourced from basement derived rift clastics, whereas barium originates from reducing pore fluids associated with carbonaceous mustones at a shallow level in the basin. Stratiform barite is associated with faults that do not penetrate deep into the basin. Box highlights the area presented in Figure 17.
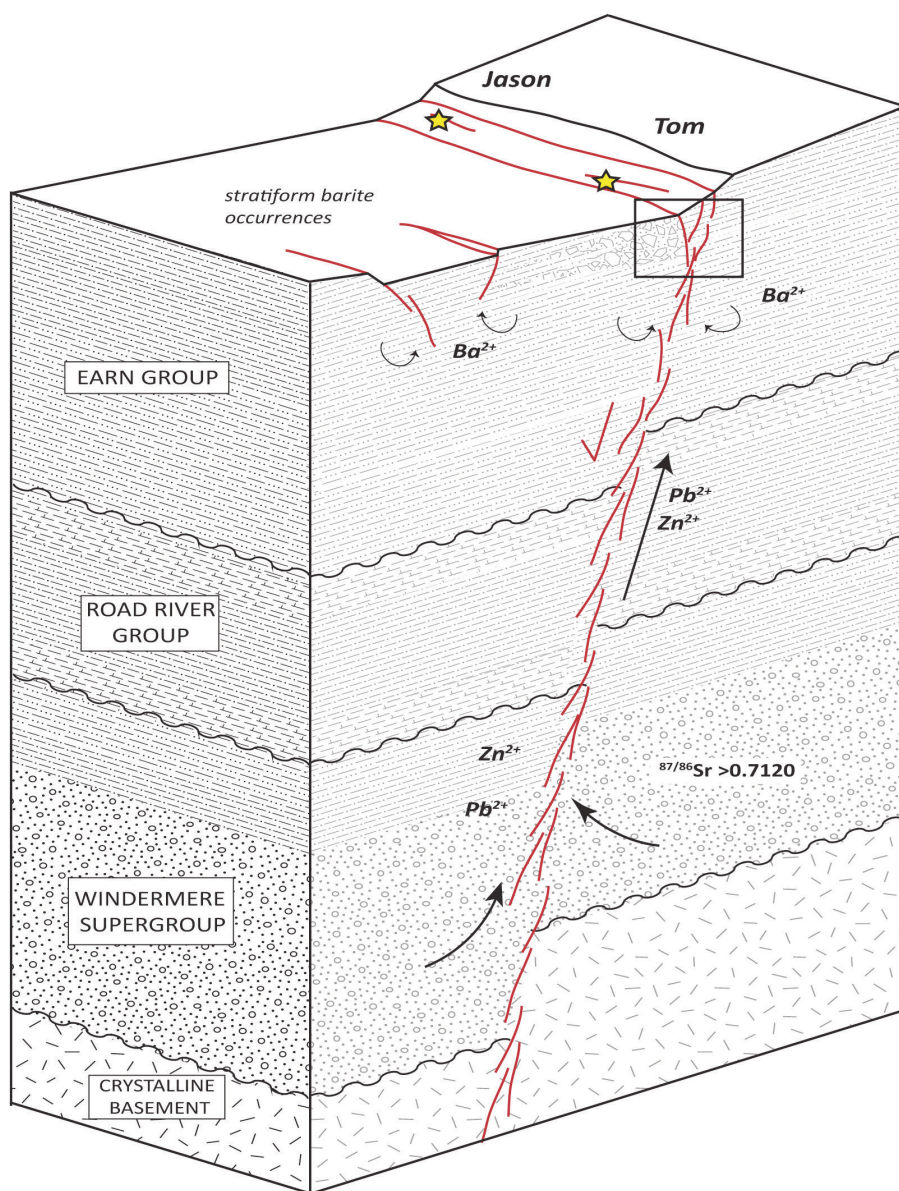
Figure 5.17. Schematic of the alteration profile and sources of reduced sulphur in the Tom and Jason CD-type deposits. The operation of bacteriogenic sulphate reduction (BSR), anaerobic oxidation of methane coupled with sulphate reduction (AOM-SR) and barite replacement combine to produce the broad range of $\delta^{34}S$ values that occur in the bedded mineralisation. A schematic $\delta^{34}S$ curve has been drawn through the line A' to A, and the different pathways of sulphate reduction are labelled on the right hand side. The blue bar represents the $\delta^{34}S$ value of Late Devonian seawater sulphate (John et al. 2010).
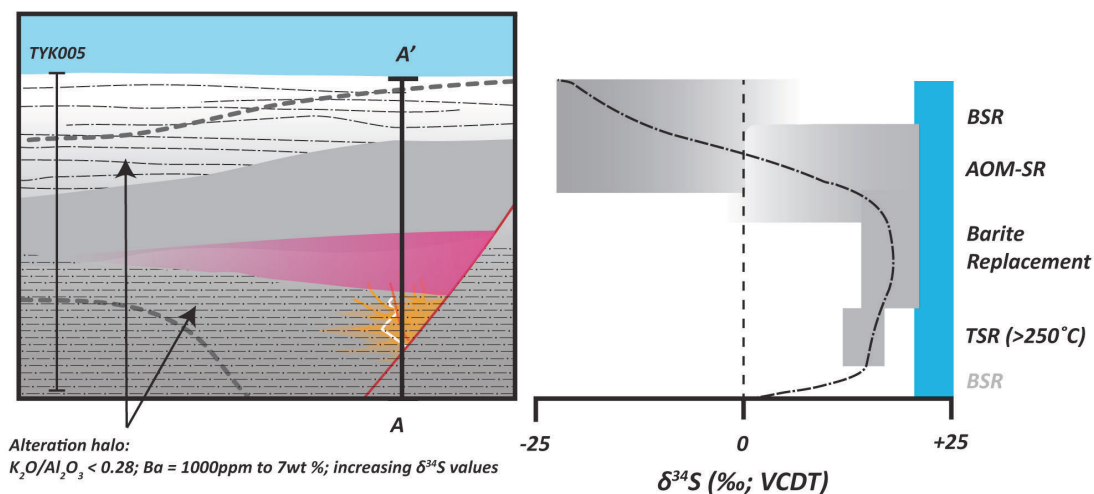
References

Abbott J. G. (1982) Structure and stratigraphy of the Macmillan Fold Belt: evidence for Devonian faulting. In *Yukon Geology and Exploration* Department of Inidian Affairs and Northern Development Canada. pp. 22–23.

Abbott J. G. and Turner R. J. (1991) Character and paleotectonic setting of Devonian stratiform sediment-hosted Zn, Pb, Ba deposits, Macmillan Fold Belt, Yukon. In *Geological Survey of Canada Open File 2169* (eds. J. G. Abbott and R. J. Turner). pp. 99–136.

Ansdell K. M., Nesbitt B. E. and Longstaffe F. J. (1989) A Fluid Inclusion and Stable Isotope Study of the Tom Ba-Pb-Zn Deposit, Yukon Territory, Canada. *Econ. Geol.* **84**, 841–856.

Bailes R. J., Smee B. W., Blackader D. W. and Gardner H. D. (1986) Geology of the Jason Lead-Zinc-Silver Deposits, Macmillan Pass, Eastern Yukon. In *Mineral Deposits of Northern Cordillera* (ed. J. A. Morin). The Canadian Institute of Mining and Metallurgy. pp. 87–99.

Borowski W. S., Rodriguez N. M., Paull C. K. and Ussler W. (2013) Are [34]S-enriched authigenic sulfide minerals a proxy for elevated methane flux and gas hydrates in the geologic record? *Mar. Pet. Geol.* **43**, 381–395.

Buzon M. R., Simonetti A. and Creaser R. a. (2007) Migration in the Nile Valley during

the New Kingdom period: a preliminary strontium isotope study. *J. Archaeol. Sci.* **34**, 1391–1401.

Campbell A. R. and Larson P. B. (1998) Introduction to stable isotope applications in hydrothermal systems. In *Techniques in Hydrothermal Ore Deposits Geology* (eds. J. P. Richards and A. R. Larson). Society of Economic Geologists, Littleton.

Carne R. C. and Cathro R. J. (1982) Sedimentary exhalative (sedex) zinc-lead-silver deposits, northern Canadian Cordillera. *Can. Min. Metall. Bull.* **75**, 66–78.

Denison R. E., Koepnick R. B., Burke W. H., Hetherington E. A. and Fletcher A. (1997) Construction of the Silurian and Devonian seawater ^{87}Sr/^{86}Sr curve. *Chem. Geol.* **140**, 109–121.

Eisbacher G. H. (1985) Late proterozoic rifting, glacial sedimentation, and sedimentary cycles in the light of Windermere deposition, Western Canada. *Palaeogeogr. Palaeoclimatol. Palaeoecol.* **51**, 231–254.

Eldridge C. S., Williams N. and Walshe J. L. (1993) Sulfur isotope variability in sediment-hosted massive sulfide deposits as determined using the ion microprobe SHRIMP: II. A study of the H.Y.C. deposit at McArthur River, Northern Territory, Australia. *Econ. Geol.* **88**, 1–26.

Fernandes N. A. (2011) Geology and Geochemistry of Late Devonian-Mississippian Sediment-Hosted Barite Sequences of the Selwyn Basin, NWT and Yukon, Canada. University of Alberta.

Galley A. G., Hannington M. and Jonasson I. (2007) Volcanogenic massive sulphide

deposits. In *Mineral deposits of Canada: a synthesis of major deposit-types, district metallogeny, the evolution of geological provinces, and exploration methods* (ed. W. D. Goodfellow). pp. 141–161.

Gardner D. H. (1983) Petrologic and geochemical constraints on genesis of the Jason Pb-Zn deposits, Yukon Territory. University of Calgary.

Gardner H. D. and Hutcheon I. (1985) Geochemistry, Mineralogy, and Geology of the Jason Pb-Zn Deposits, Macmillan Pass, Yukon, Canada. *Econ. Geol.* **80**, 1257–1276.

Goldhaber M. B. and Kaplan I. R. (1975) Controls and consequences of sulfate reduction rates in recent marine sediments. *Soil Sci.* **119**, 42–55.

Goodfellow W. D. (1987) Anoxic Stratified Oceans as a Source of Sulphur in Sediment-Hosted Stratiform Zn-Pb Deposits (Selwyn Basin, Yukon, Canada). *Chem. Geol.* **65**, 359–382.

Goodfellow W. D., Cecile M. P. and Leybourne M. I. (1995) Geochemistry, petrogenesis, and tectonic setting of lower Paleozoic alkalic and potassic volcanic rocks, Northern Canadian Cordilleran miogeocline. *Can. J. Earth Sci.* **32**, 1236–1254.

Goodfellow W. D. and Jonasson I. R. (1986) Environment of formation of the Howards Pass (XY) Zn-Pb deposit, Selwyn Basin, Yukon. In *Mineral Deposits of Northern Cordillera* (ed. J. A. Morin). The Canadian Institute of Mining and Metallurgy. pp. 19–50.

Goodfellow W. D. and Jonasson I. R. (1984) Ocean stagnation and ventilation defined by 34-S secular trends in pyrite and barite, Selwyn Basin, Yukon. *Geology* **12**, 583–586.

Goodfellow W. D. and Lydon J. W. (2007) Sedimentary Exhalative (SEDEX) Deposits. In *Mineral Deposits of Canada: A Synthesis of Major Deposit-Types, District Metallogeny, the Evolution of Geological Provinces, and Exploration Methods* pp. 163–183.

Goodfellow W. D., Lydon J. W. and Turner R. J. (1993) Geology and genesis of stratiform sediment-hosted (SEDEX) zinc-lead-silver sulphide deposits. In *Mineral Deposit Modeling* (eds. R. W. Kirkham, R. Sinclair, R. I. Thorpe, and J. M. Duke). Geological Association of Canada. pp. 201–252.

Goodfellow W. D. and Rhodes D. (1991) Geological setting, geochemsitry and origin of the Tom stratiform Zn-Pb-Ag-barite deposits. In *Geological Survey of Canada Open File 2169* (eds. J. G. Abbott and R. J. Turner). pp. 177–239.

Goodfellow W. D. and Turner R. J. W. (1988) Sulfur isotope variability in sediment-hosted massive sulfide deposits as determined using the ion microprobe SHRIMP: I. An example from the Rammelsberg Orebody – a discussion. *Econ. Geol.* **84**, 451–452.

Gordey S. P. (1981) *Geology of the Nahanni map-area, Yukon Territory and District of Mackenzie.*,

Gordey S. P. and Anderson R. G. (1993) *Evolution of the northern cordilleran miogeocline, Nahanni map area (105I), Yukon and Northwest Territories.*

Memoir 428., Geological Survey of Canada, Memoir 428.

Gordey S. P., Macdonald J. D., Turner E. C. and Long D. G. F. (2010) Structural Geology of the Central Mackenzie Mountains. In *Geology of the central Mackenzie mountains of the North Canadian Cordillera, Sekwi Mountain (105P), Mount Eduni (106A), and northwestern Wrigley Lake (95M) map-areas, Northwest Territories* (eds. E. Martel, E. C. Turner, and B. J. Fischer). NWT Geoscience Office. pp. 215–250.

Gromek P., Gleeson S. a. and Simonetti A. (2012) A basement-interacted fluid in the N81 deposit, Pine Point Pb-Zn District, Canada: Sr isotopic analyses of single dolomite crystals. *Miner. Depos.* **47**, 749–754.

Hemley J. J. and Hunt J. P. (1992) Hydrothermal ore-forming processes in the light of studies in rock-buffered systems; II, Some general geologic applications. *Econ. Geol.* **87**, 23–43.

Irwin S. E. B. and Orchard M. J. (1991) Upper Devonian–Lower Carboniferous conodont biostratigraphy of the Earn Group and overlying units, northern Cordillera. In *Ordovician to Triassic Conodont Paleontology of the Canadian Cordillera* (eds. M. J. Orchard and A. D. McCracken). Geological Survey of Canada, Bulletin 417. pp. 185–213.

Jakubowicz M., Dopieralska J. and Belka Z. (2015) Tracing the composition and origin of fluids at an ancient hydrocarbon seep (Hollard Mound, Middle Devonian, Morocco): A Nd, REE and stable isotope study. *Geochim. Cosmochim. Acta* **156**, 50–74.

Kelley K. D., Dumoulin J. A. and Jennings S. (2004) The Anarraaq Zn-Pb-Ag and Barite Deposit, Northern Alaska: Evidence for Replacement of Carbonate by Barite and Sulfides. *Econ. Geol.* **99**, 1577–1591.

Kelley K. K. and Jennings S. (2004) A Special Issue Devoted to Barite and Zn-Pb-Ag Deposits in the Red Dog District, Western Brooks Range, Northern Alaska. *Econ. Geol.* **99**, 1267–1280.

Large R. R., Bull S. W., Cooke D. R. and Mcgoldrick P. J. (1998) A genetic model for the HYC deposit, Australia: Based on regional sedimentology, geochemistry, and sulfide-sediment relationships. *Econ. Geol.* **93**, 1345–1368.

Large R. R., Bull S. W., McGoldrick P. J., Walters S., Derrick G. M. and Carr G. R. (2005) Strata-Bound and Stratiform Zn-Pb-Ag Deposits in Proterozoic Sedimentary Basins, Northern Australia. *Econ. Geol.*, 931– 963.

Leach D. L., Bradley D. C., Huston D., Pisarevsky S. A., Taylor R. D. and Gardoll J. (2010) Sediment-Hosted Lead-Zinc Deposits in Earth History. *Econ. Geol.* **105**, 593–625.

Longstaffe F. J., Nesbitt B. E. and Muehlenbachs K. (1982) *Oxygen isotope geochemistry of the shales hosting Pb-Zn-Ba mineralization at the Jason prospect, Selwyn Basin, Yukon.*,

Machel H. G. and Cavell P. A. (1999) Low-flux, tectonically induced squeegee fluid flow ("hot flash") into the Rocky Mountain Foreland Basin. *Bull. Can. Pet. Geol.* **47**, 510–533.

Machel H. G., Krouse H. R. and Sassen R. (1995) Products and distinguishing criteria of bacterial and thermochemical sulfate reduction. *Appl. Geochemistry* **10**, 373–389.

Macquaker J. H. S., Taylor K. G. and Gawthorpe R. L. (2007) High-Resolution Facies Analyses of Mudstones: Implications for Paleoenvironmental and Sequence Stratigraphic Interpretations of Offshore Ancient Mud-Dominated Successions. *J. Sediment. Res.* **77**, 324–339.

McClay K. R. and Bidwell G. E. (1986) Geology of the Tom deposit, Macmillan Pass, Yukon. In *Mineral Deposits of Northern Cordillera* (ed. J. A. Morin). The Canadian Institute of Mining and Metallurgy. pp. 100–114.

McCollom T. M. and Seewald J. S. (2007) Abiotic synthesis of organic compounds in deep-sea hydrothermal environments. *Chem. Rev.* **107**, 382–401.

Nelson J. and Colpron M. (2007) Tectonics and metallogeny of the British Columbia, Yukon and Alaskan Cordillera, 1.8 Ga to the present. *Miner. Depos. Canada A Synth. Major Depos. Dist. Metallog. Evol. Geol. Prov. Explor. Methods* **2703**, 755–791.

Nelson J. L., Survey B. C. G., Box P. O., Govt S. P., Columbia B., Colpron M., Piercey S. J., Road R. L., Dusel-bacon C., Park M. and Murphy D. C. (2006) Paleozoic tectonic and metallogenetic evolution of pericratonic terranes in Yukon , northern British Columbia and eastern Alaska 1. *GAC Spec. Pap. 45*, 323–360.

Nelson J., Paradis S., Christensen J. and Gabites J. (2002) Canadian Cordilleran Mississippi Valley-Type Deposits : A Case for Devonian-Mississippian Back-Arc

Hydrothermal Origin. *Econ. Geol.* **97**, 1013–1036.

Ohmoto H. and Goldhaber M. B. (1997) Sulfur and Carbon Isotopes. In *Geochemistry of Hydrothermal Ore Deposits* (ed. H. L. Barnes). John Wiley & Sons. pp. 517–612.

Orberger B., Gallien J.-P., Pinti D. L., Fialin M., Daudin L., Gröcke D. R. and Pasava J. (2005) Nitrogen and carbon partitioning in diagenetic and hydrothermal minerals from Paleozoic Black Shales, (Selwyn Basin, Yukon Territories, Canada). *Chem. Geol.* **218**, 249–264.

Plint a. G., Macquaker J. H. S. and Varban B. L. (2012) Bedload Transport of Mud Across A Wide, Storm-Influenced Ramp: Cenomanian-Turonian Kaskapau Formation, Western Canada Foreland Basin. *J. Sediment. Res.* **82**, 801–822.

Rye D. M. and Williams N. (1981) Studies of the Base Metal Sulfide Deposits at McArthur River, Northern Territory, Australia: III. The Stable Isotope Geochemistry of the H.Y.C., Ridge, and Cooley Deposits. *Econ. Geol.*

Schieber J., Krinsley D. and Riciputi L. (2000) Diagenetic origin of quartz silt in mudstones and implications for silica cycling. *Nature* **406**, 981–5.

Schieber J., Southard J. B. and Schimmelmann A. (2010) Lenticular Shale Fabrics Resulting from Intermittent Erosion of Water-Rich Muds--Interpreting the Rock Record in the Light of Recent Flume Experiments. *J. Sediment. Res.* **80**, 119–128.

Schwinn G., Wagner T., Baatartsogt B. and Markl G. (2006) Quantification of mixing processes in ore-forming hydrothermal systems by combination of stable isotope

and fluid inclusion analyses. *Geochim. Cosmochim. Acta* **70**, 965–982.

Spangenberg J., Fontboté L., Sharp Z. D. and Hunziker J. (1996) Carbon and oxygen isotope study of hydrothermal carbonates in the zinc-lead deposits of the San Vicente district, central Peru: a quantitative modeling on mixing processes and CO2 degassing. *Chem. Geol.* **2541**.

Taylor B. D. (1987) Stable isotope geochemistry of ore-forming fluids. In *Short Course Handbook* Mineralogical Association of Canada. pp. 337–445.

Turner R. J. (1991) Jason stratiform Zn-Pb-barite deposit, Selwyn Basin, Canada (NTS 105-0-1): geological setting, hydrothermal facies and genesis. In *Geological Survey of Canada Open File 2169* (eds. J. G. Abbott and R. J. Turner). pp. 137–175.

Turner R. J. . (1986) The genesis of stratiform lead-zinc deposits, Jason property, Macmillan Pass, Yukon. Stanford University.

Turner R. J. W. (1992) Formation of Phanerozoic stratiform sediment-hosted zinc-lead deposits : Evidence for the critical role of ocean anoxia. *Chem. Geol.* **99**, 165–188.

Turner R. J. W., Goodfellow W. D. and Taylor B. D. (1989) Isotopic Geochemistry of the Jason stratiform sediment-hosted zinc-lead deposit, Macmillan Pass, Yukon. In *Current Research, Geological Survey of Canada, Paper 89-1E* pp. 21–30.

Wankel S. D., Adams M. M., Johnston D. T., Hansel C. M., Joye S. B. and Girguis P. R. (2012) Anaerobic methane oxidation in metalliferous hydrothermal sediments: influence on carbon flux and decoupling from sulfate reduction. *Environ.*

Microbiol. **14**, 2726–40.

Williams N. (1978) Studies of the Base Metal Sulfide Deposits at McArthur River, Northern Territory, Australia: I. the Cooley and Ridge Deposits. *Econ. Geol.*

Winn R. D. and Bailes R. J. (1987) Stratiform lead-zinc sulfides, mudflows, turbidites: Devonian sedimentation along fault scarp of extensional origin, Jason deposit, Yukon Territory, Canada. *Geol. Soc. Am. Bull.* **98**, 528–539.

Zheng Y. F. (1990) Carbon-oxygen isotopic covariation in hydrothermal calcite during degassing of CO_2 - A quantitative evaluation and application to the Kushikino gold mining area in Japan. *Miner. Depos.* **25**, 246–250.

Chapter 6. Conclusions

Clastic-dominated Pb-Zn sulphide (CD-type) deposits represent anomalous accumulations of reduced sulphur in sedimentary basins (Leach et al., 2005; Leach et al., 2010). The distribution of CD-type deposits within the geologic record is irregular, and they are typically hosted in lithologies deposited during periods of low seawater sulphate concentrations (Wilkinson, 2014). This represents a key obstacle for the formation of CD-type deposit, considering reduced sulphur (H_2S), which forms the metal trap, is widely considered to ultimately derive from seawater sulphate (SO_4^{2-}). In these systems it is also unclear how metal solubility is impacted during the interaction between hydrothermal fluids and reducing lithologies that are often abundant within underlying stratigraphic sequences (Cooke et al., 2000; Tornos and Heinrich, 2008). To address these issues it is necessary to accurately interpret rocks that are both texturally and geochemically complex.

The overarching question this thesis attempted to answer was how fluid geochemistry in CD-type systems might have evolved through time and space. To this end, the hydrothermal evolution of two CD-type systems hosted in Late Devonian strata at Macmillan Pass (Selwyn Basin, YT, Canada) were evaluated within the context of three broad themes: (i) host rock sedimentology and chemistry (Chapters 2 and 5), (ii) hydrothermal fluid chemistry and metal transport (Chapter 4 and 5), and (iii) sources of reduced sulphur and pathways of metal deposition (Chapters 3, 4 and 5). The main conclusions of these themes will now be summarised.

6.1. Host rock sedimentology and chemistry (Chapters 2 and 5)

The original work on Selwyn Basin CD-type systems was produced in the 1980s (Goodfellow and Jonasson, 1984; 1986; Goodfellow, 1987), and since that time new and evolving models of mudstone deposition have developed (Macquaker et al., 2007; Macquaker and Bohacs, 2007; Schieber et al., 2007; Schieber et al., 2010; Aplin and Macquaker, 2011). Importantly, the Selwyn Basin model, in which organic rich mudstones were deposited via pelagic processes in a stagnant (euxinic), restricted basin with limited clastic input, no longer provides a unique explanation for the host rocks at Macmillan Pass. Indeed, work presented in Chapters 2 and 5 present new ideas on the physical and chemical nature of the host rock at Macmillan Pass.

The lenticular laminations within sharply bedded mudstones that are discussed in Chapter 5 provide evidence of non-pelagic, higher-energy processes responsible for sediment transport and deposition (Schieber et al., 2010). This is an important departure from the previous model, in which slow sedimentation rates were invoked (<0.4cm yr^{-3}; Goodfellow and Jonasson, 1986). Slow sedimentation rates formed a key parameter for the interpretation of $\delta^{34}S$ values in pyrite, with sediment pore fluids and the overlying water column considered an open system. However, a more energetic depositional environment introduces greater complexity to this model, and non steady state conditions will have been more characteristic in this setting (e.g. Aller et al., 2010). The relevance of this for the interpretation of $\delta^{34}S$ values in pyrite will be summarised in section 6.3.

This dynamic sedimentary environment was also the setting of enhanced biological productivity, and the work presented in Chapter 2 provides evidence that

biogenic silica was an important component of the host rock. This is supported by the presence of abundant radiolarians, concentrated within certain beds in the host rock. Re-sedimented muds are water-saturated (Schieber et al. 2007), and sediments comprised of biogenic silica can retain enhanced porosities to depths exceeding 500 m in sedimentary basins (Isaacs et al., 1982). Indeed, one of the ideas presented in Chapter 2 is that biogenic silica had an important role in enhancing sub-surface fluid flow. The other major conclusion of Chapter 2 concerns the identification of productivity within the basin, in the form of biogenic silica and total organic carbon (TOC) in the host rock. Recognising biogenic input is particularly important for identifying prospective host rocks in CD-type systems – this relates to the role that organic carbon has in pathways of sulphate reduction, either directly via bacterial sulphate reduction (BSR) or indirectly via abiogenic pathways involving methane oxidation (Chapter 3) or thermochemical sulphate reduction (TSR). A hypothesis put forth here, is that host rocks deposited in productive settings are a fundamental characteristic of CD-type deposits. Given this, the manner in which hydrothermal fluids interacted with organic-rich, saturated and semi-consolidated sediment is an important but under-evaluated aspect of hydrothermal processes in CD-type systems.

6.2. Hydrothermal fluid chemistry and metal transport (Chapters 4 and 5)

Direct evidence of hydrothermal fluid flow is typically lacking in most CD-type deposits. However, at Macmillan Pass, the primary conduit of fluid up-flow (vent complex) is well preserved at both the Tom and Jason deposits. In Chapters 4 and 5, fluid chemistry and fluid-rock interaction were evaluated using a combination of techniques. Both fluid inclusion microthermometry and stable isotope ($\delta^{13}C$, $\delta^{18}O$

values) modeling provide robust evidence that the fluid entering the vent complex was both hot (>250°C) and acidic (pH < 4.5), and therefore capable of transporting metals at relatively modest salinities (<6 wt. % NaCl). Once in an environment more proximal to the seafloor, multiple lines of evidence point towards changing fluid chemistry: (i) rare earth element (REE) composition of ankerite provides evidence of diagenetic fluid input, and (ii) negative $\delta^{13}C$ values in Stage 1 ankerite, pyrobitumen and primary CO_2-bearing fluid inclusions are evidence of organic carbon alteration, which resulted in the evolution to more reducing conditions and the development of the Stage 2 mineral assemblage.

An important conclusion of Chapter 4 is the recognition that in CD-type systems, fluid chemistry and mineral assemblages are influenced most at a local level in a diagenetic environment. This is an key factor when developing thermodynamic models of metal solubility and deposition (e.g. Cooke et al. 2000), and means that the solubility of base metals in hydrothermal fluids need not necessarily be inhibited when passing through sedimentary basins comprised dominantly of organic rich lithologies (e.g. Tornos and Heinrich, 2008).

6.3. Sources of reduced sulphur in the bedded mineralisation (Chapters 3 and 5)

In CD-type systems, debate has frequently focused on the nature of the metal trap and whether sub-seafloor (replacement) or water column (sedimentary exhalative; SEDEX) processes are responsible for producing mineralisation (e.g. Eldridge et al., 1988a, 1988b; Goodfellow and Turner, 1988). The results presented in Chapters 3 and 5 are

an important contribution to this debate.

In the Selwyn Basin, the bedded mineralisation in all CD-type deposits is considered to have formed via sedimentary exhalative processes (Goodfellow and Lydon, 2007). The implications are non-trivial, as syn-sedimentary processes imply water column euxinia, and potentially long-lasting periods of basin-scale stagnation (Turner, 1992). In Chapter 3, isotopic microanalysis (secondary ion mass spectrometry; SIMS) of barite and pyrite was used to critically assess the evidence for euxinia in the bedded mineralisation at Tom and Jason. Stratiform barite and pyrite were targeted for analysis, as they provide a valuable record of mutually evolving sulphate and sulphide reservoirs. Furthermore, the isotopic data from which the conventional SEDEX model is constructed (Goodfellow and Jonasson, 1984) suggests complementary increases in $\delta^{34}S$ values for both barite and pyrite should be observed, i.e. evidence of closed system Rayleigh fractionation and an evolved sulphate reservoir.

The results presented in Chapter 3 are not consistent with the euxinic model, and provide evidence supporting a sub-seafloor replacement style model of CD-type mineralisation. Barite preserves a relatively narrow range of $\delta^{34}S$ values (+24 to +34‰), consistent with little to no modification from a Late Devonian seawater sulphate reservoir (~24‰; John et al., 2010). However, high $\delta^{34}S$ values, approaching +24‰, are preserved in stratiform pyrite located directly beneath stratiform barite. In Chapter 3, it is reasoned that this isotopic relationship can only have developed in a diagenetic environment, during anaerobic oxidation of methane coupled with sulphate reduction (AOM-SR). If the high $\delta^{34}S$ values in pyrite were not formed in a euxinic setting, then what was the source of sulphur for the bedded mineralisation at the Tom

and Jason deposits?

In the mineralogical paragenesis for the bedded mineralisation described in Chapter 3, barite formation pre-dates the hydrothermal base metal event, and in Chapter 5, evidence is presented of hydrothermal sulphides replacing barite. Furthermore, a barium halo preserved around the bedded mineralisation at Tom provides compelling evidence of barium remobilisation as a result of barite dissolution. Mass balance calculations, although complicated by the number of barium-bearing phases present (including carbonates and feldspars), suggest that barite dissolution may have contributed an important source of sulphur. This process is particularly interesting within the context of low seawater sulphate concentrations during the Late Devonian (approximately 7 mM; Lowenstein et al., 2003). Specifically, where concentration of sulphur is an important factor for the formation of a successful metal trap, barite pre-enrichment in the host rock would have been an effective mechanism by which to achieve this. In Chapters 3 and 5, an argument is made that multiple sources of reduced sulphur, rather than a single step process operating in the water column (i.e. BSR and euxinia), are more relevant for mineralising processes in the Macmillan Pass CD-type systems.

6.4. Final comments and future work

The physical and chemical nature of the host rock is a unifying aspect in all the chapters of this thesis. This represents the key departure from previous models of CD-type metallogenesis in the Selwyn Basin, which directed attention towards processes operating in the water column. This change is largely related to an improving ability to

258

interpret the complex samples that are characteristic of CD-type systems. This is directly linked to technological advancements and the capabilities of modern micro-analytical techniques (e.g. secondary ion mass spectrometry, laser ablation inductively coupled mass spectrometry) to sample at high resolution and resolve geochemical signals at a small scale. Notable highlights include the interpretation of $\delta^{34}S$ values in coeval pyrite and barite (Chapter 3), something not typically afforded in many CD-type systems. These data provide valuable context for the mutual interpretation of both reduced and oxidised forms of sulphur during diagenesis. Importantly, the observation of enriched $\delta^{34}S$ values in mudstones from older sections of Selwyn Basin stratigraphy (Goodfellow and Jonasson, 1984) raises the possibility that processes such as sulphate reduction coupled with methane oxidation may also have been important during older periods of the lower Paleozoic (Cambrian, Silurian).

Processes operating in the diagenetic environment have been emphasised in many parts of this thesis; however, this is not intended to disregard the overarching influence of seawater chemistry. Indeed, the correlation between low seawater sulphate and development of $CaCl_2$ brines has been commented on before as a factor in the generation of metal-rich hydrothermal fluids (Wilkinson, 2015). Exploration of the relationship between extended periods of low seawater sulphate and barium solubility may be particularly informative for understanding the role of barite in CD-type systems. Specifically, the saturation state of barite is dependent upon the respective concentrations of barium and sulphate, and it is reasonable to assume that a low sulphate ocean would accommodate higher concentrations of barium. Considering the evidence linking biogenic activity to a sedimentary barium flux (Chapter 3), the correlation between productive environments, organic matter and barite precipitation, and periods of low seawater sulphate (e.g. Late Devonian) is compelling. The

evidence of barite replacement (by sulphide) at Macmillan Pass suggests barite accumulation may be an important process by which sulphur is concentrated into a host rock in a low sulphate environment. Therefore it may not be coincidental that one of the largest Paleozoic accumulations of CD-type mineralisation occurs in the Red Dog district (Alaska), in strata that also host over a billion tonnes of barite (Kelley and Jennings, 2004).

Evidence presented in this thesis supports a model in which reduced sulphur is generated by a number of different processes (TSR, AOM-SR, BSR, barite dissolution). Analysis of δ^{34}S values in sulphides is the most commonly applied technique for tracing these processes; however, different processes often produce broad and overlapping ranges of δ^{34}S values meaning there can be multiple non-unique solutions in a given data set. Therefore mass balance in hydrothermal systems commonly remains ambiguous with regards to the relative importance of these processes. The application of multiple sulphur isotope analysis to CD-type systems could form an approach by which to identify the relative contribution of sulphate reduction pathways (Johnston, 2011), at least with regard to distinguishing biogenic (BSR) versus abiogenic (AOM-SR) processes.

Finally, attempts have been made in this thesis to combine new interpretations of both sedimentology and geochemistry. However, this approach can be limited when dealing only with mineralised samples. In Chapter 2, samples of un-mineralised, un-altered mudstone were described and analysed. Much could be gained from undertaking a more detailed structural and sedimentological investigation of un-mineralised Late Devonian lithologies in the Selwyn Basin. Such an approach may prove to be informative for a more accurate determination of location in the basin, and

add a further layer of detail when interpreting the geochemistry of the hydrothermal system. In many ways, the work presented in this thesis forms a foundation for such future work.

References

Aller R. C., Madrid V., Chistoserdov A., Aller J. Y. and Heilbrun C. (2010) Unsteady diagenetic processes and sulfur biogeochemistry in tropical deltaic muds : Implications for oceanic isotope cycles and the sedimentary record. *Geochim. Cosmochim. Acta* **74**, 4671–4692.

Aplin A. C. and Macquaker J. H. S. (2011) Mudstone diversity : Origin and implications for source , seal , and reservoir properties in petroleum systems. *Am. Assoc. Pet. Geol. Bull.* **12**, 2031–2059.

Cooke D. R., Bull S. W., Large R. R. and McGoldrick P. J. (2000) The Importance of Oxidized Brines for the Formation of Australian Proterozoic Stratiform Sediment-Hosted Pb-Zn (Sedex) Deposits. *Econ. Geol.* **95**, 1–18.

Eldridge C. S., Walshe J. L., Compston W., Williams I. S., Both R. A., Ohmoto H., Goodfellow W. D. and Turner R. J. W. (1988) Sulfur isotope variability in sediment-hosted massive sulfide deposits as determined using the ion microprobe SHRIMP: I. An example from the Rammelsberg Orebody – a reply. *Econ. Geol.* **84**, 443–449.

Goodfellow W. D. (1987) Anoxic Stratified Oceans as a Source of Sulphur in Sediment-Hosted Stratiform Zn-Pb Deposits (Selwyn Basin, Yukon, Canada). *Chem. Geol.*

65, 359–382.

Goodfellow W. D. and Jonasson I. R. (1984) Ocean stagnation and ventilation defined by 34-S secular trends in pyrite and barite, Selwyn Basin, Yukon. *Geology* **12**, 583–586.

Goodfellow W. D. and Lydon J. W. (2007) Sedimentary Exhalative (SEDEX) Deposits. In *Mineral Deposits of Canada: A Synthesis of Major Deposit-Types, District Metallogeny, the Evolution of Geological Provinces, and Exploration Methods* pp. 163–183.

Goodfellow W. D. and Turner R. J. W. (1988) Sulfur isotope variability in sediment-hosted massive sulfide deposits as determined using the ion microprobe SHRIMP: I. An example from the Rammelsberg Orebody – a discussion. *Econ. Geol.* **84**, 451–452.

Isaacs C. M., Survey U. S. G., Road M. and Park M. (1982) Influence of rock composition on kinetics of silica phase changes in the Monterey Formation , Santa Barbara area , California.

John E. H., Wignall P. B., Newton R. J. and Bottrell S. H. (2010) $\delta34SCAS$ and $\delta18OCAS$ records during the Frasnian–Famennian (Late Devonian) transition and their bearing on mass extinction models. *Chem. Geol.* **275**, 221–234.

Johnston D. T. (2011) Multiple sulfur isotopes and the evolution of Earth's surface sulfur cycle. *Earth-Science Rev.* **106**, 161–183.

Kelley K. K. and Jennings S. (2004) A Special Issue Devoted to Barite and Zn-Pb-Ag

Deposits in the Red Dog District, Western Brooks Range, Northern Alaska. *Econ. Geol.* **99**, 1267–1280.

Leach D. L., Bradley D. C., Huston D., Pisarevsky S. A., Taylor R. D. and Gardoll J. (2010) Sediment-Hosted Lead-Zinc Deposits in Earth History. *Econ. Geol.* **105**, 593–625.

Leach D. L., Sangster D. F., Kelley K. D., Large R. R., Garven G., Allen C. R., Gutzmer J. and Walters J. (2005) Sediment-Hosted Lead-Zinc Deposits: A Global Perspective. *Econ. Geol.* **100**, 561–607.

Lowenstein T. K., Hardie L. a., Timofeeff M. N. and Demicco R. V. (2003) Secular variation in seawater chemistry and the origin of calcium chloride basinal brines. *Geology* **31**, 857.

Macquaker J. H. S. and Bohacs K. M. (2007) Geology. On the accumulation of mud. *Science* **318**, 1734–5.

Macquaker J. H. S., Taylor K. G. and Gawthorpe R. L. (2007) High-Resolution Facies Analyses of Mudstones: Implications for Paleoenvironmental and Sequence Stratigraphic Interpretations of Offshore Ancient Mud-Dominated Successions. *J. Sediment. Res.* **77**, 324–339.

Schieber J., Southard J. B. and Schimmelmann A. (2010) Lenticular Shale Fabrics Resulting from Intermittent Erosion of Water-Rich Muds--Interpreting the Rock Record in the Light of Recent Flume Experiments. *J. Sediment. Res.* **80**, 119–128.

Schieber J., Southard J. and Thaisen K. (2007) Accretion of mudstone beds from

migrating floccule ripples. *Science* **318**, 1760–3.

Tornos F. and Heinrich C. (2008) Shale basins, sulfur-deficient ore brines and the formation of exhalative base metal deposits. *Chem. Geol.* **247**, 195–207.

Turner R. J. W. (1992) Formation of Phanerozoic stratiform sediment , hosted zinc-lead deposits : Evidence for the critical role of ocean anoxia. *Chem. Geol.* **99**, 165–188.

Wilkinson J. J. (2014) Sediment-Hosted Zinc–Lead Mineralization: Processes and Perspectives. In *Treatise on Geochemistry: Second Edition* Elsevier Ltd. pp. 219–249.

Bibliography

Abbott J. G. (1982) Structure and stratigraphy of the Macmillan Fold Belt: evidence for Devonian faulting. In *Yukon Geology and Exploration* Department of Inidian Affairs and Northern Development Canada. pp. 22–23.

Abbott J. G. and Turner R. J. (1991) Character and paleotectonic setting of Devonian stratiform sediment-hosted Zn, Pb, Ba deposits, Macmillan Fold Belt, Yukon. In *Geological Survey of Canada Open File 2169* (eds. J. G. Abbott and R. J. Turner). pp. 99–136.

Adams M. M., Hoarfrost A. L., Bose A., Joye S. B. and Girguis P. R. (2013) Anaerobic oxidation of short-chain alkanes in hydrothermal sediments: potential influences on sulfur cycling and microbial diversity. *Front. Microbiol.* **4**, 1–11.

Aharon P., Fu B. and Rouge B. (2000) Microbial sulfate reduction rates and sulfur and oxygen isotope fractionations at oil and gas seeps in deepwater Gulf of Mexico. *Geochim. Cosmochim. Acta* **64**, 233–246.

Alibo D. S. and Nozaki Y. (1999) Rare earth elements in seawater: Particle association, shale-normalization, and Ce oxidation. *Geochim. Cosmochim. Acta* **63**, 363–372.

Aller R. C. (2014) Sedimentary Diagenesis, Depositional Environments, and Benthic Fluxes. In *Treatise on Geochemistry* Elsevier Ltd. pp. 293–334.

Aller R. C., Madrid V., Chistoserdov A., Aller J. Y. and Heilbrun C. (2010) Unsteady diagenetic processes and sulfur biogeochemistry in tropical deltaic muds :

Implications for oceanic isotope cycles and the sedimentary record. *Geochim. Cosmochim. Acta* **74**, 4671–4692.

Anderson G. M. and Thom J. (2007) The role of thermochemical sulfate reduction in the origin of Mississippi Valley-type deposits. II. Carbonate–sulfide relationships. *Geofluids*, 27–34.

Anderson I. K., Ashton J. H., Boyce A. J., Fallick A. E. and Russel M. J. (1998) Ore Depositional Processes in the Navan Zn-Pb Deposit, Ireland. *Econ. Geol.*

Anderson R. O. (1983) *Radiolaria.*, New York Springer-Verlag.

Ansdell K. M., Nesbitt B. E. and Longstaffe F. J. (1989) A Fluid Inclusion and Stable Isotope Study of the Tom Ba-Pb-Zn Deposit, Yukon Territory, Canada. *Econ. Geol.* **84**, 841–856.

Antler G., Turchyn A. V., Rennie V., Herut B. and Sivan O. (2013) Coupled sulfur and oxygen isotope insight into bacterial sulfate reduction in the natural environment. *Geochim. Cosmochim. Acta* **118**, 98–117.

Aplin A. C. and Macquaker J. H. S. (2011) Mudstone diversity : Origin and implications for source , seal , and reservoir properties in petroleum systems. *Am. Assoc. Pet. Geol. Bull.* **12**, 2031–2059.

Appold M. S. and Wenz Z. J. (2011) Composition of Ore Fluid Inclusions from the Viburnum Trend, Southeast Missouri District, United States: Implications for Transport and Precipitation Mechanisms. *Econ. Geol.* **106**, 55–78.

Arndt S., Hetzel A. and Brumsack H.-J. (2009) Evolution of organic matter

degradation in Cretaceous black shales inferred from authigenic barite: A reaction-transport model. *Geochim. Cosmochim. Acta* **73**, 2000–2022.

Arning E. T., Gaucher E. C., van Berk W. and Schulz H.-M. (2015) Hydrogeochemical models locating sulfate-methane transition zone in marine sediments overlying black shales: A new tool to locate biogenic methane? *Mar. Pet. Geol.* **59**, 563–574.

Arthur M. A. and Sageman B. B. (1994) Marine black shales: depositional mechanisms and environments of ancient deposits. *Annu. Rev. Earth Planet. Sci.* **22**, 499–551.

Azmy K. and Blamey N. J. F. F. (2013) Source of diagenetic fluids from fluid-inclusion gas ratios. *Chem. Geol.* **347**, 246–254.

Bailes R. J., Smee B. W., Blackader D. W. and Gardner H. D. (1986) Geology of the Jason Lead-Zinc-Silver Deposits, Macmillan Pass, Eastern Yukon. In *Mineral Deposits of Northern Cordillera* (ed. J. A. Morin). The Canadian Institute of Mining and Metallurgy. pp. 87–99.

Barnes R. O. and Goldberg E. D. (1976) Methane production and consumption in anoxic marine sediments. *Geology* **4**, 297–300.

Barrie C. D., Boyce A. J., Boyle A. P., Williams P. J., Blake K., Wilkinson J. J., Lowther M., Mcdermott P. and Prior D. J. (2009) On the growth of colloform textures: a case study of sphalerite from the Galmoy ore body, Ireland. *J. Geol. Soc. London* **166**, 563–582.

Bau M. (1991) Rare-earth element mobility during hydrothermal and metamorphic fluid-rock interaction and the significance of the oxidation state of europium.

Chem. Geol. **93**, 219–230.

Bau M. and Dulski P. (1995) Comparative study of yttrium and rare-earth element behaviours in fluorine-rich hydrothermal fluids. *Contrib. to Mineral. Petrol.* **119**, 213–223.

Bau M. and Dulski P. (1999) Comparing yttrium and rare earths in hydrothermal fluids from the Mid-Atlantic Ridge: implications for Y and REE behaviour during near-vent mixing and for the Y r Ho ratio of Proterozoic seawater. *Chem. Geol.* **155**, 77–90.

Bau M., Moller P. and Möller P. (1992) Rare earth element fractionation in metamorphogenic hydrothermal calcite, magnesite and siderite. *Mineral. Petrol.* **45**, 231–246.

Birgel D., Feng D., Roberts H. H. and Peckmann J. (2011) Changing redox conditions at cold seeps as revealed by authigenic carbonates from Alaminos Canyon, northern Gulf of Mexico. *Chem. Geol.* **285**, 82–96.

Bishop J. K. B. (1988) The barite-opal-organic carbon association in oceanic particulate matter. *Nature* **332**, 341–343.

Blamey N. J. F. (2012) Composition and evolution of crustal, geothermal and hydrothermal fluids interpreted using quantitative fluid inclusion gas analysis. *J. Geochemical Explor.* **116-117**, 17–27.

Blamey N. J. F., Parnell J., McMahon S., Mark D. F., Tomkinson T., Lee M., Shivak J., Izawa M. R. M., Banerjee N. R. and Flemming R. L. (2015) Evidence for methane

in Martian meteorites. *Nat. Commun.* **6**, 7399.

Blamey N. and Norman D. (2002) New interpretations of geothermal fluid inclusion volatiles: Ar/He and N2/Ar ratios – a better indicator of magmatic volatiles, and equilibrium gas geothermometry. In *Twenty-Seventh Workshop on Geothermal Reservoir Engineering*

Bodnar R. J. (1993) Revised equation and table for determining the freezing point depression of H2O-NaCl solutions. *Geochim. Cosmochim. Acta* **57**, 683–684.

Böning P., Brumsack H.-J., Böttcher M. E., Schnetger B., Kriete C., Kallmeyer J. and Borchers S. L. (2004) Geochemistry of Peruvian near-surface sediments. *Geochim. Cosmochim. Acta* **68**, 4429–4451.

Borowski W. S., Rodriguez N. M., Paull C. K. and Ussler W. (2013) Are [34]S-enriched authigenic sulfide minerals a proxy for elevated methane flux and gas hydrates in the geologic record? *Mar. Pet. Geol.* **43**, 381–395.

Böstrom K. (1973) The origin and fate of ferromanganoan active ridge sediments. *Stock. Contrib. to Geol.* **27**, 147–243.

Bottrell S. H. and Newton R. J. (2006) Reconstruction of changes in global sulfur cycling from marine sulfate isotopes. *Earth-Science Rev.* **75**, 59–83.

Broadbent C., Myers R. E. and Wright V. (1998) Geology and Origin of Shale-Hosted Mineralization at the Century Deposit, Queensland, Eromanga. *Econ. Geol.* **93**, 1264–1294.

Brown T. J., Wrighton C. E., Raycraft E. R., Shaw R. A., Deady E. A., Rippingale J.,

Bide T. and Idoine N. (2015) *British Geological Survey – World mineral production (2009-2013).*, NERC.

Brunner B. and Bernasconi S. M. (2005) A revised isotope fractionation model for dissimilatory sulfate reduction in sulfate reducing bacteria. *Geochim. Cosmochim. Acta* **69**, 4759–4771.

Buzon M. R., Simonetti A. and Creaser R. a. (2007) Migration in the Nile Valley during the New Kingdom period: a preliminary strontium isotope study. *J. Archaeol. Sci.* **34**, 1391–1401.

Campbell A. R. and Larson P. B. (1998) Introduction to stable isotope applications in hydrothermal systems. In *Techniques in Hydrothermal Ore Deposits Geology* (eds. J. P. Richards and A. R. Larson). Society of Economic Geologists, Littleton.

Canet C., Anadón P., González-partida E., Alfonso P., Rajabi A., Pérez-segura E. and Alba-aldave L. A. (2014) Paleozoic bedded barite deposits from Sonora (NW Mexico): Evidence for a hydrocarbon seep environment of formation. *Ore Geol. Rev.* **56**, 292–300.

Canfield D. E. (2001) Isotope fractionation by natural populations of sulfate-reducing bacteria. *Geochim. Cosmochim. Acta* **65**, 1117–1124.

Canfield D. E. (2004) The evolution of the earth surface sulfur reservoir. *Am. J. Sci.* **304**, 839–861.

Canfield D. E., Raiswell R., Westrich J. T., Reaves C. M. and Berner R. a. (1986) The use of chromium reduction in the analysis of reduced inorganic sulfur in

sediments and shales. *Chem. Geol.* **54**, 149–155.

Carne R. C. and Cathro R. J. (1982) Sedimentary exhalative (sedex) zinc-lead-silver deposits, northern Canadian Cordillera. *Can. Min. Metall. Bull.* **75**, 66–78.

Cathles L. M. and Schoell M. (2007) Modeling CO_2 generation, migration, and titration in sedimentary basins. *Geofluids* **7**, 441-450.

Cecile M. P., Shakur M. A. and Krouse H. R. (1983) The isotopic composition of western Canadian barites and the possible derivation of oceanic sulphate δ34S and δ18O age curves. *Can. J. Earth Sci.* **20**, 1528–1535.

Chen D., Wang J., Racki G., Li H., Wang C., Ma X. and Whalen M. T. (2013) Large sulfur isotopic perturbations and oceanic changes during the Frasnian-Famennian transition of the Late Devonian. *J. Geol. Soc. London* **170**, 465–476.

Claypool G. E., Holser W. T., Kaplan I. R., Sakai H. and Zak I. (1980) The age curves of sulfur and oxygen isotopes in marine sulfate and their mutual interpretation. *Chem. Geol.* **28**, 199–260.

Conliffe J., Wilton D. H. C., Blamey N. J. F. and Archibald S. M. (2013) Paleoproterozoic Mississippi Valley Type Pb-Zn mineralization in the Ramah Group, Northern Labrador: Stable isotope, fluid inclusion and quantitative fluid inclusion gas analyses. *Chem. Geol.* **362**, 211–223.

Cooke D. R., Bull S. and Large R. R. (2003) Processes of ore formation in the stratiform sediment-hosted Zn-Pb deposits of Northern Australia: testing the Century model. *J. Geochemical Explor.* **78-79**, 519–524.

Cooke D. R., Bull S. W., Large R. R. and McGoldrick P. J. (2000) The Importance of Oxidized Brines for the Formation of Australian Proterozoic Stratiform Sediment-Hosted Pb-Zn (Sedex) Deposits. *Econ. Geol.* **95**, 1–18.

Crowe S. A., Paris G., Katsev S., Jones C., Kim S.-T., Zerkle A. L., Nomosatryo S., Fowle D. A., Adkins J. F., Sessions A. L., Farquhar J. and Canfield D. E. (2014) Sulfate was a trace constituent of Archean seawater. *Science (80-.).* **346**, 735–739.

Cruse A. M. and Seewald J. S. (2006) Geochemistry of low-molecular weight hydrocarbons in hydrothermal fluids from Middle Valley, northern Juan de Fuca Ridge. *Geochim. Cosmochim. Acta* **70**, 2073–2092.

Cruse A. M. and Seewald J. S. (2010) Low-molecular weight hydrocarbons in vent fluids from the Main Endeavour Field, northern Juan de Fuca Ridge. *Geochim. Cosmochim. Acta* **74**, 6126–6140.

Cruse A. M. and Seewald J. S. (2001) Metal mobility in sediment-covered ridge-crest hydrothermal systems: *Geochim. Cosmochim. Acta* **65**, 3233–3247.

Davies R. J., Goulty N. R. and Meadows D. (2008) Fluid flow due to the advance of basin-scale silica reaction zones. *Geol. Soc. Am. Bull.* **120**, 195–206.

Davies R. J., Huuse M., Hirst P., Cartwright J. and Yang Y. (2006) Giant clastic intrusions primed by silica diagenesis. *Geology* **34**, 917.

Dehairs F., Chesselet R. and Jedwab J. (1980) Discrete suspended particles of barite and the barium cycle in the open ocean. *Earth Planet. Sci. Lett.* **49**, 528–550.

DeMaster D. J. (2002) The accumulation and cycling of biogenic silica in the Southern

Ocean: revisiting the marine silica budget. *Deep Sea Res. Part II Top. Stud. Oceanogr.* **49**, 3155–3167.

Denison R. E., Koepnick R. B., Burke W. H., Hetherington E. A. and Fletcher A. (1997) Construction of the Silurian and Devonian seawater ^{87}Sr/^{86}Sr curve. *Chem. Geol.* **140**, 109–121.

Dickens G. R. D. (2001) Sulfate profiles and barium fronts in sediment on the Blake Ridge : Present and past methane fluxes through a large gas hydrate reservoir. *Geochim. Cosmochim. Acta* **65**, 529–543.

Douville E., Bienvenu P., Charlou J. L., Donval J. P., Fouquet Y., Appriou P. and Gamo T. (1999) Yttrium and rare earth elements in fluids from various deep-sea hydrothermal systems. *Geochim. Cosmochim. Acta* **63**, 627–643.

Dymond J. and Collier R. (1996) Particulate barium fluxes and their relationships to biological productivity. *Deep Sea Res. Part II* **43**, 1283–1308.

Eisbacher G. H. (1985) Late proterozoic rifting, glacial sedimentation, and sedimentary cycles in the light of Windermere deposition, Western Canada. *Palaeogeogr. Palaeoclimatol. Palaeoecol.* **51**, 231–254.

Elderfield H. H. and Greaves M. J. (1982) The rare earth elements in seawater. *Nature* **296**, 214–219.

Eldridge C. S., Walshe J. L., Compston W., Williams I. S., Both R. A., Ohmoto H., Goodfellow W. D. and Turner R. J. W. (1988) Sulfur isotope variability in sediment-hosted massive sulfide deposits as determined using the ion microprobe

SHRIMP: I. An example from the Rammelsberg Orebody – a reply. *Econ. Geol.* **84**, 443–449.

Eldridge C. S., Williams N. and Walshe J. L. (1993) Sulfur isotope variability in sediment-hosted massive sulfide deposits as determined using the ion microprobe SHRIMP: II. A study of the H.Y.C. deposit at McArthur River, Northern Territory, Australia. *Econ. Geol.* **88**, 1–26.

Emerson S. and Hedges J. (2003) Sediment Diagenesis and Benthic Flux. In *Treatise on Geochemistry* (eds. H. D. Holland and K. K. Turekian).

Everett C. E., Wilkinson J. J. and Rye D. M. (1999) Fracture-controlled fluid flow in the Lower Palaeozoic basement rocks of Ireland: implications for the genesis of Irish-type Zn-Pb deposits. *Geol. Soc. London, Spec. Publ.* **155**, 247–276.

Farquhar J., Nanping W., Canfield D. E. and Oduro H. (2010) Connections between Sulfur Cycle Evolution, Sulfur Isotopes, Sediments, and Base Metal Sulfide Deposits. *Econ. Geol.* **105**, 509–533.

Fernandes N. A. (2011) Geology and Geochemistry of Late Devonian-Mississippian Sediment-Hosted Barite Sequences of the Selwyn Basin, NWT and Yukon, Canada. University of Alberta.

Fritz P., Basharmal G. M., Drimmie R. J., Ibsen J. and Qureshi R. M. (1989) Oxygen isotope exchange between sulphate and water during bacterial reduction of sulphate. *Chem. Geol. Isot. Geosci. Sect.* **79**, 99–105.

Froelich P. N., Klinkhammer G. P., Bender M. L., Luedtke N. A., Heath G. R., Cullen

D., Dauphin P., Hammond D. and Hartman B. (1979) Early oxidation of organic matter in pelagic sediments of the eastern equatorial Atlantic: suhoxic diagenesis. *Geochim. Cosmochim. Acta* **43**, 1075–1090.

Fusswinkel T., Wagner T., Wenzel T., Wälle M. and Lorenz J. (2013) Evolution of unconformity-related MnFeAs vein mineralization, Sailauf (Germany): Insight from major and trace elements in oxide and carbonate minerals. *Ore Geol. Rev.* **50**, 28–51.

Gaboury D. (2013) Does gold in orogenic deposits come from pyrite in deeply buried carbon-rich sediments?: Insight from volatiles in fluid inclusions. *Geology* **41**, 1207-1210.

Gabrielse H. (1967) Tectonic evolution of the northern Canadian Cordillera. *Can. J. Earth Sci.* **4**, 271–298.

Galley A. G., Hannington M. and Jonasson I. (2007) Volcanogenic massive sulphide deposits. In *Mineral deposits of Canada: a synthesis of major deposit-types, district metallogeny, the evolution of geological provinces, and exploration methods* (ed. W. D. Goodfellow). pp. 141–161.

Gardner D. H. (1983) Petrologic and geochemical constraints on genesis of the Jason Pb-Zn deposits, Yukon Territory. University of Calgary.

Gardner H. D. and Hutcheon I. (1985) Geochemistry, Mineralogy, and Geology of the Jason Pb-Zn Deposits, Macmillan Pass, Yukon, Canada. *Econ. Geol.* **80**, 1257–1276.

Giggenbach W. F. (1996) Chemical Composition of Volcanic Gases. In *Monitoring and Mitigration of Volcano Hazards* Springer Berlin Heidelberg. pp. 221–256.

Goldhaber M. B. and Kaplan I. R. (1975) Controls and consequences of sulfate reduction rates in recent marine sediments. *Soil Sci.* **119**, 42–55.

Gonzalez-Muñoz M. T., Martinez-Ruiz F., Morcillo F., Martin-Ramos J. D. and Paytan A. (2012) Precipitation of barite by marine bacteria: A possible mechanism for marine barite formation. *Geology* **40**, 675–678.

Goodfellow W. D. (1987) Anoxic Stratified Oceans as a Source of Sulphur in Sediment-Hosted Stratiform Zn-Pb Deposits (Selwyn Basin, Yukon, Canada). *Chem. Geol.* **65**, 359–382.

Goodfellow W. D. (2007) Base metal metallogeny of the Selwyn Basin, Canada. In *Mineral Deposits of Canada: A Synthesis of Major Deposit-Types, District Metallogeny, the Evolution of Geological Provinces, and Exploration Methods* Geological Association of Canada, Mineral Deposits Division, Special Publication. pp. 553–579.

Goodfellow W. D., Cecile M. P. and Leybourne M. I. (1995) Geochemistry, petrogenesis, and tectonic setting of lower Paleozoic alkalic and potassic volcanic rocks, Northern Canadian Cordilleran miogeocline. *Can. J. Earth Sci.* **32**, 1236–1254.

Goodfellow W. D. and Jonasson I. R. (1986) Environment of formation of the Howards Pass (XY) Zn-Pb deposit, Selwyn Basin, Yukon. In *Mineral Deposits of Northern Cordillera* (ed. J. A. Morin). The Canadian Institute of Mining and Metallurgy. pp.

19–50.

Goodfellow W. D. and Jonasson I. R. (1984) Ocean stagnation and ventilation defined by 34-S secular trends in pyrite and barite, Selwyn Basin, Yukon. *Geology* **12**, 583–586.

Goodfellow W. D. and Lydon J. W. (2007) Sedimentary Exhalative (SEDEX) Deposits. In *Mineral Deposits of Canada: A Synthesis of Major Deposit-Types, District Metallogeny, the Evolution of Geological Provinces, and Exploration Methods* pp. 163–183.

Goodfellow W. D. and Lydon J. W. (2007) Sedimentary Exhalative (SEDEX) Deposits. In *Mineral Deposits of Canada: A Synthesis of Major Deposit-Types, District Metallogeny, the Evolution of Geological Provinces, and Exploration Methods* pp. 163–183.

Goodfellow W. D., Lydon J. W. and Turner R. J. (1993) Geology and genesis of stratiform sediment-hosted (SEDEX) zinc-lead-silver sulphide deposits. In *Mineral Deposit Modeling* (eds. R. W. Kirkham, R. Sinclair, R. I. Thorpe, and J. M. Duke). Geological Association of Canada. pp. 201–252.

Goodfellow W. D. and Rhodes D. (1991) Geological setting, geochemsitry and origin of the Tom stratiform Zn-Pb-Ag-barite deposits. In *Geological Survey of Canada Open File 2169* (eds. J. G. Abbott and R. J. Turner). pp. 177–239.

Goodfellow W. D. and Turner R. J. W. (1988) Sulfur isotope variability in sediment-hosted massive sulfide deposits as determined using the ion microprobe SHRIMP: I. An example from the Rammelsberg Orebody – a discussion. *Econ.*

Geol. **84**, 451–452.

Gordey S. P. (1981) Geology of the Nahanni map-area, Yukon Territory and District of Mackenzie. *Geol. Surv. Canada*, Open File 780.

Gordey S. P. and Anderson R. G. (1993) *Evolution of the northern cordilleran miogeocline, Nahanni map area (105I), Yukon and Northwest Territories.* Memoir 428., Geological Survey of Canada, Memoir 428.

Gordey S. P., Macdonald J. D., Turner E. C. and Long D. G. F. (2010) Structural Geology of the Central Mackenzie Mountains. In *Geology of the central Mackenzie mountains of the North Canadian Cordillera, Sekwi Mountain (105P), Mount Eduni (106A), and northwestern Wrigley Lake (95M) map-areas, Northwest Territories* (eds. E. Martel, E. C. Turner, and B. J. Fischer). NWT Geoscience Office. pp. 215–250.

Grassineau N. V, Mattey D. P. and Lowry D. (2001) Sulfur isotope analysis of sulfide and sulfate minerals by continuous flow-isotope ratio mass spectrometry. *Anal. Chem.* **73**, 220–5.

Greinert J., Bollwerk S. M., Derkachev A., Bohrmann G. and Suess E. (2002) Massive barite deposits and carbonate mineralization in the Derugin Basin, Sea of Okhotsk: precipitation processes at cold seep sites. *Earth Planet. Sci. Lett.* **203**, 165–180.

Griffith E. M. and Paytan A. (2012) Barite in the ocean - occurrence, geochemistry and palaeoceanographic applications. *Sedimentology* **59**, 1817–1835.

Gromek P., Gleeson S. a. and Simonetti A. (2012) A basement-interacted fluid in the N81 deposit, Pine Point Pb-Zn District, Canada: Sr isotopic analyses of single dolomite crystals. *Miner. Depos.* **47**, 749–754.

Gromet L. P., Haskin L. a., Korotev R. L. and Dymek R. F. (1984) The "North American shale composite": Its compilation, major and trace element characteristics. *Geochim. Cosmochim. Acta* **48**, 2469–2482.

Habicht K. S. and Canfield D. E. (1997) Sulfur isotope fractionation during bacterial sulfate reduction in organic-rich sediments. *Geochim. Cosmochim. Acta* **61**, 5351–61.

Haley B. A., Klinkhammer G. P. and McManus J. (2004) Rare earth elements in pore waters of marine sediments. *Geochim. Cosmochim. Acta* **68**, 1265–1279.

Hanor J. S. (2000) Barite-Celestine Geochemistry and Environments of Formation. *Rev. Mineral. Geochemistry* **40**, 193–275.

Harris N. B., Mnich C. a., Selby D. and Korn D. (2013) Minor and Trace Element and Re-Os Chemistry of the Upper Devonian Woodford Shale, Permian Basin, West Texas: Insights into Metal Abundance and Basin Processes. *Chem. Geol.* **356**, 76–93.

Harrison A. G. G. and Thode H. G. (1958) Mechanism of the bacterial reduction of sulphate from isotope fractionation studies. *Trans. Faraday Soc.* **54**, 84–92.

Hein J. R., Zierenberg R. a., Maynard J. B. and Hannington M. D. (2007) Barite-forming environments along a rifted continental margin, Southern California

Borderland. *Deep Sea Res. Part II* **54**, 1327–1349.

Hemley J. J. and Hunt J. P. (1992) Hydrothermal ore-forming processes in the light of studies in rock-buffered systems; II, Some general geologic applications. *Econ. Geol.* **87**, 23–43.

Henkel S., Mogollón J. M., Nöthen K., Franke C., Bogus K., Robin E., Bahr A., Blumenberg M., Pape T., Seifert R., März C., de Lange G. J. and Kasten S. (2012) Diagenetic barium cycling in Black Sea sediments – A case study for anoxic marine environments. *Geochim. Cosmochim. Acta* **88**, 88–105.

Himmler T., Bach W., Bohrmann G. and Peckmann J. (2010) Rare earth elements in authigenic methane-seep carbonates as tracers for fluid composition during early diagenesis. *Chem. Geol.* **277**, 126–136.

Hinrichs K.-U., Hayes J. M., Bach W., Spivack A. J., Hmelo L. R., Holm N. G., Johnson C. G. and Sylva S. P. (2006) Biological formation of ethane and propane in the deep marine subsurface. *Proc. Natl. Acad. Sci. U. S. A.* **103**, 14684–14689.

Horita J., Zimmerman H. and Holland H. D. (2002) Chemical evolution of seawater during the Phanerozoic : Implications from the record of marine evaporites. *Geochim. Cosmochim. Acta* **66**, 3733–3756.

Hunt J. M. (1996) *Petroleum Geochemistry and Geology*., Freeman, New York.

Irwin S. E. B. and Orchard M. J. (1991) Upper Devonian–Lower Carboniferous conodont biostratigraphy of the Earn Group and overlying units, northern Cordillera. In *Ordovician to Triassic Conodont Paleontology of the Canadian*

Cordillera (eds. M. J. Orchard and A. D. McCracken). Geological Survey of Canada, Bulletin 417. pp. 185–213.

Isaacs C. M. (1982) Influence of rock composition on kinetics of silica phase changes in the Monterey Formation , Santa Barbara area , California. *Geology* **10**, 304–308.

Isenhour T. L. and Jurs P. C. (1972) *Introduction to computer programming for chemists.*, Allyn & Baco.

Iversen N. and Jørgensen B. B. (1985) Anaerobic methane oxidation rates at the sulfate-methane transition in marine sediments from Kattegat and Skagerrak (Denmark). *Limnol. Oceanogr.* **1985**, 944–955.

Jaekel U., Musat N., Adam B., Kuypers M., Grundmann O. and Musat F. (2013) Anaerobic degradation of propane and butane by sulfate-reducing bacteria enriched from marine hydrocarbon cold seeps. *ISME J.* **7**, 885–95.

Jakubowicz M., Dopieralska J. and Belka Z. (2015) Tracing the composition and origin of fluids at an ancient hydrocarbon seep (Hollard Mound, Middle Devonian, Morocco): A Nd, REE and stable isotope study. *Geochim. Cosmochim. Acta* **156**, 50–74.

Jewell P. W. (1994) Paleoredox Conditions and the Origin of Bedded Barites along the Late Devonian North American Continental Margin. *J. Geol.* **102**, 151–164.

Jochum K. P., Scholz D., Stoll B., Weis U., Wilson S. a., Yang Q., Schwalb A., Börner N., Jacob D. E. and Andreae M. O. (2012) Accurate trace element analysis of speleothems and biogenic calcium carbonates by LA-ICP-MS. *Chem. Geol.* **318-**

319, 31–44.

Johannesson K. H. and Zhou X. (1999) Origin of middle rare earth element enrichments in acid waters of a Canadian High Arctic lake. *Geochim. Cosmochim. Acta* **63**, 153–165.

John E. H., Wignall P. B., Newton R. J. and Bottrell S. H. (2010) $\delta34SCAS$ and $\delta18OCAS$ records during the Frasnian–Famennian (Late Devonian) transition and their bearing on mass extinction models. *Chem. Geol.* **275**, 221–234.

Johnson C. a., Emsbo P., Poole F. G. and Rye R. O. (2009) Sulfur- and oxygen-isotopes in sediment-hosted stratiform barite deposits. *Geochim. Cosmochim. Acta* **73**, 133–147.

Johnson C. A., Kelley K. D. and Leach D. L. (2004) Sulfur and Oxygen Isotopes in Barite Deposits of the Western Brooks Range, Alaska, and Implications for the Origin of the Red Dog Massive Sulfide Deposits. *Econ. Geol.* **99**, 1435–1448.

Johnston D. T. (2011) Multiple sulfur isotopes and the evolution of Earth's surface sulfur cycle. *Earth-Science Rev.* **106**, 161–183.

Jørgensen B. B., Böttcher M. E., Lüschen H., Neretin L. N. and Volkov I. I. (2004) Anaerobic methane oxidation and a deep H2S sink generate isotopically heavy sulfides in Black Sea sediments. *Geochim. Cosmochim. Acta* **68**, 2095–2118.

Jørgensen B. B. J. (1979) A theoretical model of the stable sulfur isotope distribution in marine sediments. *Geochim. Cosmochim. Acta* **43**, 363–374.

Jørgensen B. B. J. and Kasten S. (2006) Sulfur Cycling and Methane Oxidation. In

Marine Geochemistry (eds. H. D. Schulz and M. Zabel).

Jørgensen B. B. J., Weber A. and Zopfi J. (2001) Sulfate reduction and anaerobic methane oxidation in Black Sea sediments. *Deep. Res. I* **48**, 2097–2120.

Joye S. B., Boetius A., Orcutt B. N., Montoya J. P., Schulz H. N., Erickson M. J. and Lugo S. K. (2004) The anaerobic oxidation of methane and sulfate reduction in sediments from Gulf of Mexico cold seeps. *Chem. Geol.* **205**, 219–238.

Kaplan I. R. and Rittenberg S. C. (1964) Microbiological Fractionation of Sulphur Isotopes. *J. Gen. Microbiol.* **34**, 195–212.

Kelley K. D., Dumoulin J. A. and Jennings S. (2004) The Anarraaq Zn-Pb-Ag and Barite Deposit, Northern Alaska: Evidence for Replacement of Carbonate by Barite and Sulfides. *Econ. Geol.* **99**, 1577–1591.

Kelley K. K. and Jennings S. (2004) A Special Issue Devoted to Barite and Zn-Pb-Ag Deposits in the Red Dog District, Western Brooks Range, Northern Alaska. *Econ. Geol.* **99**, 1267–1280.

Kiyosu Y. and Krouse R. H. (1990) The role of organic and acid the in the sulfur abiogenic isotope reduction effect. *Geochem. J.* **24**, 21–27.

Klinkhammer G. ., Elderfield H., Edmond J. . and Mitra a (1994) Geochemical implications of rare earth element patterns in hydrothermal fluids from mid-ocean ridges. *Geochim. Cosmochim. Acta* **58**, 5105–5113.

Kozdon R., Kita N. T., Huberty J. M., Fournelle J. H., Johnson C. a. and Valley J. W. (2010) In situ sulfur isotope analysis of sulfide minerals by SIMS: Precision and

accuracy, with application to thermometry of ~3.5Ga Pilbara cherts. *Chem. Geol.* **275**, 243–253.

Large R. R., Bull S. W., Cooke D. R. and Mcgoldrick P. J. (1998) A genetic model for the HYC deposit, Australia: Based on regional sedimentology, geochemistry, and sulfide-sediment relationships. *Econ. Geol.* **93**, 1345–1368.

Large R. R., Bull S. W., McGoldrick P. J., Walters S., Derrick G. M. and Carr G. R. (2005a) Strata-Bound and Stratiform Zn-Pb-Ag Deposits in Proterozoic Sedimentary Basins, Northern Australia. *Econ. Geol.* **100**, 931– 963.

Large R. R., Bull S. W., McGoldrick P. J., Walters S., Derrick G. M. and Carr G. R. (2005b) Strata-Bound and Stratiform Zn-Pb-Ag Deposits in Proterozoic Sedimentary Basins, Northern Australia. *Econ. Geol.*, 931– 963.

Large R. R. and Mcgoldrick P. J. (1998) Lithogeochemical halos and geochemical vectors to stratiform sediment hosted Zn – Pb – Ag deposits, 1. Lady Loretta Deposit, Queensland. *J. Geochemical Explor.* **63**, 37–56.

Leach D. L., Bradley D. C., Huston D., Pisarevsky S. A., Taylor R. D. and Gardoll J. (2010) Sediment-Hosted Lead-Zinc Deposits in Earth History. *Econ. Geol.* **105**, 593–625.

Leach D. L., Marsh E., Emsbo P., Rombach C. S., Kelley K. K. and Anthony M. (2004) Nature of Hydrothermal Fluids at the Shale-Hosted Red Dog Zn-Pb-Ag Deposits, Brooks Range, Alaska. *Econ. Geol.* **99**, 1449–1480.

Leach D. L., Sangster D. F., Kelley K. D., Large R. R., Garven G., Allen C. R., Gutzmer J.

and Walters J. (2005) Sediment-Hosted Lead-Zinc Deposits: A Global Perspective. *Econ. Geol.* **100**, 561–607.

Leach D. and Sangster D. F. (1993) Mississippi Valley-type lead-zinc deposits. In *Mineral Deposit Modeling* (eds. R. V. Kirkham, W. D. Sinclair, R. I. Thorpe, and J. M. Duke). Geological Association of Canada. pp. 289–314.

Longstaffe F. J., Nesbitt B. E. and Muehlenbachs K. (1982) Oxygen isotope geochemistry of the shales hosting Pb-Zn-Ba mineralization at the Jason prospect, Selwyn Basin, Yukon. *Canada Geol. Surv. Pap. 82-1C*, 45–49.

Lowenstein T. K., Hardie L. a., Timofeeff M. N. and Demicco R. V. (2003) Secular variation in seawater chemistry and the origin of calcium chloride basinal brines. *Geology* **31**, 857.

Lowenstein T. K., Kendall B. and Anbar A. D. (2014) The Geologic History of Seawater. In *Treatise on Geochemistry* Elsevier Ltd. pp. 569–629.

Lyons T. W., Gellatly A. M., Mcgoldrick P. J. and Kah L. C. (2006) Proterozoic sedimentary exhalative (SEDEX) deposits and links to evolving ocean chemistry. *Geol. Soc. Am. Mem.* **198**, 169–184.

Machel H. G. (2001) Bacterial and thermochemical sulfate reduction in diagenetic settings - old and new insights. *Sediment. Geol.* **140**, 143–175.

Machel H. G. (1987) Some aspects of diagenetic sulphate-hydrocarbon redox reactions Some aspects of diagenetic sulphate-hydrocarbon redox reactions. *Geol. Soc. London, Spec. Publ.* **36**, 15–28.

Machel H. G. and Cavell P. A. (1999) Low-flux, tectonically induced squee- gee fluid flow ("hot flash") into the Rocky Mountain Foreland Basin. *Bull. Can. Pet. Geol.* **47**, 510–533.

Machel H. G., Krouse H. R. and Sassen R. (1995) Products and distinguishing criteria of bacterial and thermochemical sulfate reduction. *Appl. Geochemistry* **10**, 373–389.

MacIntyre D. G. (1998) Geology, geochemistry and mineral deposits of the Akie River area, northeast British Columbia. *Br. Columbia Minist. Energy Miner. Div. Geol. Surv. Branch*, 91.

Macquaker J. H. S., Bentley S. J. and Bohacs K. M. (2010) Wave-enhanced sediment-gravity flows and mud dispersal across continental shelves: Reappraising sediment transport processes operating in ancient mudstone successions. *Geology* **38**, 947–950.

Macquaker J. H. S. and Bohacs K. M. (2007) Geology. On the accumulation of mud. *Science* **318**, 1734–5.

Macquaker J. H. S., Taylor K. G. and Gawthorpe R. L. (2007) High-Resolution Facies Analyses of Mudstones: Implications for Paleoenvironmental and Sequence Stratigraphic Interpretations of Offshore Ancient Mud-Dominated Successions. *J. Sediment. Res.* **77**, 324–339.

McClay K. R. (1991) Deformation of stratiform Zn-Pb (-barite) deposits in the northern Canadian Cordillera. *Ore Geol. Rev.* **6**, 435–462.

McClay K. R. and Bidwell G. E. (1986) Geology of the Tom deposit, Macmillan Pass, Yukon. In *Mineral Deposits of Northern Cordillera* (ed. J. A. Morin). The Canadian Institute of Mining and Metallurgy. pp. 100–114.

McCollom T. M. and Seewald J. S. (2007) Abiotic synthesis of organic compounds in deep-sea hydrothermal environments. *Chem. Rev.* **107**, 382–401.

Michard A. and Albarède F. (1986) The REE content of some hydrothermal fluids. *Chem. Geol.* **55**, 51–60.

Morganti J. M. (1979) The geology and ore deposits of the Howards Pass area, Yukon and Northwest Territories: the origin of basinal sedimentary stratiform sulphide deposits. University of British Columbia.

Nelson J. and Colpron M. (2007) Tectonics and metallogeny of the British Columbia, Yukon and Alaskan Cordillera, 1.8 Ga to the present. *Miner. Depos. Canada A Synth. Major Depos. Dist. Metallog. Evol. Geol. Prov. Explor. Methods* **2703**, 755–791.

Nelson J. L., Survey B. C. G., Box P. O., Govt S. P., Columbia B., Colpron M., Piercey S. J., Road R. L., Dusel-bacon C., Park M. and Murphy D. C. (2006) Paleozoic tectonic and metallogenetic evolution of pericratonic terranes in Yukon , northern British Columbia and eastern Alaska 1. *GAC Spec. Pap. 45*, 323–360.

Nelson J., Paradis S., Christensen J. and Gabites J. (2002) Canadian Cordilleran Mississippi Valley-Type Deposits : A Case for Devonian-Mississippian Back-Arc Hydrothermal Origin. *Econ. Geol.* **97**, 1013–1036.

Nesbitt H. W. and Young G. M. (1982) Early Proterozoic climates and plate motions inferred from major element chemistry of lutites. *Nature* **299**, 715–717.

Newton R. J., Reeves E. P., Kafousia N., Wignall P. B., Bottrell S. H. and Sha J.-G. (2010) Low marine sulfate concentrations and the isolation of the European epicontinental sea during the Early Jurassic. *Geology* **39**, 7–10.

Niewöhner C., Hensen C., Kasten S., Zabel M. and Schulz H. D. (1998) Deep sulfate reduction completely mediated by anaerobic methane oxidation in sediments of the upwelling area off Namibia. *Geochim. Cosmochim. Acta* **62**, 455–464.

Ohmoto H. and Goldhaber M. B. (1997) Sulfur and Carbon Isotopes. In *Geochemistry of Hydrothermal Ore Deposits* (ed. H. L. Barnes). John Wiley & Sons. pp. 517–612.

Orberger B., Gallien J.-P., Pinti D. L., Fialin M., Daudin L., Gröcke D. R. and Pasava J. (2005) Nitrogen and carbon partitioning in diagenetic and hydrothermal minerals from Paleozoic Black Shales, (Selwyn Basin, Yukon Territories, Canada). *Chem. Geol.* **218**, 249–264.

Paradis S., Nelson J. L. and Irwin S. E. B. (1998) Age constraints on the devonian shale-hosted Zn-Pb-Ba deposits, Gataga District, Northeastern British Columbia, Canada. *Econ. Geol.* **93**, 184–200.

Passier H. F., Middelburg J. J., Lange G. J. De and Böttcher M. E. (1997) Pyrite contents, microtextures, and sulfur isotopes in relation to formation of the youngest eastern Mediterranean sapropel. *Geology* **25**, 519–522.

Paytan A. and Griffith E. M. (2007) Marine barite: Recorder of variations in ocean export productivity. *Deep Sea Res. Part II* **54**, 687–705.

Paytan A., Mearon S., Cobb K. and Kastner M. (2002) Origin of marine barite deposits: Sr and S isotope characterization. *Geology* **30**, 747.

Peter J. M., Peltonen P., Scott S. D., Simoneit B. R. T. and Kawka O. E. (1991) 14C ages of hydrothermal petroleum and carbonate in Guaymas Basin, Gulf of California: implications for oil generation, expulsion, and migration. *Geology* **19**, 253–256.

Potter R.W. II. (1977) Pressure corrections for fluid inclusion homogenization temperatures based on the volumetric properties of the system NaCl-H_2O. *U.S. Geol. Surv. Jour. Res.* **5**, 602-608.

Pigage L. C. (1991) Field guide Anvil Pb-Zn-Ag District, Yukon Territory, Canada. In *Geological Survey of Canada Open File 2169* (eds. J. G. Abbott and R. J. W. Turner). pp. 177–244.

Pigage L. C. (1986) Geology of the Cirque barite-zinc-lead-silver deposits, northeastern British Columbia. In *Mineral Deposits of Northern Cordillera* (ed. J. A. Morin). Canadian Institute of Mining and Metallurgy. pp. 71–86.

Plint a. G., Macquaker J. H. S. and Varban B. L. (2012) Bedload Transport of Mud Across A Wide, Storm-Influenced Ramp: Cenomanian-Turonian Kaskapau Formation, Western Canada Foreland Basin. *J. Sediment. Res.* **82**, 801–822.

Radha A. V. and Navrotsky A. (2013) Thermodynamics of Carbonates. *Rev. Mineral. Geochemistry* **77**, 73–121.

Raiswell R. (1982) Pyrite texture, isotopic composition and the availability of iron. *Am. J. Sci.* **282**, 1244–1263.

Rajabi A., Rastad E., Canet C. and Alfonso P. (2014) The early Cambrian Chahmir shale-hosted Zn–Pb deposit, Central Iran: an example of vent-proximal SEDEX mineralization. *Miner. Depos.*

Rasmussen B. and Buick R. (2000) Oily old ores: Evidence for hydrothermal petroleum generation in an Archean volcanogenic massive sulfide deposit. *Geology* **28**, 731–734.

Reeburgh W. S. (1976) Methane consumption in cariaco trench waters and sediments. *Earth Planet. Sci. Lett.* **28**, 337–344.

Reeburgh W. S. (2007) Oceanic methane biogeochemistry. *Chem. Rev.* **107**, 486–513.

Reeder R. J. (1983) Crystal chemistry of the rhombohedral carbonates ed. R. J. Reeder. *Rev. Mineral.* **11**, 1–48.

Rees C. E. (1973) A steady-state model for sulphur isotope fractionation in bacterial reduction processes. *Geochim. Cosmochim. Acta* **37**, 1141–1162.

Roedder E. (1984) Fluid inclusions. *Rev. Mineral.* **12**, 646p.

Rye D. M. and Williams N. (1981) Studies of the Base Metal Sulfide Deposits at McArthur River, Northern Territory, Australia: III. The Stable Isotope Geochemistry of the H.Y.C., Ridge, and Cooley Deposits. *Econ. Geol.*

Samson I. M. and Russell M. J. (1987) Genesis of the Silvermines zinc-lead-barite

deposit, Ireland; fluid inclusion and stable isotope evidence. *Econ. Geol.* **82**, 371–394.

Sánchez-España J., Velasco F., Boyce A. J. and Fallick A. E. (2003) Source and evolution of ore-forming hydrothermal fluids in the northern Iberian Pyrite Belt massive sulphide deposits (SW Spain): evidence from fluid inclusions and stable isotopes. *Miner. Depos.* **38**, 519–537.

Schieber J., Krinsley D. and Riciputi L. (2000) Diagenetic origin of quartz silt in mudstones and implications for silica cycling. *Nature* **406**, 981–5.

Schieber J., Southard J. B. and Schimmelmann A. (2010) Lenticular Shale Fabrics Resulting from Intermittent Erosion of Water-Rich Muds--Interpreting the Rock Record in the Light of Recent Flume Experiments. *J. Sediment. Res.* **80**, 119–128.

Schieber J., Southard J. and Thaisen K. (2007) Accretion of mudstone beds from migrating floccule ripples. *Science* **318**, 1760–3.

Schmitz B. (1987) Barium, equatorial high productivity, and the northward wandering of the Indian continent. *Paleoceanography* **2**, 63–77.

Scholz F., Hensen C., Noffke A., Rohde A., Liebetrau V. and Wallmann K. (2011) Early diagenesis of redox-sensitive trace metals in the Peru upwelling area – response to ENSO-related oxygen fluctuations in the water column. *Geochim. Cosmochim. Acta* **75**, 7257–7276.

Schwinn G., Wagner T., Baatartsogt B. and Markl G. (2006) Quantification of mixing processes in ore-forming hydrothermal systems by combination of stable isotope

and fluid inclusion analyses. *Geochim. Cosmochim. Acta* **70**, 965–982.

Seal R. R. (2006) Sulfur Isotope Geochemistry of Sulfide Minerals. *Rev. Mineral. Geochemistry* **61**, 633–677.

Seal R. R., Alpers C. N. and Rye R. O. (2000) Stable Isotope Systematics of Sulfate Minerals. *Rev. Mineral. Geochemistry* **40**, 541–602.

Seewald J. S., Seyfried W. E. and Shanks W. C. (1994) Variations in the chemical and stable isotope composition of carbon and sulfur species during organic-rich sediment alteration: An experimental and theoretical study of hydrothermal activity at guaymas basin, gulf of california. *Geochim. Cosmochim. Acta* **58**, 5065–5082.

Shepherd T.J., Rankin A.H. and Alderton A.H. (1985) A Practical Guide to Fluid Inclusion Studies. Blackie and Son, Glastgow, 239 pp.

Shock E. L., Canovas P., Yang Z., Boyer G., Johnson K., Robinson K., Fecteau K., Windman T. and Cox A. (2013) Thermodynamics of Organic Transformations in Hydrothermal Fluids. *Rev. Mineral. Geochemistry* **76**, 311–350.

Sholkovitz E. and Shen G. T. (1995) The incorporation of rare earth elements in modern coral. *Geochim. Cosmochim. Acta* **59**, 2749–2756.

Singer D. A. (1995) World Class Base and Precious Metal Deposits – A Quantitative Analysis. *Econ. Geol.* **90**, 88–104.

Slack J. F., Kelley K. D., Anderson V. M., Clark J. L. and Ayuso R. a. (2004) Multistage hydrothermal silicification and Fe-Tl-As-Sb-Ge-REE enrichment in the Red Dog

Zn-Pb-Ag district, northern Alaska: Geochemistry, origin, and exploration applications. *Econ. Geol.* **99**, 1481–1508.

Spangenberg J., Fontboté L., Sharp Z. D. and Hunziker J. (1996) Carbon and oxygen isotope study of hydrothermal carbonates in the zinc-lead deposits of the San Vicente district, central Peru: a quantitative modeling on mixing processes and CO2 degassing. *Chem. Geol.* **2541**.

Stamatakis M. G. and Hein J. R. (1993) Origin of barite in Tertiary marine sedimentary rocks from Lefkas Island, Greece. *Econ. Geol.* **88**, 91–103.

Stein R., Rullkötter J. and Welte D. H. (1986) Accumulation of organic-carbon-rich sediments in the Late Jurassic and Cretaceous Atlantic Ocean — A synthesis. *Chem. Geol.* **56**, 1–32.

Stoffell B., Appold M. S., Wilkinson J. J., McClean N. A. and Jeffries T. E. (2008) Geochemistry and Evolution of Mississippi Valley-Type Mineralizing Brines from the Tri-State and Northern Arkansas Districts Determined by LA-ICP-MS Microanalysis of Fluid Inclusions. *Econ. Geol.* **103**, 1411–1435.

Sverjensky D. a. (1984) Europium redox equilibria in aqueous solution. *Earth Planet. Sci. Lett.* **67**, 70–78.

Taylor B. D. (1987) Stable isotope geochemistry of ore-forming fluids. In *Short Course Handbook* Mineralogical Association of Canada. pp. 337–445.

Taylor R. D., Leach D. L., Bradley D. C. and Psarevsky S. A. (2009) Compilation of mineral resource data for Mississippi Valley-type and CD sediment-hosted lead-

zinc deposits. *U.S. Geol. Surv. Open-File Rep. 2009-1297*, 42.

Thode H. G., Monster J. and Dunford H. B. (1961) Sulphur isotope geochemistry. *Geochim. Cosmochim. Acta* **25**, 159–174.

Thom J. and Anderson G. M. (2007) The role of thermochemical sulfate reduction in the origin of Mississippi Valley-type deposits. I. Experimental results. *Geofluids*.

Tornos F. and Heinrich C. (2008) Shale basins, sulfur-deficient ore brines and the formation of exhalative base metal deposits. *Chem. Geol.* **247**, 195–207.

Torres M. E., Bohrmann G., Dubé T. E., Poole F. G., Poole, Forrest G. and Poole F. G. (2003) Formation of modern and Paleozoic stratiform barite at cold methane seeps on continental margins. *Geology* **31**, 897–900.

Torres M. E., Brumsack H. J., Bohrmann G. and Emeis K. C. (1996) Barite fronts in continental margin sediments: a new look at barium remobilization in the zone of sulfate reduction and formation of heavy barites in diagenetic fronts. *Chem. Geol.* **127**, 125–139.

Tréguer P. J. and De La Rocha C. L. (2013) The world ocean silica cycle. *Ann. Rev. Mar. Sci.* **5**, 477–501.

Turchyn A. V., Sivan O. and Schrag D. P. (2006) Oxygen isotopic composition of sulfate in deep sea pore fluid: evidence for rapid sulfur cycling. *Geobiology* **4**, 191–201.

Turner R. J. (1991) Jason stratiform Zn-Pb-barite deposit, Selwyn Basin, Canada (NTS 105-0-1): geological setting, hydrothermal facies and genesis. In *Geological*

Survey of Canada Open File 2169 (eds. J. G. Abbott and R. J. Turner). pp. 137–175.

Turner R. J. . (1986) The genesis of stratiform lead-zinc deposits, Jason property, Macmillan Pass, Yukon. Stanford University.

Turner R. J. W. (1992) Formation of Phanerozoic stratiform sediment , hosted zinc-lead deposits : Evidence for the critical role of ocean anoxia. *Chem. Geol.* **99**, 165–188.

Turner R. J. W., Goodfellow W. D. and Taylor B. D. (1989) Isotopic Geochemistry of the Jason stratiform sediment-hosted zinc-lead deposit, Macmillan Pass, Yukon. In *Current Research, Geological Survey of Canada, Paper 89-1E* pp. 21–30.

Wankel S. D., Adams M. M., Johnston D. T., Hansel C. M., Joye S. B. and Girguis P. R. (2012) Anaerobic methane oxidation in metalliferous hydrothermal sediments: influence on carbon flux and decoupling from sulfate reduction. *Environ. Microbiol.* **14**, 2726–40.

Warren J. (2000) Dolomite: occurrence, evolution and economically important associations. *Earth-Science Rev.* **52**, 1–81.

Van Der Weijden C. H. (2002) Pitfalls of normalization of marine geochemical data using a common divisor. *Mar. Geol.* **184**, 167–187.

Welhan J. a. and Lupton J. E. (1987) Light hydrocarbon gases in Guaymas Basin hydrothermal fluids: thermogenic versus abiogenic origin. *Am. Assoc. Pet. Geol. Bull.* **71**, 215–223.

De Wever P. and Baudin F. (1996) Palaeogeography of radiolarite and organic-rich deposits in Mesozoic Tethys. *Geol. Rundschau* **85**, 310–326.

De Wever P., Dumitrica P., Caulet J. P., Nigrini C. and Caridroit M. (2001) *Radiolarians in the sedimentary record.*, Taylor and Francis.

Widerlund A., Nowell G. M., Davison W. and Pearson D. G. (2012) High-resolution measurements of sulphur isotope variations in sediment pore-waters by laser ablation multicollector inductively coupled plasma mass spectrometry. *Chem. Geol.* **291**, 278–285.

Wilkinson J. J. (2003) On diagenesis, dolomitisation and mineralisation in the Irish Zn-Pb orefield. *Miner. Depos.* **38**, 968–983.

Wilkinson J. J. (2014) Sediment-Hosted Zinc–Lead Mineralization: Processes and Perspectives. In *Treatise on Geochemistry: Second Edition* Elsevier Ltd. pp. 219–249.

Williams N. (1978) Studies of the Base Metal Sulfide Deposits at McArthur River, Northern Territory, Australia: I. the Cooley and Ridge Deposits. *Econ. Geol.* **73**, 1005–1035.

Wilson N. S. F. (2000) Organic petrology, chemical composition, and reflectance of pyrobitumen from the El Soldado Cu deposit, Chile. *Int. J. Coal Geol.* **43**, 53–82.

Winn R. D. and Bailes R. J. (1987) Stratiform lead-zinc sulfides, mudflows, turbidites: Devonian sedimentation along fault scarp of extensional origin, Jason deposit, Yukon Territory, Canada. *Geol. Soc. Am. Bull.* **98**, 528–539.

Yardley B. W. D. (2005) Metal Concentrations in Crustal Fluids and Their Relationship to Ore Formation. *Econ. Geol.* **100**, 613–632.

Zhang W., Guan P., Jian X., Feng F. and Zou C. (2014) In situ geochemistry of Lower Paleozoic dolomites in the north-western Tarim basin: Implications for the nature, origin, and evolution of diagenetic fluids. *Geochemistry, Geophys. Geosystems* **15**, 2744–2764.

Zhelezinskaia I., Kaufman A. J., Farquhar J. and Cliff J. (2014) Large sulfur isotope fractionations associated with Neoarchean microbial sulfate reduction. *Science (80-.).* **346**, 742–744.

Zheng Y. F. (1990) Carbon-oxygen isotopic covariation in hydrothermal calcite during degassing of CO_2 - A quantitative evaluation and application to the Kushikino gold mining area in Japan. *Miner. Depos.* **25**, 246–250.

Appendix A. Major element oxide, bulk rock δ³⁴S values and total organic carbon (TOC) data from un-mineralised mudstones of DH-TYK005 and DH-76-17.

Table A.1.

Method	4X	4X	4X	4X	4X	4X	4X	4X	4X	4X	4X	4X	4X	4X	LECO	
Analyte	SiO2	Al2O3	Fe2O3	CaO	MgO	Na2O	K2O	MnO	TiO2	P2O5	Cr2O3	Ba	LOI	SUM	TOC	$\delta^{34}S$
Unit	%	%	%	%	%	%	%	%	%	%	%	%	%	%	%	‰ (VCDT)
MDL	0.01	0.01	0.01	0.01	0.01	0.01	0.01	0.01	0.01	0.01	0	0.01		0.01		
Sample ID (meters)																
Silica Glass																
76-17_15 (298)	99.45	0.04	0.48	<0.01	<0.01	<0.01	0.01	<0.01	<0.01	<0.01	0.03	<0.01	-0.09	99.89	4.04	-5.7
76-17_17 (292.5)	77.00	7.39	2.42	1.43	0.80	0.03	2.05	0.02	0.38	0.27	0.03	0.14	7.43	99.40	3.38	-1.4
76-17_18 (292)	83.05	6.38	1.53	0.60	0.37	<0.01	1.80	<0.01	0.30	0.33	0.03	0.12	5.27	99.80	3.86	-1.3
76-17_20 (290)	81.62	7.18	1.89	0.56	0.44	0.01	2.01	<0.01	0.37	0.25	0.03	0.13	6.21	100.73	3.25	-3.5
76-17_22 (287)	81.63	6.54	2.10	0.74	0.54	<0.01	1.84	0.01	0.35	0.16	0.03	0.11	5.84	99.89	3.80	-4.2
76-17_23 (286.8)	80.12	7.62	2.16	0.49	0.45	<0.01	2.13	<0.01	0.40	0.21	0.03	0.13	6.31	100.08	4.01	-8.3
76-17_24 (286.5)	81.51	6.89	1.61	0.73	0.44	<0.01	1.91	<0.01	0.32	0.37	0.03	0.13	6.17	100.13	3.31	-4.3
76-17_26 (285.9)	83.18	5.89	1.67	0.80	0.54	<0.01	1.66	0.01	0.29	0.16	0.02	0.11	5.59	99.92	3.18	-3.2
76-17_29 (285)	68.38	4.85	11.07	1.93	0.94	<0.01	1.34	0.10	0.24	0.19	0.02	0.09	9.64	98.79	2.53	-0.7
76-17_31 (282)	80.74	7.81	1.91	0.82	0.60	<0.01	2.19	0.01	0.30	0.23	0.02	0.15	5.23	100.03	4.04	-1.4
76-17_32 (280)	76.08	7.69	2.78	1.32	0.94	<0.01	2.13	0.02	0.40	0.12	0.03	0.14	7.85	99.53	3.27	-4.1
76-17_33 (279.6)	73.06	9.67	2.57	1.47	1.04	<0.01	2.68	0.02	0.46	0.24	0.02	0.17	8.30	99.74	3.57	-4.1
76-17_34 (279)	78.97	7.78	2.56	0.73	0.54	<0.01	2.15	0.01	0.40	0.30	0.03	0.14	6.48	100.10	3.74	-8.6
76-17_35 (275)	78.91	8.13	1.87	0.85	0.58	<0.01	2.26	<0.01	0.41	0.36	0.02	0.15	6.46	100.04	2.89	-13.9
76-17_36 (274)	73.89	7.73	6.93	0.18	0.40	<0.01	2.17	0.01	0.36	0.14	0.02	0.15	7.70	99.68	2.67	-14.6
76-17_38 (260)	78.27	7.38	2.10	1.51	0.93	<0.01	2.07	0.03	0.35	0.35	0.02	0.14	6.11	99.25	3.82	-3.6
76-17_40 (238)	80.41	7.78	1.69	0.45	0.46	<0.01	2.23	<0.01	0.37	0.24	0.03	0.15	6.13	99.96	4.74	-1.2
76-17_41 (225)	72.98	10.13	3.82	0.42	0.56	0.01	2.83	<0.01	0.54	0.33	0.02	0.23	8.44	100.35	5.11	-15.6
	78.70	8.10	1.70	0.55	0.67	0.01	2.19	<0.01	0.42	0.11	0.02	0.19	7.76	100.46		

Table A.2.

Method Analyte Unit Sample ID — MDL	meters	4X SiO2 % 0.01	4X Al2O3 % 0.01	4X Fe2O3 % 0.01	4X CaO % 0.01	4X MgO % 0.01	4X Na2O % 0.01	4X K2O % 0.01	4X MnO % 0.01	4X TiO2 % 0.01	4X P2O5 % 0.01	4X Cr2O3 % 0	4X Ba % 0.01	4X LOI % 0.01	4X SUM % 0.01	LECO TOC % 0.01	δ34S ‰ (VCDT)
TYK5-1	155.4	76.01	7.08	5.78	0.34	0.24	<0.01	1.24	0.04	0.36	0.26	0.02	0.59	7.98	100.00	3.30	8.7
TYK5-2	155	71.08	9.59	4.48	0.38	0.44	<0.01	2.31	0.02	0.61	0.30	0.03	1.15	9.10	99.64	4.98	6.9
TYK5-3	154.2	70.71	8.27	4.49	0.51	0.39	<0.01	1.73	0.04	0.51	0.30	0.03	2.03	9.78	99.03	5.58	6.5
TYK5-6	149.1	75.10	8.13	3.91	0.28	0.26	<0.01	1.28	<0.01	0.43	0.22	0.03	2.78	7.78	100.52	3.81	3.1
TYK5-7	147.5	73.38	7.66	3.98	0.44	0.26	<0.01	0.97	0.03	0.38	0.21	0.03	5.65	6.17	99.81	2.73	6.5
TYK5-8	141.3	72.82	8.00	3.96	0.25	0.22	<0.01	0.90	0.02	0.49	0.14	0.03	6.45	6.97	101.02	3.46	4.3
TYK5-10	99.41	72.08	7.34	3.44	1.29	0.81	<0.01	0.91	0.02	0.40	0.27	0.03	5.08	6.65	98.89	2.76	8.1
TYK5-11	96.37	72.37	9.17	2.54	0.63	0.52	<0.01	1.41	0.01	0.51	0.27	0.03	5.07	6.21	99.32	2.88	1.7
TYK5-12	90.66	68.93	8.03	3.84	2.47	1.78	<0.01	1.48	0.04	0.45	0.16	0.02	2.72	7.99	98.23	2.98	-1.2
TYK5-13	83.84	75.22	10.20	1.88	0.39	0.59	<0.01	2.23	<0.01	0.56	0.19	0.03	1.82	6.18	99.51	3.24	-4.4
TYK5-14	81.36	78.14	6.28	2.67	1.40	0.98	<0.01	1.40	0.02	0.33	0.18	0.03	1.19	6.17	98.92	3.02	3.2
TYK5-14A	80.82	67.63	6.78	4.99	3.85	2.41	<0.01	1.48	0.04	0.36	0.18	0.02	1.19	7.62	96.70	2.44	8.3
TYK5-15	77.82	70.16	7.84	4.14	2.62	1.77	<0.01	1.74	0.03	0.41	0.20	0.02	0.93	8.47	98.45	3.06	7.8
TYK5-16	76.19	77.66	9.57	2.46	0.36	0.44	<0.01	2.06	<0.01	0.49	0.28	0.03	1.08	5.61	100.17	2.20	-0.3
TYK5-17	73.52	80.87	8.02	1.98	0.30	0.39	<0.01	1.80	<0.01	0.41	0.22	0.02	0.94	4.97	100.04	2.45	1.7
TYK5-18	72.7	80.77	8.07	1.76	0.30	0.39	<0.01	1.83	<0.01	0.42	0.23	0.02	0.95	5.24	100.10	2.85	-0.8
TYK5-19	69.81	81.67	7.69	1.72	0.39	0.46	<0.01	1.80	<0.01	0.40	0.22	0.02	0.88	5.19	100.55	2.78	-0.7
TYK5-20	68.72	79.89	8.25	1.68	0.47	0.53	<0.01	1.93	<0.01	0.42	0.22	0.02	0.94	5.56	100.02	2.90	-0.5
TYK5-21	29.33	74.64	11.22	1.88	0.15	0.56	0.03	2.66	<0.01	0.56	0.14	0.03	0.90	7.34	100.22	4.24	-5.3

QA/QC USGS SBC-1 and SGR-1b (certified values in grey)

Sample ID	meters	SiO2	Al2O3	Fe2O3	CaO	MgO	Na2O	K2O	MnO	TiO2	P2O5	Cr2O3	Ba	LOI	SUM	TOC	δ34S
SBC-1.1		47.46	21.00	9.63	2.90	2.58	0.19	3.50	0.15	0.84	0.37	0.015	0.09	9.95	98.68	1.17	
SBC-1.2		47.49	21.00	9.62	2.93	2.57	0.19	3.48	0.15	0.85	0.37	0.017	0.09	9.99	98.75	1.19	
SBC-1.3																1.18	
SBC-1.4																1.19	
SBC-1.5																1.18	
SBC-1-5A																1.18	
SBC-1		*47.64*	*21.00*	*9.71*	*2.95*	*2.60*	*<0.45*	*3.45*	*0.15*	*0.86*	*0.37*		*0.08*	*10.20*		*1.23*	
SGR-1b		28.30	6.55	2.91	8.26	4.46	3.05	1.58	0.03	0.25	0.27	0.01	0.03	41.34	97.03		
SGR-1b		*28.20*	*6.52*	*4.19*	*8.38*	*4.44*	*2.99*	*1.66*		*0.25*	*0.33*		*0.03*				

Appendix B. Sulphur isotope data acquired by Secondary Ion Mass Spectrometry (SIMS). $\delta^{34}S$ values in pyrite (B.1.), $\delta^{34}S$ values in barite (B.2.) and $\delta^{18}O$ values in barite (B.3.). Analyses in grey hit non-target minerals and are unreliable.

Table B.1.

Spot ID	Sample	δ³⁴S (‰ VCDT)	2σ (‰)
P1333C_M1270_IP14043_34S32S_S2904C_3B_Py_1@1	T91.14-3	13.82	0.16
P1333C_M1270_IP14043_34S32S_S2904C_3B_Py_1@2	T91.14-3	13.83	0.14
P1333C_M1270_IP14043_34S32S_S2904C_3B_Py_1@3	T91.14-3	-16.99	0.30
P1333C_M1270_IP14043_34S32S_S2904C_3B_Py_1@4	T91.14-3	14.39	0.17
P1333C_M1270_IP14043_34S32S_S2904C_3B_Py_1@5	T91.14-3	9.06	0.16
P1333C_M1270_IP14043_34S32S_S2904C_3C_Py_2@1	T91.14-3	-27.24	0.12
P1333C_M1270_IP14043_34S32S_S2904C_3C_Py_2@2	T91.14-3	-24.75	0.08
P1333C_M1270_IP14043_34S32S_S2904C_3C_Py_2@3	T91.14-3	8.58	0.17
P1333C_M1270_IP14043_34S32S_S2904C_3C_Py_2@4	T91.14-3	8.82	0.15
P1333C_M1270_IP14043_34S32S_S2904C_3C_Py_2@5	T91.14-3	8.92	0.15
P1333C_M1270_IP14043_34S32S_S2904C_3C_Py_2@6	T91.14-3	6.61	0.25
P1333C_M1270_IP14043_34S32S_S2904C_3C_Py_3@1	T91.14-3	14.56	0.14
P1333C_M1270_IP14043_34S32S_S2904C_3C_Py_3@2	T91.14-3	16.01	0.13
P1333C_M1270_IP14043_34S32S_S2904C_3C_Py_3@3	T91.14-3	11.86	0.16
P1333C_M1270_IP14043_34S32S_S2906G_3A_Py_1@1	TYK2-8	10.10	0.16
P1333C_M1270_IP14043_34S32S_S2906G_3A_Py_1@2	TYK2-8	10.61	0.17
P1333C_M1270_IP14043_34S32S_S2906G_3A_Py_1@3	TYK2-8	10.54	0.18
P1333C_M1270_IP14043_34S32S_S2906G_3A_Py_1@4	TYK2-8	9.61	0.19
P1333C_M1270_IP14043_34S32S_S2906G_3B_Py_2@1	TYK2-8	9.87	0.20
P1333C_M1270_IP14043_34S32S_S2906G_3B_Py_2@2	TYK2-8	10.75	0.16
P1333C_M1270_IP14043_34S32S_S2906G_3B_Py_2@3	TYK2-8	16.30	0.28
P1333C_M1270_IP14043_34S32S_S2906G_3B_Py_2@4	TYK2-8	13.92	0.19
P1333C_M1270_IP14043_34S32S_S2906G_3B_Py_2@5	TYK2-8	13.07	0.17
P1333C_M1270_IP14043_34S32S_S2906G_2-6_Py_3@1	TYK2-8	12.66	0.15
P1333C_M1270_IP14043_34S32S_S2906G_2-6_Py_3@2	TYK2-8	-22.44	0.36
P1333C_M1270_IP14043_34S32S_S2906G_2-6_Py_3@3	TYK2-8	10.39	0.21
P1333C_M1270_IP14043_34S32S_S2906G_2-6A_Py_4@1	TYK2-8	-23.38	0.37
P1333C_M1270_IP14043_34S32S_S2906G_2-6A_Py_4@2	TYK2-8	-20.81	0.17
P1333C_M1270_IP14043_34S32S_S2906G_2-6A_Py_4@3	TYK2-8	-25.48	0.43
P1333C_M1270_IP14043_34S32S_S2906H_2-2_Py_2@1	TYK2-8	-26.78	0.18
P1333C_M1270_IP14043_34S32S_S2906H_2-2_Py_2@2	TYK2-8	11.07	0.17
P1333C_M1270_IP14043_34S32S_S2906H_2-2_Py_2@3	TYK2-8	-29.98	0.24
P1333C_M1270_IP14043_34S32S_S2906H_2-2_Py_2@4	TYK2-8	11.23	0.25
P1333C_M1270_IP14043_34S32S_S2906H_2-2_Py_2@5	TYK2-8	11.55	0.15
P1333C_M1270_IP14043_34S32S_S2906H_2-2_Py_2@6	TYK2-8	11.45	0.13
P1333C_M1270_IP14043_34S32S_S2906H_2-2_Py_2@7	TYK2-8	11.10	0.16
P1333C_M1270_IP14043_34S32S_S2906H_2-5_Py_1@1	TYK2-8	10.63	0.12
P1333C_M1270_IP14043_34S32S_S2906H_2-5_Py_1@2	TYK2-8	10.24	0.13
P1333C_M1270_IP14043_34S32S_S2906H_2-5_Py_1@3	TYK2-8	14.31	0.17
P1333C_M1270_IP14043_34S32S_S2906H_2-5_Py_1@4	TYK2-8	10.15	0.13
P1333C_M1270_IP14043_34S32S_S2906H_2-5_Py_1@5	TYK2-8	14.27	0.19
P1333C_M1270_IP14043_34S32S_S2906H_2-5_Py_1@6	TYK2-8	9.30	0.23
P1333C_M1270_IP14043_34S32S_S2906H_2-5_Py_1@7	TYK2-8	-21.51	0.20
P1333C_M1270_IP14043_34S32S_S2907C_3A_Py_1@1	TU68-3	11.21	0.17
P1333C_M1270_IP14043_34S32S_S2907C_3A_Py_1@2	TU68-3	10.98	0.15
P1333C_M1270_IP14043_34S32S_S2907C_3A_Py_1@3	TU68-3	10.47	0.15
P1333C_M1270_IP14043_34S32S_S2907C_3A_Py_1@4	TU68-3	10.55	0.16

Table B.1. (cont.)

Spot ID	Sample	δ³⁴S (‰ VCDT)	2σ (‰)
P1333C_M1270_IP14043_34S32S_S2907C_3A_Py_1@5	TU68-3	10.47	0.15
P1333C_M1270_IP14043_34S32S_S2907C_3A_Py_1@6	TU68-3	10.42	0.17
P1333C_M1270_IP14043_34S32S_S2907C_3A_Py_1@7	TU68-3	10.50	0.16
P1333C_M1270_IP14043_34S32S_S2907C_3A_Py_1@8	TU68-3	11.02	0.17
P1333C_M1270_IP14043_34S32S_S2907C_3A_Py_1@9	TU68-3	10.25	0.17
P1333C_M1270_IP14043_34S32S_S2907C_3A_Py_1@10	TU68-3	9.51	0.19
P1333C_M1270_IP14043_34S32S_S2907C_3A_Py_1@11	TU68-3	10.23	0.12
P1333C_M1270_IP14043_34S32S_S2907C_3A_Py_1@12	TU68-3	10.71	0.15
P1333C_M1270_IP14043_34S32S_S2907C_3A_Py_2@1	TU68-3	9.99	0.16
P1333C_M1270_IP14043_34S32S_S2907C_3A_Py_2@2	TU68-3	6.88	0.32
P1333C_M1270_IP14043_34S32S_S2907C_3A_Py_2@3	TU68-3	10.99	0.15
P1333C_M1270_IP14043_34S32S_S2907C_3A_Py_2@4	TU68-3	8.39	0.28
P1333C_M1270_IP14043_34S32S_S2907C_3A_Py_2@5	TU68-3	10.58	0.15
P1333C_M1270_IP14043_34S32S_S2907C_3A_Py_2@6	TU68-3	10.13	0.17
P1333C_M1270_IP14043_34S32S_S2907C_3A_Py_2@7	TU68-3	10.10	0.16
P1333C_M1270_IP14043_34S32S_S2907D_4A_Py_2@1	TU68-3	11.87	0.25
P1333C_M1270_IP14043_34S32S_S2907D_4A_Py_2@2	TU68-3	12.01	0.15
P1333C_M1270_IP14043_34S32S_S2907D_4A_Py_2@3	TU68-3	12.08	0.19
P1333C_M1270_IP14043_34S32S_S2907D_4A_Py_2@4	TU68-3	16.40	0.13
P1333C_M1270_IP14043_34S32S_S2907D_2A_Py_2@1	TU68-3	18.96	0.13
P1333C_M1270_IP14043_34S32S_S2907D_2A_Py_2@2	TU68-3	11.41	0.15
P1333C_M1270_IP14043_34S32S_S2907D_2A_Py_2@3	TU68-3	11.04	0.11
P1333C_M1270_IP14043_34S32S_S2907D_2A_Py_2@4	TU68-3	12.07	0.13
P1333C_M1270_IP14043_34S32S_S2907D_2A_Py_2@5	TU68-3	11.43	0.15
P1333C_M1270_IP14043_34S32S_S2907D_2A_Py_2@6	TU68-3	10.51	0.15
P1333C_M1270_IP14043_34S32S_S2907D_4A_Py_3@1	TU68-3	11.14	0.17
P1333C_M1270_IP14043_34S32S_S2907D_4A_Py_3@2	TU68-3	9.94	0.17
P1333C_M1270_IP14043_34S32S_S2907D_4A_Py_3@3	TU68-3	11.02	0.15
P1333C_M1269_IP14044_34S32S_S2898C_3B_Py_1@1	81-68A-69	13.11	0.17
P1333C_M1269_IP14044_34S32S_S2898C_3B_Py_1@2	81-68A-69	15.11	0.15
P1333C_M1269_IP14044_34S32S_S2898C_3C_Py_3@1	81-68A-69	13.39	0.21
P1333C_M1269_IP14044_34S32S_S2899A_3A_Py_4@1	81-68A-69	12.08	0.16
P1333C_M1269_IP14044_34S32S_S2899A_3A_Py_4@2	81-68A-69	11.91	0.17
P1333C_M1269_IP14044_34S32S_S2899A_3A_Py_4@3	81-68A-69	11.15	0.18
P1333C_M1269_IP14044_34S32S_S2899A_3A_Py_4@4	81-68A-69	10.54	0.29
P1333C_M1269_IP14044_34S32S_S2899A_3A_Py_4@5	81-68A-69	14.63	0.24
P1333C_M1269_IP14044_34S32S_S2899A_3A_Py_4@6	81-68A-69	15.00	0.28
P1333C_M1269_IP14044_34S32S_S2899A_3A_Py_4@7	81-68A-69	18.63	0.24
P1333C_M1269_IP14044_34S32S_S2899A_3A_Py_4@8	81-68A-69	16.58	0.35
P1333C_M1269_IP14044_34S32S_S2899A_3A_Py_4@9	81-68A-69	13.62	0.27
P1333C_M1269_IP14044_34S32S_S2899A_3A_Py_4@10	81-68A-69	5.28	0.68
P1333C_M1269_IP14044_34S32S_S2899A_3E_Py_5@1	81-68A-69	14.35	0.21
P1333C_M1269_IP14044_34S32S_S2899A_3E_Py_5@2	81-68A-69	14.40	0.23
P1333C_M1269_IP14044_34S32S_S2899A_3E_Py_5@3	81-68A-69	14.91	0.22
P1333C_M1269_IP14044_34S32S_S2899A_3D_Py_6@1	81-68A-69	12.75	0.15
P1333C_M1269_IP14044_34S32S_S2899A_3D_Py_6@2	81-68A-69	21.45	0.29
P1333C_M1269_IP14044_34S32S_S2899A_3D_Py_6@3	81-68A-69	18.34	0.19

Table B.1. (cont.)

Spot ID	Sample	δ³⁴S (‰ VCDT)	2σ (‰)
P1333C_M1269_IP14044_34S32S_S2899A_3D_Py_6@4	81-68A-69	19.62	0.15
P1333C_M1269_IP14044_34S32S_S2899F_3E_Py_1@1	81-68A-69	19.56	0.20
P1333C_M1269_IP14044_34S32S_S2899F_3E_Py_1@2	81-68A-69	21.20	0.15
P1333C_M1269_IP14044_34S32S_S2899F_3E_Py_1@3	81-68A-69	21.30	0.27
P1333C_M1269_IP14044_34S32S_S2899F_3E_Py_1@4	81-68A-69	20.42	0.17
P1333C_M1269_IP14044_34S32S_S2899F_3E_Py_1@5	81-68A-69	17.36	0.14
P1333C_M1269_IP14044_34S32S_S2899F_3E_Py_1@6	81-68A-69	22.51	0.18
P1333C_M1269_IP14044_34S32S_S2899F_3E_Py_1@7	81-68A-69	23.38	0.18
P1333C_M1269_IP14044_34S32S_S2899F_3E_Py_1@8	81-68A-69	21.22	0.26
P1333C_M1269_IP14044_34S32S_S2899F_3C_Py_3@1	81-68A-69	21.12	0.24
P1333C_M1269_IP14044_34S32S_S2899F_3E_Py_1@9	81-68A-69	22.19	0.12
P1333C_M1269_IP14044_34S32S_S2899F_3E_Py_1@10	81-68A-69	23.37	0.19
P1333C_M1269_IP14044_34S32S_S2899F_3E_Py_1@11	81-68A-69	23.88	0.15
P1333C_M1269_IP14044_34S32S_S2899F_3E_Py_1@12	81-68A-69	20.68	0.18
P1333C_M1269_IP14044_34S32S_S2899F_3E_Py_1@13	81-68A-69	18.04	0.16
P1333C_M1269_IP14044_34S32S_S2899F_3B_Py_4@1	81-68A-69	10.96	0.12
P1333C_M1269_IP14044_34S32S_S2899F_3B_Py_4@2	81-68A-69	20.47	0.14
P1333C_M1269_IP14044_34S32S_S2899F_3B_Py_4@3	81-68A-69	24.70	0.19
P1333C_M1269_IP14044_34S32S_S2899F_3B_Py_4@4	81-68A-69	19.49	0.15
P1333C_M1269_IP14044_34S32S_S2899F_3F_Py_8@1	81-68A-69	23.59	0.18
P1333C_M1269_IP14044_34S32S_S2899F_3F_Py_8@2	81-68A-69	23.51	0.14
P1333C_M1269_IP14044_34S32S_S2899F_3F_Py_8@3	81-68A-69	19.90	0.15
P1333C_M1269_IP14044_34S32S_S2900B_3A_Py_6@1	81-68A-54B	11.37	0.17
P1333C_M1269_IP14044_34S32S_S2900B_3A_Py_6@2	81-68A-54B	11.93	0.20
P1333C_M1269_IP14044_34S32S_S2900B_3A_Py_6@3	81-68A-54B	9.02	0.18
P1333C_M1269_IP14044_34S32S_S2900B_3A_Py_6@4	81-68A-54B	13.88	0.17
P1333C_M1269_IP14044_34S32S_S2900B_3A_Py_6@5	81-68A-54B	10.40	0.11
P1333C_M1269_IP14044_34S32S_S2900B_3C_Py_3@1	81-68A-54B	10.72	0.24
P1333C_M1269_IP14044_34S32S_S2900B_3C_Py_3@2	81-68A-54B	8.23	0.21
P1333C_M1269_IP14044_34S32S_S2900B_3C_Py_3@3	81-68A-54B	11.88	0.17
P1333C_M1269_IP14044_34S32S_S2900B_3C_Py_3@4	81-68A-54B	11.17	0.22
P1333C_M1269_IP14044_34S32S_S2900B_3D_Py_4@1	81-68A-54B	9.23	0.20
P1333C_M1269_IP14044_34S32S_S2900B_3D_Py_4@2	81-68A-54B	11.61	0.19
P1333C_M1269_IP14044_34S32S_S2900C_3A_Py_2@1	81-68A-54B	11.25	0.15
P1333C_M1269_IP14044_34S32S_S2900C_3A_Py_2@2	81-68A-54B	9.97	0.20
P1333C_M1269_IP14044_34S32S_S2900C_3A_Py_2@3	81-68A-54B	9.39	0.15
P1333C_M1269_IP14044_34S32S_S2900C_3A_Py_2@4	81-68A-54B	12.46	0.29
P1333C_M1269_IP14044_34S32S_S2900C_3A_Py_2@5	81-68A-54B	9.63	0.18
P1333C_M1269_IP14044_34S32S_S2900C_3A_Py_2@6	81-68A-54B	11.78	0.16
P1333C_M1269_IP14044_34S32S_S2900C_3B_Py_4@1	81-68A-54B	9.38	0.17
P1333C_M1269_IP14044_34S32S_S2900C_3B_Py_4@2	81-68A-54B	9.16	0.21
P1333C_M1269_IP14044_34S32S_S2903E_3A_Py_1@1	TYK2-6	3.52	0.20
P1333C_M1269_IP14044_34S32S_S2903E_3A_Py_1@2	TYK2-6	10.53	0.17
P1333C_M1269_IP14044_34S32S_S2903E_3A_Py_1@3	TYK2-6	10.76	0.18
P1333C_M1269_IP14044_34S32S_S2903E_3A_Py_1@4	TYK2-6	3.59	0.13
P1333C_M1269_IP14044_34S32S_S2903E_3A_Py_1@5	TYK2-6	9.94	0.19
P1333C_M1269_IP14044_34S32S_S2903E_3A_Py_1@6	TYK2-6	9.51	0.16

Table B.1. (cont.)

Spot ID	Sample	δ³⁴S (‰ VCDT)	2σ (‰)
P1333C_M1269_IP14044_34S32S_S2903E_3A_Py_1@7	TYK2-6	3.36	0.13
P1333C_M1269_IP14044_34S32S_S2903E_3A_Py_1@8	TYK2-6	6.62	0.22
P1333C_M1269_IP14044_34S32S_S2903E_3A_Py_1@9	TYK2-6	9.63	0.11
P1333C_M1269_IP14044_34S32S_S2903E_3D_Py_3@1	TYK2-6	5.32	0.17
P1333C_M1269_IP14044_34S32S_S2903E_3D_Py_3@2	TYK2-6	10.48	0.18
P1333C_M1269_IP14044_34S32S_S2903E_3D_Py_3@3	TYK2-6	10.83	0.17
P1333C_M1269_IP14044_34S32S_S2903E_3D_Py_3@4	TYK2-6	10.70	0.18
P1333C_M1269_IP14044_34S32S_S2903E_3D_Py_3@5	TYK2-6	8.36	0.16
P1333C_M1269_IP14044_34S32S_S2903E_3D_Py_3@6	TYK2-6	10.37	0.18
P1333C_M1269_IP14044_34S32S_S2903E_3D_Py_3@7	TYK2-6	4.40	0.18
P1333C_M1269_IP14044_34S32S_S2903E_3D_Py_3@8	TYK2-6	7.70	0.15
P1333C_M1269_IP14044_34S32S_S2903E_3D_Py_3@9	TYK2-6	10.00	0.18
P1333C_M1269_IP14044_34S32S_S2903E_3C_Py_2@1	TYK2-6	5.71	0.18
P1333C_M1269_IP14044_34S32S_S2903E_3C_Py_2@2	TYK2-6	9.40	0.18
P1333C_M1269_IP14044_34S32S_S2903E_3C_Py_2@3	TYK2-6	3.87	0.17
P1333C_M1269_IP14044_34S32S_S2903E_3C_Py_2@4	TYK2-6	5.82	0.17
P1333C_M1269_IP14044_34S32S_S2903E_3C_Py_2@5	TYK2-6	3.03	0.18
P1333C_M1269_IP14044_34S32S_S2903E_3C_Py_2@6	TYK2-6	3.11	0.16
P1333C_M1269_IP14044_34S32S_S2903E_3C_Py_2@7	TYK2-6	3.35	0.16
P1333C_M1269_IP14044_34S32S_S2903E_3C_Py_2@8	TYK2-6	5.75	0.42
P1333C_M1269_IP14044_34S32S_S2903E_3C_Py_2@9	TYK2-6	3.72	0.18
P1333C_M1269_IP14044_34S32S_S2903E_3E_Py_4@1	TYK2-6	11.45	0.15
P1333C_M1269_IP14044_34S32S_S2903E_3E_Py_4@2	TYK2-6	12.04	0.17
P1333C_M1269_IP14044_34S32S_S2903E_3E_Py_4@3	TYK2-6	11.51	0.22
P1333C_M1269_IP14044_34S32S_S2899E_3C_Py_1@1	81-68A-69	13.22	0.22
P1333C_M1269_IP14044_34S32S_S2899E_3C_Py_1@2	81-68A-69	20.49	0.19
P1333C_M1269_IP14044_34S32S_S2899E_3C_Py_1@3	81-68A-69	14.54	0.17
P1333C_M1269_IP14044_34S32S_S2899E_3C_Py_1@4	81-68A-69	18.47	0.23
P1333C_M1269_IP14044_34S32S_S2899E_3D_Py_2@1	81-68A-69	19.91	0.17
P1333C_M1269_IP14044_34S32S_S2899E_3D_Py_2@2	81-68A-69	20.51	0.28
P1333C_M1269_IP14044_34S32S_S2899E_3D_Py_2@3	81-68A-69	19.01	0.17
P1333C_M1269_IP14044_34S32S_S2899E_3D_Py_2@4	81-68A-69	18.73	0.34
P1333C_M1269_IP14044_34S32S_S2899E_2-2_Py_3@1	81-68A-69	22.30	0.19
P1333C_M1269_IP14044_34S32S_S2899E_2-2_Py_3@2	81-68A-69	13.66	0.20
P1333C_M1269_IP14044_34S32S_S2899E_2-2_Py_3@3	81-68A-69	12.45	0.28
P1333C_M1269_IP14044_34S32S_S2899E_2-2_Py_3@4	81-68A-69	20.21	0.21
P1333C_M1269_IP14044_34S32S_S2899E_2-2_Py_3@5	81-68A-69	20.86	0.21
P1333C_M1269_IP14044_34S32S_S2899E_2-2_Py_3@6	81-68A-69	25.70	0.20
P1333C_M1269_IP14044_34S32S_S2899E_2-2_Py_3@7	81-68A-69	12.93	0.19
P1333C_M1269_IP14044_34S32S_S2899E_2-2_Py_3@8	81-68A-69	15.68	0.32
P1333C_M1269_IP14044_34S32S_S2899E_2-2_Py_3@9	81-68A-69	10.13	0.18
P1333C_M1269_IP14044_34S32S_S2899E_2-2_Py_3@10	81-68A-69	20.82	0.17

Table B.2.

Spot ID	Sample	δ³⁴S (‰ VCDT)	2σ (‰)
P1333A_M1269_IP14041_34S32S_S2897B_3A_Ba_1@1	81-68A-62	26.52	0.17
P1333A_M1269_IP14041_34S32S_S2897B_3A_Ba_1@2	81-68A-62	26.57	0.19
P1333A_M1269_IP14041_34S32S_S2897B_3A_Ba_1@3	81-68A-62	24.91	0.18
P1333A_M1269_IP14041_34S32S_S2897B_3B_Ba_2@1	81-68A-62	26.68	0.19
P1333A_M1269_IP14041_34S32S_S2897B_3B_Ba_2@2	81-68A-62	27.02	0.19
P1333A_M1269_IP14041_34S32S_S2897D_3E_Ba_1@1	81-68A-62	24.32	0.19
P1333A_M1269_IP14041_34S32S_S2897D_3E_Ba_1@2	81-68A-62	25.17	0.12
P1333A_M1269_IP14041_34S32S_S2897D_3E_Ba_1@3	81-68A-62	25.56	0.18
P1333A_M1269_IP14041_34S32S_S2897D_3D_Ba_2@1	81-68A-62	25.68	0.19
P1333A_M1269_IP14041_34S32S_S2897D_3D_Ba_2@2	81-68A-62	23.71	0.17
P1333A_M1269_IP14041_34S32S_S2897D_3D_Ba_2@3	81-68A-62	27.49	0.17
P1333A_M1269_IP14041_34S32S_S2897D_3C_Ba_3@1	81-68A-62	24.28	0.16
P1333A_M1269_IP14041_34S32S_S2897D_3C_Ba_3@2	81-68A-62	23.80	0.17
P1333A_M1269_IP14041_34S32S_S2897D_3C_Ba_3@3	81-68A-62	23.66	0.19
P1333A_M1269_IP14041_34S32S_S2897D_3B_Ba_4@1	81-68A-62	25.07	0.17
P1333A_M1269_IP14041_34S32S_S2897D_3B_Ba_4@2	81-68A-62	25.60	0.13
P1333A_M1269_IP14041_34S32S_S2897D_3B_Ba_4@3	81-68A-62	23.55	0.18
P1333A_M1269_IP14041_34S32S_S2897D_3B_Ba_4@4	81-68A-62	27.40	0.17
P1333A_M1269_IP14041_34S32S_S2897D_3B_Ba_4@5	81-68A-62	23.48	0.19
P1333A_M1269_IP14041_34S32S_S2897D_3A_Ba_5@1	81-68A-62	25.15	0.28
P1333A_M1269_IP14041_34S32S_S2897D_3A_Ba_5@2	81-68A-62	25.53	0.12
P1333A_M1269_IP14041_34S32S_S2897D_3A_Ba_5@3	81-68A-62	26.64	0.30
P1333A_M1269_IP14041_34S32S_S2897D_3A_Ba_5@4	81-68A-62	23.94	0.19
P1333A_M1269_IP14041_34S32S_S2898A_3B_Ba_1@1	81-68A-65	27.77	0.19
P1333A_M1269_IP14041_34S32S_S2898A_3B_Ba_1@2	81-68A-65	26.57	0.21
P1333A_M1269_IP14041_34S32S_S2898A_3B_Ba_1@3	81-68A-65	27.65	0.16
P1333A_M1269_IP14041_34S32S_S2898A_3B_Ba_1@4	81-68A-65	24.60	0.19
P1333A_M1269_IP14041_34S32S_S2898A_3B_Ba_1@5	81-68A-65	27.00	0.18
P1333A_M1269_IP14041_34S32S_S2898A_3A_Ba_2@1	81-68A-65	28.93	0.19
P1333A_M1269_IP14041_34S32S_S2898A_3A_Ba_2@2	81-68A-65	25.10	0.19
P1333A_M1269_IP14041_34S32S_S2898A_3A_Ba_2@3	81-68A-65	28.18	0.18
P1333A_M1269_IP14041_34S32S_S2898A_3A_Ba_2@4	81-68A-65	24.75	0.17
P1333A_M1269_IP14041_34S32S_S2898A_3A_Ba_2@5	81-68A-65	27.94	0.14
P1333A_M1269_IP14041_34S32S_S2898C_3B_Ba_1@1	81-68A-65	29.25	0.18
P1333A_M1269_IP14041_34S32S_S2898C_3B_Ba_1@2	81-68A-65	24.48	0.16
P1333A_M1269_IP14041_34S32S_S2898C_3B_Ba_1@3	81-68A-65	24.96	0.16
P1333A_M1269_IP14041_34S32S_S2898C_3B_Ba_1@4	81-68A-65	24.24	0.18
P1333A_M1269_IP14041_34S32S_S2898C_3B_Ba_1@5	81-68A-65	28.21	0.19
P1333A_M1269_IP14041_34S32S_S2898C_3A_Ba_2@1	81-68A-65	28.29	0.17
P1333A_M1269_IP14041_34S32S_S2898C_3A_Ba_2@2	81-68A-65	28.31	0.17
P1333A_M1269_IP14041_34S32S_S2898C_3A_Ba_2@3	81-68A-65	28.41	0.18
P1333A_M1269_IP14041_34S32S_S2898C_3A_Ba_2@4	81-68A-65	29.09	0.17
P1333A_M1269_IP14041_34S32S_S2898C_3A_Ba_2@5	81-68A-65	29.31	0.19
P1333A_M1269_IP14041_34S32S_S2898C_3A_Ba_2@7	81-68A-65	24.23	0.20
P1333A_M1269_IP14041_34S32S_S2898C_3A_Ba_2@8	81-68A-65	28.32	0.19
P1333A_M1269_IP14041_34S32S_S2898C_3A_Ba_2@9	81-68A-65	28.36	0.16
P1333A_M1269_IP14041_34S32S_S2898C_3A_Ba_2@10	81-68A-65	28.83	0.17
P1333A_M1269_IP14041_34S32S_S2898C_2-1_Ba_4@1	81-68A-65	28.50	0.17

Table B.2. (cont.)

Spot ID	Sample	δ³⁴S (‰ VCDT)	2σ (‰)
P1333A_M1269_IP14041_34S32S_S2898C_2-1_Ba_4@2	81-68A-65	28.45	0.18
P1333A_M1269_IP14041_34S32S_S2898C_2-1_Ba_4@3	81-68A-65	28.62	0.18
P1333A_M1269_IP14041_34S32S_S2898C_2-1_Ba_4@4	81-68A-65	28.01	0.20
P1333A_M1269_IP14041_34S32S_S2898C_2-1_Ba_4@5	81-68A-65	28.44	0.17
P1333A_M1269_IP14041_34S32S_S2898C_2-1_Ba_4@6	81-68A-65	28.33	0.18
P1333A_M1269_IP14041_34S32S_S2898C_2-3_Ba_5@1	81-68A-65	27.56	0.18
P1333A_M1269_IP14041_34S32S_S2898C_2-3_Ba_5@2	81-68A-65	26.97	0.16
P1333A_M1269_IP14041_34S32S_S2898C_2-3_Ba_5@3	81-68A-65	27.46	0.18
P1333A_M1269_IP14041_34S32S_S2898C_3C_Ba_3@1	81-68A-65	28.86	0.17
P1333A_M1269_IP14041_34S32S_S2898C_3C_Ba_3@2	81-68A-65	29.27	0.15
P1333A_M1269_IP14041_34S32S_S2898C_3C_Ba_3@3	81-68A-65	28.38	0.18
P1333A_M1269_IP14041_34S32S_S2899A_3B_Ba_1@1	81-68A-69	29.45	0.17
P1333A_M1269_IP14041_34S32S_S2899A_3B_Ba_1@2	81-68A-69	29.71	0.18
P1333A_M1269_IP14041_34S32S_S2899A_3B_Ba_1@3	81-68A-69	29.67	0.18
P1333A_M1269_IP14041_34S32S_S2899A_3F_Ba_2@1	81-68A-69	28.58	0.37
P1333A_M1269_IP14041_34S32S_S2899A_3C_Ba_3@1	81-68A-69	29.36	0.18
P1333A_M1269_IP14041_34S32S_S2899A_3C_Ba_3@2	81-68A-69	29.22	0.14
P1333A_M1269_IP14041_34S32S_S2899A_3C_Ba_3@3	81-68A-69	29.37	0.17
P1333A_M1269_IP14041_34S32S_S2899A_3C_Ba_3@4	81-68A-69	27.13	0.19
P1333A_M1269_IP14041_34S32S_S2899A_3C_Ba_3@5	81-68A-69	30.00	0.17
P1333A_M1269_IP14041_34S32S_S2899A_3C_Ba_3@6	81-68A-69	29.45	0.17
P1333A_M1269_IP14041_34S32S_S2899A_3C_Ba_3@7	81-68A-69	29.41	0.18
P1333A_M1269_IP14041_34S32S_S2899F_3E_Ba_1@1	81-68A-69	27.65	0.18
P1333A_M1269_IP14041_34S32S_S2899F_3E_Ba_1@2	81-68A-69	27.19	0.16
P1333A_M1269_IP14041_34S32S_S2899F_3E_Ba_1@3	81-68A-69	27.37	0.18
P1333A_M1269_IP14041_34S32S_S2899F_3E_Ba_1@4	81-68A-69	24.60	0.19
P1333A_M1269_IP14041_34S32S_S2899F_3B_Ba_2@1	81-68A-69	24.79	0.17
P1333A_M1269_IP14041_34S32S_S2899F_3B_Ba_2@2	81-68A-69	24.70	0.17
P1333A_M1269_IP14041_34S32S_S2899F_3B_Ba_2@3	81-68A-69	24.50	0.17
P1333A_M1269_IP14041_34S32S_S2899F_3B_Ba_2@4	81-68A-69	27.54	0.16
P1333A_M1269_IP14041_34S32S_S2899F_3G_Ba_5@1	81-68A-69	26.73	0.18
P1333A_M1269_IP14041_34S32S_S2899F_3G_Ba_5@3	81-68A-69	26.08	0.18
P1333A_M1269_IP14041_34S32S_S2899F_3G_Ba_5@4	81-68A-69	26.90	0.16
P1333A_M1269_IP14041_34S32S_S2899F_3G_Ba_5@5	81-68A-69	25.68	0.17
P1333A_M1269_IP14041_34S32S_S2899F_3G_Ba_5@6	81-68A-69	25.41	0.20
P1333A_M1269_IP14041_34S32S_S2899F_3G_Ba_6@1	81-68A-69	25.62	0.23
P1333A_M1269_IP14041_34S32S_S2899F_3G_Ba_6@2	81-68A-69	27.86	0.20
P1333A_M1269_IP14041_34S32S_S2899F_3G_Ba_6@3	81-68A-69	27.47	0.18
P1333A_M1269_IP14041_34S32S_S2899F_3G_Ba_7@1	81-68A-69	27.05	0.18
P1333A_M1269_IP14041_34S32S_S2899F_3G_Ba_7@2	81-68A-69	24.34	0.19
P1333A_M1269_IP14041_34S32S_S2899F_3G_Ba_7@3	81-68A-69	26.52	0.17
P1333A_M1269_IP14041_34S32S_S2899F_3G_Ba_8@1	81-68A-69	29.80	0.17
P1333A_M1269_IP14041_34S32S_S2900A_3A_Ba_2@1	81-68A-54B	27.42	0.19
P1333A_M1269_IP14041_34S32S_S2900A_3A_Ba_2@2	81-68A-54B	27.52	0.20
P1333A_M1269_IP14041_34S32S_S2900A_3A_Ba_2@3	81-68A-54B	27.28	0.18
P1333A_M1269_IP14041_34S32S_S2900A_3A_Ba_2@4	81-68A-54B	27.58	0.18
P1333A_M1269_IP14041_34S32S_S2900A_3A_Ba_2@5	81-68A-54B	28.36	0.18

Table B.2. (cont.)

Spot ID	Sample	δ³⁴S (‰ VCDT)	2σ (‰)
P1333A_M1269_IP14041_34S32S_S2900A_3A_Ba_2@6	81-68A-54B	28.15	0.13
P1333A_M1269_IP14041_34S32S_S2900A_3B_Ba_1@1_r	81-68A-54B	18.46	0.25
P1333A_M1269_IP14041_34S32S_S2900A_3B_Ba_1@2	81-68A-54B	28.07	0.18
P1333A_M1269_IP14041_34S32S_S2900A_3B_Ba_1@3	81-68A-54B	27.57	0.17
P1333A_M1269_IP14041_34S32S_S2900B_3E_Ba_1@1	81-68A-54B	26.10	0.18
P1333A_M1269_IP14041_34S32S_S2900B_3E_Ba_1@2	81-68A-54B	26.11	0.18
P1333A_M1269_IP14041_34S32S_S2900B_3E_Ba_1@3	81-68A-54B	26.57	0.18
P1333A_M1269_IP14041_34S32S_S2900B_3E_Ba_1@4	81-68A-54B	27.23	0.19
P1333A_M1269_IP14041_34S32S_S2900B_3E_Ba_1@5	81-68A-54B	26.99	0.18
P1333A_M1269_IP14041_34S32S_S2900B_3E_Ba_1@6	81-68A-54B	25.93	0.22
P1333A_M1269_IP14041_34S32S_S2900B_3F_Ba_2@1	81-68A-54B	30.32	0.26
P1333A_M1269_IP14041_34S32S_S2900B_3F_Ba_2@2	81-68A-54B	26.85	0.18
P1333A_M1269_IP14041_34S32S_S2900B_3C_Ba_3@1	81-68A-54B	27.03	0.19
P1333A_M1269_IP14041_34S32S_S2900B_3C_Ba_3@2	81-68A-54B	27.07	0.17
P1333A_M1269_IP14041_34S32S_S2900B_3C_Ba_3@3	81-68A-54B	26.42	0.19
P1333A_M1269_IP14041_34S32S_S2900B_3C_Ba_3@4	81-68A-54B	26.83	0.15
P1333A_M1269_IP14041_34S32S_S2900B_3D_Ba_4@1	81-68A-54B	25.94	0.19
P1333A_M1269_IP14041_34S32S_S2900B_3D_Ba_4@2	81-68A-54B	25.33	0.38
P1333A_M1269_IP14041_34S32S_S2900B_3D_Ba_4@3	81-68A-54B	26.17	0.17
P1333A_M1269_IP14041_34S32S_S2900B_3D_Ba_4@4	81-68A-54B	26.89	0.19
P1333A_M1269_IP14041_34S32S_S2900B_3D_Ba_4@5	81-68A-54B	26.83	0.16
P1333A_M1269_IP14041_34S32S_S2900B_3A_Ba_6@1	81-68A-54B	27.01	0.18
P1333A_M1269_IP14041_34S32S_S2900B_3A_Ba_6@12	81-68A-54B	27.03	0.19
P1333A_M1269_IP14041_34S32S_S2900B_3A_Ba_6@3	81-68A-54B	27.84	0.16
P1333A_M1269_IP14041_34S32S_S2900B_3A_Ba_6@4	81-68A-54B	27.18	0.18
P1333A_M1269_IP14041_34S32S_S2900C_3D_Ba_1@1	81-68A-54B	26.04	0.17
P1333A_M1269_IP14041_34S32S_S2900C_3D_Ba_1@2	81-68A-54B	26.20	0.19
P1333A_M1269_IP14041_34S32S_S2900C_3D_Ba_1@3	81-68A-54B	25.84	0.17
P1333A_M1269_IP14041_34S32S_S2900C_3D_Ba_1@4	81-68A-54B	26.37	0.17
P1333A_M1269_IP14041_34S32S_S2900C_3A_Ba_2@1	81-68A-54B	26.84	0.17
P1333A_M1269_IP14041_34S32S_S2900C_3A_Ba_2@2	81-68A-54B	26.70	0.20
P1333A_M1269_IP14041_34S32S_S2900C_3A_Ba_2@3	81-68A-54B	27.22	0.16
P1333A_M1269_IP14041_34S32S_S2900C_3A_Ba_2@4	81-68A-54B	26.93	0.20
P1333A_M1269_IP14041_34S32S_S2900C_3C_Ba_3@1	81-68A-54B	26.84	0.17
P1333A_M1269_IP14041_34S32S_S2900C_3C_Ba_3@2	81-68A-54B	26.93	0.19
P1333A_M1269_IP14041_34S32S_S2900C_3B_Ba_4@1	81-68A-54B	26.53	0.18
P1333A_M1269_IP14041_34S32S_S2900C_3B_Ba_4@2	81-68A-54B	26.82	0.19
P1333A_M1269_IP14041_34S32S_S2900C_3B_Ba_4@3	81-68A-54B	27.02	0.19
P1333A_M1269_IP14041_34S32S_S2900C_3B_Ba_4@4	81-68A-54B	26.68	0.19
P1333A_M1269_IP14041_34S32S_S2900C_3B_Ba_4@5	81-68A-54B	26.97	0.18
P1333A_M1269_IP14041_34S32S_S2900D_3C_Ba_1@1	81-68A-54B	25.42	0.18
P1333A_M1269_IP14041_34S32S_S2900D_3C_Ba_1@2	81-68A-54B	25.92	0.19
P1333A_M1269_IP14041_34S32S_S2900D_3C_Ba_1@3	81-68A-54B	26.34	0.19
P1333A_M1269_IP14041_34S32S_S2900D_3B_Ba_2@1	81-68A-54B	26.67	0.17
P1333A_M1269_IP14041_34S32S_S2900D_3B_Ba_2@2	81-68A-54B	25.81	0.22
P1333A_M1269_IP14041_34S32S_S2900D_3B_Ba_2@3	81-68A-54B	26.48	0.19
P1333A_M1269_IP14041_34S32S_S2900D_3B_Ba_2@4	81-68A-54B	25.17	0.19
P1333A_M1269_IP14041_34S32S_S2900D_3B_Ba_2@5	81-68A-54B	25.28	0.17

Table B.2. (cont.)

Spot ID	Sample	δ³⁴S (‰ VCDT)	2σ (‰)
P1333A_M1269_IP14041_34S32S_S2900D_3B_Ba_2@6	81-68A-54B	25.53	0.18
P1333A_M1269_IP14041_34S32S_S2900D_3B_Ba_2@7	81-68A-54B	25.29	0.17
P1333A_M1269_IP14041_34S32S_S2900D_3B_Ba_2@8	81-68A-54B	25.08	0.17
P1333A_M1269_IP14041_34S32S_S2900D_3B_Ba_2@9	81-68A-54B	25.19	0.17
P1333A_M1269_IP14041_34S32S_S2900D_3A_Ba_3@1	81-68A-54B	26.88	0.26
P1333A_M1269_IP14041_34S32S_S2900D_3A_Ba_3@2	81-68A-54B	26.59	0.17
P1333A_M1270_IP14042_34S32S_S2906E_6A_Ba_1@1	TYK2-8	26.10	0.12
P1333A_M1270_IP14042_34S32S_S2906E_6A_Ba_1@2	TYK2-8	30.60	0.13
P1333A_M1270_IP14042_34S32S_S2906E_1A_Ba_4@1	TYK2-8	26.76	0.14
P1333A_M1270_IP14042_34S32S_S2906E_1A_Ba_4@2	TYK2-8	30.47	0.13
P1333A_M1270_IP14042_34S32S_S2906E_1A_Ba_4@3	TYK2-8	29.90	0.12
P1333A_M1270_IP14042_34S32S_S2906E_1A_Ba_4@4	TYK2-8	30.61	0.13
P1333A_M1270_IP14042_34S32S_S2906E_2-3_Ba_6@1	TYK2-8	30.35	0.15
P1333A_M1270_IP14042_34S32S_S2906E_2-3_Ba_6@2	TYK2-8	25.58	0.17
P1333A_M1270_IP14042_34S32S_S2906E_2-3_Ba_6@3	TYK2-8	30.38	0.15
P1333A_M1270_IP14042_34S32S_S2906E_2-3_Ba_6@4	TYK2-8	28.12	0.12
P1333A_M1270_IP14042_34S32S_S2906E_5A_Ba_3@1	TYK2-8	26.22	0.14
P1333A_M1270_IP14042_34S32S_S2906E_5A_Ba_3@2	TYK2-8	26.00	0.13
P1333A_M1270_IP14042_34S32S_S2906H_2-4_Ba_1@1	TYK2-8	26.10	0.16
P1333A_M1270_IP14042_34S32S_S2906H_2-4_Ba_1@2	TYK2-8	30.47	0.12
P1333A_M1270_IP14042_34S32S_S2906H_2-4_Ba_1@3	TYK2-8	30.64	0.11
P1333A_M1270_IP14042_34S32S_S2906H_2-3_Ba_2@1	TYK2-8	30.58	0.12
P1333A_M1270_IP14042_34S32S_S2906H_2-3_Ba_2@2	TYK2-8	33.99	0.17
P1333A_M1270_IP14042_34S32S_S2906H_2-6_Ba_4@1	TYK2-8	30.46	0.12
P1333A_M1270_IP14042_34S32S_S2906H_2-2_Ba_5@1	TYK2-8	26.29	0.14
P1333A_M1270_IP14042_34S32S_S2906H_2-2_Ba_5@2	TYK2-8	30.57	0.12
P1333A_M1270_IP14042_34S32S_S2906H_2-2_Ba_5@2	TYK2-8	30.57	0.12
P1333A_M1270_IP14042_34S32S_S2906H_2-2_Ba_5@3	TYK2-8	27.56	0.13
P1333A_M1270_IP14042_34S32S_S2907C_3A_Ba_1@1	TU68-3	28.48	0.15
P1333A_M1270_IP14042_34S32S_S2907C_3A_Ba_1@2	TU68-3	27.95	0.13
P1333A_M1270_IP14042_34S32S_S2907C_3A_Ba_1@3	TU68-3	28.93	0.15
P1333A_M1270_IP14042_34S32S_S2907C_3A_Ba_1@4	TU68-3	28.57	0.15
P1333A_M1270_IP14042_34S32S_S2907D_1A_Ba_1@1	TU68-3	23.67	0.12
P1333A_M1270_IP14042_34S32S_S2907D_1A_Ba_1@2	TU68-3	24.42	0.16
P1333A_M1270_IP14042_34S32S_S2907D_1A_Ba_1@3	TU68-3	26.85	0.13
P1333A_M1270_IP14042_34S32S_S2907D_4A_Ba_2@1	TU68-3	26.34	0.14
P1333A_M1270_IP14042_34S32S_S2907D_4A_Ba_3@2	TU68-3	28.44	0.16
P1333A_M1270_IP14042_34S32S_S2907E_1A_Ba_1@1	TU68-3	24.92	0.16
P1333A_M1270_IP14042_34S32S_S2907E_1A_Ba_1@2	TU68-3	28.15	0.14
P1333A_M1270_IP14042_34S32S_S2907E_1A_Ba_1@3	TU68-3	28.64	0.15
P1333A_M1270_IP14042_34S32S_S2907E_1A_Ba_1@4	TU68-3	28.92	0.13
P1333A_M1270_IP14042_34S32S_S2907E_2A_Ba_2@1	TU68-3	28.93	0.14
P1333A_M1270_IP14042_34S32S_S2907E_2A_Ba_2@2	TU68-3	28.99	0.16
P1333A_M1270_IP14042_34S32S_S2907E_2A_Ba_2@3	TU68-3	29.04	0.14
P1333A_M1270_IP14042_34S32S_S2907E_2A_Ba_2@4	TU68-3	28.57	0.11

Table B.3.

Spot ID	Sample	δ18O (‰ SMOW)	2σ (‰)
P1333B_M1269_IP14048_18O16O_S2897B_3A_Ba_1@1	81-68A-62	17.82	0.28
P1333B_M1269_IP14048_18O16O_S2897B_3A_Ba_1@2	81-68A-62	17.69	0.21
P1333B_M1269_IP14048_18O16O_S2897B_3B_Ba_2@1	81-68A-62	17.59	0.28
P1333B_M1269_IP14048_18O16O_S2897B_3B_Ba_2@2	81-68A-62	17.69	0.23
P1333B_M1269_IP14048_18O16O_S2897D_3E_Ba_1@1	81-68A-62	17.51	0.23
P1333B_M1269_IP14048_18O16O_S2897D_3E_Ba_1@2	81-68A-62	16.89	0.25
P1333B_M1269_IP14048_18O16O_S2897D_3E_Ba_1@3	81-68A-62	17.61	0.25
P1333B_M1269_IP14048_18O16O_S2897D_3D_Ba_2@1	81-68A-62	17.29	0.24
P1333B_M1269_IP14048_18O16O_S2897D_3D_Ba_2@2	81-68A-62	17.00	0.26
P1333B_M1269_IP14048_18O16O_S2897D_3C_Ba_3@1	81-68A-62	17.46	0.24
P1333B_M1269_IP14048_18O16O_S2897D_3C_Ba_3@2	81-68A-62	17.49	0.23
P1333B_M1269_IP14048_18O16O_S2897D_3C_Ba_3@3	81-68A-62	16.66	0.23
P1333B_M1269_IP14048_18O16O_S2897D_3B_Ba_1@1	81-68A-62	17.13	0.25
P1333B_M1269_IP14048_18O16O_S2897D_3B_Ba_1@2	81-68A-62	17.11	0.20
P1333B_M1269_IP14048_18O16O_S2897D_3B_Ba_1@3	81-68A-62	16.42	0.24
P1333B_M1269_IP14048_18O16O_S2897D_3B_Ba_1@4	81-68A-62	17.26	0.24
P1333B_M1269_IP14048_18O16O_S2897D_3A_Ba_5@1	81-68A-62	16.71	0.24
P1333B_M1269_IP14048_18O16O_S2897D_3A_Ba_5@3	81-68A-62	17.40	0.22
P1333B_M1269_IP14048_18O16O_S2897D_3A_Ba_5@4	81-68A-62	17.19	0.26
P1333B_M1269_IP14048_18O16O_S2898A_3B_Ba_1@1	81-68A-65	17.67	0.21
P1333B_M1269_IP14048_18O16O_S2898A_3B_Ba_1@5	81-68A-65	17.60	0.24
P1333B_M1269_IP14048_18O16O_S2898A_3B_Ba_1@2	81-68A-65	17.69	0.17
P1333B_M1269_IP14048_18O16O_S2898A_3B_Ba_1@3	81-68A-65	17.69	0.22
P1333B_M1269_IP14048_18O16O_S2898A_3B_Ba_1@4	81-68A-65	17.44	0.23
P1333B_M1269_IP14048_18O16O_S2898A_3A_Ba_2@1	81-68A-65	17.56	0.24
P1333B_M1269_IP14048_18O16O_S2898A_3A_Ba_2@2	81-68A-65	17.38	0.24
P1333B_M1269_IP14048_18O16O_S2898A_3A_Ba_2@3	81-68A-65	17.55	0.26
P1333B_M1269_IP14048_18O16O_S2898A_3A_Ba_2@5	81-68A-65	17.65	0.25
P1333B_M1269_IP14048_18O16O_S2898C_3B_Ba_1@2	81-68A-65	16.50	0.17
P1333B_M1269_IP14048_18O16O_S2898C_3B_Ba_1@4	81-68A-65	17.08	0.27
P1333B_M1269_IP14048_18O16O_S2898C_3B_Ba_1@5	81-68A-65	16.68	0.36
P1333B_M1269_IP14048_18O16O_S2898C_3A_Ba_2@1	81-68A-65	17.77	0.17
P1333B_M1269_IP14048_18O16O_S2898C_3A_Ba_2@2	81-68A-65	17.63	0.26
P1333B_M1269_IP14048_18O16O_S2898C_3A_Ba_2@6	81-68A-65	17.69	0.21
P1333B_M1269_IP14048_18O16O_S2898C_3A_Ba_2@8	81-68A-65	17.63	0.22
P1333B_M1269_IP14048_18O16O_S2898C_3A_Ba_2@10	81-68A-65	17.64	0.22
P1333B_M1269_IP14048_18O16O_S2898C_3C_Ba_3@1	81-68A-65	17.52	0.23
P1333B_M1269_IP14048_18O16O_S2898C_3C_Ba_3@2	81-68A-65	17.57	0.21
P1333B_M1269_IP14048_18O16O_S2898C_3C_Ba_3@3	81-68A-65	17.73	0.30
P1333B_M1269_IP14048_18O16O_S2898C_2-1_Ba_4@3	81-68A-65	17.59	0.22
P1333B_M1269_IP14048_18O16O_S2898C_2-1_Ba_4@4	81-68A-65	17.55	0.23
P1333B_M1269_IP14048_18O16O_S2898C_2-1_Ba_4@5	81-68A-65	17.63	0.26
P1333B_M1269_IP14048_18O16O_S2898C_2-1_Ba_4@6	81-68A-65	17.63	0.31
P1333B_M1269_IP14048_18O16O_S2898C_2-3_Ba_5@1	81-68A-65	17.60	0.22
P1333B_M1269_IP14048_18O16O_S2898C_2-3_Ba_5@2	81-68A-65	17.64	0.21
P1333B_M1269_IP14048_18O16O_S2898C_2-3_Ba_5@3	81-68A-65	17.66	0.22

Table B.3. (cont.)

Spot ID	Sample	δ18O (‰ SMOW)	2σ (‰)
P1333B_M1269_IP14048_18O16O_S2899A_3B_Ba_1@1	81-68A-69	17.38	0.27
P1333B_M1269_IP14048_18O16O_S2899A_3B_Ba_1@2	81-68A-69	17.48	0.26
P1333B_M1269_IP14048_18O16O_S2899A_3C_Ba_3@1	81-68A-69	17.46	0.25
P1333B_M1269_IP14048_18O16O_S2899A_3C_Ba_3@2	81-68A-69	17.43	0.27
P1333B_M1269_IP14048_18O16O_S2899A_3C_Ba_3@3	81-68A-69	17.15	0.26
P1333B_M1269_IP14048_18O16O_S2899A_3C_Ba_3@7	81-68A-69	17.38	0.21
P1333B_M1269_IP14048_18O16O_S2899F_3E_Ba_1@1	81-68A-69	17.46	0.21
P1333B_M1269_IP14048_18O16O_S2899F_3E_Ba_1@2	81-68A-69	17.24	0.22
P1333B_M1269_IP14048_18O16O_S2899F_3E_Ba_1@3	81-68A-69	17.34	0.30
P1333B_M1269_IP14048_18O16O_S2899F_3E_Ba_1@4	81-68A-69	17.08	0.24
P1333B_M1269_IP14048_18O16O_S2899F_3E_Ba_1@5	81-68A-69	17.22	0.20
P1333B_M1269_IP14048_18O16O_S2899F_3E_Ba_1@6	81-68A-69	17.39	0.25
P1333B_M1269_IP14048_18O16O_S2899F_3E_Ba_1@7	81-68A-69	17.28	0.24
P1333B_M1269_IP14048_18O16O_S2899F_3E_Ba_1@8	81-68A-69	17.43	0.23
P1333B_M1269_IP14048_18O16O_S2899F_3B_Ba_4@1	81-68A-69	17.29	0.23
P1333B_M1269_IP14048_18O16O_S2899F_3B_Ba_4@2	81-68A-69	17.16	0.23
P1333B_M1269_IP14048_18O16O_S2899F_3B_Ba_4@3	81-68A-69	17.17	0.28
P1333B_M1269_IP14048_18O16O_S2899F_3B_Ba_4@5	81-68A-69	17.40	0.20
P1333B_M1269_IP14048_18O16O_S2899F_3B_Ba_4@6	81-68A-69	17.31	0.21
P1333B_M1269_IP14048_18O16O_S2899F_3G_Ba_5@6	81-68A-69	17.35	0.20
P1333B_M1269_IP14048_18O16O_S2899F_3G_Ba_5@4	81-68A-69	17.29	0.22
P1333B_M1269_IP14048_18O16O_S2899F_3G_Ba_5@3	81-68A-69	17.35	0.30
P1333B_M1269_IP14048_18O16O_S2899F_3G_Ba_7@1	81-68A-69	17.23	0.16
P1333B_M1269_IP14048_18O16O_S2899F_3G_Ba_7@2	81-68A-69	17.27	0.21
P1333B_M1269_IP14048_18O16O_S2899F_3G_Ba_7@3	81-68A-69	17.36	0.20
P1333B_M1269_IP14048_18O16O_S2900A_3A_Ba_2@1	81-68A-54B	17.98	0.24
P1333B_M1269_IP14048_18O16O_S2900A_3A_Ba_2@6	81-68A-54B	17.36	0.24
P1333B_M1269_IP14048_18O16O_S2900A_3B_Ba_1@1	81-68A-54B	17.21	0.30
P1333B_M1269_IP14048_18O16O_S2900A_3A_Ba_2@3	81-68A-54B	17.85	0.29
P1333B_M1269_IP14048_18O16O_S2900B_3E_Ba_1@1	81-68A-54B	18.00	0.30
P1333B_M1269_IP14048_18O16O_S2900B_3E_Ba_1@2	81-68A-54B	18.07	0.23
P1333B_M1269_IP14048_18O16O_S2900B_3E_Ba_1@3	81-68A-54B	18.08	0.24
P1333B_M1269_IP14048_18O16O_S2900B_3E_Ba_1@6	81-68A-54B	17.98	0.19
P1333B_M1269_IP14048_18O16O_S2900B_3C_Ba_3@1	81-68A-54B	18.21	0.25
P1333B_M1269_IP14048_18O16O_S2900B_3E_Ba_1@4	81-68A-54B	18.01	0.23
P1333B_M1269_IP14048_18O16O_S2900B_3E_Ba_1@5	81-68A-54B	17.82	0.23
P1333B_M1269_IP14048_18O16O_S2900B_3D_Ba_4@1	81-68A-54B	17.87	0.26
P1333B_M1269_IP14048_18O16O_S2900B_3D_Ba_4@2	81-68A-54B	17.97	0.23
P1333B_M1269_IP14048_18O16O_S2900B_3D_Ba_4@4	81-68A-54B	18.02	0.28
P1333B_M1269_IP14048_18O16O_S2900B_3D_Ba_4@5	81-68A-54B	18.26	0.26
P1333B_M1269_IP14048_18O16O_S2900C_3D_Ba_1@1	81-68A-54B	17.59	0.29
P1333B_M1269_IP14048_18O16O_S2900C_3D_Ba_1@2	81-68A-54B	17.95	0.22
P1333B_M1269_IP14048_18O16O_S2900C_3D_Ba_1@3	81-68A-54B	18.00	0.23
P1333B_M1269_IP14048_18O16O_S2900C_3D_Ba_1@4	81-68A-54B	18.01	0.26
P1333B_M1269_IP14048_18O16O_S2900C_3A_Ba_2@1	81-68A-54B	17.98	0.27
P1333B_M1269_IP14048_18O16O_S2900C_3A_Ba_2@4	81-68A-54B	18.07	0.31
P1333B_M1269_IP14048_18O16O_S2900C_3C_Ba_3@2	81-68A-54B	17.70	0.18
P1333B_M1269_IP14048_18O16O_S2900C_3C_Ba_3@1a	81-68A-54B	12.52	0.24

Table B.3. (cont.)

Spot ID	Sample	δ18O (‰ SMOW)	2σ (‰)
P1333B_M1270_IP14049_18O16O_S2907D_2A_Ba_2@4	TU68-3	17.24	0.20
P1333B_M1270_IP14049_18O16O_S2907D_4A_Ba_2@5	TU68-3	17.23	0.19
P1333B_M1270_IP14049_18O16O_S2907D_4A_Ba_2@6	TU68-3	17.32	0.18
P1333B_M1270_IP14049_18O16O_S2907D_4A_Ba_2@7	TU68-3	17.31	0.24
P1333B_M1270_IP14049_18O16O_S2907D_4A_Ba_2@8	TU68-3	17.38	0.22
P1333B_M1270_IP14049_18O16O_S2907E_1A_Ba_1@2	TU68-3	17.02	0.19
P1333B_M1270_IP14049_18O16O_S2907E_1A_Ba_1@3	TU68-3	17.00	0.21
P1333B_M1270_IP14049_18O16O_S2907E_1A_Ba_1@4	TU68-3	16.85	0.14
P1333B_M1270_IP14049_18O16O_S2907E_2E_Ba_2@1	TU68-3	17.13	0.24
P1333B_M1270_IP14049_18O16O_S2907E_2E_Ba_2@2	TU68-3	17.30	0.25
P1333B_M1270_IP14049_18O16O_S2907E_2E_Ba_2@3	TU68-3	17.15	0.18

Appendix C. Fluid inclusion data. Incremental crush fast scan mass spectrometry (C.1.). Fluid inclusion microthermometry (C.2.).

Table C.1.

Sample 86A-22 Q2

#	9285a	9285b	9285c	9285d	9285e	9285f	9285g	9285h	9285j	9285k	Weighted Mean
H_2 (mol. %)	0.000	0.037	0.010	0.000	0.000	0.000	0.000	0.000	0.000	0.000	0.0012
He	0.000	0.000	0.000	0.000	0.000	0.000	0.000	0.000	0.000	0.000	0.0003
CH_4	0.406	0.253	0.208	0.596	0.345	0.395	0.471	0.347	0.500	0.385	0.4129
H_2O	50.08	60.19	47.59	40.55	29.94	39.72	43.00	37.21	46.70	37.25	40.66
N_2	1.33	1.00	1.03	1.59	1.15	1.53	1.17	1.12	1.29	1.03	1.21
H_2S	0.000	0.000	0.000	0.000	0.000	0.000	0.000	0.000	0.000	0.000	0.0002
Ar	0.006	0.002	0.002	0.002	0.001	0.002	0.002	0.003	0.003	0.002	0.0024
CO_2	48.09	38.46	51.08	57.10	68.44	58.19	55.16	61.19	51.31	61.05	57.54
SO_2	0.000	0.000	0.000	0.000	0.000	0.000	0.000	0.000	0.000	0.000	0.0000
C_2H_4	0.000	0.000	0.000	0.000	0.000	0.000	0.000	0.000	0.000	0.000	0.0000
C_2H_6	0.079	0.038	0.051	0.070	0.070	0.105	0.078	0.050	0.070	0.072	0.0692
C_3H_6	0.000	0.000	0.000	0.000	0.000	0.000	0.000	0.000	0.000	0.000	0.0000
C_3H_8	0.012	0.019	0.026	0.090	0.059	0.050	0.116	0.075	0.120	0.217	0.1091
C_4H_8	0.001	0.000	0.000	0.001	0.001	0.000	0.001	0.000	0.001	0.001	0.0006
C_4H_{10}	0.000	0.000	0.000	0.000	0.000	0.000	0.000	0.000	0.000	0.000	0.0002
Benzene	0.000	0.000	0.000	0.000	0.000	0.000	0.000	0.000	0.000	0.001	0.0004
Mols Gas	4.2E-10	2.3E-10	1.9E-10	7.2E-10	6.1E-10	6.3E-10	9.8E-10	1.7E-09	1.2E-09	1.8E-09	8E-09
CO_2 / CH_4	118.3	151.9	245.3	95.7	198.1	147.4	117.1	176.5	102.6	158.5	139.4
N_2/Ar	213.4	541.1	462.0	806.8	892.7	830.8	652.6	367.1	456.6	548.3	548.3
Ar/He	26.1	7.0	9.5	5.7	5.6	7.6	6.4	10.7	12.2	5.4	8.5

Sample 82-86A-37 Q2

#	9286a	9286b	9286c	9286d	9286e	9286f	92986g	9286h	9286j	9286k	Weighted Mean
H_2 (mol. %)	0.000	0.000	0.000	0.000	0.000	0.000	0.000	0.000	0.000	0.000	0.000
He	0.000	0.000	0.000	0.000	0.000	0.000	0.000	0.000	0.000	0.000	0.000
CH_4	0.472	0.292	0.942	1.007	1.139	2.849	1.771	1.242	1.037	0.821	1.031
H_2O	63.37	62.50	49.46	56.51	68.39	57.89	62.15	55.10	53.20	58.49	58.38
N_2	0.675	0.833	1.266	1.127	1.071	1.370	0.918	1.211	1.012	1.089	1.022
H_2S	0.000	0.000	0.001	0.000	0.000	0.000	0.000	0.001	0.001	0.001	0.001
Ar	0.005	0.004	0.004	0.005	0.005	0.005	0.004	0.004	0.004	0.004	0.004
CO_2	35.33	36.26	48.23	41.07	29.30	37.80	34.98	42.32	44.57	39.46	39.40
SO_2	0.000	0.000	0.000	0.000	0.000	0.000	0.000	0.000	0.000	0.000	0.000
C_2H_4	0.000	0.000	0.000	0.000	0.000	0.000	0.000	0.000	0.000	0.000	0.000
C_2H_6	0.035	0.039	0.049	0.057	0.039	0.050	0.057	0.048	0.032	0.037	0.044
C_3H_6	0.000	0.000	0.000	0.000	0.000	0.000	0.000	0.000	0.000	0.000	0.000
C_3H_8	0.118	0.066	0.045	0.219	0.055	0.040	0.123	0.071	0.143	0.100	0.115
C_4H_8	0.002	0.001	0.001	0.001	0.001	0.001	0.001	0.001	0.001	0.001	0.001
C_4H_{10}	0.001	0.000	0.000	0.001	0.000	0.000	0.001	0.001	0.001	0.000	0.001
Benzene	0.001	0.000	0.000	0.001	0.000	0.000	0.001	0.001	0.001	0.000	0.001
Mols Gas	1.96E-09	9.69E-10	9.73E-10	#####	7.61E-10	4.51E-10	1.34E-09	1.53E-09	1.71E-09	1.33E-09	1.31E-08
CO_2 / CH_4	74.9	124.1	51.2	40.8	25.7	13.3	19.8	34.1	43.0	48.1	38.2
N_2/Ar	137.2	206.0	351.5	242.8	204.6	300.1	215.1	278.5	230.3	250.2	548.3
Ar/He	14.1	36.0	23.3	16.1	66.6	47.4	28.6	19.7	19.8	29.4	21.2

Table C.1. cont.

Sample					TYK1-9 Q2					
#	9283a	9283b	9283c	9283d	9283e	9283f	9283g	9283h		Weighted Mean
H_2 (mol. %)	0.000	0.003	0.000	0.000	0.000	0.000	0.002	0.003		0.001
He	0.000	0.000	0.000	0.000	0.000	0.000	0.000	0.000		0.000
CH_4	0.155	0.087	0.043	0.069	0.129	0.015	0.087	0.090		0.095
H_2O	91.34	83.91	94.10	93.37	87.52	97.31	94.72	90.56		91.16
N_2	0.273	0.565	0.754	0.184	0.575	0.068	0.307	0.227		0.384
H_2S	0.002	0.000	0.000	0.000	0.000	0.000	0.000	0.000		0.001
Ar	0.001	0.005	0.009	0.001	0.004	0.001	0.003	0.001		0.003
CO_2	8.22	15.41	5.09	6.36	11.76	2.61	4.88	9.11		8.35
SO_2	0.000	0.000	0.000	0.000	0.000	0.000	0.000	0.000		0.000
C_2H_4	0.000	0.000	0.000	0.000	0.000	0.000	0.000	0.000		0.000
C_2H_6	0.009	0.010	0.002	0.005	0.008	0.002	0.003	0.004		0.006
C_3H_6	0.000	0.000	0.000	0.000	0.000	0.000	0.000	0.000		0.000
C_3H_8	0.003	0.002	0.000	0.002	0.004	0.000	0.001	0.002		0.002
C_4H_8	0.000	0.001	0.000	0.000	0.000	0.000	0.000	0.000		0.000
C_4H_{10}	0.000	0.000	0.000	0.000	0.000	0.000	0.000	0.000		0.000
Benzene	0.000	0.000	0.000	0.000	0.000	0.000	0.000	0.000		0.000
Mols Gas	7.68E-11	4.75E-11	4.64E-11	6.80E-11	7.23E-11	2.33E-11	5.20E-11	3.95E-11		4.26E-10
CO_2 / CH_4	53.2	177.3	118.8	92.4	91.4	177.4	56.1	101.7		88.1
N_2/Ar	255.8	118.0	82.9	247.6	156.5	90.5	111.0	300.8		131.9
Ar/He	26.1		316.7	13.7	2775.9		59.9	13.0		95.6

Sample					TYK1-11 Q1						
#	9284a	9284b	9284c	9284d	9284e	9284f	9284g	9284h	9284j	9284k	Weighted Mean
H_2 (mol. %)	0.000	0.000	0.000	0.000	0.000	0.000	0.000	0.000	0.000	0.000	0.000
He	0.000	0.000	0.001	0.000	0.000	0.000	0.000	0.000	0.000	0.001	0.000
CH_4	0.197	0.213	0.212	0.230	0.192	0.253	0.248	0.297	0.179	0.219	0.228
H_2O	67.43	52.54	54.47	51.25	54.61	51.29	50.09	58.29	55.03	52.18	53.68
N_2	0.290	0.595	0.433	0.604	0.742	0.732	0.523	0.437	0.428	0.567	0.534
H_2S	0.000	0.000	0.001	0.001	0.001	0.000	0.001	0.001	0.001	0.001	0.001
Ar	0.001	0.001	0.001	0.001	0.000	0.001	0.001	0.001	0.001	0.001	0.001
CO_2	32.06	46.31	44.37	47.61	44.39	47.53	49.01	40.44	43.88	46.63	45.18
SO_2	0.000	0.000	0.000	0.004	0.000	0.000	0.000	0.000	0.000	0.000	0.000
C_2H_4	0.000	0.000	0.000	0.000	0.000	0.000	0.000	0.000	0.000	0.000	0.000
C_2H_6	0.020	0.055	0.014	0.023	0.042	0.038	0.049	0.043	0.039	0.047	0.038
C_3H_6	0.000	0.000	0.000	0.000	0.000	0.000	0.000	0.000	0.000	0.000	0.000
C_3H_8	0.010	0.279	0.493	0.273	0.023	0.157	0.076	0.487	0.440	0.350	0.337
C_4H_8	0.000	0.001	0.001	0.001	0.000	0.001	0.000	0.001	0.001	0.001	0.001
C_4H_{10}	0.000	0.000	0.000	0.000	0.000	0.000	0.000	0.000	0.000	0.000	0.000
Benzene	0.000	0.001	0.001	0.001	0.000	0.000	0.000	0.001	0.001	0.001	0.001
Mols Gas	1.73E-10	2.59E-09	2.85E-09	2.32E-09	5.95E-10	1.85E-09	1.16E-09	2.74E-09	2.76E-09	2.87E-09	1.99E-08
CO_2 / CH_4	163.1	217.6	208.8	207.0	230.7	188.1	197.5	136.1	244.5	212.5	198.4
N_2/Ar	514.9	901.6	650.1	875.0	5064.4	1241.6	864.8	510.0	687.6	1021.7	828.1
Ar/He	100.7	1.8	1.3	2.0	1.1	2.5	3.8	1.9	1.3	1.1	1.6

Table C.1. cont.

Sample						**TYK1-7**				
#	*9287a*	*9287b*	*9287c*	*9287d*	*9287e*	*9287f*	*9287g*	*9287h*		*Weighted Mean*
H_2 (mol. %)	0.000	0.000	0.000	0.000	0.000	0.000	0.000	0.000		0.000
He	0.000	0.000	0.000	0.000	0.000	0.000	0.000	0.000		0.000
CH_4	0.415	0.258	0.201	0.412	0.202	0.225	0.373	0.277		0.295
H_2O	65.62	74.05	73.40	74.05	79.88	75.92	73.83	82.40		74.15
N_2	0.694	0.334	0.343	0.407	0.229	0.417	0.259	0.340		0.379
H_2S	0.000	0.001	0.001	0.000	0.000	0.000	0.000	0.000		0.000
Ar	0.001	0.000	0.001	0.000	0.000	0.000	0.000	0.000		0.000
CO_2	33.15	25.13	25.86	24.85	19.58	23.27	25.25	16.91		24.98
SO_2	0.000	0.000	0.000	0.000	0.000	0.000	0.000	0.000		0.000
C_2H_4	0.000	0.000	0.000	0.240	0.105	0.159	0.227	0.065		0.096
C_2H_6	0.055	0.046	0.046	0.000	0.000	0.000	0.000	0.000		0.022
C_3H_6	0.000	0.000	0.000	0.000	0.007	0.000	0.000	0.008		0.001
C_3H_8	0.067	0.168	0.141	0.040	0.000	0.008	0.061	0.000		0.074
C_4H_8	0.001	0.001	0.001	0.001	0.000	0.001	0.001	0.000		0.001
C_4H_{10}	0.000	0.001	0.001	0.001	0.000	0.001	0.001	0.000		0.001
Benzene	0.000	0.002	0.002	0.001	0.000	0.001	0.001	0.000		0.001
Mols Gas	1.44E-09	1.97E-09	2.00E-09	1.52E-09	1.11E-09	1.55E-09	1.67E-09	6.68E-10		1.19E-08
CO_2 / CH_4	*79.8*	*97.6*	*128.7*	*60.3*	*96.9*	*103.3*	*67.7*	*60.9*		*84.8*
N_2/Ar	*1205.1*	*748.2*	*474.2*	*2434.2*	*2362.3*	*5463.4*	*2878.8*			*1194.9*
Ar/He	2.8	1.0	1.7	1.0	1.3	0.6	0.6	0.0		1.3

Sample						**TYK1-9 Q1**				
#	*9288a*	*9288b*	*9288c*	*9288e*	*9288f*	*9288g*	*9288h*	*9288j*	*9288k*	*Weighted Mean*
H_2 (mol. %)	0.000	0.001	0.000	0.000	0.001	0.001	0.001	0.002	0.000	0.000
He	0.000	0.000	0.000	0.000	0.000	0.000	0.000	0.000	0.000	0.000
CH_4	0.158	0.124	0.192	0.190	0.114	0.109	0.112	0.101	0.115	0.145
H_2O	85.91	79.24	74.22	81.41	79.65	79.53	78.54	79.02	77.01	78.29
N_2	0.399	0.332	0.377	0.386	0.324	0.339	0.363	0.303	0.306	0.352
H_2S	0.000	0.000	0.000	0.000	0.000	0.000	0.000	0.000	0.000	0.000
Ar	0.000	0.000	0.002	0.000	0.000	0.000	0.000	0.000	0.000	0.001
CO_2	13.48	20.28	24.90	17.93	19.88	19.99	20.87	20.53	22.38	21.06
SO_2	0.000	0.000	0.000	0.000	0.000	0.000	0.000	0.000	0.000	0.000
C_2H_4	0.050	0.028	0.290	0.076	0.029	0.029	0.105	0.047	0.167	0.136
C_2H_6	0.000	0.000	0.000	0.000	0.000	0.000	0.000	0.000	0.000	0.000
C_3H_6	0.003	0.001	0.021	0.002	0.001	0.002	0.010	0.003	0.021	0.011
C_3H_8	0.000	0.000	0.000	0.000	0.000	0.000	0.000	0.000	0.000	0.000
C_4H_8	0.000	0.000	0.001	0.001	0.000	0.000	0.001	0.000	0.001	0.001
C_4H_{10}	0.000	0.000	0.001	0.001	0.000	0.000	0.000	0.000	0.000	0.000
Benzene	0.000	0.000	0.001	0.000	0.000	0.000	0.000	0.000	0.000	0.000
Mols Gas	5.05E-10	3.88E-10	1.73E-09	8.70E-10	3.59E-10	4.64E-10	8.78E-10	5.64E-10	1.23E-09	6.99E-09
CO_2 / CH_4	*85.4*	*163.9*	*129.7*	*94.5*	*174.8*	*183.4*	*186.6*	*203.1*	*195.3*	*145.4*
N_2/Ar	*5836.0*		*194.7*				*827.2*		*35253.1*	*650.4*
Ar/He	1.1	0.0	13.9	0.0	0.0	0.0	6.8	0.0	0.1	6.4

Table C.1. cont.

#	9290a	9290b	9290c	9290d	9290e	9290f	9290g	9290h	Weighted Mean
Sample					TY71-13 Q2				
H_2 (mol. %)	0.000	0.000	0.000	0.000	0.000	0.000	0.000	0.000	0.000
He	0.000	0.000	0.000	0.000	0.000	0.000	0.000	0.000	0.000
CH_4	0.246	0.189	0.226	0.202	0.181	0.220	0.199	0.210	0.209
H_2O	69.71	77.90	78.88	63.46	74.24	74.43	63.55	68.08	69.46
N_2	0.721	0.720	0.710	0.746	0.670	0.611	0.771	0.407	0.667
H_2S	0.000	0.000	0.000	0.000	0.000	0.000	0.000	0.000	0.000
Ar	0.004	0.002	0.001	0.001	0.002	0.002	0.002	0.001	0.002
CO_2	28.88	21.02	20.09	35.10	24.65	24.52	34.90	30.92	29.28
SO_2	0.000	0.000	0.000	0.000	0.000	0.000	0.000	0.000	0.000
C_2H_4	0.226	0.152	0.085	0.204	0.213	0.176	0.237	0.331	0.219
C_2H_6	0.000	0.000	0.000	0.000	0.000	0.000	0.000	0.000	0.000
C_3H_6	0.000	0.018	0.000	0.000	0.000	0.000	0.000	0.000	0.001
C_3H_8	0.206	0.000	0.008	0.278	0.048	0.045	0.344	0.053	0.156
C_4H_8	0.001	0.000	0.000	0.001	0.001	0.001	0.001	0.001	0.001
C_4H_{10}	0.001	0.000	0.000	0.001	0.000	0.000	0.001	0.001	0.001
Benzene	0.001	0.000	0.000	0.001	0.000	0.000	0.001	0.001	0.001
Mols Gas	2.15E-09	1.09E-09	1.05E-09	2.87E-09	1.81E-09	1.79E-09	2.79E-09	2.49E-09	1.60E-08
CO_2 / CH_4	117.3	111.4	89.1	173.8	136.4	111.4	175.4	147.0	140.2
N_2/Ar	189.6	434.6	848.1	554.9	345.4	345.9	371.2	433.1	362.1
Ar/He	15.7	24.0	10.4	2.9	14.5	15.6	4.9	2.9	6.7

Table C.2.

					Temperature °Celsius					
Sample	Chip	Section	Inclusion #	Mineral	T_mCO_2	T_mICE	T_mCLATH	T_HCO_2	T_mICE	T_H
82-86A-22		E	1		-57					
			2		-57					
82-86A-22*		E	1	Quartz						
			2	Quartz	-56.7		10	16		
			3	Quartz						188
			4	Quartz						188
			5	Quartz						180
			6	Quartz						176
			7	Quartz					-3.5	204
			8	Quartz						193
			9	Quartz					-3.5	172
82-86A-22.1	A	B	1.1	Quartz	-56.9		10	27		
			1.2	Quartz	-56.9		9			
			1.3	Quartz			9			
			1.4	Quartz				27		
			1.5	Quartz					-2	215
			1.6	Quartz					-2.2	208
			1.7	Quartz					-2	203
			1.8	Quartz						194
			1.9	Quartz						200
			1.1	Quartz						208
			1.11	Quartz						200
		C	1.1	Ankerite						251
			1.2	Ankerite						250
			1.3	Ankerite						250
			1.4	Ankerite						252
			1.5	Ankerite						248
82-86A-22.1	B	A	1	Quartz						266
		C	1	Ankerite						216
			2	Ankerite						230
			3	Ankerite						238
TU71-4	1	A	1	Barytocalcite						120
			2	Barytocalcite						126
			3	Barytocalcite						120
			4	Barytocalcite						120
			5	Barytocalcite						120
			6	Barytocalcite						120
			7	Barytocalcite						
			8	Barytocalcite						
			9	Barytocalcite						120
			10	Barytocalcite						130
		B	1	Barytocalcite						
			2	Barytocalcite						
			3	Barytocalcite						
			4	Barytocalcite						
			5	Barytocalcite						
			6	Barytocalcite						
			7	Barytocalcite						136
			1	Barytocalcite						109
			2	Barytocalcite						108
			3	Barytocalcite					-2	110
			4	Barytocalcite						109
			5	Barytocalcite						110
			6	Barytocalcite						125
			7	Barytocalcite						125

Appendix D. Major element oxide data (EPMA) for carbonates (D.1.).

Table D.1.

	Wt. %					
	MgO	CaO	MnO	FeO	SrO	BaO
	Ankerite					
Count	248	248	248	248	156	5
Min	2.80	22.87	0.16	9.08	0.03	0.08
Max	15.52	36.85	2.35	28.27	1.16	0.10
Mean	11.32	27.85	0.89	15.87	0.36	0.09
% SD	17.27	3.47	58.80	17.71	93.43	6.58
	Siderite					
Count	42	43	43	43	3	2
Min	0.01	0.07	0.20	50.66	0.04	0.09
Max	5.70	3.64	1.16	62.11	0.05	0.09
Mean	1.76	0.89	0.59	58.55	0.04	0.09
% SD	84.77	95.63	44.70	4.78	10.17	0.80
	Barytocalcite					
Count	42	86	9	9	86	86
Min	0.01	17.45	0.00	0.00	0.18	51.50
Max	0.12	18.06	0.07	0.07	0.60	54.22
Mean	0.04	17.78	0.03	0.03	0.37	52.59
% SD	51.85	0.73	103.57	87.58	23.61	1.14
	Calcite					
Count	20	20	20	20	7	2
Min	0.08	54.52	0.11	0.35	0.03	0.11
Max	0.32	57.86	0.21	0.73	0.15	0.14
Mean	0.15	56.31	0.15	0.52	0.06	0.12
% SD	41.52	1.44	16.12	21.16	69.43	15.33

Instrumental Detection Limit (3σ)

	MgO	CaO	MnO	FeO	SrO	BaO
	0.03	0.01	0.02	0.03	0.04	0.08

Appendix E. Rare earth elements and yttrium (LA-ICP-MS) data for ankerite (E.1.) and siderite (E.2).

Table E.1.

ID	Mineral	La m139	Ce m140	Pr m141	Nd m146	Sm m147	Eu m153	Gd m157	Tb m159	Dy m163	Y m89	Ho m165	Er m166	Tm m169	Yb m172	Lu m175
TU-70-2_C.4	Ank-1b	0.67	2.04	0.41	2.47	1.56	2.40	2.03	0.36	2.30	12.90	0.44	1.23	0.17	1.00	0.13
TU-70-2_C.5	Ank-1b	1.39	4.01	0.74	4.30	2.46	4.28	3.35	0.53	3.38	18.45	0.60	1.54	0.20	1.16	0.15
TU-70-2_C.6	Ank-1b	1.38	3.55	0.61	3.43	1.90	3.21	2.54	0.43	2.74	14.38	0.47	1.27	0.16	0.97	0.12
TU-70-2_C.11	Ank-1b	0.50	1.52	0.31	1.91	1.22	2.03	1.46	0.25	1.61	7.92	0.29	0.78	0.10	0.66	0.09
TU-70-2_C.12	Ank-1b	1.24	4.28	0.93	5.78	3.71	5.70	4.44	0.67	3.99	20.62	0.69	1.72	0.21	1.24	0.17
TU-70-2_E.2	Ank-1a	0.52	1.30	0.21	1.18	1.02	2.12	1.94	0.37	2.93	17.19	0.62	1.88	0.27	1.74	0.23
82-86A-39_A.1	Ank-1a	0.10	0.23	0.05	0.49	1.36	1.68	3.48	0.71	4.97	27.26	0.91	2.28	0.28	1.62	0.21
82-86A-39_A.2	Ank-1a	0.06	0.16	0.04	0.51	1.37	1.70	3.52	0.68	4.75	27.81	0.86	2.22	0.27	1.56	0.21
82-86A-39_A.4	Ank-1a	0.08	0.19	0.06	0.66	1.71	2.02	4.09	0.79	5.45	31.06	0.97	2.51	0.30	1.81	0.22
82-86A-39_A.5	Ank-1a	0.06	0.16	0.04	0.50	1.39	1.71	3.49	0.65	4.47	26.21	0.79	2.05	0.25	1.41	0.18
82-86A-39_A.6	Ank-1a	0.03	0.13	0.05	0.66	1.82	2.22	4.50	0.86	5.78	34.34	1.05	2.65	0.31	1.76	0.23
82-86A-39_A.8	Ank-1a	0.51	0.92	0.13	0.80	1.33	1.77	4.01	0.79	5.09	30.15	0.87	2.19	0.25	1.32	0.16
82-86A-39_B.2	Ank-1a	0.15	0.36	0.07	0.69	1.68	1.94	3.70	0.72	4.99	26.44	0.91	2.35	0.29	1.74	0.22
82-86A-39_B.4	Ank-1a	0.27	0.94	0.29	3.45	11.15	12.35	25.10	4.85	33.60	197.30	6.24	16.34	2.04	11.68	1.53
82-86A-39_B.7	Ank-1a	0.12	0.39	0.08	0.75	1.84	2.08	4.97	1.03	7.20	43.60	1.32	3.56	0.45	2.97	0.44
82-86A-39_B.8	Ank-1a	0.04	0.17	0.05	0.64	2.00	2.13	3.85	0.73	5.20	28.87	0.94	2.36	0.28	1.78	0.21
82-86A-39_B.10	Ank-1a	0.07	0.21	0.06	0.69	2.00	2.39	4.78	0.92	6.41	37.90	1.18	3.12	0.37	2.20	0.27
82-86A-39_B.11	Ank-1a	0.09	0.25	0.06	0.61	1.75	2.06	4.18	0.81	5.60	32.33	1.03	2.65	0.32	1.84	0.24
82-86A-39_Map1.8	Ank-1a	2.93	5.41	0.55	2.65	2.31	2.85	10.70	3.19	29.40	271.70	8.20	35.70	8.55	90.00	20.59
82-86A-39_Map2.1	Ank-1a	0.50	1.76	0.28	1.46	2.20	2.93	9.96	2.35	16.87	112.30	3.43	10.87	1.67	12.98	2.40
82-86A-39_Map2.3	Ank-1a	0.56	1.72	0.27	1.54	2.19	2.92	9.59	2.24	15.72	105.60	3.15	10.07	1.56	12.04	2.24
82-86A-39_Map2.7	Ank-1a	0.45	1.60	0.28	1.61	2.32	2.38	10.31	2.50	16.90	87.70	2.87	7.18	0.89	5.25	0.63
82-86A-39_Map2.8	Ank-1a	0.42	1.49	0.26	1.54	2.35	2.44	10.28	2.52	17.33	90.60	2.90	7.48	0.93	5.63	0.69
82-86A-39_Map2.11	Ank-1a	0.53	1.65	0.29	1.57	2.21	2.44	10.06	2.42	16.24	93.30	2.87	7.54	0.98	6.05	0.86
82-86A-39_Map2.13	Ank-1a	0.11	0.32	0.06	0.55	1.38	1.87	3.87	0.73	4.80	28.11	0.88	2.19	0.25	1.38	0.18
82-86A-39_C.1	Ank-1b	0.46	1.51	0.28	1.45	2.46	2.57	11.93	2.98	20.86	125.40	3.67	10.16	1.40	9.77	1.58
82-86A-39_C.2	Ank-1b	0.40	1.43	0.24	1.45	2.29	2.56	11.39	2.84	19.64	122.50	3.54	9.81	1.35	9.55	1.65
82-86A-39_C.5	Ank-1a	0.46	1.78	0.31	1.69	2.57	2.56	11.13	2.66	18.08	97.20	3.06	7.44	0.96	5.50	0.64
82-86A-39_C.6	Ank-1a	0.37	1.44	0.24	1.42	2.32	2.43	9.87	2.34	15.69	85.70	2.70	6.64	0.78	4.52	0.50
82-86A-39_C.7	Ank-1a	0.53	1.79	0.31	1.72	2.45	2.65	10.87	2.61	17.61	92.90	3.04	7.49	0.91	5.23	0.59
82-86A-39_D.1a	Ank-1a	0.03	0.11	0.03	0.34	0.90	0.98	2.49	0.48	3.21	17.05	0.59	1.51	0.19	1.16	0.15
82-86A-39_D.1b	Ank-1a	0.04	0.13	0.04	0.36	1.02	0.98	2.48	0.49	3.28	16.80	0.60	1.51	0.20	1.09	0.15
82-86A-39_D.1c	Ank-1a	0.03	0.13	0.04	0.35	1.00	1.14	2.56	0.50	3.46	19.35	0.63	1.63	0.20	1.16	0.16

Table E.1. (cont.)

ppm ID	Mineral	La m139	Ce m140	Pr m141	Nd m146	Sm m147	Eu m153	Gd m157	Tb m159	Dy m163	Y m89	Ho m165	Er m166	Tm m169	Yb m172	Lu m175
82-86A-39_D.1d	Ank-1a	0.07	0.21	0.04	0.32	0.85	0.86	2.22	0.43	2.98	16.36	0.56	1.41	0.18	1.07	0.13
82-86A-39_D.1e	Ank-1a	0.09	0.30	0.05	0.43	1.21	1.29	2.87	0.56	3.65	20.03	0.65	1.70	0.20	1.22	0.15
82-86A-39_D.3	Ank-1a	0.06	0.20	0.04	0.38	0.93	1.05	2.52	0.49	3.39	18.98	0.61	1.58	0.19	1.06	0.14
82-86A-39_D.5	Ank-1a	0.07	0.20	0.05	0.45	1.17	1.28	2.99	0.56	3.87	22.20	0.68	1.75	0.21	1.23	0.16
82-86A-39_D.8	Ank-1a	0.06	0.21	0.06	0.71	2.03	2.38	4.94	0.93	6.30	34.70	1.10	2.78	0.32	1.83	0.24
82-86A-39_D.11	Ank-1a	0.05	0.18	0.04	0.38	1.10	1.12	2.69	0.53	3.50	20.07	0.67	1.74	0.22	1.29	0.16
82-86A-35_A.1	Ank-1a	0.03	0.08	0.02	0.12	0.20	0.28	1.16	0.25	1.73	10.48	0.33	0.89	0.11	0.65	0.09
82-86A-35_A.4	Ank-1a	0.14	0.38	0.07	0.44	0.27	0.33	0.87	0.19	1.28	7.65	0.25	0.66	0.08	0.50	0.07
82-86A-35_A.6	Ank-1a	0.02	0.07	0.01	0.07	0.13	0.18	0.73	0.17	1.22	7.35	0.25	0.66	0.08	0.51	0.07
82-86A-35_A.7	Ank-1a	0.02	0.07	0.01	0.09	0.12	0.18	0.74	0.20	1.52	7.91	0.29	0.83	0.11	0.67	0.10
82-86A-35_A.8	Ank-1a	0.04	0.08	0.01	0.09	0.19	0.25	1.10	0.27	1.97	10.29	0.37	1.02	0.13	0.82	0.12
82-86A-35_B.1	Ank-1a	0.01	0.03	0.01	0.05	0.17	0.19	0.99	0.24	1.74	9.14	0.33	0.83	0.10	0.62	0.08
82-86A-35_B.3	Ank-1a	0.07	0.15	0.02	0.18	0.21	0.34	1.00	0.26	1.96	9.53	0.36	0.99	0.13	0.82	0.12
82-86A-35_B.5	Ank-1a	0.00	0.01	0.00	0.02	0.11	0.19	0.90	0.21	1.48	8.40	0.30	0.78	0.09	0.58	0.08
82-86A-35_B.6	Ank-1a	0.03	0.07	0.01	0.08	0.12	0.17	0.54	0.14	1.05	5.64	0.20	0.53	0.07	0.47	0.07
82-86A-35_B.8	Ank-1a	0.03	0.05	0.01	0.07	0.24	0.27	1.71	0.39	2.98	17.10	0.57	1.44	0.17	0.95	0.12
82-86A-35_B.10	Ank-1a	0.06	0.12	0.02	0.14	0.23	0.25	1.09	0.23	1.61	9.57	0.30	0.77	0.10	0.58	0.08
82-86A-35_C.1	Ank-1a	0.02	0.04	0.01	0.05	0.11	0.20	0.61	0.18	1.31	6.87	0.26	0.67	0.09	0.57	0.08
82-86A-35_C.3	Ank-1a	0.06	0.11	0.01	0.10	0.30	0.49	1.60	0.43	3.37	16.80	0.61	1.70	0.22	1.40	0.19
82-86A-35_C.7	Ank-1a	0.61	2.00	0.40	2.58	1.41	1.74	3.16	0.63	4.39	27.50	0.79	1.98	0.23	1.28	0.17
82-86A-35_D.1a	Ank-1a	0.06	0.11	0.02	0.12	0.23	0.27	1.19	0.26	1.82	10.58	0.35	0.93	0.12	0.72	0.10
82-86A-35_D.1b	Ank-1a	0.03	0.05	0.01	0.07	0.24	0.31	1.52	0.32	2.21	12.15	0.41	1.12	0.13	0.80	0.11
82-86A-35_D.1c	Ank-1a	0.03	0.08	0.01	0.12	0.26	0.28	1.36	0.29	2.05	10.43	0.39	1.06	0.13	0.83	0.12
82-86A-35_D.1d	Ank-1a	0.23	0.45	0.06	0.29	0.30	0.34	1.35	0.31	2.27	12.25	0.42	1.08	0.14	0.84	0.11
82-86A-35_D.1e	Ank-1a	0.11	0.25	0.03	0.17	0.22	0.26	1.17	0.25	1.85	10.24	0.35	0.99	0.13	0.81	0.12
82-86A-35_E.1	Ank-1a	0.04	0.09	0.01	0.09	0.11	0.16	0.59	0.15	1.27	6.10	0.24	0.71	0.09	0.62	0.09
82-86A-35_E.3	Ank-1a	0.13	0.32	0.06	0.32	0.31	0.31	1.36	0.29	2.03	11.69	0.37	0.97	0.11	0.63	0.09
82-86A-35_E.4	Ank-1a	0.23	0.46	0.07	0.40	0.26	0.31	1.01	0.23	1.69	8.74	0.31	0.84	0.10	0.64	0.09
82-86A-35_E.8	Ank-1a	0.08	0.14	0.03	0.14	0.17	0.18	0.71	0.15	1.12	5.68	0.20	0.56	0.07	0.45	0.07
82-86A-35_E.10	Ank-1a	0.38	0.67	0.10	0.51	0.38	0.42	1.38	0.29	2.10	12.29	0.38	1.06	0.13	0.77	0.10
82-86A-35_E.12	Ank-1a	0.80	1.53	0.22	1.17	0.51	0.49	1.24	0.26	1.84	10.89	0.35	0.89	0.11	0.65	0.09

Table E.1. (cont.)

ID	Mineral	La m139	Ce m140	Pr m141	Nd m146	Sm m147	Eu m153	Gd m157	Tb m159	Dy m163	Y m89	Ho m165	Er m166	Tm m169	Yb m172	Lu m175
	ppm															
TYK2-20a_Map1.9	Ank-1a	0.33	1.65	0.48	3.40	2.07	2.32	3.37	0.68	3.96	16.76	0.60	1.45	0.17	1.14	0.16
TYK2-20a_D.1	Ank-1a	0.94	4.38	1.15	7.23	3.34	3.27	5.97	1.30	7.94	34.11	1.27	2.98	0.35	2.16	0.29
TYK2-20a_D.2	Ank-1b	0.77	3.93	1.02	6.51	3.15	3.11	6.46	1.41	8.44	37.20	1.35	3.23	0.38	2.23	0.30
TYK2-20a_D.3	Ank-1a	0.64	3.02	0.79	5.23	2.64	2.51	4.42	0.94	5.51	23.30	0.88	2.07	0.26	1.62	0.23
TYK2-20a_D.4	Ank-1a	0.48	2.60	0.74	4.91	2.66	2.59	4.22	0.89	5.16	21.13	0.80	1.95	0.24	1.59	0.22
TYK2-20a_D.7	Ank-1a	0.56	3.09	0.88	5.84	3.09	2.98	5.05	1.06	6.17	25.14	0.94	2.27	0.28	1.74	0.24
TYK2-20a_D.8	Ank-1a	0.40	2.19	0.64	4.41	2.49	2.57	4.19	0.88	5.15	20.94	0.80	1.93	0.25	1.61	0.23
TYK2-20a_E.5	Ank-1a	0.04	0.24	0.07	0.57	0.44	0.39	1.27	0.30	2.06	10.30	0.34	0.82	0.10	0.52	0.06
82-86A-37_A.1	Ank-1a	0.06	0.19	0.06	0.62	1.60	1.80	3.41	0.66	4.83	26.34	0.89	2.34	0.29	1.70	0.23
82-86A-37_A.2	Ank-1a	0.07	0.22	0.07	0.72	1.86	1.99	3.77	0.71	5.02	29.18	0.95	2.44	0.30	1.85	0.24
82-86A-37_A.3	Ank-1a	0.03	0.13	0.04	0.56	1.74	1.98	3.64	0.71	4.95	28.25	0.92	2.43	0.28	1.71	0.24
82-86A-37_Map3.8	Ank-1a	0.30	0.66	0.11	0.84	1.64	1.94	3.81	0.69	4.67	26.84	0.83	2.01	0.24	1.33	0.17
82-86A-37_C.1	Ank-1b	1.83	5.85	0.87	4.18	1.82	3.41	3.10	0.55	3.53	21.21	0.62	1.55	0.18	1.03	0.12
82-86A-37_C.2	Ank-1b	1.24	3.95	0.57	2.71	1.37	2.91	2.50	0.43	2.79	18.16	0.50	1.17	0.14	0.74	0.09
82-86A-37_C.3	Ank-1b	1.10	3.55	0.51	2.49	1.35	3.03	2.54	0.45	2.92	19.01	0.50	1.22	0.14	0.80	0.10
82-86A-37_C.5	Ank-1b	1.29	4.15	0.63	3.00	1.51	3.08	2.77	0.47	3.07	20.06	0.52	1.32	0.14	0.76	0.10
82-86A-37_C.6	Ank-1b	1.39	5.17	0.84	4.17	1.88	3.15	2.83	0.47	3.19	21.41	0.57	1.45	0.16	0.92	0.12
82-86A-37_C.7	Ank-1b	1.53	5.56	0.88	4.33	1.95	3.25	2.99	0.49	3.45	23.08	0.62	1.60	0.18	1.04	0.12
82-86A-37_D.1	Ank-1b	1.60	5.57	0.83	4.05	1.87	3.40	3.26	0.57	3.81	23.26	0.68	1.69	0.19	1.13	0.14
82-86A-37_D.3	Ank-1b	1.14	4.91	0.92	5.12	2.29	2.63	2.51	0.42	2.94	21.88	0.52	1.35	0.16	0.87	0.10
82-86A-37_D.5	Ank-1b	0.11	0.40	0.12	1.43	3.72	4.91	6.42	0.74	4.00	23.42	0.58	1.27	0.13	0.65	0.07
82-86A-37_E.1	Ank-1a	0.11	0.37	0.08	0.73	1.60	1.83	3.65	0.69	4.68	27.70	0.88	2.18	0.26	1.53	0.20
82-86A-37_E.3	Ank-1a	0.04	0.16	0.05	0.52	1.42	1.59	3.32	0.64	4.78	27.84	0.89	2.34	0.29	1.72	0.22
82-86A-37_E.4	Ank-1a	0.15	0.38	0.08	0.74	1.61	1.95	3.84	0.70	4.81	28.80	0.88	2.24	0.26	1.49	0.19
82-86A-37_E.5	Ank-1a	0.10	0.29	0.07	0.66	1.52	1.86	3.75	0.72	4.81	26.97	0.87	2.13	0.25	1.40	0.18
82-86A-37_F.5	Ank-1a	0.08	0.23	0.06	0.73	1.70	2.17	4.57	0.81	5.28	31.98	0.91	2.16	0.25	1.32	0.17
82-86A-37_F.6	Ank-1a	0.08	0.24	0.06	0.63	1.49	1.85	3.81	0.71	4.76	28.90	0.87	2.14	0.26	1.43	0.17
82-86A-37_F.7	Ank-1a	0.09	0.33	0.09	0.89	2.27	2.68	5.17	0.90	5.93	35.72	1.02	2.47	0.28	1.55	0.19
82-86A-37_F.8	Ank-1a	0.11	0.29	0.07	0.73	1.74	2.03	4.07	0.72	4.93	28.08	0.86	2.08	0.23	1.26	0.16

Table E.2.

ppm		La	Ce	Pr	Nd	Sm	Eu	Gd	Tb	Dy	Y	Ho	Er	Tm	Yb	Lu
ID	Mineral	m139	m140	m141	m146	m147	m153	m157	m159	m163	m89	m165	m166	m169	m172	m175
TU.70-2_A.2	Sd-2b	0.00	0.01	0.00	0.01	0.01	0.02	0.02	0.01	0.06	0.36	0.01	0.04	0.00	0.03	0.00
TU.70-2_A.3	Sd-2b	0.05	0.10	0.02	0.11	0.14	0.20	0.57	0.17	1.62	9.95	0.38	1.11	0.13	0.77	0.09
TU.70-2_A.5	Sd-2b	0.01	0.03	0.01	0.06	0.07	0.14	0.34	0.11	1.17	8.40	0.32	1.11	0.16	0.99	0.14
TU.70-2_B.2	Sd-2b	0.03	0.03	0.01	0.05	0.07	0.13	0.15	0.03	0.21	1.00	0.04	0.08	0.01	0.05	0.01
TU.70-2_B.10	Sd-2b	0.02	0.06	0.01	0.06	0.05	0.10	0.06	0.01	0.10	0.60	0.02	0.04	0.01	0.03	0.00
TU.70-2_C.1	Sd-2b	0.17	0.49	0.11	0.90	0.86	1.27	1.96	0.36	2.49	12.99	0.44	1.16	0.13	0.72	0.09
TU.70-2_D.1	Sd-2b	0.06	0.15	0.02	0.13	0.10	0.11	0.22	0.04	0.36	2.27	0.08	0.32	0.05	0.42	0.07
TU.70-2_D.2	Sd-2a	0.01	0.02	0.00	0.02	0.01	0.02	0.04	0.01	0.13	0.90	0.03	0.12	0.02	0.14	0.02
TU.70-2_D.3	Sd-2b	0.06	0.15	0.02	0.16	0.19	0.32	0.49	0.09	0.72	4.35	0.16	0.53	0.07	0.51	0.06
TU.70-2_D.4	Sd-2b	0.14	0.39	0.06	0.38	0.29	0.44	0.52	0.10	0.75	4.12	0.15	0.46	0.06	0.38	0.05
82-86A-39_Map1.5	Sd-2b	0.25	0.51	0.06	0.34	0.35	0.39	1.67	0.30	1.88	10.45	0.30	0.78	0.11	0.82	0.16
TYK2-20a_B.2	Sd-2a	0.02	0.06	0.01	0.07	0.03	0.05	0.09	0.02	0.15	0.66	0.03	0.11	0.02	0.21	0.04
TYK2-20a_Map3.5	Sd-2a	0.03	0.06	0.01	0.03	0.03	0.04	0.06	0.01	0.11	0.73	0.02	0.10	0.02	0.16	0.03
TYK2-20a_Map3.6	Sd-2a	0.04	0.10	0.01	0.04	0.03	0.04	0.07	0.02	0.13	0.97	0.03	0.12	0.02	0.20	0.03
TYK2-20a_Map3.7	Sd-2a	0.04	0.11	0.02	0.14	0.07	0.11	0.17	0.04	0.27	1.22	0.05	0.17	0.03	0.27	0.05
TYK2-20a_E.1	Sd-2a	0.19	0.46	0.08	0.43	0.18	0.15	0.30	0.06	0.38	1.87	0.07	0.21	0.03	0.24	0.04
82-86A-37_Map3.5	Sd-2b	0.03	0.06	0.01	0.03	0.03	0.04	0.06	0.01	0.11	0.73	0.02	0.10	0.02	0.16	0.03
82-86A-37_Map3.6	Sd-2b	0.04	0.10	0.01	0.04	0.03	0.04	0.07	0.02	0.13	0.97	0.03	0.12	0.02	0.20	0.03

Appendix F. Mineral separate analyses of ^{87}Sr / ^{86}Sr, δ^{18}O and δ^{13}C values in carbonate (F.1.) and δ^{34}S values in sulphides (F.2.)

Table F.1.

Sample ID	Mineral	δ^{13}C$_{PDB}$ (‰)	δ^{18}O$_{VSMOW}$ (‰) TOM	^{87}Sr/^{86}Sr
TYK1-11	Ankerite	-1.5	20.5	
TYK2-14	Ankerite	-2.9	19.0	
TYK2-15	Ankerite	-2.2	19.9	0.7154
TYK2-17	Ankerite	-2.3	20.2	0.7147
TYK2-20	Ankerite	-4.0	17.9	0.7161
TYK2-21b	Ankerite	-5.0	19.9	
TYK4-3	Barium Carbonate	-20.0	15.3	0.7131
T91.14-10	Ankerite	-4.7	13.7	
T91.14-24	Ankerite	-7.1	20.4	
T91.14-27	Ankerite	-2.4	20.3	
TU.65-7	Barium Carbonate	-12.4	15.2	0.7145
TU.67-8	Ankerite	-2.6	20.1	
TU.70-16	Ankerite	-0.5	20.1	
TU.71-4	Ankerite	-2.7	19.1	
TU.71-9	Ankerite	-3.3	19.6	0.7163
TU.71-9a	Ankerite	-3.2	20.3	

Sample ID	Mineral	δ^{13}C$_{PDB}$ (‰)	δ^{18}O$_{VSMOW}$ (‰) JASON	^{87}Sr/^{86}Sr
82-86A-20	Ankerite	-4.7	16.3	
82-86A-21	Ankerite	-2.6	18.2	
82-86A-24	Ankerite	-4.1	16.3	0.7140
82-86A-24.1	Ankerite	-3.6	16.6	
82-86A-26	Ankerite	-3.4	16.9	
82-86A-29B	Ankerite	-4.4	16.0	
82-86A-29C	Ankerite	-2.5	17.8	
82-86A-30	Ankerite	-3.7	16.3	
82-86A-31	Ankerite	-2.5	17.2	0.7168
82-86A-37	Ankerite	-2.1	17.7	0.7165

Table F.2.

Sample ID	Mineral	δ^{34}S
	JASON	
82-86A-20	Galena	17.6
82-86A-24	Galena	16.7
82-86A-24	Pyrrhotite	20.5
82-86A-24	Galena	16.6
82-86A-26	Sphalerite	19.0
82-86A-26	Galena	17.4
82-86A-26	Galena	17.3
82-86A-26	Sphalerite	19.0
82-86A-30	Galena	18.1
82-86A-31	Galena	17.7
82-86A-37	Galena	19.0
82-86A-37	Sphalerite	18.6
	TOM	
TYK2-11	Sphalerite	12.5
TYK2-11a	Sphalerite	10.7
TYK2-13	Sphalerite	10.6
TYK2-14a	Galena	7.7
TYK2-16	Galena	10.8
TYK2-17a	Pyrite	12.7
TYK2-19	Galena	14.2
TYK2-20a	Galena	10.0
TYK2-21	Pyrite	19.3
TYK2-21a	Galena	15.9
TYK3-8	Pyrite	16.4
TYK4-3	Galena	5.2
T91.14e.1	Sphalerite	11.5
T91.14e	Galena	6.5
T91.14-8	Pyrite	11.1
T91.14-10a	Pyrite	10.2
T91.14-10b	Pyrite	9.6
T91.14-27a	Pyrite	-12.6
TU.65-7	Galena	2.4
TU.67-13	Pyrite	-1.6
TU.68-21	Pyrite	8.1
TU.70-2	Pyrite	12.4
TU.70-2a	Sphalerite	13.2
TU.71-9b	Pyrite	12.1
TU.71-9c	Pyrite	10.0